Loughborough University

This item was submitted to Loughborough's Research Repository by the author.
Items in Figshare are protected by copyright, with all rights reserved, unless otherwise indicated.

Modelling and real-time control of a high performance rotary wood planing machine

PLEASE CITE THE PUBLISHED VERSION

PUBLISHER

© Philips Ogun

LICENCE

CC BY-NC-ND 4.0

REPOSITORY RECORD

Ogun, Philips S.. 2019. “Modelling and Real-time Control of a High Performance Rotary Wood Planing Machine”. figshare. https://hdl.handle.net/2134/10133.

Loughborough University

This item was submitted to Loughborough's Institutional Repository (https://dspace.lboro.ac.uk/) by the author and is made available under the following Creative Commons Licence conditions.

creative commons

COMMONS DEED

Attribution-NonCommercial-NoDerivs 2.5

You are free:

- to copy, distribute, display, and perform the work

Under the following conditions:



Attribution. You must attribute the work in the manner specified by the author or licensor.



Noncommercial. You may not use this work for commercial purposes.



No Derivative Works. You may not alter, transform, or build upon this work.

- For any reuse or distribution, you must make clear to others the license terms of this work.
- Any of these conditions can be waived if you get permission from the copyright holder.

Your fair use and other rights are in no way affected by the above.

This is a human-readable summary of the Legal Code (the full license).

Disclaimer

For the full text of this licence, please go to:
http://creativecommons.org/licenses/by-nc-nd/2.5/

Modelling and Real-Time Control of a High Performance Rotary Wood Planing Machine

By

Philips S. Ogun

A doctoral thesis submitted in partial fulfilment of the requirements for the award of Doctor of Philosophy of Loughborough University

July 2012

© by Philips Ogun 2012

Abstract

Rotary planing is one of the most valuable machining operations in the timber processing industry. It has been established that cutting tool inaccuracy and forced vibration during the machining process are the primary causes of surface quality degradation. The main aim of this thesis is to design a control architecture that is suitable for adaptive operation of a wood planing machining in order to improve the quality of its surface finish.

In order to achieve the stated goal, thorough understanding of the effects of machine deficiencies on surface finish quality is required. Therefore, a generic simulation model for synthesising the surface profiles produced by wood planing process is first developed. The model is used to simulate the combined effects of machining parameters, vibration and cutting tool inaccuracy on the resultant surface profiles.

It has been postulated that online monitoring of surface finish quality can be used to provide feedback information for a secondary control loop for the machining process, which will lead to the production of consistently high quality surface finishes. There is an existing vision-based wood surface profile measurement technique, but the application of the technique has been limited to static wood samples. This thesis extends the application of the technique to moving wood samples. It is shown experimentally that the method is suitable for in-process surface profile measurements.

The current industrial wood planing machines do not have the capability of measuring and adjusting process parameters in real-time. Therefore, knowledge of the causes of surface finish degradation would enable the operators to optimise the mechanical structure of the machines offline. For this reason, two novel approaches for characterising defects on planed timber surfaces have been created in this thesis using synthetic data. The output of this work is a software tool that can assist machine operators in inferring the causes of defects based on the waviness components of the workpiece surface finish.

The main achievement in this research is the design of a new active wood planing technique that combines real-time cutter path optimisation (cutting tool inaccuracy compensation) with vibration disturbance rejection. The technique is based on real-time vertical displacements of the machine spindle. Simulation and experimental results obtained from a smart wood planing machine show significant improvements in the dynamic performance of the machine and the produced surface finish quality.

Potential areas for future research include application of the defects characterisation techniques to real data and full integration of the dynamic surface profile measurements with the smart wood planing machine.

Acknowledgements

I give glory to the Almighty God for his grace and protection over my life throughout the period of this research.

I owe my deepest gratitude to Loughborough University and the EPSRC Innovative Manufacturing and Construction Research Centre for awarding me a scholarship.

I am thankful to my supervisors, Professor Mike Jackson and Professor Rob Parkin for their encouragements, guidance and supports. Your feedbacks during our several meetings helped me to develop more confidence in myself and also gain broader knowledge of the subject area. I will also like to thank the technical and administrative staff of the Wolfson School of Mechanical and Manufacturing Engineering for their help.

I do appreciate my friends and colleagues at the Intelligent Automation Research Centre for their contributions, especially Mathavan, Matt, Tuss and Luk.

I am very much indebted to all my family members for their prayers. I thank my father, Mr Pascal Ogun for his love. To my uncle and his wife, Mr and Mrs Thomas M. Ogun, I say a big thank you for your kindness and generosity towards me. My God will reward you.

How can I forget the ladies in my life? I say a big thank you to my wife, Bukola (olo emi). It would have been much more difficult without your help, understanding, cooperation, love and care. Nido my daughter, we can now visit the parks and all the beautiful places.

This thesis is dedicated to my late mother. She was not formally educated but she would definitely be proud of my achievement.

Table of Contents

Abstract ii

Acknowledgements iii

Table of Contents v

List of Figures x

List of Tables xv

Notations xvii

Glossary of Terms ..... **xx**

1 Introduction 1

1.1 Project Background 1

1.2 Research Aim and Objectives 5

1.3 Project Work Breakdown Structure 6

1.4 Existing Facilities for the Project 8

1.5 Research Scope and Methodology 10

1.6 Proposed Control Architecture 10

1.7 Overview 13

2 Literature Review 17

2.1 Rotary Wood Planing – A Brief Review 18

2.1.1 Surface Waviness Quality 18

2.2 Waviness Simulation Algorithms 19

2.3 Surface Quality Improvements 22

2.4 Real-time Optimisation of Process Kinematics 23

2.5 Vibration Control 26

2.5.1 Passive Vibration Control Method 28

2.5.2 Active Vibration Control 30

2.5.3 Semi-Active Vibration Control (SA) 35

2.6 Surface Quality Assessments 39
2.7 Signal and Data Processing Techniques 45
2.8 Adaptive Control 49
2.9 Intelligent Control 54
3 Simulation Model for the Rotary Wood Planing Process 58
3.1 Justification for the New Algorithm 58
3.2 Description of the Algorithm 60
3.3 Generalised Model for the Circular Arc Theory 63
3.4 Model for the Extended Circular Arc Theory 68
3.4.1 Cutting Tool Kinematics Modelling 68
3.4.2 Cutterhead Vibration Modelling 70
3.4.3 Cutterhead Inaccuracy Modelling 73
3.5 Extraction of the Surface Profile 76
3.6 Depth of Cut Consideration 81
3.7 Simulation Examples 82
3.8 Summary and Conclusions 90
4 Dynamic Wood Surface Profile Measurements 91
4.1 Background 91
4.2 Theory of Photometric Stereo and Shape from Shading 93
4.2.1 Surface Albedo Recovery using PS 94
4.2.2 Surface Gradients Recovery using PS 95
4.2.3 Surface Gradients Recovery using SFS 98
4.2.4 Height Recovery from the Surface Gradients 99
4.3 Camera Calibration 99
4.4 Determination of the Optimum Light Source Positions 101
4.5 Recovery of Wood Surface Reflectance Properties (Albedo) 103
4.6 Dynamic Photometric Stereo (DPS) 107

4.6.1 Test Rig Setup 109
4.6.2 Challenges with the DPS 110
4.7 Experimental Results 112
4.8 Summary and Conclusions 115
5 Characterisation of Defects on Planed Timber Surfaces 117
5.1 Introduction 117
5.2 Empirical Mode Decomposition 119
5.2.1 Physical Significance of the IMFs 123
5.2.2 Apriori Knowledge Requirements 128
5.3 Comparisons between EMD and Fourier Analysis 129
5.4 Principal Component Analysis Method 132
5.4.1 Procedure for Applying PCA 133
5.4.2 Significance of the Principal Components 135
5.4.3 Classification of the Principal Components 144
5.5 Considerations for Practical Applications 147
5.6 Summary and Conclusions 149
6 Test Rig Characterisation and System Identification 151
6.1 Sensors and Actuators Arrangement 151
6.2 Spindle Support Operation 156
6.3 Characteristics of the Piezoelectric Actuators 158
6.4 Feed and Cutting Motors Tests 161
6.5 Plant Modelling 164
6.5.1 Background 164
6.5.2 System Identification and Parameter Estimation 167
6.5.3 Input-Output Data Collection 169
6.5.4 Model Parameters Estimation and Validation 175
6.6 Summary and Conclusions 178

7 Optimal Controller Design for the Active Machining System 180

7.1 Principles of the Cutter Run out Compensation 180

7.2 Structure of the Proposed Control System 184

7.3 The Optimal Control Problem 187

7.3.1 Optimal Tracking Controller Design 188

7.3.2 Optimal Observer Design (Kalman Filter) 191

7.3.3 Optimal Linear Quadratic Gaussian (LQG) Compensator Design 192

7.4 Vibration Disturbance Feedforward Compensation 196

7.5 Simulation and Rapid Control Prototyping 201

7.5.1 Control System Simulation 201

7.5.2 Real-Time Testing Environment 204

7.5.3 Real-Time Controller Performance Test 205

7.6 Knowledge-Based Adaptive Control Strategy 213

7.7 Summary and Conclusions 217

8 Experimental Results and Discussions 218

8.1 Planer Rig Closed-loop Performance Tests – Engineering Tests 218

8.2 Influence of cutterhead displacement on the surface form 228

8.3 Wood Machining Experiments - Two-Knife Tests 229

8.4 Wood Machining Experiments - Four-Knife Tests 233

9 Conclusions and Recommendations 242

9.1 Conclusions 242

9.2 Recommendations for Further Work 245

References 247

Appendix A Camera Calibration 257

Appendix B Test Rig State-Space Model 259

Appendix C Simulink Models for the Tracking Controller 260

Appendix D Mitutoyo 543-391B Dial Indicator 263

Appendix E Machine Vision Test Rig Components 264
Appendix F Alicona InfiniteFocus Instrument 271
Appendix G Publications 272

List of Figures

Figure 1.1 Principles of the rotary machining process 2
Figure 1.2 Sharp and jointed cutters (Elmas, 2008) 4
Figure 1.3 Project work breakdown structure 7
Figure 1.4 The small-scale wood planing machine 8
Figure 1.5 The vision-based wood surface measurement system 9
Figure 1.6 Proposed knowledge-based adaptive control architecture 12
Figure 2.1 Non-defective and defective wood surfaces 19
Figure 2.2 Circular arc approximation method 20
Figure 2.3 Surface quality improvement techniques 23
Figure 2.4 Cutterhead advance detail (Brown et al., 2002) 24
Figure 2.5 Cutterhead retract detail (Brown et al., 2002) 25
Figure 2.6 Modification of rotary machining process (Hynek, 2004) 25
Figure 2.7 A structure with three vibration control methods: (a) passive, (b) active, and (c) semi-active configuration (Jalili, 2002) 28
Figure 2.8 Hardware setup for the chatter control test rig (Dohner et al., 2004) 33
Figure 2.9 Structure of saw blade vibration control test rig (Chen et al., 2003) 35
Figure 2.10 Structure of the MR fluid-controlled boring bar (Mei et al., 2009) 37
Figure 2.11 Components of the stylus measurement system 41
Figure 2.12 Image acquisition sequence for the photometric stereo technique 42
Figure 2.13 Gain scheduling adaptive control diagram (Karray and De Silva, 2004) 50
Figure 2.14 Model reference adaptive control diagram (Karray and De Silva, 2004) 51
Figure 2.15 Model identification adaptive control diagram (Karray and De Silva, 2004) 52
Figure 2.16 Structure of the internal model control 56
Figure 3.1 Idealised and the actual surface waviness (Hynek, 2004) 61
Figure 3.2 Fundamental principles of the surface waviness modelling (Jackson, 1986) 63
Figure 3.3 Assumed movements of the workpiece in circular arc theory model 67
Figure 3.4 Assumed cutterhead vibration in circular arc theory model 67
Figure 3.5 Instantaneous positions of the knife tip 70
Figure 3.6 Representation of the rotary machining process of timber 74

Figure 3.7 Effects of coarse sampling of the cutterhead movement 77
Figure 3.8 Calculating the point of intersection between two adjacent curves 79
Figure 3.9 Knife tip paths and the extracted surface profile 80
Figure 3.10 Extraction of cuttermarks height and width 81
Figure 3.11 Depth of cut consideration 81
Figure 3.12 Effect of small depth of cut 82
Figure 3.13 Six-knife finish without any defect 83
Figure 3.14 The effect of proud knives 85
Figure 3.15 Initial cutting conditions of the cutterhead 86
Figure 3.16 The effect of once per revolution vibration on two-knife finish 87
Figure 3.17 The effect of once per revolution vibration on four-knife finish 88
Figure 3.18 The effect of vibration and proud knives on six-knife finish 89
Figure 4.1 Geometry of the generalised Lambertian surface photometric function 93
Figure 4.2 Schematic of the 2-image photometric stereo setup 97
Figure 4.3 Conversion from 3D to 2D profile by column-wise averaging (Yang, 2006) 98
Figure 4.4 Images of wood obtained from different lightening directions 103
Figure 4.5 Beech sample captured with light source at azimuth angle of 0^0 104
Figure 4.6 Beech sample captured with light source at azimuth angle of 150^0 104
Figure 4.7 Beech sample captured with light source at azimuth angle of 180^0 104
Figure 4.8 PS and SFS profiles of a Beech sample with 2.5mm cuttermarks 106
Figure 4.9 PS and SFS profiles of a Spruce sample with 2mm cuttermarks 107
Figure 4.10 Interconnections between the components of the machine vision test rig 110
Figure 4.11 Skewed cuttermarks due to the rolling shutter effect 111
Figure 4.12 Static PS profile vs. Dynamic PS profile for Beech sample 112
Figure 4.13 Static PS profile vs. Dynamic PS profile for Oak sample 113
Figure 4.14 Perfectly matched and 8 pixels mismatched surface profiles 114
Figure 4.15 Perfectly matched and 15 pixels mismatched surface profiles 115
Figure 5.1 The data with the upper and lower envelopes 121
Figure 5.2 The data with the mean of the upper and lower envelopes 121
Figure 5.3 The difference between the data and the mean of the envelopes 121
Figure 5.4 Case 1: (a) The original surface profile; (b) The first intrinsic mode function; (c) The second intrinsic mode function 124

Figure 5.5 Case 2: (a) The original surface profile; (b) The first intrinsic mode function; (c) The second intrinsic mode function 125
Figure 5.6 Case 3: (a) The original surface profile; (b) The first intrinsic mode function; (c) The second intrinsic mode function 126
Figure 5.7 Case 4: (a) The original surface profile; (b) The first intrinsic mode function; (c) The second intrinsic mode function 128
Figure 5.8 Waviness defect produced by extreme values of the vibration amplitude .. 130
Figure 5.9 Defects caused by varying imbalance mass positions 131
Figure 5.10 Vibration recovered from profiles with varying imbalance mass positions 132
Figure 5.11 Four-knife finish with once per revolution vibration defect 136
Figure 5.12 Four-knife finish with once per revolution vibration defect ($\psi = \pi/2$).... 137
Figure 5.13 Four-knife finish with once per revolution vibration defect ($\psi = \pi/4$).... 137
Figure 5.14 Four-knife finish with once per revolution vibration defect ($\psi = \pi/6$).... 137
Figure 5.15 Four-knife finish with once per revolution vibration defect ($\psi = \pi/8$).... 138
Figure 5.16 Four-knife finish with twice per revolution vibration defect 139
Figure 5.17 Four-knife finish with once per two revolutions vibration defect..... 140
Figure 5.18 Six-knife finish with once per revolution vibration defect 141
Figure 5.19 Six-knife finish with twice per revolution vibration defect ($\psi = 0$)..... 142
Figure 5.20 Six-knife finish with twice per revolution vibration defect ($\psi = \pi/10$)... 142
Figure 5.21 The upper, lower and average envelops of a surface profile..... 144
Figure 5.22 Structure of the competitive neural network..... 145
Figure 5.23 The simulated noisy surface profile 147
Figure 5.24 The original and the filtered surface profiles 149
Figure 6.1 Actuators and sensors arrangement on the smart spindle unit..... 152
Figure 6.2 Geometry of the spindle unit 153
Figure 6.3 Experimental setup for the spindle displacement measurements 155
Figure 6.4 Mechanical supports for the spindle 156
Figure 6.5 Vibration of the spindle rotating at 3000rpm..... 157
Figure 6.6 The hysteresis curves for piezoelectric actuator B 160
Figure 6.7 The hysteresis curves for piezoelectric actuator D 160
Figure 6.8 Spindle responses to step voltage inputs..... 162
Figure 6.9 Speed-time graph of the feed motor 163
Figure 6.10 Time-domain response: spindle without cutterhead 172

Figure 6.11 Time-domain response: spindle with cutterhead of mass 106g 172
Figure 6.12 Time-domain response: spindle with cutterhead of mass 190g 173
Figure 6.13 Time-domain response: spindle with cutterhead of mass 293g 173
Figure 6.14 Frequency response function: spindle with cutterhead of mass 293g..... 175
Figure 6.15 Measured and predicted outputs for second order model 176
Figure 6.16 Measured and predicted outputs for fourth order model..... 177
Figure 6.17 Measured and predicted outputs for sixth order model..... 177
Figure 7.1 Principle of the cutterhead inaccuracy compensation..... 181
Figure 7.2 Relationship between pulse width and cutting speed 183
Figure 7.3 Control system with both feedforward and feedback control..... 186
Figure 7.4 Structure of the LQG tracking controller with integral action..... 193
Figure 7.5 Cutterhead and the attached imbalance mass of 116g 197
Figure 7.6 Spindle vibrations against angular positions of the spindle..... 198
Figure 7.7 Real-time measured and generated spindle vibrations 199
Figure 7.8 Tracking response obtained without integral action..... 202
Figure 7.9 Tracking response obtained with integral action..... 202
Figure 7.10 Tracking response for the plant with unknown vibration disturbance..... 203
Figure 7.11 Tracking response for the plant with feedforward vibration compensation 204
Figure 7.12 Schematic of the active wood machining control environment..... 205
Figure 7.13 Tracking response of the spindle (2-knife cutterhead rotating at 2000rpm) 207
Figure 7.14 Tracking response of the spindle (4-knife cutterhead rotating at 1000rpm) 208
Figure 7.15 Tracking response of the spindle (4-knife cutterhead rotating at 3000rpm) 208
Figure 7.16 Comparison between uncontrolled and feedback-controlled vibration ... 210
Figure 7.17 Comparison between uncontrolled and hybrid-controlled vibration 210
Figure 7.18 Tracking response obtained without vibration compensation..... 212
Figure 7.19 Tracking response obtained with hybrid vibration compensation 213
Figure 7.20 The integrated active wood machining system..... 216
Figure 8.1 Trapezoidal pulse..... 219
Figure 8.2 Tracking response of the spindle rotating at 2000rpm 220
Figure 8.3 Tracking response of the spindle rotating at 3000rpm 220

Figure 8.4 Tracking response of the spindle rotating at 4000rpm 221
Figure 8.5 Tracking response of the spindle rotating at 5000rpm 221
Figure 8.6 Controlled and uncontrolled vibration of the spindle rotating at 1000rpm . 223
Figure 8.7 Controlled and uncontrolled vibration of the spindle rotating at 2000rpm . 223
Figure 8.8 Controlled and uncontrolled vibration of the spindle rotating at 3000rpm . 224
Figure 8.9 Controlled and uncontrolled vibration of the spindle rotating at 4000rpm . 224
Figure 8.10 Tracking response of the spindle with imbalance mass at 1000rpm..... 226
Figure 8.11 Tracking response of the spindle with imbalance mass at 2000rpm..... 226
Figure 8.12 Tracking response of the spindle with imbalance mass at 3000rpm..... 227
Figure 8.13 Tracking response of the spindle with imbalance mass at 4000rpm..... 227
Figure 8.14 Two-knife test machined without compensation (Experiment 1)..... 231
Figure 8.15 Two-knife test machined with compensation (Experiment 1)..... 231
Figure 8.16 Two-knife test machined without compensation (Experiment 2)..... 232
Figure 8.17 Two-knife test machined with compensation (Experiment 2)..... 233
Figure 8.18 Four-knife test machined without compensation 234
Figure 8.19 Four-knife test machined with 14µm downward displacement of cutter one 235
Figure 8.20 Four-knife test machined with 14µm downward displacement of cutter two 235
Figure 8.21 Four-knife test machined with 14µm downward displacement of cutter three 236
Figure 8.22 Four-knife test machined with 14µm downward displacement of cutter four 236
Figure 8.23 Four-knife test machined with compensation at 1000rpm..... 237
Figure 8.24 Four-knife test machined with compensation at 4000rpm..... 238
Figure 8.25 Four-knife finish with cutterhead inaccuracy and vibration defects..... 240
Figure 8.26 Four-knife finish with cutterhead inaccuracy and vibration compensation 240

List of Tables

Table 3.1 Surface waviness assessment for example 1 84
Table 3.2 Surface waviness assessment for example 2 85
Table 3.3 Surface waviness assessment for example 3 87
Table 3.4 Surface waviness assessment for example 4 89
Table 3.5 Surface waviness assessment for example 5 90
Table 4.1 Albedo uniformity for various wood samples 106
Table 4.2 Percentage correlation between static and dynamic surface profile measurements for some selected wood samples 113
Table 5.1 Machining Parameters for EMD 123
Table 5.2 Principal components for four-knife finish with once per revolution vibration 136
Table 5.3 Principal components for four-knife finish with once per revolution vibration at varying imbalance positions 138
Table 5.4 Principal components for four-knife finish with twice per revolution vibration 139
Table 5.5 Principal components for four-knife finish with once per two revolutions vibration 140
Table 5.6 Principal components for six-knife finish with once per revolution vibration 141
Table 5.7 Principal components for six-knife finish with twice per revolution vibration 142
Table 5.8 Principal components for ten-knife finish with once per revolution vibration 143
Table 5.9 Principal components for ten-knife finish with once per two revolutions vibration 143
Table 6.1 Spindle displacements measurement 154
Table 6.2 Spindle vibrations due to mass imbalance 157
Table 7.1 Machining parameters for control system simulation 201
Table 8.1 Reference spindle position specifications 219
Table 8.2 Controller efficiency for cutterhead inaccuracy compensation 222
Table 8.3 Controlled and uncontrolled vibration amplitudes 225

Table 8.4 Theoretical and actual uncontrolled vibration amplitudes 225
Table 8.5 Controller efficiency for cutterhead inaccuracy and spindle vibration compensation 228
Table 8.6 Angular positions and static run outs of the two cutting knives 230
Table 8.7 Angular positions and static run outs of the four cutters 233
Table 8.8 Surface finish quality evaluation 239

Notations

a, b	cutterhead centre point
a_i, b_i	cutterhead centre position when the i^{th} knife is engaged with the workpiece
$a(t), b(t)$	instantaneous cutterhead centre point
$b_i(t)$	instantaneous cutterhead vertical displacement for the i^{th} knife (mm)
$c_i(t)$	instantaneous cutterhead horizontal displacement for the i^{th} knife (mm)
d	cutterhead vibration amplitude (mm)
d_{pixel}	workpiece displacement in pixel
d_{rev}	number of displacements per cutterhead revolution
d_t	distance moved by cutterhead (mm)
e	radial position of resultant mass imbalance (mm)
F	imbalance force (N)
G_s	piezoelectric actuator static gain (μm/V)
h	cuttermark height (mm)
h_a	cuttermark actual height (mm)
H	peak-to-peak amplitude of a surface profile (mm)
i	knife index
I	image intensity matrix
I_i	image intensity matrix for the i^{th} frame
I_o	intensity of incident light
$I(x, y)$	intensity of light reflected at local point (x, y)
j	cutterhead revolution index
k	effective stiffness of actuators and spindle support (N/m)
k_1	coefficient of camera lens 2^{nd} order radial distortion

k_2	coefficient of camera lens 4th order radial distortion
k_3	coefficient of camera lens 6th order radial distortion
k_p	piezoelectric actuator stiffness (N/m)
k_s	flexural hinges support stiffness (N/m)
K_x	state feedback gain
K_i	steady state error integral gain
K_r	reference signal feedforward gain
L	Kalman filter gain matrix
m	resultant imbalance mass (kg)
N	number of cutting knives
N_c	number of cuttermarks
N_p	number of peaks in recovered vibration signal
p	cuttermark pitch (mm)
$p_1,\ p_2$	coefficients of tangential distortion
$p(x)$	Gradient of a surface at any local point in the x direction
R	knife radius (mm)
R_i	radius of ith knife (mm)
R_s	radius of reference knife (mm)
R_{max}	maximum peak to valley height of a surface profile (mm)
S_R	camera spatial resolution (pixel/mm)
x, y	point on cutterhead circumference
x_a, y_a	spindle displacements in the actuator coordinate system (mm)
x_d, y_d	original location of distorted point
x_o, y_o	image principal point
x_u, y_u	new location of corrected point

x_s, y_s	spindle displacements measured in the sensor coordinate system(mm)
X	spindle vibration amplitude (mm)
t	time (s)
T	period of cutterhead revolution (s)
T_k	knife-passing period (s)
v_f	feed speed (mm/s)
v_c	cutterhead linear speed (mm/s)
w	cuttermark width (mm)
$y(t)$	instantaneous vertical position of the spindle (mm)
α	phase shift of cutterhead vibration after each revolution (rad)
γ	angle between two successive knives on a cutterhead (rad)
λc	filter cut-off wavelength (mm)
ω	cutting speed (rev/s)
ω_c	cutterhead angular speed (rad/s)
ω_{osc}	frequency of cutterhead oscillation (rad/s)
φ	angle between sensor axis and actuator axis (degree)
ψ	angular position of resultant mass imbalance (rad)
ρ	surface albedo
τ	light source azimuth or tilt angle (rad)
θ	cutterhead angular position (rad)
θ_a	angular position of resultant imbalance mass (rad)
θ_i	cutterhead angular position at the lowest point of the i^{th} knife (rad)
θ_o	initial cutterhead angular position (rad)
$\theta(t)$	instantaneous cutterhead angular position (rad)
σ	light source zenith or slant angle (rad)

Glossary of Terms

Albedo:	A measure of the reflectivity of a surface. It is defined as the fraction of incident light that is being reflected by the surface.
Chatter:	Machining vibrations that occur due to the relative movement between the workpiece and the cutting tool
Cuttermarks:	Waves produced on a rotary planed timber due to the kinematics of the machining process
Jointing:	A term used to describe the dressing of cutting tools in rotary wood planing in order to true all the cutting edges to a common cutting circle
Kerf:	The width of a groove made a cutting tool, such as a saw
Stability lobe:	A tool used to predict and control vibration (chatter) during machining operations

1 Introduction

1.1 Project Background

Machining of parts is central to almost every production and manufacturing process. Modern day machining processes are characterised by subtle material and process element variations, inaccurate tooling conditions, and process disturbances, such as vibration. These undesirable conditions are the main causes of reduced product quality. There is an ever increasing desire to produce components with very high surface integrity requirements. Such requirements have not always been met by existing machinery. There is the need for machines to have some level of awareness of these quality deteriorating conditions and also respond appropriately in order to nullify or minimise their effects.

Research and development interests in actively controlled machining have grown over the years within the academic and industrial communities but the main focus has been on metalworking operations. Nevertheless, wood machining has been an area of research within the Mechatronics Research Group at Loughborough University (MRGLU), where the research work reported in this thesis is being undertaken. A number of novel non-conventional machining techniques and surface profile measurement systems have been developed by previous researchers at the MRGLU. The purpose of the research reported in this thesis is to further improve on the existing ideas, investigate new approaches and finally integrate all the ideas in order to support the development of a high performance wood machining system.

The wood machining operations can be generally classified into orthogonal and peripheral processes. In the orthogonal process, the cutters are in a straight line and are perpendicular to the workpiece; while in the peripheral process, the cutters are located at the periphery of a rotating cutterhead. Most applications within the woodworking industry make use of the rotary machining operations. Rotary planing and moulding are by far the most valuable machining processes in the value-added woodworking industry (Ratnasingham, 2008).

The basic principle of the rotary machining process is such that wood chips are severed from an advancing workpiece by one or more cutting knives, which are clamped into the rotating cutterhead (Figure 1.1). The process is similar to the milling of metal. The primary differences are that the feed speed and the cutting speed in rotary wood planing far exceed those of metal milling. Wood planing is characterised by high cutting speed typically within the range of 30-80m/s, with corresponding high feed speeds ranging from 0.083-1.67m/s (Brown et al., 2002). In industrial planing machines, the cutting knives are usually between four and eight in number and can be as many as twenty for very high feed speed applications (Jackson, 1986). In contrast to the helical cutting edges used in metal milling, the cutting edges are mostly straight in rotary wood machining.

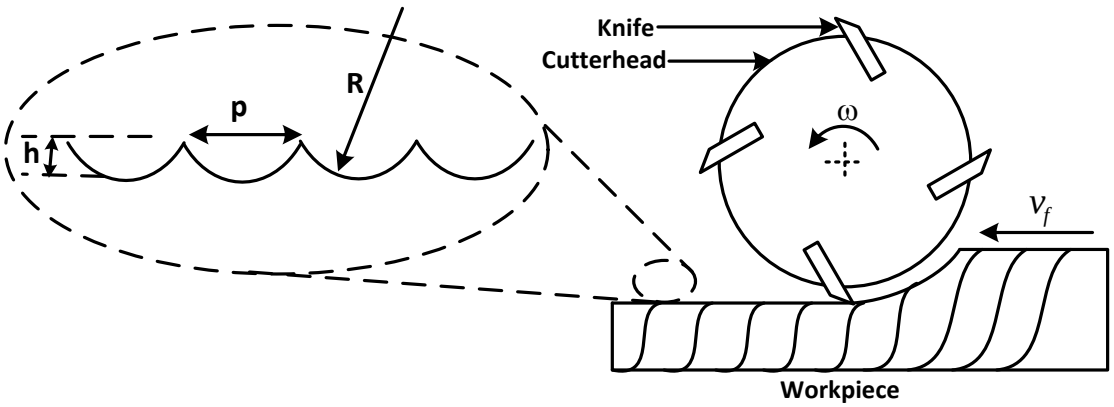


Figure 1.1 Principles of the rotary machining process

The surfaces produced by the planing process will first appear to have a flat topography when viewed from far away distance. However, on close and detailed examination of the surfaces, the majority of the machined surfaces exhibit some wave patterns (known as cuttermarks), which are orthogonal to the workpiece feed direction. The waves results from the intermittent engagement of the cutting knives with the timber.

The primary factors that influence the sizes of the cuttermarks are the machining parameters (number of cutting knives, the radius of the cutting knives, cutting speed and feed speed). These machining parameters are selected by the operators in order to produce the desired waviness pitch and height. However, it has been observed in practice that some conditions such as forced spindle vibration and cutting tool inaccuracy introduce significant surface finish defects. These defects manifest in form of inconsistency and non-uniformity of the cuttermarks. Although waviness defects can also be amplified by the type and condition of the wood being machined, they are generally a function of the machine deficiencies (Jackson, 1986; Sitkei and Magoss, 2003). The planing operation can produce various types of defective surfaces, which have been estimated to reduce the processing yield by almost 27% (Ratnasingham, 2008).

The cutting tool inaccuracy is caused by proud knives or eccentric running of the cutterhead relative to the machined timber surface. Traditional mechanical solution to the problem of cutterhead inaccuracy in the woodworking industry is to apply a process known as *jointing*. Jointing is the term used to describe cutting tool dressing at the spindle speed in order to true all the cutting edges to a common cutting circle (Jackson et. al, 2007). Without the jointing process, the uneven knives produce significant repeating patterns of non-uniform cuttermarks on the workpiece.

The disadvantage of the jointing process is that it introduces "*joint lands*" on the cutting knives thereby removing or decreasing any back clearance angle from the cutter (Figure 1.2). This accelerated tool wear does not only increase the tooling cost, it also increases the normal cutting forces generated during the machining process, and hence increase in power consumption (Jackson et. al, 2007). The jointing can also cause significant variation in cutting forces due to joint land variation from one cutting knife to the other. The resulting cutting force variation will lead to surface defects depending on its severity. In some cases, the jointing device could also modify the cutting tool tracking orbit due to jointer vibration excited by cutterhead imbalance (Jackson et al., 2007). It is noted that this current method used in the woodworking industry to achieve good quality surface finish has disadvantages that defeat its original attractiveness.

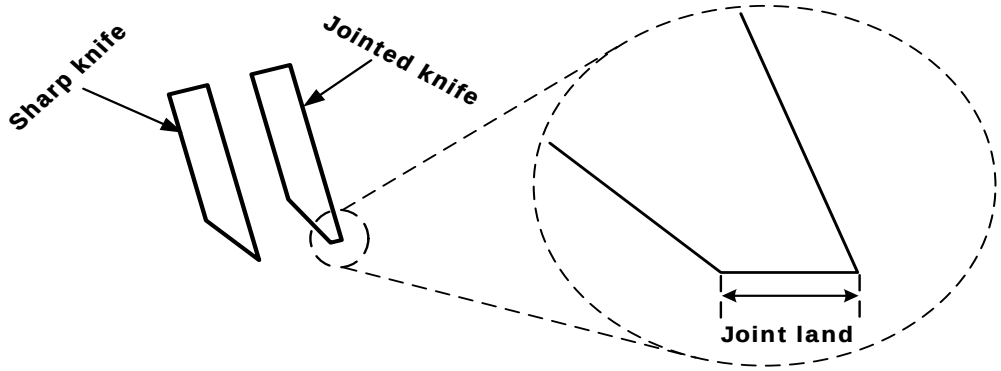


Figure 1.2 Sharp and jointed cutters (Elmas, 2008)

Apart from the cutterhead inaccuracy, structural vibration is another major cause of defects in rotary wood machining. Vibration has been a major inhibitor to high-speed machining as its effects become more pronounced at higher rotational speeds. Vibrations can arise from multiple sources, such as mass imbalances and bearing misalignments. The problem of forced vibration could be tackled through mass balancing, proper bearing alignments, dynamic isolation, or modification of the structural characteristics using tuned dampers.

However, these approaches are passive and would require repeated corrections as they cannot cope with dynamic changes in the system characteristics.

The current state and operations of industrial rotary planing machines indicate that the natural limits of purely mechanical design solutions have been reached (Jackson et al., 2007). Integrated mechatronic solutions that involve the use of sensors and actuators to monitor and adjust the machining process in real-time are required for high performances. The adoption of such holistic approach to machine system design will transform existing machinery from being just mechanical systems that are limited in performance to intelligent machines, which are capable of performing their tasks in the presence of subtle process element and material variations. This will lead to an increase in production efficiency and quality.

1.2 Research Aim and Objectives

The overall aim of this research is to establish a control architecture that is suitable for adaptive operation of a high performance rotary wood planing machining in order to improve the quality of the surface finish produced by the machine. The specific objectives towards achieving this aim are:

- Surface Form Modelling
    - To create a generic and flexible simulation model for rotary wood planing
- Surface Profile Assessments
    - To investigate a range of non-contact surface profile measurement techniques
    - To determine the surface reflectance properties of wood
    - To develop an in-process surface quality monitoring system for wood planing

- Surface Defects Characterisation
    - To investigate a range of data analysis and signal processing techniques
    - To create novel techniques for characterising defects on planed timber surfaces

- Active Wood Machining
    - To create a new active machining technique for wood planing (vibration control and cutting tool inaccuracy compensation)
    - To design a suitable controller for implementing the active machining technique
    - To implement the active machining technique and the designed control system on a smart wood planing machine
    - To perform engineering tests on the smart wood planing machine in order to determine the effects of the active machining technique on the dynamic performance of the machine
    - To perform wood cutting experiments on the smart wood planing machine in order to determine the effects of the active machining technique on the quality of the surface finish produced by the machine

1.3 Project Work Breakdown Structure

The work reported in this thesis is part of a team project involving P. S. Ogun (PSO), who is the author of this thesis, and M. R. Chamberlain (MRC). The work packages are listed as follows:

- Formulation of a generic simulation model for rotary wood planing process (PSO)
- Creation of approaches for characterising defects on planed timber surfaces (PSO)
- Dynamic wood surface profile assessments using vision-based techniques (PSO)
- Design of a controller for an active wood machining system (PSO)

- Design of an expert system for defect characterisation (MRC)
- Generation of an a-priori knowledge base and a high level reasoning mechanism for an intelligent rotary wood machining system (MRC)
- Development of an adaptive controller gain tuning system for an active wood machining system (MRC)
- Creation of a heuristic process adjustment technique based on real-time product quality assessments (MRC)
- Test rig upgrade (MRC)
- System identification (PSO)
- System integration and experimental validation tests (PSO and MRC)

A view of the work breakdown structure is shown in Figure 1.3. The areas in which the work reported in this thesis contributes to the project are shown in the highlighted blocks.

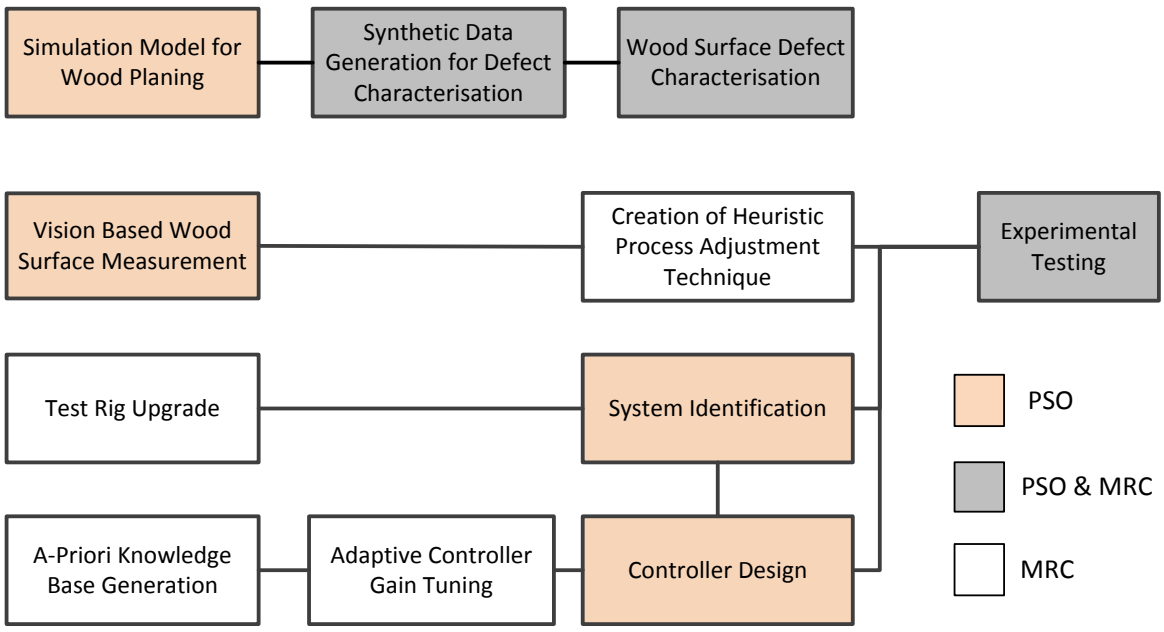


Figure 1.3 Project work breakdown structure

1.4 Existing Facilities for the Project

There is an existing small-scale mechatronic wood planing machine, which was originally designed by Hynek (2004). It was used to carry out preliminary investigations into alternative ways of improving the performance of industrial wood planing machines. The machine is equipped with four piezoelectric actuators for actively controlling the spindle unit. It is instrumented with two non-contact eddy current sensors for measuring the position of the spindle in the plane perpendicular to the spindle axis. The spindle is also equipped with an encoder for measuring its angular position. More details of the design and instrumentation of the machine can be found in Hynek (2004). The test rig has been re-designed for more realistic machining conditions (Figure 1.4) and is also used in this research for experimental validation.

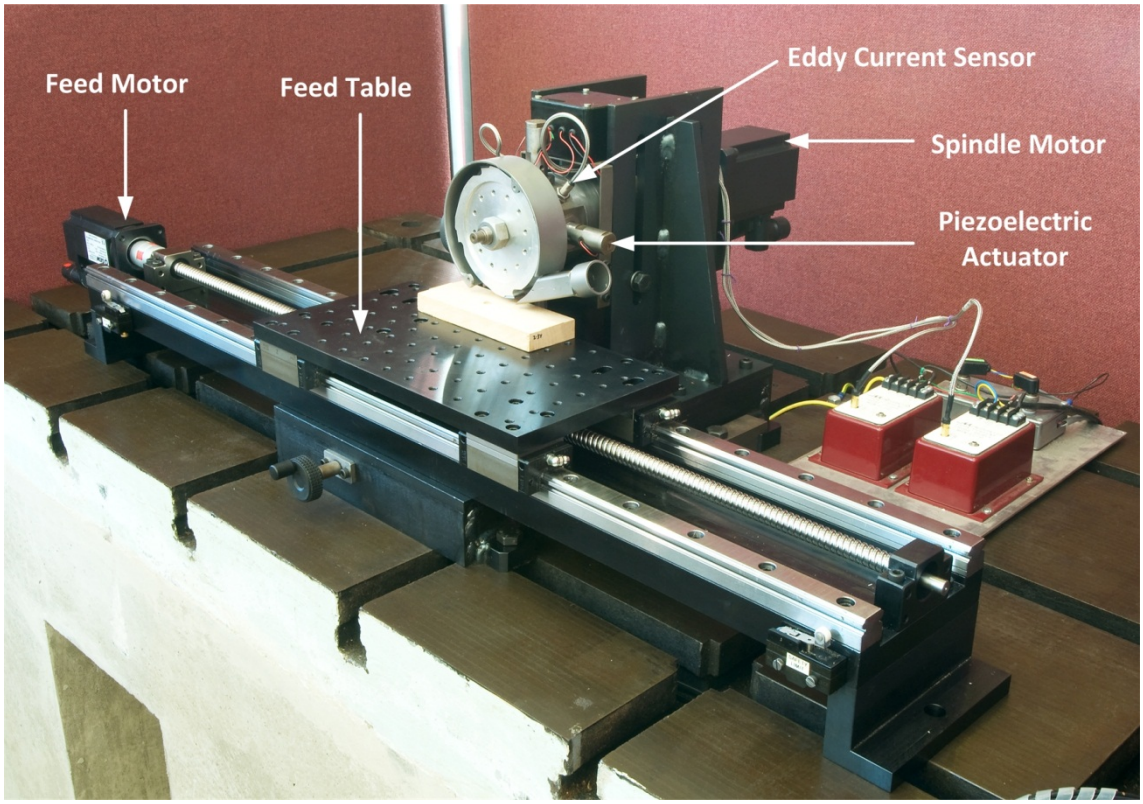


Figure 1.4 The small-scale wood planing machine

It is postulated in Jackson et al. (2002) that in-process surface quality monitoring could be used to provide a secondary control loop for wood machining operations so as to produce consistently high quality surface finish. This led to the design of a vision-based wood surface measurement system by Yang (2006). The system has been constructed to simulate a real machining environment for in-process surface profile assessments (Figure 1.5). Although the test rig was designed to measure dynamic surfaces, only static wood samples were assessed by Yang (2006). Further experiments are performed on the rig in terms of dynamic surface measurements.

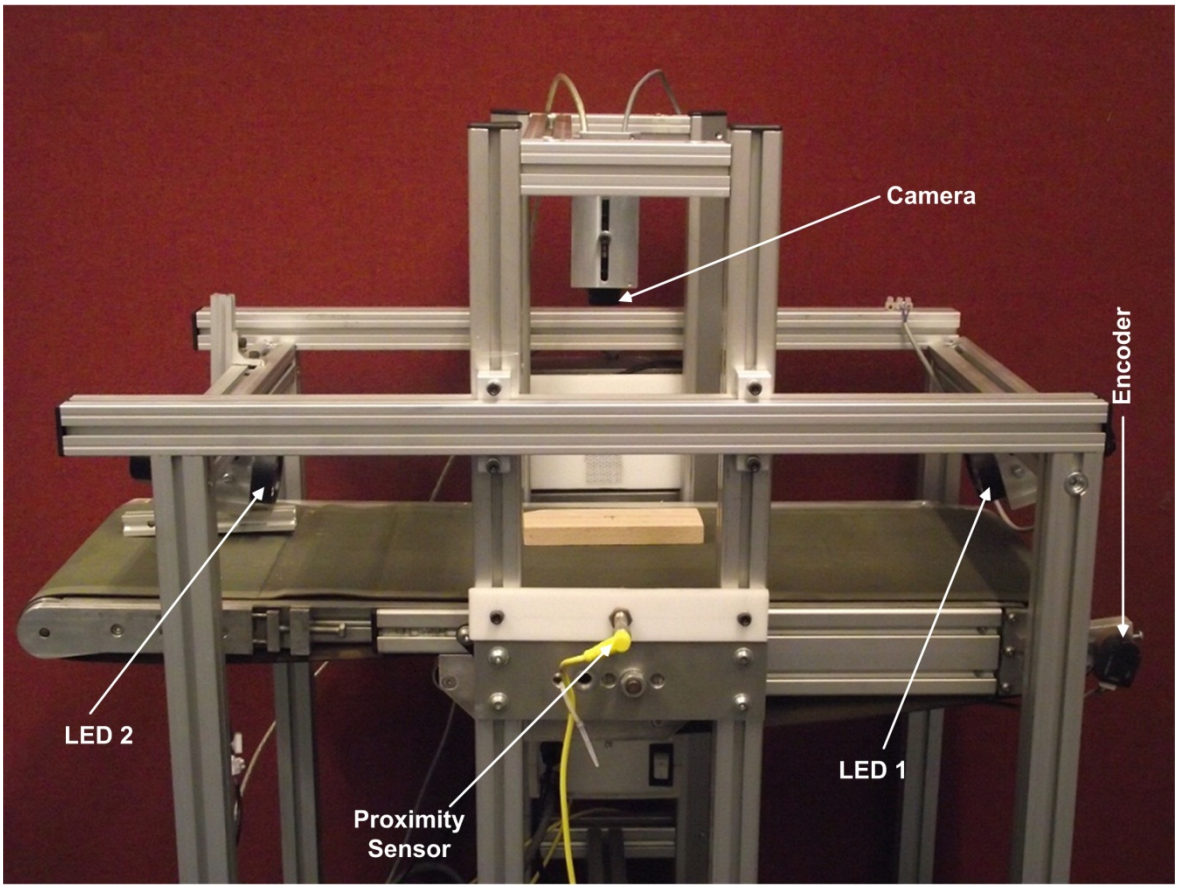


Figure 1.5 The vision-based wood surface measurement system

1.5 Research Scope and Methodology

The research reported in this thesis starts from top level modelling and simulation work in order to examine the fundamentals of mechatronic design and adaptive control approach to the development of a high performance woodworking machine. The model-based approach has been chosen because it allows the design and testing of multiple solutions. Because this approach is software driven, it is possible to explore new concepts, investigate competing designs, and accurately predict the performance and behaviour of the system.

Firstly, a generic simulation algorithm for rotary wood machining process is created. The algorithm is used to investigate the effects of various machine defects on the resultant surface profile. It is also used to generate synthetic data for classification of products quality variation. Further work involves the use of machine vision techniques for in-process assessment of wood surface profile, and initial investigations into established techniques for characterising the defects through the analysis of the surface profile data. It is a well-known fact that there are challenges in using first principles to completely describe the behaviour of dynamic systems. Therefore, data-driven modelling through system identification and parameter estimation is used to develop models of the test rig. Finally, research efforts are directed towards the design of an overall control architecture for achieving an adaptive operation of the machine.

1.6 Proposed Control Architecture

The smart spindle unit of the wood planing machine shown in Figure 1.4 can be used for a number of possible applications. One of them is to achieve a surface waviness height reduction through periodic vertical movement of the cutterhead (Hynek, 2004). Secondly, it can be used to implement an active vibration control system in order to compensate for

the effects of disturbances, such as imbalance forces and cutting forces. The active vibration control is the main subject of study in Elmas (2008). The spindle unit can also be used for cutterhead inaccuracy compensation by displacing the cutterhead based on apriori knowledge of the difference between the finishing knives and a common cutting circle. This has not been thoroughly investigated by any of the previous researchers.

It is common knowledge that cutterhead inaccuracy and structural vibration are the main causes of defects on planed wood surfaces. Therefore, the work reported in this thesis is focused on the design of a single control system that is able to compensate for the cutterhead inaccuracy and at the same time minimise the effects of process disturbances, such as vibration. Although real-time cutter path optimisation and active vibration control have been separately studied by Hynek (2004) and Elmas (2008) respectively, this is the first attempt to design a control strategy that is capable of combining the real-time tool trajectory adjustment with process disturbance compensation. The proposed control architecture is shown in Figure 1.6.

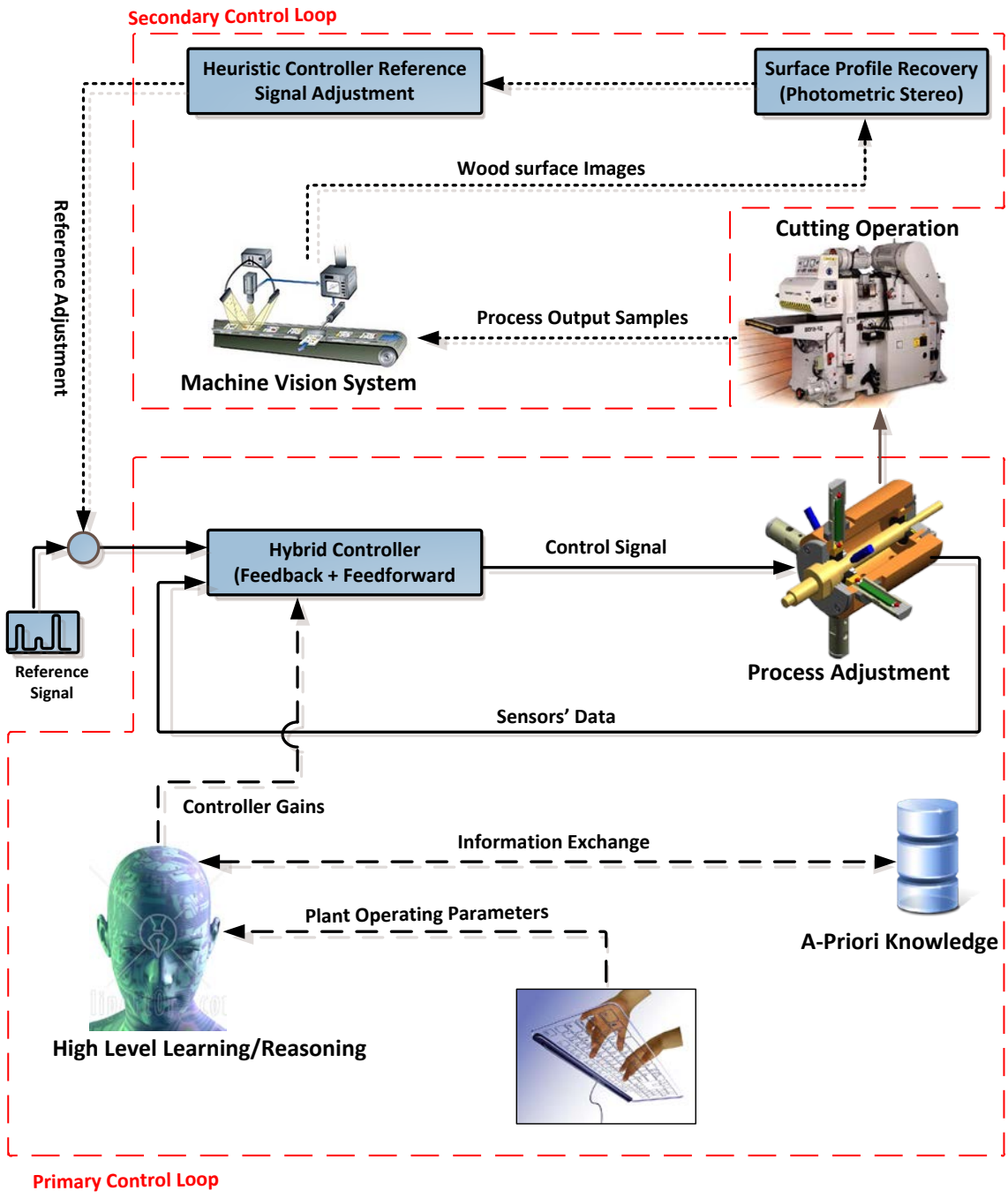


Figure 1.6 Proposed knowledge-based adaptive control architecture

The system consists of a primary and a secondary control loop. The primary control loop is based on real-time monitoring and adjustments of the plant's process parameters. In the primary loop, sensors are used to measure and estimate the dynamic state of the plant; a controller is then used to drive the dynamic state of the plant to a desired state. The desired

state is pre-determined based on apriori knowledge of the machine characteristics and the process disturbances. The only way to ensure that the primary control yields the desired results (improved surface finish) is to have a feedback of the quality of the actual surface finish. The secondary loop then uses the feedback information to adjust the desired state of the plant in a heuristic or algorithmic manner. This approach enables the machine to produce consistently high quality surface finishes because it is able to adjust its actions based on the quality of its outputs.

1.7 Overview

This thesis consists of nine chapters organised as follows:

Chapter 1: The first chapter provides a general introduction to this research. It explains rotary wood machining and the main causes of poor surface quality. It then goes on to discuss the limitations of the current mechanical techniques used in the woodworking industry to improve surface finish quality. The main aim this research and how it is achieved is also discussed in this chapter.

Chapter 2: This chapter presents a review of the research activities that are relevant to the project. Focus is placed on the work related to the development of simulation models for wood machining, surface quality assessments, data processing techniques, and surface quality improvements through vibration control and real-time cutter path optimisation. The review also covers adaptive and intelligent control systems since they are very important elements of this research.

Chapter 3: A new simulation model for rotary wood machining is developed in this chapter. A generalised model for the existing circular arc theory is first formulated so that equations would not have to be derived for each defect case. The main purpose of this is to show that the circular arc theory can be used as a general-purpose simulator. This is then followed by the development of a new simulation model termed extended "circular arc theory". The extended circular arc theory is more flexible and it represents the actual kinematics of the cutting process more accurately than the circular arc theory. Simulation results obtained from the extended circular arc theory are compared with those from the circular arc theory.

Chapter 4: The focus of this chapter is on the in-process measurements of cuttermarks on planed wood surfaces using machine vision techniques. Although this has earlier been investigated by Yang (2006), only measurements of static wood samples were reported. This chapter extends the measurement to moving wood samples and also identifies the key parameters that could possibly introduce measurement errors. One of the recommendations made by Yang (2006) is to find a way to extract the point-by-point albedo of wood samples so as to understand their reflective properties. Consequently, a suitable method that uses a three-image photometric stereo technique is developed to achieve this purpose.

Chapter 5: This chapter is focused on the development of two novel approaches for the analysis and characterisation of defects on planed timber surfaces. The general aim is to develop a software tool that can assist the machine operators to easily infer the machining conditions that produce a particular waviness defect on the workpiece. The two methods investigated are empirical mode decomposition (EMD) and principal component analysis (PCA). Due to the practical difficulty in generating sufficient amount of real machining

data, the techniques are applied to synthetic data generated using the simulation algorithm developed in chapter three. Necessary considerations for practical applications of the methods are also presented.

Chapter 6: Some characterisation tests performed to ensure that the improved rig produces the desired performances under operating conditions are reported in this chapter. The adaptive control system designed in chapter seven requires a state-space model of the plant. The previous researchers have modelled the test rig using finite element (FE) method. The problems with the FE approach are that it is time-consuming and may produce less accurate models of the plant. Moreover, it is not suitable for adaptive control of the plant. An experimental system identification method is used in this research to build mathematical models of the plant from measured input-output data.

Chapter 7: An optimal and adaptive control system for the active wood machining system is designed in this chapter. The primary objective of the control system is to compensate for cutting tool inaccuracy and also reject the effect of cutterhead vibration. The principle behind the cutting tool inaccuracy compensation is clearly explained, followed by the design of a suitable controller. The dynamic performance of the control system is tested both in simulation and on the actual test rig using a real-time rapid prototyping environment known as xPC Target.

Chapter 8: The results of further tests performed on the planer rig in order to determine the limits of its dynamic performance in terms of cutting speeds and vibration amplitudes are presented in this chapter. Results of real wood machining experiments performed in

order to physically investigate the effect of the real-time compensation on the resultant surface finish are also presented and discussed.

Chapter 9: This chapter summarises and concludes the research work and also identifies possible areas of further work.

2 Literature Review

Apart from the Mechatronics Research Group at Loughborough University (MRGLU), two other communities conducting research in the area of wood machining have also been identified. These are the Wood Machining Institute, Berkeley, California, and the North Carolina State University Wood Machining and Tooling Research Program (WMTRP). Similarly to the MRGLU, the mission of the centres is to conduct research aimed at improving wood machining efficiency and wood utilisation.

Generally, research in metal machining has gained more attention than wood machining. Nevertheless, there are a number of practical investigations into rotary wood machining and the different types of waviness defects that can be produced. Suitable methods for assessing the quality of machined wood surfaces have also been investigated. A few other recent researches have focused on the improvement of the machined surface quality through dynamic optimisation of the cutter path and active vibration control. The purpose of this chapter is to review some of these research activities that are relevant to the current project. Outlines of the areas that are covered in this review are given below:

- Rotary wood machining
- Simulation and modelling algorithms for wood planing and metal machining
- Wood surface measurements and assessments
- Data and signal processing techniques
- Vibration control in wood and metal machining
- Adaptive and intelligent control systems

2.1 Rotary Wood Planing – A Brief Review

The principle of the rotary machining of timber has been shown earlier in Figure 1.1 as a process during which wood chips are removed from an advancing workpiece by one or more knives clamped into the rotating cutterhead. The process would superficially appear to be a straightforward operation, which should not attract any significant research interests. Whereas, it is a complex machining operation that provides as much research challenges as metal machining operations.

2.1.1 Surface Waviness Quality

Planed timber surfaces comprise of waves known as cuttermarks. The surface waviness is primarily dependent upon the machining parameters, tooling conditions and any other shortcomings in the mechanical design of the machine that could lead to excessive vibration. The influence of the machining parameters, cutterhead inaccuracy and vibration on the resultant surface waviness has been studied extensively by Jackson (1986).

Other factors that can affect the waviness quality are the cutting forces generated during the machining process. The highly impulsive forces occur with each cutter engagement, and have been typically found to be of the order of 30N to 1000N. Some of the most significant parameters affecting cutting forces are chip thickness, cutter geometry, cutting direction, and the type of timber material being cut (Jackson, 1986).

The surface waviness is the key parameter used in the woodworking industry to determine the quality and production efficiency of the machine. A high quality surface finish is classified by cuttermarks width typically less than *1.5mm*, and cuttermarks width greater than *2.5mm* is typically considered to be a lower quality surface finish (Jackson et al.,

2002). The more the uniformity and consistency of the cuttermarks, the higher the quality rating of the produced surface finish (Figure 2.1).

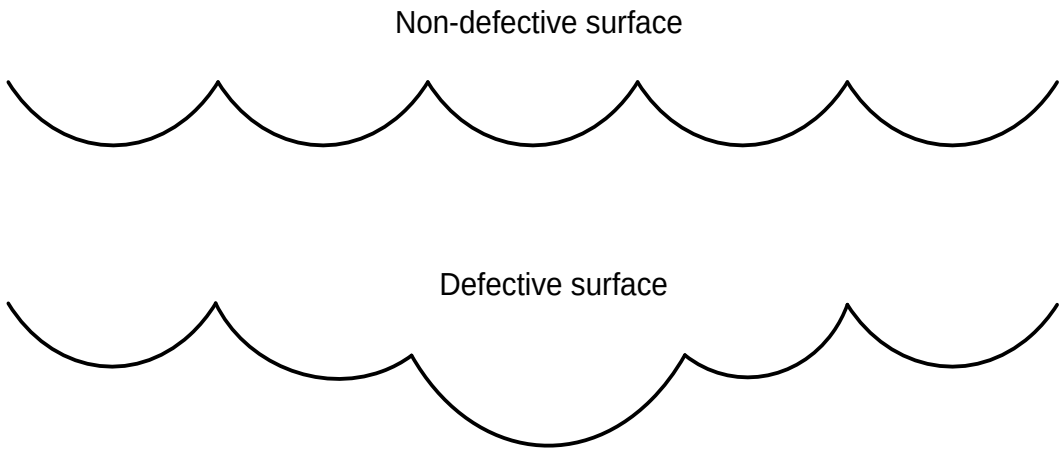


Figure 2.1 Non-defective and defective wood surfaces

2.2 Waviness Simulation Algorithms

Established surface modelling and simulation algorithms for machining processes are required to investigate the effects of various cutting conditions, such as proud knives, spindle vibration, cutting edge wear, multi-knife cutting, and cutting forces on the resultant surface finish. There are some existing algorithms for simulating the topography of the surface produced by the wood planing process. Many simulation models have also been developed for metal milling operations.

A model termed surface-shaping has been developed by Ehmann and Hong (1994) for predicting the topography of the surfaces generated by metal milling operations. The generalised analytical model is based on the kinematics of the machining operations and the geometries of the cutting tools. The model takes into account errors during the machining process, such as machine vibration (chatter) and higher order motions. Similar

models for synthesising surface profile and roughness in high-speed end milling are described in Ismail et al. (1993) and Lee et al. (2001). The algorithms also consider the spindle vibrations, wear and spindle tilt run outs. It is shown that simulated surfaces and actual machined surfaces are in good agreement.

The simulation models that are of more interests are those for surface generation in wood planing. Due to the fact that the cutting edges are usually straight in wood planing compared to the helical shape in metalworking, 2D surface profiles are sufficient to describe the overall surface topography. The first model created for the rotary machining process is based on what is known as the circular arc theory (CAT). It was first used in Goodchild (1963) and later employed extensively in Jackson (1986) and Jackson et al. (2002) to simulate the effects of cutter errors and vertical cutterhead displacements on the quality of the surfaces produced by the wood planing process. The theory approximates the machined surface cuttermarks by using series of intersecting circular arcs with a radius equal to the radius of the cutting knives. The approximation is illustrated in Figure 2.2.

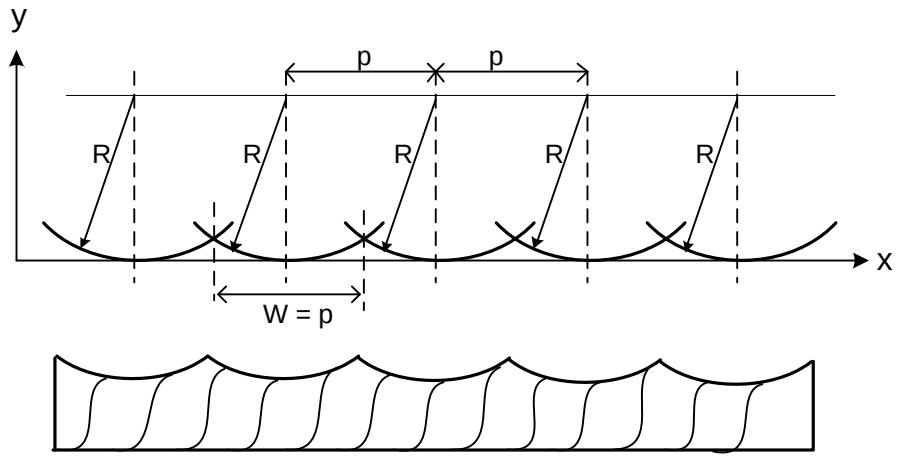


Figure 2.2 Circular arc approximation method

Even though the CAT has the inherent ability to be used as a generalised simulator, it has only been used previously in such a way that different sets of equations are generated for each defect case (Jackson, 1986). This means that the model is not flexible and it cannot be used to simulate generalised defect cases. The CAT makes two simplifying assumptions. Firstly, it assumes that the movement of the workpiece has periodic discontinuities along the feed direction**.** Secondly, when using the CAT to simulate the effects of cutterhead vibrations, it also assumes that the vibration is a rectangular wave instead of a sinusoidal waveform. This means that the CAT represents periodic snapshots of the machining process rather than its actual kinematics.

More accurate algorithms were developed by Maycock (1993) and Brown (1999) . These algorithms are based on surface extraction from the knife tip path, generated as a series of discrete points. Very fine sampling of the cutterhead movement is required in order to achieve good spatial resolution of the resultant surface. The fine sampling is necessary because only an insignificantly small fraction of the knife tip discrete points produce the resultant surface profile. Sophisticated searching algorithms are employed to select those knife tip loci that form the overall resultant surface. It is worth mentioning that there are certain problems associated with the extraction algorithms as reported by the authors.

A more recent algorithm, which addresses some of the above problems in Maycock (1993) and Brown (1999), has been created by Hynek (2004). The algorithm approximates the machined surface by using a set of cubic splines. The algorithm can easily handle the effects of cutterhead vibration and cutterhead inaccuracy without the need for any complicated procedure to find the intersections between adjacent spline functions. However, the author (Hynek, 2004) clearly stated that further processing of the splines is

required in order to obtain information about the sizes of the cuttermarks. Fourier analysis is used to extract information about the frequency contents of the surface waveform. The need for further Fourier analysis of the surface waveform to extract the heights and widths of the cuttermarks is a major limitation of this algorithm**.** This limitation has motivated the creation of a new algorithm described in chapter three.

2.3 Surface Quality Improvements

A number of possible techniques have been devised to improve the quality of rotary planed timber surfaces. An overview of these techniques is presented in Figure 2.3. The categories in which the techniques explored in this thesis fall into are shown in the highlighted blocks.

The mechanical design and setup of the rotating components is very important because a major cause of vibration during the machining process is mass imbalance. It is a condition that occurs when the mass of any of the rotating components is unevenly distributed around the centre of rotation, generating a sinusoidal forced vibration along the cutting plane. There are always some inherent imbalances in the system, which cause the cutterhead to vibrate during the machining process. An active vibration control technique is investigated in this thesis.

The accuracy of cutter tracking is traditionally being improved by jointing the cutting edges in order to minimise the effects of cutter inaccuracy. This process has some disadvantages mentioned earlier in chapter one. For this reason, a new technique that modifies the trajectory of the cutting tool in real-time is explored in this thesis.

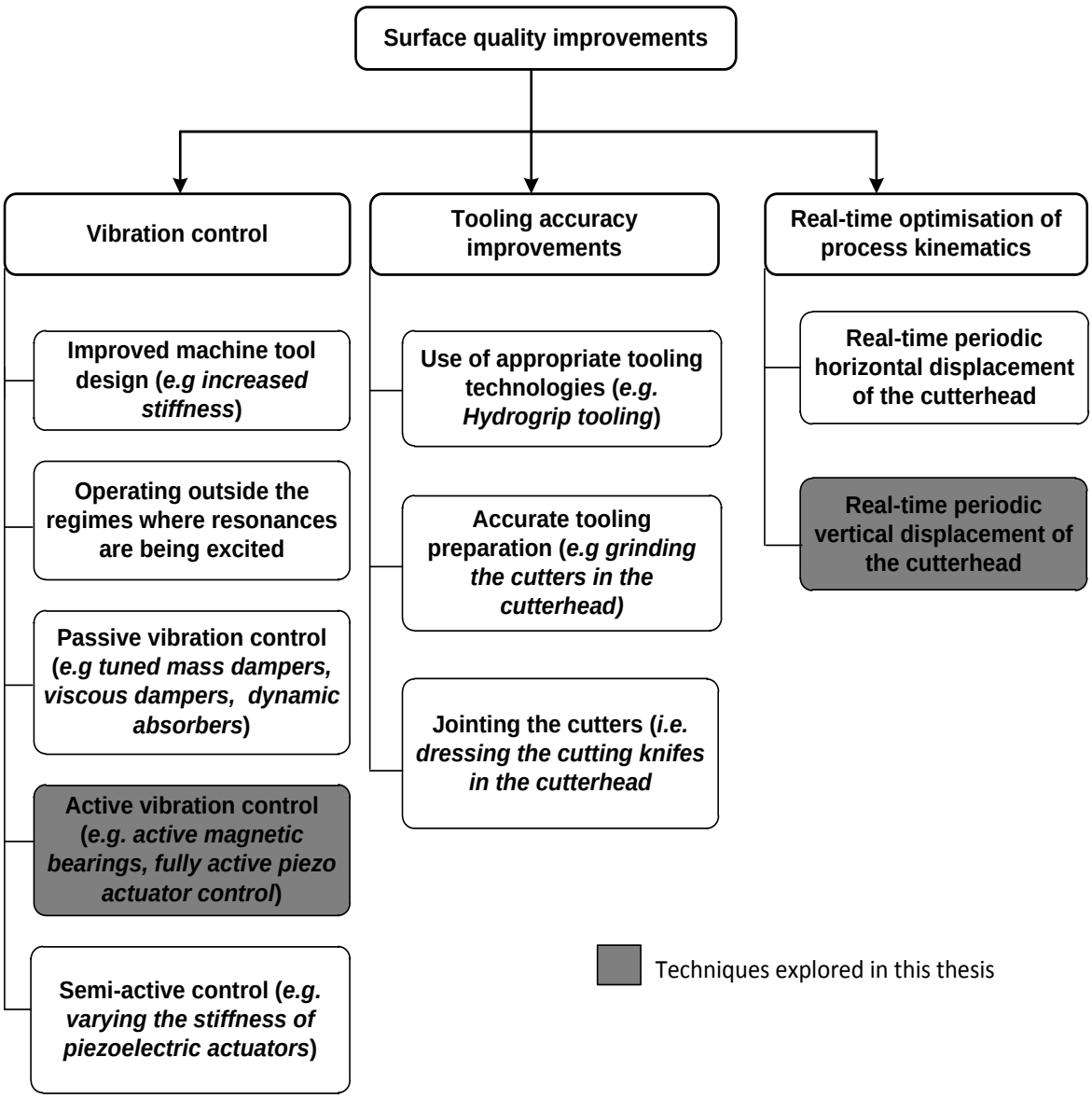


Figure 2.3 Surface quality improvement techniques

2.4 Real-time Optimisation of Process Kinematics

Real-time modifications of the rotary machining process have been investigated by earlier researchers. The first one, being the introduction of additional horizontal cutterhead movement, is reported in Brown (1999), Brown and Parkin (1999), and Brown et al. (2002). The principle of the cutterhead horizontal movement is such that when each knife engages with the workpiece, the cutterhead is advanced in a horizontal plane across the timber surface by a magnitude in the order of the cuttermarks width (Figure 2.4). This is

followed by a retraction of the cutterhead prior to the next knife contacting the workpiece (Figure 2.5). The frequency of these forward and backward movements is related to the knife passing frequency of the cutterhead.

Results show that the modified machining process produces trough-like cuttermarks instead of the conventional scallop-shaped ones. The cuttermarks have reduced heights compared to the ones produced by conventional planing process under the same tooling and machining conditions. It was reported that a perfectly flat surface would be possible if the cutterhead could be stopped from rotating during the horizontal movement. However, the inertia and the kinetic energy due to the cutterhead mass (20-80kg) and rotational speed in the range of 62-1800rad/s would make this to be impracticable. Moreover, the magnitude of the movement is related to the cuttermarks width and its frequency is related to the cutting speed. Therefore, high-speed machining will require actuator with significantly short response time.

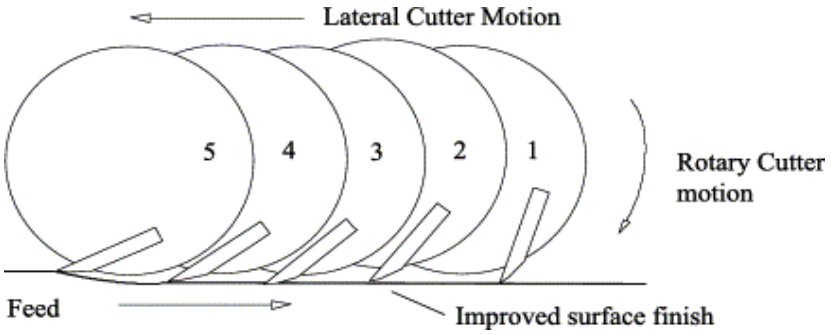


Figure 2.4 Cutterhead advance detail (Brown et al., 2002)

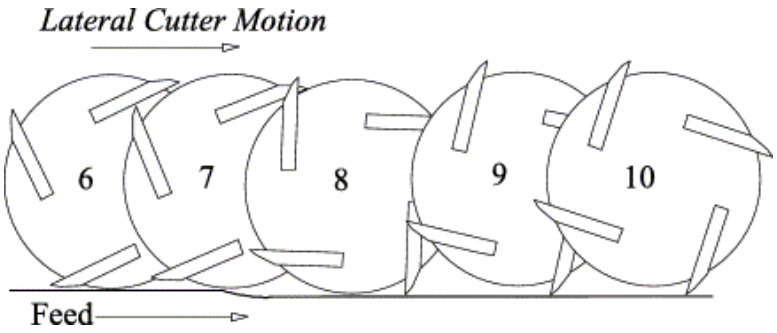


Figure 2.5 Cutterhead retract detail (Brown et al., 2002)

The modification of the machining process kinematics was also studied by Hynek (2004), but a vertical cutterhead movement was introduced instead. The principle of the proposed method is that the cutterhead starts moving upward in a sinusoidal manner when the knife tip is at the start of the cutting path. The cutterhead then starts moving downwards in a similar manner immediately after the knife tip reaches the midpoint of the cuttermark. The idea is illustrated in Figure 2.6.

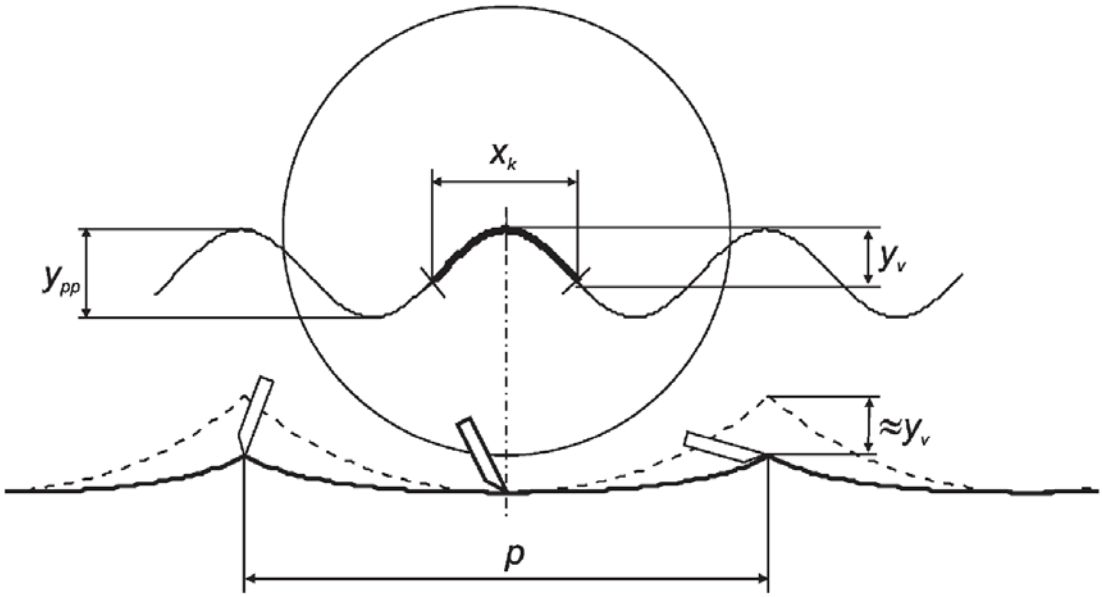


Figure 2.6 Modification of rotary machining process (Hynek, 2004)

The author (Hynek, 2004) pointed out that the proposed method is theoretically capable of completely removing the surface waviness if the vertical cutterhead movement is such that the knife tip follows a straight line for a distance equal to at least the length of the cuttermark. Similarly to the case of additional horizontal movement, the relatively large mass of the cutterhead needs to be controlled within a very narrow time window. The speed of response of commercially available actuators might not be sufficient for high-speed machining. Insertion of the actuators into the knives might provide a more viable solution but this is not the focus of the investigation to be carried out in the current project.

2.5 Vibration Control

Engineers at different levels approach the subject of machine vibration in different ways. From a maintenance engineer's point of view, vibration standards and guidelines are used to monitor the health of equipment for their timely repair and refurbishment. This has moved industries from preventive and corrective maintenance into predictive maintenance practices, which reduce plant downtimes and premature replacement of machine components considerably.

From a design engineer's point of view, vibrations have ever since been major limiting factors in the performance of many industrial machines. A machine design engineer has to recognise the potential sources of vibration and control them within acceptable limits. Vibration occurs in any machining process and it has severe implications on surface quality, tool life and process capability. Minor imbalances in rapidly rotating parts can cause significant vibrations and high dynamic loads on the machine tool components (Rojas et al., 1996). Vibration can also be caused by the cutting forces generated as a result of the relative motion between the cutting tool and the workpiece.

The presence of vibration during machining operations has made it difficult to attain the much desired requirements of productivity and surface quality. Advances in machine tool materials and spindle motor power have opened the possibility of substantially reducing production time and cost through high-speed machining. However, vibration characteristics of machining systems are major limiting factors preventing the utilisation of these advances to full advantage. In metal cutting, vibrations often lead to cutting instability known as machine tool chatter. A detailed technical insight into the effects of vibration in rotary wood machining is reported in (Jackson et al., 2007).

The control of vibration is very important to improve performance efficiency and productivity. The effects of vibration can be minimised in two ways. The first is through modification of the cutting process and the second approach is through modification of the machine dynamic characteristics (Sims and Zhang, 2003).

In the first approach, models that predict vibration (stability lobes) are used to choose cutting conditions that avoid excessive vibration. This involves online optimisation and variation of the cutting parameters (cutting speed and feed speed) so that the cutting process adapts to the dynamic properties of the structure and the machining process always lies in a stable regime (Rashid and Nicolescu, 2006). Examples of such control approaches can be found in Al-Regib et al. (2003) and Ismail and Ziaei (2002). The cutting parameters variation approach is not suitable for the rotary wood planing where constant speed is required to obtain consistent cuttermarks.

In the second approach, the structure of the machine is modified in some ways so as to improve its dynamic characteristics (stiffness and damping). The common classifications of this approach as found in literature are passive, active and semi-active methods. These classifications are based on the amount of external power required for the vibration control system to perform its functions. A simple structure with the three vibration control methods is shown in Figure 2.7.

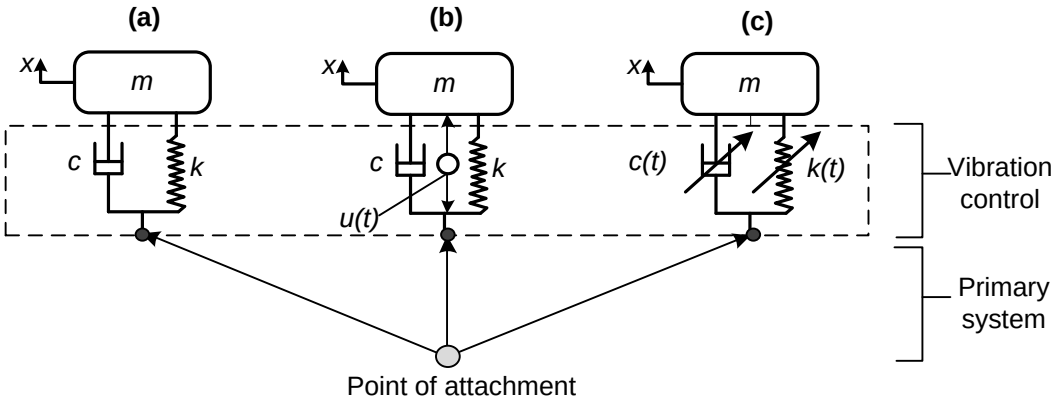


Figure 2.7 A structure with three vibration control methods: (a) passive, (b) active, and (c) semi-active configuration (Jalili, 2002)

2.5.1 Passive Vibration Control Method

The passive methods include the use of dissipative devices, such as viscoelastic materials and viscous dampers, as well as reactive devices, such as tuned mass dampers and dynamic vibration absorbers (Lee et al., 2001). Magnetic dampers and shunted piezoceramic dampers are other elements that are commonly used. Dampers absorb the vibration energy from the primary system and gradually dissipate the energy in form of heat

Vibration problem may be solved in part through proper machine design, which stiffens the machine structure (Pettersson et al., 2001). Vibration in circular wood sawing has been minimised by improving the design of the saw blade such that the stiffness can be increased, thereby shifting the resonance frequency to a higher level in order to minimise vibration (Renshaw, 1998). This approach of altering the dynamic characteristics of the saw blades in a passive way restricts the frequency range and the amplitude of vibration that can be controlled.

Tarng et al. (2000) investigated the use of a piezoelectric inertia actuator, mounted on a cutting tool to act as a tuned vibration absorber for the suppression of chatter in a turning operation. For this system to be effective, the vibration absorber must be tuned such that its natural frequency is equal to the resonance frequency of the cutting tool. The passive vibration control method is very effective within the frequency region of its highest sensitivity but may be of little use at lower frequencies unless devices with high masses are used (Moheimani et al., 2004).

A particular feature of the passive method is that there is no feedback between the vibration absorber and the structure to be controlled. A vibration control system is always required to operate over a wide band load and frequency range, which cannot be met with a single choice of stiffness and damping provided by the passive devices (Rojas et al., 1996). A phenomenon known as “de-tuning” often reduces the effectiveness of passive vibration control systems. This occurs due to deterioration of the structural parameters or variations in the excitation frequency of the primary system. Passive vibration control systems lack versatility because they are unable to adapt to changes in the disturbance or structural

dynamic characteristics. However, they are relatively simpler to implement and much more stable compared to fully active systems.

2.5.2 Active Vibration Control

Technological advancements have led to the emergence of active vibration control techniques as solutions to the limitations of passive control. The active control methods involve the use of sensors to measure the vibration produced by the machine, and actuators to generate the corrective force required to counteract the vibration. It allows for continuously adjustable parameters of the damping and stiffness characteristics based on feedback signals from the sensors.

Boring Process

Boring bars are very susceptible to vibration. Their large length to diameter ratio and associated low dynamic stiffness can make chatter to easily develop during cutting operations. Tewani et al. (1995) investigated the use of an active dynamic absorber to suppress machine tool chatter in a boring bar. The vibrations of the system are reduced by using piezoelectric actuator to generate an inertia force that counteracts the disturbance acting on the main system. Two different control strategies were applied, one which involves the use of acceleration and velocity feedback, and the other which involves obtaining the state-space model of the system and calculating Kalman gains for sub-optimal control. A number of tests were performed for different length to diameter ratios of the boring bar to show the effectiveness of the system.

Another application of active vibration control technology to the boring process is presented in Adkins et al. (1996). In this paper, a two-dimensional electromagnetic

actuator is used as an active vibration absorber to suppress chatter in both radial and tangential directions. The boring bar was modelled as a distributed mass using the finite element methods. A reduced-order feedback controller, which was designed using modal control theory with quadratic performance index, was examined. Simulation results show a significant increase in the damping of the boring bar's vibration.

Turning Process

Choudhury et al. (1997) developed an on-line vibration control system on a turning lathe where the relative vibration between the workpiece and the cutting tool is sensed with a bifurcated bunch of optical fibres. The signal is then fed-back into a specially designed piezoelectric vibrator supporting the tool. When vibration occurs, the closed loop feedback contour, with the help of the vibrator-exciter, generates an equal and opposite force to stabilise the vibration. It is reported that the proposed feedback control system is capable of increasing the quality of the machined surface substantially. Active vibration control in turning using piezoelectric actuator is also reported in Wang and Su (2003).

A demonstration of an active damping technique is also described in Ganguli et al. (2005). The paper is of particular interest because the authors adopted a simulation-based design approach using a mechatronic simulator on the argument that experimental demonstration of regenerative chatter in real machines is difficult due to the involvement of a huge number of parameters. With the mechatronic simulator, it was possible to study chatter in a turning machine without conducting actual cutting tests.

Milling Process

An experimental investigation, which assesses the feasibility of using piezoelectric actuators to control chatter in milling, is described in Zhang and Sims (2005). The authors argued that although chatter can be avoided by choosing stable regions of the workpiece stability lobe, certain limitations prevent the use of this approach in practice. Consequently, a position feedback active vibration controller is used to alter the dynamics of the system. The frequency response is excited using an impact hammer and the output is measured using DSP Siglab equipment and an accelerometer. In order to assess the performance of the system, cutting tests were performed at a range of spindle speeds, repeated with incrementally deeper depths of cut until chatter occurred. It is reported that the control strategy increases the critical depth of cut at which chatter occurred. This resulted into improved surface finish quality.

Active chatter control in milling is also reported in Dohner et al. (2004). The authors also supported the argument made by Zhang and Sims (2005) that variation of process parameters in order to seek regions of stability are not practicable for many ordinary materials as it might require running at speeds where tool wear can be excessive. Therefore, an active vibration control method is used to alter the dynamics of the machine. The vibration is measured with strain gauges and an optimal controller is used to generate control efforts for driving four electrostrictive actuators used to produce force against the rotating spindle. This approach effectively raises the stability limits of the machine, allowing for bigger size of cut. It also allows the machine to be operated within the range of spindle speeds that are much wider than the one without the chatter suppression system. The setup of the test rig is shown in Figure 2.8. Other active vibration control applications can be found in Rashid and Nicolescu (2006).

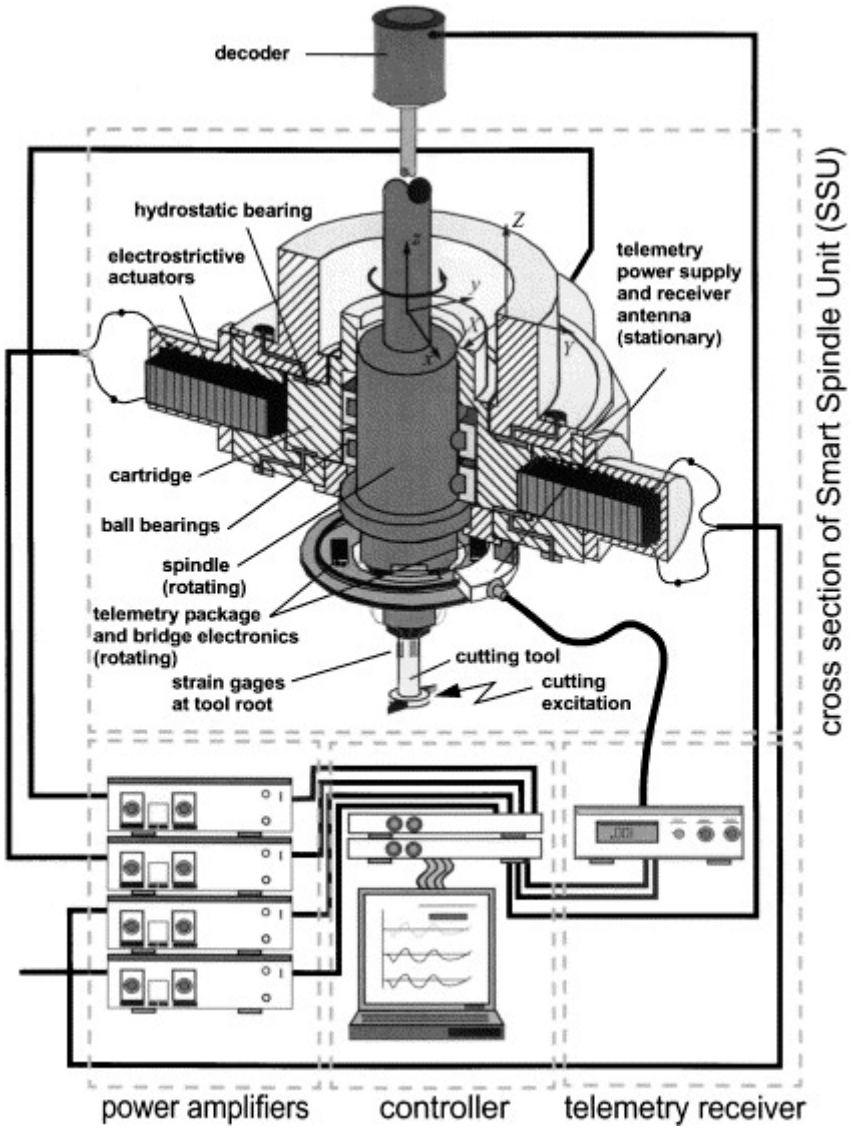


Figure 2.8 Hardware setup for the chatter control test rig (Dohner et al., 2004)

Wood Machining

It has been reported that the furniture sector strongly features in the socioeconomic equation of many countries throughout the world, and its contribution towards the development of local economies cannot be underestimated (Peck, 2002). Wood machining process is an essential part of furniture production. Most of the research efforts in this area have been focussed on cutting tool improvements, reduction of cutting edge wear and component design optimisation. Therefore, reports on active vibration control in wood machining are limited compared to metal machining.

Circular saws are widely used in wood cutting for applications ranging from primary lumber manufacture, furniture, construction and household utensils. Vibration of the saw blade during woodcutting has been identified to be the key causes of poor cutting accuracy, poor surface quality, short tool life, high noise level and excessive material wastage. It has been estimated that about 12% of the raw materials in woodcutting end up as sawdust due to excessive sawing gaps caused by vibration (Chen et al., 2003). As wood resources become more and more limited, efficient wood recovery has become an important economic issue. Active vibration control has been identified as one of the key technologies for increasing recovery in wood machining.

An active control of saw blade vibrations during woodcutting operation is reported in Chen et al. (2003). The vibration control is accomplished by mounting two pairs of electromagnetic actuators on each side of the blade in close proximity to the blade surface (Figure 2.9). The lateral displacement of the saw blade is measured using four eddy current non-contact displacement sensors, mounted closely to the blade surface. The signals generated by these sensors are used as feedback signals into an LQG controller for generating appropriate voltage signal to drive the actuators. The authors reported that an average vibration reduction of about 66% could be achieved, corresponding to about 0.5mm reduction in kerf. It is noted that an exact similar vibration control system for saw blades, employing magnetic actuators, eddy current sensors and optimal LQG controller has earlier been reported by Wang and Sun (2001).

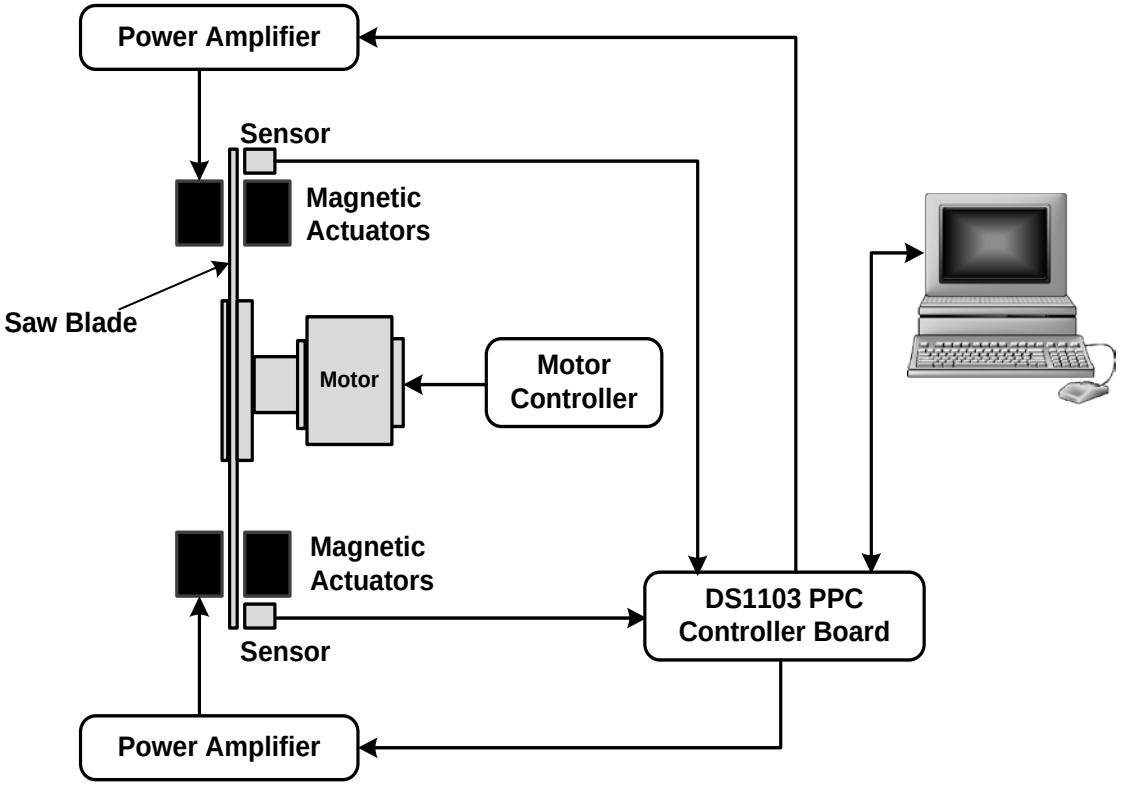


Figure 2.9 Structure of saw blade vibration control test rig (Chen et al., 2003)

An active vibration control method was implemented by Elmas (2008) and Albertelli (2008) on the small-scale planing machine shown in Figure 1.4. The Eddy current sensors are used to measure the vertical displacement of the spindle from the centre of rotation and the displacement signal is then fed back into an optimal LQG controller to generate voltage signals to activate the piezoelectric actuators. The author reported that the closed-loop control provides about 68% reduction in the vibration amplitude.

2.5.3 Semi-Active Vibration Control (SA)

Active control methods provide increased effectiveness compared to the passive techniques but they have high power requirements. They may also lead to control-induced instability. Semi-active vibration control system bridges the gap between passive and fully active control. It is a combination of active and passive treatment, which is intended to reduce the

amount of external power required to achieve the desired performance characteristics. It offers the reliability of passive systems, yet maintaining the versatility and adaptability of fully active systems.

The idea behind the semi-active control system is to replace the active force generators with adjustable elements, which can vary or shift the rate of the energy dissipation in response to the instantaneous condition of motion. It integrates a tuning control scheme with tuneable passive devices so as to adjust the natural frequency of the system continuously (Jalili, 2002). The concept of semi-active vibration control system was originally introduced by Karnopp et al. (1974), who varied the force in a viscous damper by controlling the orifice area. Since then, it has been demonstrated to be a viable vibration control alternative. This method of vibration control has been successfully applied to seismic response control of structures (Li and Zhao, 2006), vehicle suspension systems (Peter et al., 1995) and some metal machining applications (Mei et al., 2009).

Advancements in smart materials, adjustable dampers and absorbers have significantly contributed to the applicability of this method of control. The adjustable elements typically consist of variable rate damping and stiffness characteristics. Efforts have been put into the development of these elements, such as magneto-rheological fluid, electro-rheological fluid, controllable friction dampers, and other variable-stiffness devices (Jalili, 2002).

Mei et al. (2009) developed a magnetorheological (MR) fluid-controlled boring bar for chatter suppression. The structure of the boring bar is shown in Figure 2.10. When the MR fluid-controlled boring bar is subjected to varying external magnetic field strength, its stiffness and energy dissipation properties also change. The vibration of the boring bar is

measured with an accelerometer in order to determine when to increase or decrease its stiffness. Series of machining experiments were conducted at different spindle speeds and the results demonstrate that chatter suppression could be achieved using this method.

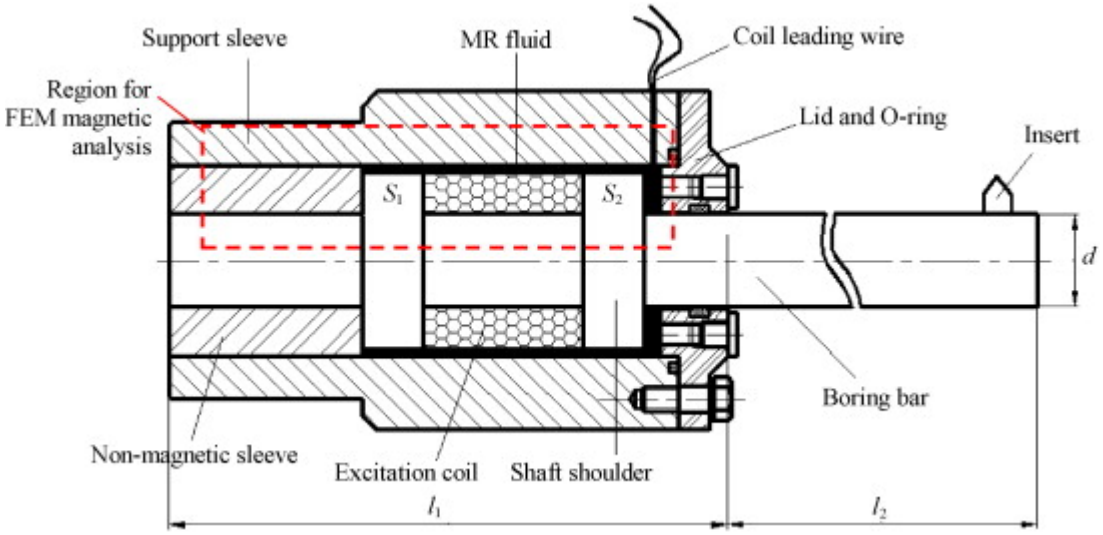


Figure 2.10 Structure of the MR fluid-controlled boring bar (Mei et al., 2009)

Similarly, Wang and Fei (1999) proposed a design method for a tuneable-stiffness boring bar, but in this case another smart fluid known as electrorheological (ER) fluid is used. The stiffness and damping characteristics of ER fluids can be tuned by varying their surrounding electric field intensities. It is used to continuously adjust the natural frequency (stiffness) of the boring bar, thereby suppressing chatter.

Lee et al. (1995) also proposed a vibration control system for a homogenous flexible beam, to which an external force is being applied, using MR fluids. Two control methods are applied and compared on the basis of control performance and energy consumption. The first method is a fully active control system where the MR fluid is energised all the time. The other method is a semi-active control of the input voltage whereby the MR fluid actuator is activated only for a part of the vibration cycle. It is reported that the semi-

actively controlled MR fluid actuator provides good vibration suppression with lower energy consumption.

In comparisons to MR fluids, ER fluids have narrow working temperature range (10-70^{o}C) and high working voltages (2-5kV) while MR fluids have lower voltage requirements (12-24V) and wider working temperature range (-40 to 150^{o}C). The response time of ER fluids is in the order of milliseconds but they are more sensitive to impurities than MR fluids (Srinivasan and McFarland, 2001). Therefore, the use of MR fluids might be more practical and suitable for machine tool applications.

Traditionally, piezoelectric actuators have been driven by voltages to control displacements and forces delivered. However, recent developments in the area of vibration control have seen them being utilised in switched-stiffness states as found in Clark (2000), Ramaratnam and Jalili (2006) and Qui et al. (2009). In these applications, the vibration energy absorbed by the piezoelectric actuator from the primary system is dissipated by switching its stiffness value from high to low. The concept can be easily implemented because piezoelectric materials have the ability to change their effective stiffness depending on the type of circuit connection (Corr and Clark, 2001).

A simple control law based on the position and velocity feedback is used in such a way that the piezoelectric actuator is switched to a high stiffness state when the system is moving away from its equilibrium position so that the potential energy stored is maximised. It is then switched to low stiffness state when the system has reached its maximum stored potential energy, which occurs when it has reached its maximum amplitude of vibration for that half-cycle. When the system reaches the equilibrium

position again, the piezoelectric actuator is switched to high stiffness state, and the switching process repeats over the next half-cycle. At the end of the vibration quarter-cycle, the stored potential energy is dissipated so that it is not given back into the system in the form of kinetic energy (Ramaratnam and Jalili, 2006). The stiffness switching suppresses vibration of the system away from the equilibrium position.

Semi-active approach finds a balance between the passive and active method. It does not only have better damping effectiveness than the passive method, but also has lower power and cost requirements than the active control method (Lam and Liao, 2001). A performance level that rivals fully active control can be achieved with a fraction of the input power required by actively controlled systems.

2.6 Surface Quality Assessments

Research into surface inspection techniques in the wood industry has received lesser attention compared to the metal industry. This might partly be due to the fact that wood is a composite material with extreme chemical diversity and structural complexity, which makes it difficult to develop a standard assessment method that is applicable to all types of timber. It is becoming increasingly valuable to quantify the surface quality of machined wooden products. Modern planing and moulding machines have advanced in speed and efficiency, and there is an increasing demand for improved quality of parts produced. It is therefore important to establish automated inspection techniques, which provide sensory information for controlling the machining processes. Through critical examination of the machined surfaces, the quality of the final products, the general state of the cutting tools and errors arising from the machining centres can be determined.

A common way of assessing surface quality in the industries is through visual inspection (Sandak et al., 2003). However, this method fails to ensure consistent standard of quality because it is subjective and highly dependent upon the operator's skills and experience. Various surface profile measurement systems have been developed over the years so as to overcome the limitations of the visual inspection method. The industrial standard for measuring surface profiles is through the use of mechanical stylus profilometer. The device measures the surfaces as the stylus tip moves laterally across the workpiece. The vertical position of the stylus tip generates analog signal, which are then converted to digital signals for storage and analysis. Figure 2.11 shows the main components of such a measuring system. The resolution of the stylus device can be as high as nanometre range (Groeger et al., 2005), which is more than sufficient for most industrial applications.

Majority of the standard surface inspections systems developed so far are only applicable to homogenous materials, mostly metallic surfaces. It has been proven that these standardised techniques developed for metals cannot be used for all materials especially wood (Parkin and Jackson, 1996). Properties of wood, such as its anatomical structure and colour variations make its assessments more challenging.

Peters and Cumming (1970) reported an extensive review of timber surface assessment using mechanical stylus. Jackson (1986) designed an instrument called Waviness Recording Instrument (WRI) specifically for machined timber surface assessment based on the experience gained from the use of other stylus instruments for metal. The size of the stylus tip is relatively larger compared to the existing ones (5mm radius), resulting into good cuttermarks waves tracing. However, the author reported that the WRI tends to provide inaccurate information relating to absolute waviness height.

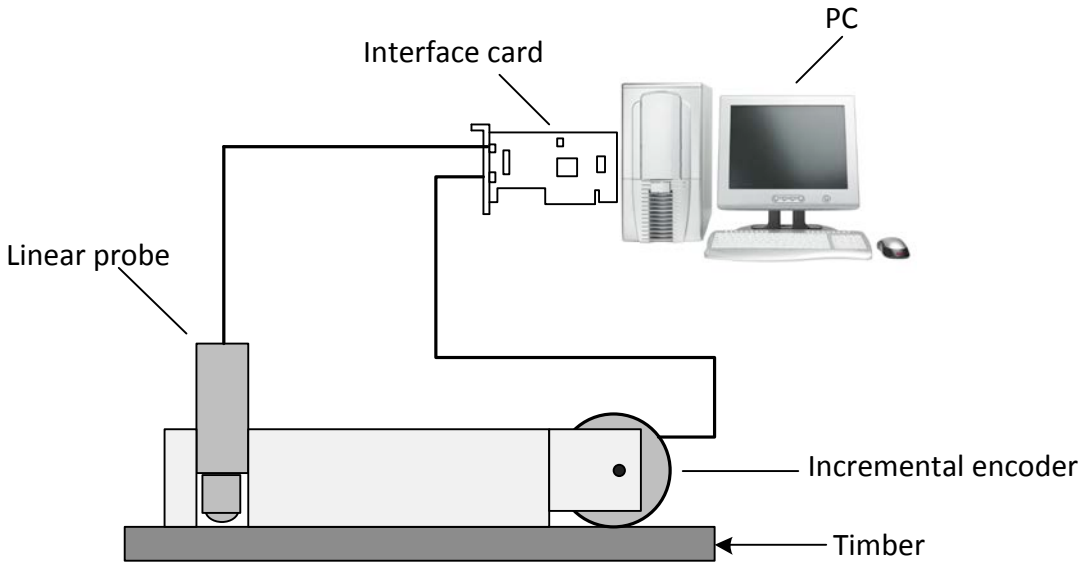


Figure 2.11 Components of the stylus measurement system

The stylus tip is insensitive to surface colour and reflection because it is in contact with the surface. In addition to that, it is suitable for dirty environments where non-contact based methods will be sensitive to surface contaminants. However, the device suffers some major setbacks. It is not suitable for in-process measurement because of its low measuring speed. The tip of the stylus tends to jump at high measuring speeds resulting leading to an effect called *bouncing*. It is also destructive (especially on soft surfaces) as it scratches the surfaces due to the force it applies on them (Jackson, 1986).

In order to overcome the limitations of the contact-based method, a range of non-contact based measurement techniques have been developed. There are non-contact optical profilometers that provide much of the same information as the stylus based profilometers. The optical tracing technique uses optical sensors instead of a mechanical stylus. The measuring speed is higher and it is not destructive compared to its mechanical counterpart due to its non-contact nature. Various researchers, such as Sandak (2003) and Lemaster and Stewart (1995) have investigated the use of optical detector systems to measure the

surface roughness profiles of wood. Experimental results and comparison with conventional stylus tracing method show that the results are in good agreement.

Wood surface profile measurements using vision-based light sectioning method have been reported in Sandak and Tanaka (2005). The use of light sectioning method to measure cuttermarks on planed wood surfaces is also reported in Yang (2006). According to the author, the light sectioning method proved to be good for measuring cuttermarks widths to some extent, but cuttermarks heights could not be reliably measured. Another limitation of the light sectioning method is that the computation is time-consuming.

Wood surface profile measurements using photometric stereo and shape-from-shading techniques are also reported in Jackson et al. (2007) and Yang (2006). The photometric stereo method is used to recover the 2D topography of planed wood surfaces from two images each captured under different illumination directions. The light sources are positioned on opposite sides of the surface, and are symmetric with respect to the camera. Two images are acquired in sequence with one light on and the other off (Figure 2.12). A special case of the photometric stereo method where an attempt is made to recover the cuttermarks from one image is known as shape-from-shading technique.

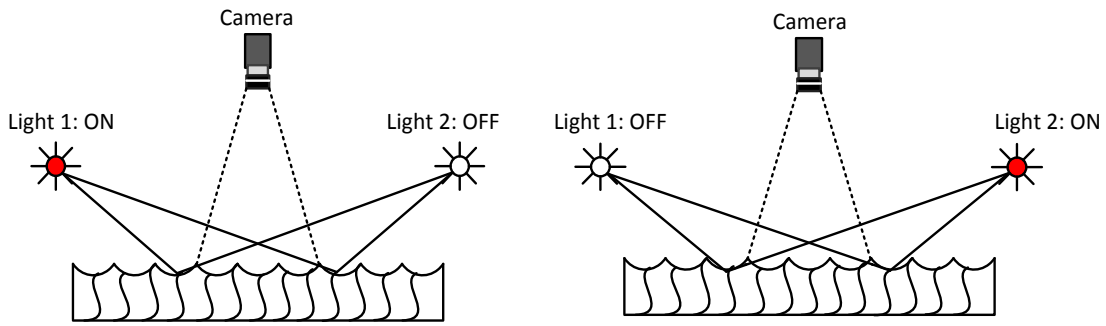


Figure 2.12 Image acquisition sequence for the photometric stereo technique

Results from the photometric stereo and shape from shading techniques were compared with results obtained from a laser profilometer. The photometric stereo method offered the most promising solution to measuring cuttermarks on planed wood surfaces. Results obtained from the photometric stereo method are fairly reliable and the reliability increases with increase in cuttermarks widths. When the surface becomes too smooth (cuttermarks widths < 1.5mm) the cuttermarks heights measurements become difficult. Although the research was carried out with the hope of using it for in-process measurement of moving samples, only static samples were tested because photometric stereo is only applicable to static objects in principle. Correspondence problem arises if the object is subjected to movements during the acquisition of images.

Some existing applications have already applied photometric stereo technique to moving surface measurements. This is referred to as dynamic photometric stereo (Smith and Smith, 2005). In order to overcome the correspondence problems in dynamic samples, the system must be able to acquire the photometric images without any temporal difference. The easiest way to approximate this is to capture the image pairs in rapid succession, within the shortest possible acquisition time frame. The method is known as temporal multiplexing (Smith and Smith, 2005). In this approach, each light source is projected onto the object at different times and the image capture is synchronised with the activation of each light in sequence. The drawback of the temporal multiplexing method is that it is only applicable to very slow moving objects because the pixel displacements in the image pairs will be significant at high speeds. The most limiting factors are the camera frame rates and the intensity of light required to achieve the shortest image acquisition period.

A case study on the dynamic inspection of ceramic tiles is presented in (Farooq et al., 2005). A method known as spatial multiplexing is used to achieve a synchronised capture of the same surface location at different points in space. The registration of the images is achieved through pre-calibration of the sample speed. The limitation of this method is that the scan lines of the camera must be synchronised with the speed of the moving surface. As such, the relative movement between the imaging system and the object must be precisely controlled. There are other applications of the dynamic photometric stereo where single coloured images are utilised instead of multiple grayscale images (Bringier et al., 2008). Application of photometric stereo technique to the measurements of cuttermarks on moving wood samples is the focus of chapter four of this thesis.

Another related work is reported in Hesselbach et al. (2007). An image processing system is used to measure the width of the cuttermarks on a planed wood by utilising a special illumination and image processing algorithm. The processing algorithm is very simple and is based on finding the average intensity values in each row of the images. According to the authors, the method is suitable for assessing moving wood samples even at high feed rate, but it is unable to reveal cuttermarks height information.

Some other indirect approaches, which monitor power consumption, spindle vibration, machining noise and acoustic emission, have been proposed to evaluate surface roughness or surface profile of wood during routing operation (Cyra and Tanaka, 2000; Iskra and Tanaka, 2006; Denaud et al., 2007). In one of the applications, an accelerometer is used to monitor tool wear during the machining operation. The tool wear is then correlated to the surface quality of the workpiece (Lemaster et al., 2000a; Lemaster et al., 2000b). The main

advantage of the indirect approaches is that they are very much suitable for in-process surface profile measurement.

An indirect approach for surface quality assessments in wood planing was proposed by Elmas (2008). This method recreates surface profiles of machined timber from the spindle speed and vibration measurements during machining operation. The cuttermarks widths and heights are calculated from the spindle speed measurement and the vibration measurement is used to calculate the contribution of vibration to the surface waviness. One obvious limitation of this method is that it does not take into account the effects of cutting tool inaccuracy. A comparative analysis of some of the measuring techniques developed for wood can be found in Elmas et al. (2011).

2.7 Signal and Data Processing Techniques

Having reviewed some of the surface profile assessment methods developed so far, it is worth pointing out that the measured surface profile data on their own are not of any great value unless there are tools that can be used to identify the defects in the surface by analysing the data. The purpose of this section is to identify potential signal processing and data analysis techniques that are suitable for this defect characterisation activity. There are some techniques that have been widely applied to the analysis of machined surface profiles in metalworking. Fourier spectrum and the autocorrelation function (ACF) have been applied to analyse the quality of parts surface finish and also monitor signals in manufacturing processes. These two methods were employed in Tumer et al. (1995) to characterise and analyse surfaces obtained from precision grinding process.

The Fourier spectrum of a machined surface is useful in observing trends and changes in the machining process, as well as identifying the modes and dominant harmonic components of the surface profile data before using more rigorous computations to determine the exact parameter values. It is a reliable method for revealing the wavelength components of a given waveform and has been used in determining the fundamental waviness pitch present in a planed wood surface profile data (Elmas, 2008). If sufficient information about the waviness components can be extracted, realistic characterisation of the surface profiles can be accomplished by fitting a deterministic model to the data.

Although the Fourier spectral analysis can be used under extremely general conditions, it has some crucial restrictions. The system must be linear and the signal must be strictly periodic or stationary, otherwise the resulting spectrum will make little physical sense (Huang et al., 1998). Data from machining processes usually have time-varying statistics and are therefore non-stationary. Statistically unpredictable freak marks on wood surface due to its heterogeneous and anisotropic material nature may give rise to non-stationary effects, which can cause the Fourier spectral analysis method to fail.

Apart from the stationarity requirement, Fourier analysis also requires linearity (Huang, 2000). Many natural processes are inherently non-linear. Imperfections in surface profile measuring devices can make the final surface profile data to be non-linear. Due to the above reasons, the measured surface data in practice are usually of finite length, non-stationary and non-linear. Some critical waviness defects conditions are also discussed later in chapter five, where defect characterisation based on frequency components of the surface profile might give misleading results.

The ACF has also been used for surface profile analysis. It is the time-domain counterpart of the Fourier spectrum. It is used to find the cross-correlation between a signal and a copy of itself. The ACF is a mathematical tool that can reflect specific properties of a data set, such as the presence of periodic signal which has been perturbed by noise, randomness, and existence of trends. It is reported in Tumer et al. (1995) that the ACF method is helpful for broad classification of grinded surface profiles and the estimation of presence or absence of particular features. However, when applied to random grinding data, the method cannot provide precise quantitative measures.

Accounting for non-stationarities in the profile is difficult with ACF because they tend to integrate out from position to position, giving an average representation of the surfaces. Just like the Fourier analysis, the application of the ACF to the defect characterisation in planed timber can also fail in some critical cases because its judgement is also based on the harmonic components of the surface profile data.

Principal component analysis (PCA), also known as the Karhunen-Loeve (KL) transform, has also been widely used in data analysis. The PCA has the ability to accurately decompose a complex signal into uncorrelated fundamental patterns in the form of empirical basis functions that contain the majority of the variations in the original data. A fault detection and diagnosis tool for manufactured parts based on the PCA was introduced by Tumer et al. (1997). The PCA was applied to parts produced by selective laser sintering process in order to identify the conditions in the machine that result in poor surface quality. The power of the PCA stems from the fact that it can be applied to any type of signal (deterministic, stochastic, stationary or non-stationary) without prior knowledge of the

characteristics of the fault patterns (Tumer et al., 1997b). The Karhunen-Loeve transform has also been proposed by Tumer et al. (1995) for analysing defects in grinded surfaces.

Another method, which has also been applied to the characterisation of errors in machined surfaces, is the Fractal-Wavelet representation. However, the applicability of this method to planed wood surfaces is not investigated and is therefore not discussed any further. A more detailed review of the advanced data processing techniques used in machining processes can be found in Teti et al. (2010).

Another signal processing method found in literature is known as the Empirical Mode Decomposition (EMD). It has the inherent ability to decompose signals into dominant individual oscillatory components. The method is useful for analysing data that are non-stationary and non-linear, and it is relatively easy to understand compared to other spectral analysis techniques. It can be compared to other signal analysis methods like the Fourier transform, but in contrast to them, the EMD is an algorithm or empirical method that is applicable to datasets rather than a mathematical tool (Huang et al., 1998).

Having considered the capabilities of the KL transform and the EMD, they are potential tools for the defect characterisation on planed timber surfaces. The applicability of these methods to the surface defect characterisation is investigated in chapter five of this thesis.

2.8 Adaptive Control

Adaptive control systems use control schemes that modify their behaviours so as to guarantee the desired performances even under parametric variations of the process dynamics. This is slightly different from robust control, which only aims to achieve good performance and stability within bounded variations of the process parameters. The three most common adaptive control schemes found in literature are gain scheduling, model reference adaptive control, and model identification adaptive control also known as a self-tuning regulator.

The gain scheduling is one of the simplest forms of adaptive control. The technique is based on the adjustment of the controller parameters in order to achieve satisfactory performance depending on the operating region of the system (Astrom and Wittenmark, 1995). Some observable variables, known as the scheduling variables, are used to determine the current operating conditions of the system. The right controller parameters are then selected from the gain scheduler, which is practically implemented in form of a look-up table. The gain scheduler is a database of the mapping between the observed process parameters and the corresponding pre-determined controller parameters. The technique is particularly useful when the changes in the process dynamics are predictable. A block diagram of the control scheme is shown in Figure 2.13.

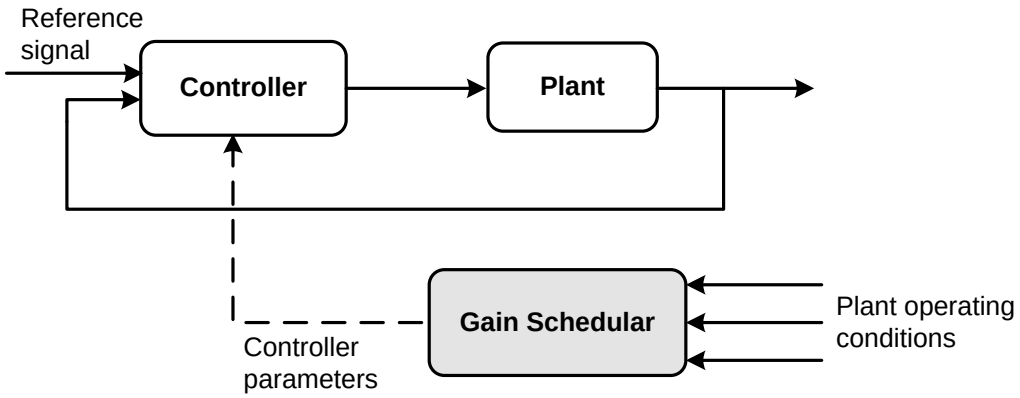


Figure 2.13 Gain scheduling adaptive control diagram (Karray and De Silva, 2004)

One of the main drawbacks of the gain scheduling control scheme is the discrete nature of the relationships between the controller parameters and the plant operating conditions. No explicit controller parameters are assigned to intermediate operating conditions and therefore interpolation techniques are usually applied.

The main idea behind the model reference adaptive control (MRAC) is to design a controller whose parameters can be updated based on the actual output of the process. This is in contrast with the gain scheduling scheme, in which the controller adjustment is based on the process operating conditions (Karray and De Silva, 2004). The MRAC scheme is also concerned with handling processes with unpredictable changes. In the MRAC scheme, the response of the plant is compared with a desired response, which is specified by a given reference model. The objective is to drive the error signal between the response of the plant and the reference model to zero. The block diagram of the MRAC is shown in Figure 2.14. The control and the adaptive loops have different time constants because the control loop is a lot faster than the loop designed for the controller parameter adjustments. This is because the process parameters of most systems are slowly time-varying in

practice. A number of algorithms for implementing the adjustment mechanism have been proposed and reference can be made to Astrom and Wittenmark (1995) for more details.

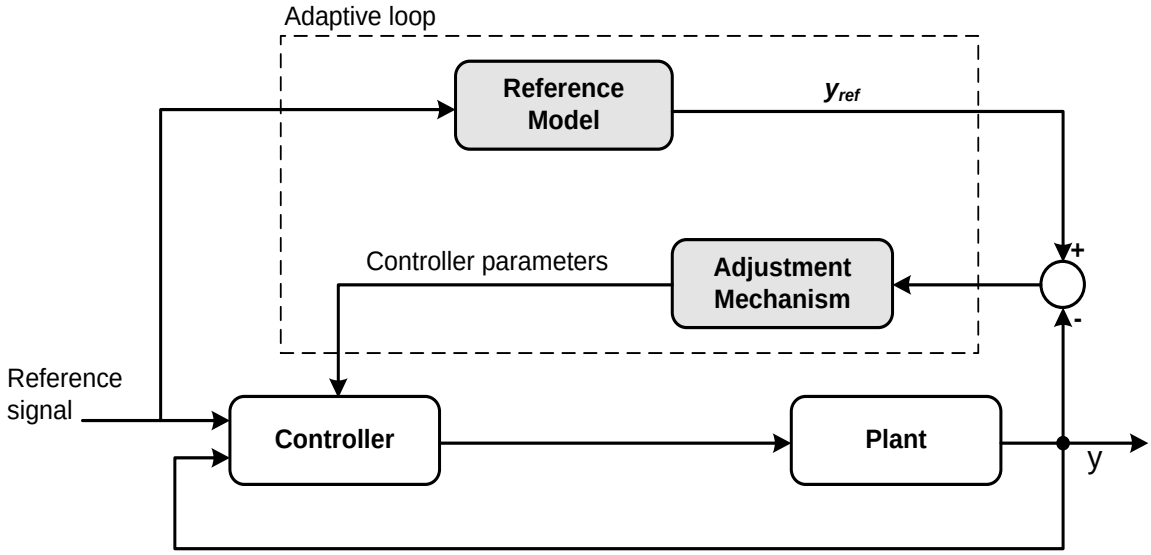


Figure 2.14 Model reference adaptive control diagram (Karray and De Silva, 2004)

The model identification adaptive control (MIAC) scheme is also designed to handle dynamic processes that may be subjected to unpredictable changes in the system parameters (Astrom and Wittenmark, 1995). In the MIAC scheme, recursive system identification of the plant is being performed while the system is running. The newly identified plant parameters are then used to adjust the controller parameters through a suitable adaptation mechanism. The block diagram of the MIAC scheme is shown in Figure 2.15. Similarly to the MRAC, the adaptive loop of MIAC would usually have much slower bandwidth than the control loop. The main difference between the MIAC and MRAC is that the design of MIAC is based on an explicit separation between identification and control. Whereas, the MRAC design uses a direct update of controller parameters to achieve an asymptotic decay of the error signal to zero (Karray and De Silva, 2004).

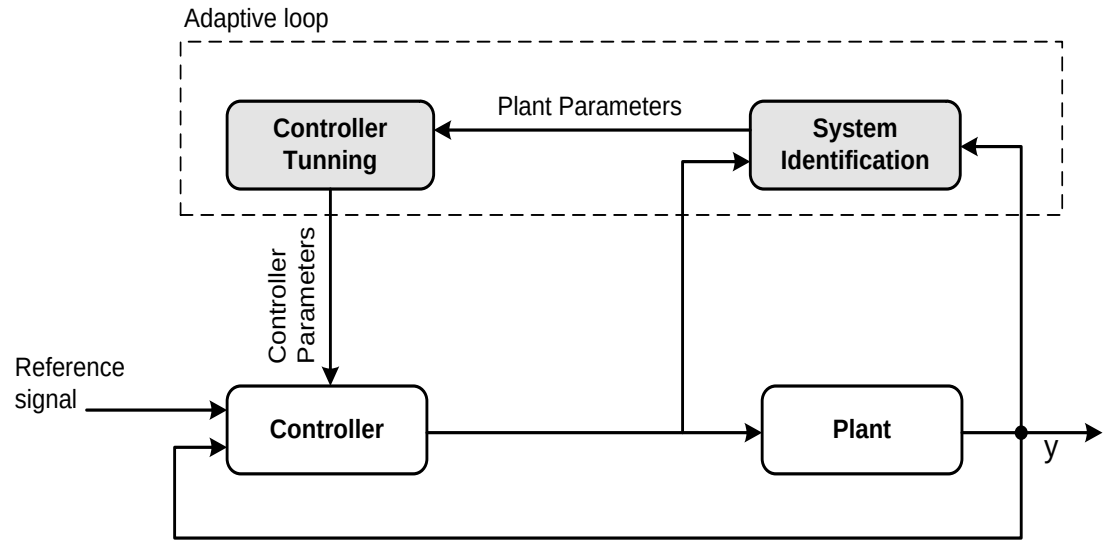


Figure 2.15 Model identification adaptive control diagram (Karray and De Silva, 2004)

Adaptive control has been extensively implemented in several industries including aerospace (Belkharraz and Sobel, 2007; Liu et al., 2009), automobile (Wang and Hsieh, 2009) chemical and petrochemical plants, amongst many others. A detailed review of these applications is beyond the scope of this thesis as the review is limited to a few ones applied to machining operations.

An adaptive system, which ensures consistent quality of surface finish by controlling the cutting forces during an end milling process, is reported in Cuz and Zuperl (2008) and Cuz et al. (2006). The cutting force is being controlled through continuous dynamic adjustment and adaptation of the cutting parameters. A similar adaptive control algorithm, designed to improve the productivity and accuracy of milling operations is also reported in Qin and Park (2005). The control algorithm was designed to maintain a desired peak cutting force in the presence of parametric uncertainty and time-varying process dynamics. The controller automatically provides optimal machining parameters so that the desired productivity and surface finish can be achieved. Experimental results confirmed the

efficiency of the adaptive control systems, which is reflected through improved surface quality and decreased tool wear.

Adaptive control applications have not been limited to metal machining operations. An adaptive optimisation system for wood routing is also reported in Iskra and Hernandez (2009) and Iskra and Hernandez (2010). In conventional machining, the machining parameters (cutting speed and feed rate) are pre-set in a rather conservative way according to the experience of the operator. As a result, the system may be operated under conditions that are far from being optimal.

The adaptive control system continuously monitors the machining process so that real-time adjustments of the process variables can be made. The surface roughness is estimated online through directionalised measurement of sound pressure. The adaptive controller is then used to continuously adjust the feed speed (PID gains) based on the surface quality measurement. The relationship between the PID gains and the surface quality has been experimentally predetermined and stored in a lookup table. The authors reported that the approach helped to maintain the surface quality within a predetermined level.

In relation to the current project, the high level reasoning and the apriori knowledge subsystems (Figure 1.4) are forms of an advanced gain scheduling scheme. The look-up table has been replaced by apriori knowledge and the high level reasoning performs the functions of the interpolation techniques in an intelligent manner. This approach allows the gain scheduling system to automatically learn from existing data and also update its knowledge base. More details about this implementation can be found in chapter seven.

2.9 Intelligent Control

The model-based adaptive control techniques described above are usually implemented under the assumption that the process dynamics and its operating environments are well understood. They require that an explicit analytical model of the system dynamics or at least a linear model developed through experimental identification be available. This may not always be the case especially for complex nonlinear systems that are characterised by poorly known dynamics and ill-defined operating environments. The conventional approach also approximates the plants as linear and time-invariant systems, whereas plants are inherently nonlinear in nature. Although it can be argued that the linear approximation is practically valid for most systems.

Moreover, conventional adaptive control techniques do not have learning capabilities. This means that they cannot use the knowledge and experience gained in the past to tackle similar situation in the future. Adaptive control techniques have been used effectively for controlling a large class of systems with predefined structure and slowly time-varying parameters. Nevertheless, they still lack the abilities to learn and also handle the global control issues of nonlinear systems (Karray and De Silva, 2004).

Knowledge-based intelligent control has emerged as an alternative to conventional model-based control. In intelligent control, knowledge gained through observation of the plant's behaviour is used instead of explicit mathematical models of the dynamic process. Techniques from the field of artificial intelligence are used to represent knowledge and for generating control actions through appropriate reasoning mechanisms. The past few years have witnessed a rapid growth in the applications of neural networks and fuzzy logic to control complex processes because they are independent of the explicit mathematical models of the plants (Karray and De Silva, 2004).

With fuzzy logic and neural networks, issues such as nonlinearities, uncertainties or unknown variations in plant parameters can be dealt with more effectively and hence improving the robustness of the control system (Denai et al., 2007). As opposed to most conventional control techniques, the implicit models of the dynamic process are not constrained to be linear. Some of the intelligent control techniques such as the ones based on neural networks have the distinctive feature of learning and also adjusting their parameters in response to unpredictable changes in the system dynamics. Needless to say, the intelligent approach is attractive due to its simplicity, learning capabilities and robustness to subtle process parameter variations.

A number of intelligent control schemes have been proposed in recent years. Two of these schemes are the direct inverse control (DIC) and internal model control (IMC). The schemes were mainly used in robotic applications and process control but are now finding applications in other fields (Norgaard et al., 2000).

The DIC is a simple open-loop approach in which an inverse model of the plant is used as the controller. The inverse model is connected in series with the plant. For the stability of the system to be guaranteed, the plant to be controlled must be open-loop stable (Norgaard et al., 2000). The main limitations of the DIC are sensitivity to the plant inverse model mismatch and inability to cope with unknown disturbances due to the absence of a feedback mechanism. The effectiveness of this configuration depends on the accuracy of the inverse model and apriori knowledge of the disturbances acting on the plant.

The IMC is the closed-loop counterpart of the DIC. The strategy utilises both the plant's forward and inverse models within a feedback loop as shown in Figure 2.16. There is a

strong support for the IMC strategy from control theory viewpoint. It has been examined thoroughly in classical a control and has been shown to provide stable and robust performance, even for nonlinear systems (Ahn and Kha, 2007). However, just as the DIC, the system to be controlled and its inverse must be causal and open-loop stable in order to achieve a global stability of the feedback loop.

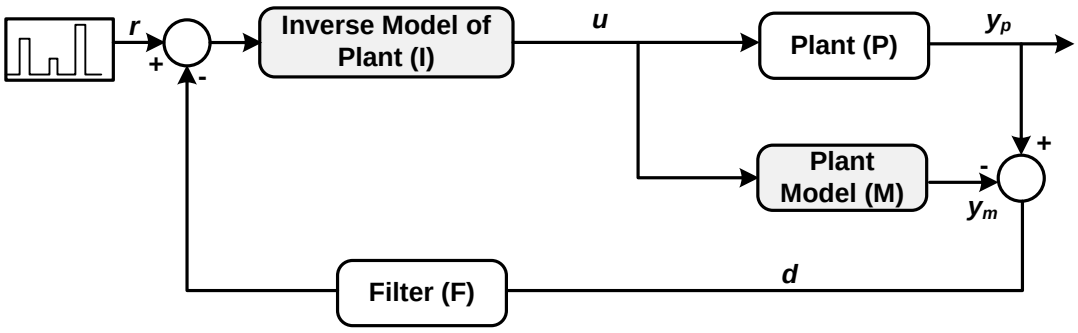


Figure 2.16 Structure of the internal model control

The application of neuro-fuzzy based internal model control has provided good results in controlling cutting forces during a milling process (Haber et al., 2005) and a high-performance drilling process (Gajate and Guerra, 2009). Neural network-based direct inverse control has also been reported in De Abreu et al. (2000) for active vibration suppression, and in the field of active power filters (Ping et al., 2010). The performances of the two control schemes in controlling a chemical plant have also been studied by Suja Mani Malar and Thyagaranjan (2009). However, no report was found on the application of these techniques to wood machining.

The open-loop stability requirements generally limit the class of systems that can be controlled with the DIC and IMC strategies. For example, the architectures are not suitable for controlling unstable systems such as an inverted pendulum. However, they are suitable

for controlling the smart planing machine since the spindle is open-loop stable. The significance of DIC and IMC within the context of this research work is that they provide direct methods for the intelligent feedback control of the machining process. Furthermore, they also provide a general framework for transparent analysis of the control system's stability and robustness properties.

3 Simulation Model for the Rotary Wood Planing Process

The existing simulation model for rotary wood planing, known as circular arc theory, is not flexible because it requires manual formulation of mathematical equations for specific machining conditions (Jackson, 1986). This means that it cannot be used to simulate generalised machining conditions and its computational implementation is difficult. It is also argued in Hynek (2004) that it is difficult to use the circular arc theory to investigate a combination of several factors at the same time.

This chapter describes the creation of a new simulation model for predicting the topography of the surface produced by the rotary wood planing process. The model, which is termed as the extended circular arc theory (ECAT), is based on a generalised model of the machine tool kinematics and the cutting parameters. It takes into account the relative motion of the machine components, and also the effect of some undesirable machining conditions such as cutting tool errors and forced vibration.

The work presented in this chapter first of all creates a generalised analytical model for the circular arc theory. The purpose is to show that the circular arc theory, which has been termed as a non-general purpose simulator, has the inherent ability to be used for simulating various defect conditions without having to manually generate equations for specific machining conditions.

3.1 Justification for the New Algorithm

Apart from the inflexibility of the circular arc theory, it represents a rather limited mathematical model of the wood planing process because it does not utilise the true locus of the cutting knives. The most recent algorithm, which represents the actual kinematics of

the machining process, was developed by Hynek (2004). The knife tip paths are represented by a set of piecewise polynomial approximators known as cubic splines. The resultant surface is then extracted by finding the point of intersection between adjacent spline functions. Although the algorithm created by Hynek (2004) can generate the resultant surface profiles, the solution to the equation used to find the intersections between adjacent spline functions only gives the horizontal coordinate of the points of intersections. Since the vertical coordinates of the points of intersections are not known, information about the waviness heights and widths of the cuttermarks cannot be extracted from the waveform. Fourier spectral analysis of the waveform is required to obtain rough values of the frequency contents and the dominant cuttermarks wavelengths.

The other issue is that the inputs to the algorithm are the cutterhead time-based centre coordinates, angular displacements of the cutterhead, and the radius of the cutterhead. All these inputs except the cutterhead radius are derived quantities from the machining parameters. Detailed analytic expressions for obtaining these derived parameters are not shown in the author's thesis (Hynek, 2004).

Thirdly, in using the algorithm created by Hynek (2004) to simulate defects caused by cutterhead vibration, there is no provision for specifying the angular position of the resultant mass imbalance. That is, the initial vertical and horizontal positions of the cutterhead at the beginning of the cutting process cannot be varied. This is deemed to be an important requirement because it determines the surface waviness. As it will be shown later, the same vibration signature can also give rise to different surface waviness depending on the angular position of the resultant mass imbalance.

The afore-mentioned limitations of the most recent algorithm (Hynek, 2004) are the justifications for creating the ECAT. The inputs to the ECAT are the machining parameters, together with other parameters that are required to simulate the defect conditions. Simple analytic expressions are derived for easy understanding and computational implementation of the algorithm. In addition to that, a new technique is used to obtain both the vertical and horizontal coordinates of the points of intersection between adjacent knife tip paths. This allows for easy extraction of the widths and heights of the cuttermarks in the surface profiles without the need for further analysis. The ECAT also makes provision for specifying the position of the resultant mass imbalance. This makes suitable for simulating the various waviness patterns that can be produced by variations in the position of the resultant mass imbalance for a fixed vibration signature.

3.2 Description of the Algorithm

The principle of the rotary machining process has already been explained in chapter one (Figure 1.1). The width of the cuttermarks, also known as the pitch *p (mm)*, is effectively the distance that the workpiece travels between two successive knives. It is primarily determined by the cutterhead rotational speed *ω (rev/s)*, workpiece feed speed v_f *(mm/s)*, and the number of knives *N*, on the cutterhead. The relationship between the pitch and the cutting parameters is expressed by:

$$p = \frac{v_f}{N.\omega} \tag{3.1}$$

The height of the cuttermarks *h (mm)*, depends on the pitch and the radius of the cutting knife *R (mm)*, as expressed by the following equation:

$$h = R - \sqrt{R^2 - \frac{p^2}{4}} \tag{3.2}$$

The above equations are well established and are widely used in the woodworking industry; although the actual cuttermarks heights are usually less than the ones computed from Equation 3.2 (Jackson 1986). The height of the actual surface h_a, is given below:

$$h_a = R - \sqrt{R^2 - \frac{(p - d_t)^2}{4}} \tag{3.3}$$

where d_t is the distance travelled by the cutterhead when the knife is cutting the width of its cuttermark p. The detailed mathematical expressions for calculating the value of d_t is found in Hynek (2004). The error can be as small as 2 - 5% for typical values of cutting speed and feed speed. The idealised and the actual surface waviness are depicted in Figure 3.1.

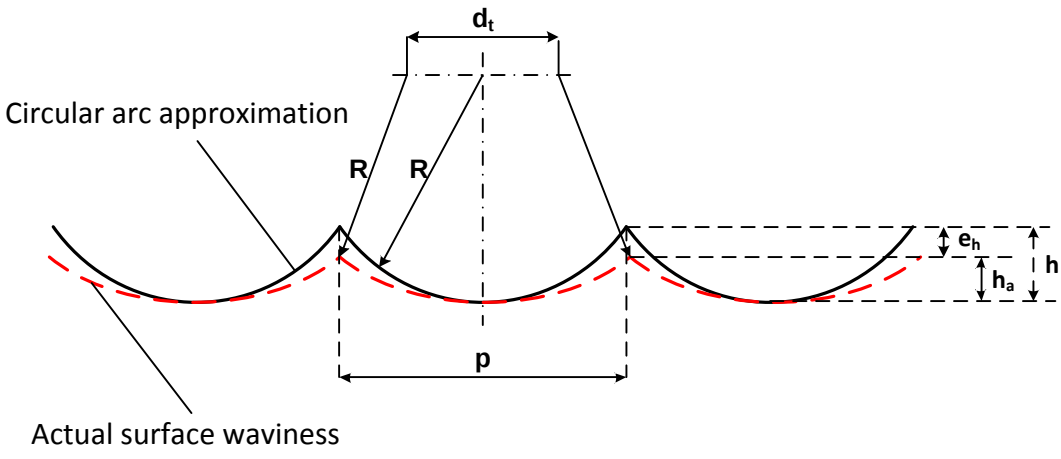


Figure 3.1 Idealised and the actual surface waviness (Hynek, 2004)

Although kinematics of the machining process can be used for accurate modelling of theoretical surfaces, some other factors must be taken into account when describing real surfaces. The geometrical shape of a machined timber surface actually depends on other factors such as the material properties of the workpiece. The ECAT generates the surface waviness by taking the following factors into consideration:-

- Instantaneous kinematics of the cutting process
- Machining parameters such as cutting speed and feed speed
- Depth of cut
- Number of cutters and the radius of each cutter
- Instantaneous vertical and horizontal vibrations of the cutterhead.

The model does not take into account the effect of the following factors:

- Timber properties such as species, moisture content, density, grain structure and direction, and temperature. These factors contribute more to the surface roughness
- Cutter geometry and accuracy such as sharpness of the cutting edge, clearance angle, rake angle, joint land width and width of cut.

The effects of cutterhead vibration and tooling inaccuracy are taken into account because they have significant influence on the surface waviness. In practice, the effect of horizontal cutterhead vibration on the cuttermarks width is almost insignificant. This is because the vibration amplitude is usually in the micrometre range while the width of each cuttermark is in millimetre range. The additional vertical cutterhead vibration is the most influential because the cuttermarks height is in micrometre range, so a superimposed vertical displacement will have significant effects on the waviness. The factors which are associated with the properties of wood also contribute to the surface texture. However, the

model neglects these factors because it is difficult to mathematically represent their influences on the machined surface.

The cutter geometry and chip thickness have significant influence on the cutting forces generated by the interaction between the cutters and the workpiece during the machining process. Variations in the magnitude of the cutting forces also influence the surface finish. The effect of each of these factors on the generated cutting forces is well understood based on earlier investigations carried out by Jackson (1986). However, exact mathematical relationships cannot be easily determined. Incorporation of the effect of cutting forces into the model is a subject of further work.

3.3 Generalised Model for the Circular Arc Theory

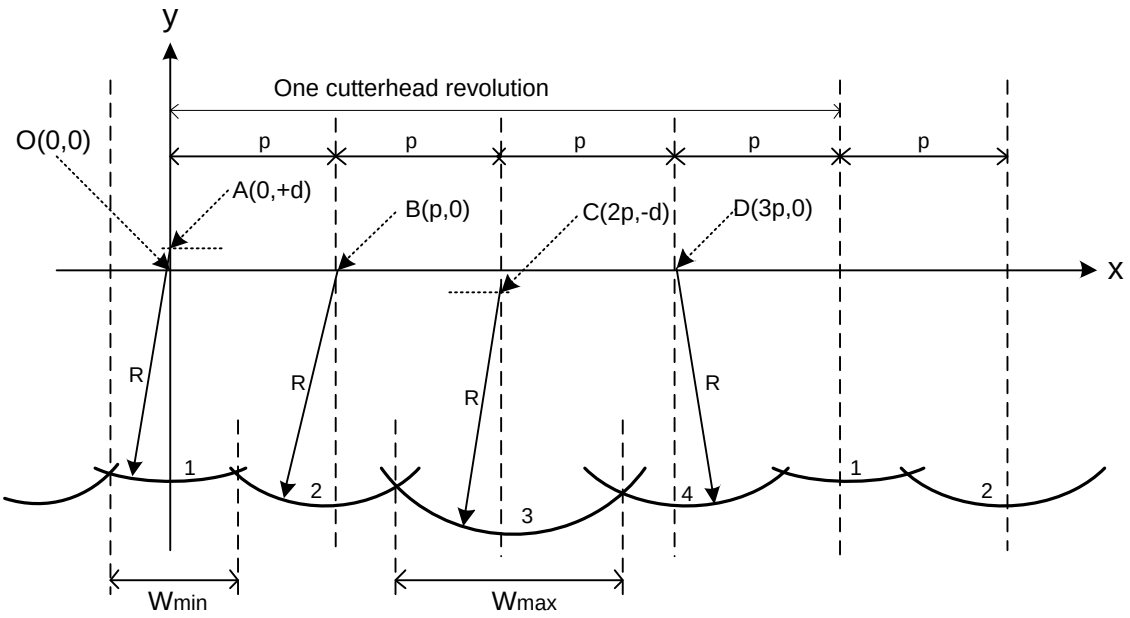


Figure 3.2 Fundamental principles of the surface waviness modelling (Jackson, 1986)

With reference to Figure 3.2, the equation of a circle of which each of the arcs is a section is defined in a Cartesian coordinate system as a set of all points *P(x, y)* such that:

$$(x - a)^2 + (y - b)^2 = R^2 \tag{3.4}$$

where *R* is the radius of the circle and *(a, b)* is the centre point of the circle (cutterhead). Re-writing Equation 3.4 in parametric form using trigonometric functions:

$$x = a + R\cos\theta \tag{3.5a}$$

$$y = b + R\sin\theta \tag{3.5b}$$

θ is a parameter which geometrically represents the angle between the line from the centre *(a, b)* to the point *P(x, y)* and the positive x-axis.

With reference to Figure 3.2, the horizontal position of the spindle centre at the point where the i^{th} knife is engaged with the workpiece can be expressed as:

$$a_i = p(i - 1) \tag{3.6}$$

Since the cutting knives are evenly distributed around the circumference of the cutterhead, the angle between successive knives is determined by:

$$\gamma = \frac{2\pi}{N} \tag{3.7}$$

Let it be assumed that the spindle has vertical vibration amplitude of *d*, occurring at d_{rev} times per revolution of the spindle. By modifying the vertical centre position of the circle, the effect of the spindle vibration can be synthesised. Without vibration, the spindle centre will remain at a constant vertical position ($b = 0$). The first finishing cutter is aligned with the positive value of *d* at the start of the cutting cycle for convenience (Jackson, 1986). The actual vertical oscillation of the spindle is a time-varying sinusoid. However, if this movement is approximated by a rectangular wave (Figure 3.3), then the vertical position of the spindle centre for the ith finishing knife can be determined by:

$$b_i = d\cos([i-1] \times \gamma \times d_{rev}) \tag{3.8}$$

It should be noted that b_i in this case is a scalar value, which is constant for each finishing knife. In reality, it is a vector containing time-varying elements as will be seen in the ECAT. Combining equations (3.5a), (3.5b), (3.6) and (3.8), the loci of the path traced by the ith knife can be obtained as follows:

$$x_i = p(i-1) + R_i\cos\theta \tag{3.9a}$$

$$y_i = d\cos([i-1] \times \gamma \times d_{rev}) + R_i\sin\theta \tag{3.9b}$$

where

i = 1,2, 3 ..... total number of knives on the cutterhead *N*

p is the pitch *(mm)*

R_i is the radius of the ith knife *(mm)*

d is the displacement amplitude of the cutterhead in *(mm)*

d_{rev} is the number of cutterhead displacements per revolution

γ is the angle between successive knives *(rad)*

If θ ranges from 0 to 2π, then x_i and y_i are vectors representing all points $P(x, y)$ on the circular path traced by the i^{th} knife. Taking θ to range from 0 to 2π will produce more data point than necessary since the whole knife tip paths do not form the resultant surface profile. Moreover, the extraction of the resultant surface profile will be more complicated because there will be two points of intersections between two adjacent circular knife-tip paths. Values of θ ranging from π to 2π are enough to generate the required knife tip loci from which the resultant surface profile can be extracted. A technique described in section 3.5 is used to extract the surface profile from the whole knife tip paths by finding the points of intersection between adjacent knife tip paths.

The circular arc theory is a geometric approximation of the actual kinematics of the rotary machining process. It makes two simplifying assumptions. Firstly, it assumes that the movement of the workpiece has periodic discontinuities along the feed direction. That is, the workpiece moves a distance p, stops until a knife finishes cutting, and then suddenly jumps by another distance p, prior to the next knife contacting the workpiece surface. It also assumes that the cutterhead vibration is a rectangular wave instead of a sinusoidal waveform. That is, the vibration amplitude jumps to a level, remains constant for a time period during which a knife is engaged with the workpiece, and then suddenly jumps to another level prior to the next knife contacting the workpiece. These two assumptions are illustrated using a four-knife cutterhead in Figure 3.3 and Figure 3.4 respectively.

It should be mentioned that these two assumptions could be valid in the case of wood machining where the cutting speed is much higher compared to the feed speed. Moreover, only a small fraction of the knife tip paths form the resultant surface finish. Although these assumptions would not introduce any significant error, an algorithm that represents the actual kinematics of the machining process is desirable.

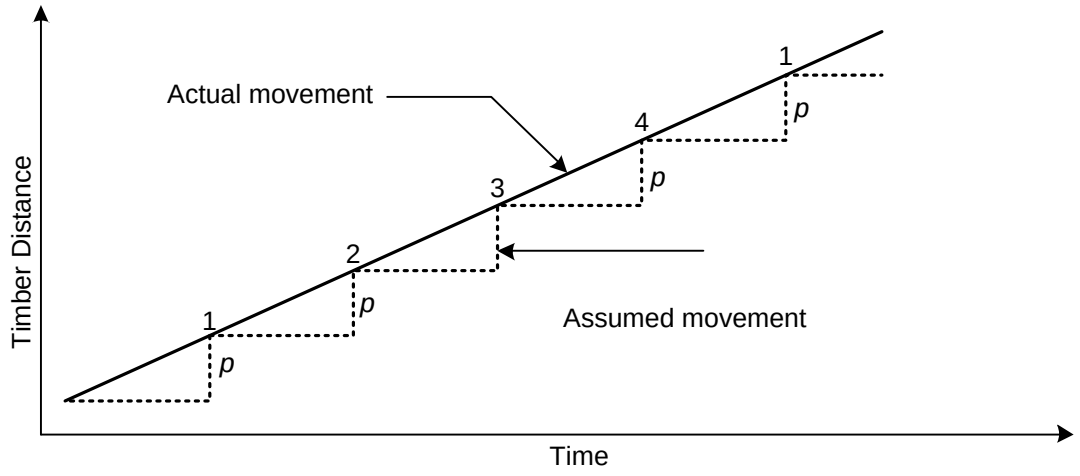


Figure 3.3 Assumed movements of the workpiece in circular arc theory model

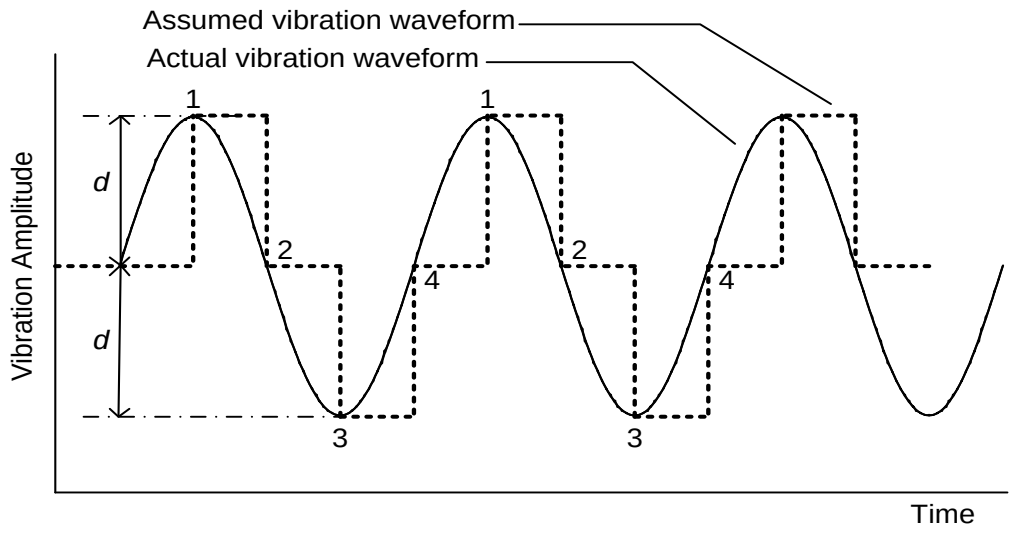


Figure 3.4 Assumed cutterhead vibration in circular arc theory model

3.4 Model for the Extended Circular Arc Theory

As mentioned earlier, the circular arc approximation does not accurately represent the actual kinematics of the rotary wood machining process. This has motivated the development of the newly improved model. For easier understanding, the model initially considers only the rotation of the cutterhead relative to the workpiece. The contributions of other factors are then added to it.

3.4.1 Cutting Tool Kinematics Modelling

The instantaneous kinematics of the rotary machining process is such that the workpiece, which is moving at a known linear speed, is fed against the cutterhead which is also rotating about a fixed position at a known angular speed. Suppose that the process is now represented in such a way that the cutterhead is rotating and also skidding on the surface of the workpiece simultaneously, Equation 3.5a and 3.5b can then be rewritten as:

$$x(t) = a(t) + R.\cos(\theta(t) + \theta_o) \qquad (3.10a)$$

$$y(t) = b(t) + R.\sin(\theta(t) + \theta_o) \qquad (3.10b)$$

where *a(t), b(t)* are the cutterhead centre coordinates, θ_o is the initial angular position of the cutterhead and *θ(t)* is its instantaneous angular position.

If the cutterhead rotates at a constant angular speed of ω_c (rad/s), then its instantaneous angular position is obtained as:

$$\theta(t) = \omega_c t \qquad (3.11)$$

Assuming that the workpiece is stationary and that the cutterhead is moving along the surface of the workpiece at speed v_f as it rotates, it can be generalised that the horizontal distance moved by the cutterhead at time *t*, for each cutting knife *i*, is given by:

$$a_i(t) = p(i-1) + v_f t \tag{3.12}$$

Let it be taken for now that the vertical centre position of the cutterhead does not change, Equation 3.10 will then become:

$$x(t) = p(i-1) + v_f t + R.\cos(\omega_c t + \theta_o) \tag{3.13a}$$

$$y(t) = R.\sin(\omega_c t + \theta_o) \tag{3.13b}$$

t is a linearly and equally spaced time vector ranging from 0 to the duration of the simulation. The number of points in the vector is the number of desired discrete points.

In order to verify the correctness of Equation 3.13, hypothetical values of 20mm/s and 60rpm were taken for the workpiece feed speed and cutterhead angular speed respectively. The locus of the knife tip obtained is shown in Figure 3.5. For a cutterhead rotating at 60rpm, it will take 3sec to make three revolutions. By this time, the workpiece would have moved a total length of 60mm. It can be seen clearly that the distance between point A and B is exactly 60mm, and the pitch is 20mm (point C to D) as expected from Equation 3.1.

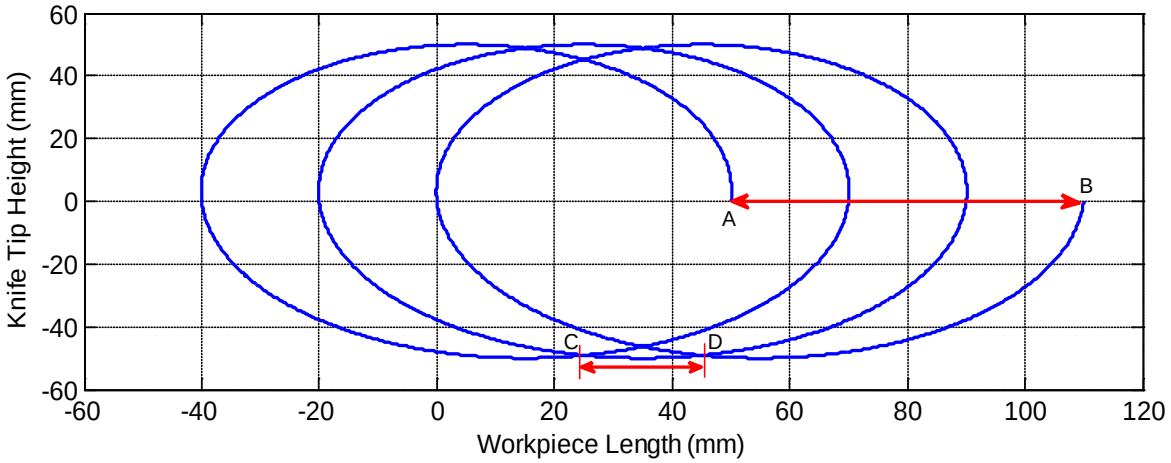


Figure 3.5 Instantaneous positions of the knife tip

3.4.2 Cutterhead Vibration Modelling

Mass imbalance in the cutterhead or spindle eccentricity will alter the vertical centre position of the cutterhead in space and hence the path followed by the cutters. Therefore, the second step is to find an expression for the instantaneous vertical centre position, *b(t)* of the cutterhead. It should be noted that the value of *b(t)* is always zero for machining conditions where there is no cutterhead vibration. The effect of vibration is accounted for by superimposing the vibration signal onto the nominal rotation of the cutterhead.

If there are *N* evenly-spaced knives around the circumference of the cutterhead, then the knife-passing period T_k, is calculated as follows:

$$T_k = \frac{T}{N} \tag{3.14}$$

T is the period of revolution of the cutterhead. As already mentioned in section 3.4.1, there would be too many unnecessary sample points if the knife tip paths are generated for a full revolution of the cutterhead and this could have a negative impact on the performance of

the algorithm. Secondly, it makes the extraction of the resultant surface profile from the knife loci more complicated.

Assuming that the oscillation of the cutterhead is a sinusoid with amplitude of *d*, occurring at d_{rev} times in one revolution of the cutterhead, the frequency of oscillation of the cutterhead ω_{osc} is given as:

$$\omega_{osc} = \omega_c \times d_{rev} \tag{3.15}$$

Suppose that the knife tips are simulated for only the lower semi-circular movement of the cutterhead, then the period of simulation will be half the period of revolution. This means that the first knife must be aligned with the negative x-axis (Cartesian coordinate) at the start of the simulation. The following knives will then align with the negative x-axis after every knife-passing period. The instantaneous vertical displacement of the cutterhead for each cutting knife *i*, can be generalised as follows:

$$b_i(t_2) = d \times cos(\omega_{osc} \times t_2 + \psi) \tag{3.16}$$

t_2 is another linearly and equally spaced time vector from t_{start} to t_{end} of each knife. The number of discrete points in t_2 must be the same as *t*:

$$t_{start} = (i-1) \times T_k \tag{3.17a}$$

$$t_{end} = t_{start} + \frac{T}{2} \tag{3.17b}$$

For a rotating body, there is always a 90^0 phase difference between the vertical and horizontal components of vibration. Taking that the cutterhead is rotating in anticlockwise direction, the horizontal component of vibration is given as:

$$c_i(t_2) = \mathrm{d} \times \cos\left(\omega_{osc} \times t_2 + \psi + \frac{\pi}{2}\right) \tag{3.18}$$

ψ is the parameter used to set the position of the resultant imbalance mass relative to the positive vertical axis, d is the amplitude of the cutterhead vibration, and ω_{osc} is the frequency of the cutterhead vibration. Since the time vectors t and t_2 are of the same length, the cutterhead knife tip vectors x and y are equal in length.

In most cases, the surface waviness patterns repeat every revolution of the cutterhead. Therefore a single revolution is enough to synthesis the resultant surface patterns. Special situations arise in cases where the wave patterns do not repeat every revolution of the cutterhead. According to Jackson (1986), a number of different types of primary waviness defects have been observed during the rotary machining process. A particular example of such defect cases is the case of vibration that occurs once every two revolutions of the cutterhead. In this situation, the wave patterns repeat every two revolutions of the cutterhead. Therefore, two cutterhead revolutions are required to generate the repeating patterns. In order for the simulation algorithm to be robust, a generalisation approach has to be established for these conditions.

Suppose that the vibration of the cutterhead occurs once every K revolutions of the cutterhead, it means that the waviness patterns will repeat every K revolutions. Therefore, K revolutions of the cutterhead will be required to synthesis the repeating surface profile

patterns. All other expressions still apply except for equations 3.12, 3.16 and 3.18, which are now further generalised as follows:

$$a_{ij}(t) = p(i-1) + v_f t + x(j-1) \tag{3.19}$$

x is the distance moved by the workpiece after every revolution of the cutterhead:

$$x = p.N \tag{3.20}$$

The phase shift of the cutterhead vibration after each revolution can be obtained as:

$$\alpha = \frac{2\pi}{K} .(j-1) \tag{3.21}$$

Therefore,

$$b_{ij}(t_2) = d \times cos(\omega_{osc} \times t_2 + \psi + \alpha) \tag{3.22}$$

$$c_{ij}(t_2) = d \times cos\left(\omega_{osc} \times t_2 + \psi + \alpha + \frac{\pi}{2}\right) \tag{3.23}$$

3.4.3 Cutterhead Inaccuracy Modelling

There are waviness defects caused by tracking inaccuracy of each individual cutting knife relative to the others within the rotating cutterhead. This is a situation where all the cutters do not have the same radius. The so called “proud knives” are slightly longer than the other ones. In order to account for the effect of proud knives, provision is made for specifying

the number of cutting knives on the cutterhead, and the radius of each knife. The knives' radii are specified using a vector containing the radius of each knife, given as:

$$R = [R_1, R_2, R_3, R_4 \ldots\ldots R_N] \tag{3.24}$$

The rotary machining process is represented by three concurrent movements of the cutterhead as depicted in Figure 3.6. The process is modelled in such a way that the cutterhead exhibits both rotational and vibrational motion as it moves linearly over the surface of the workpiece.

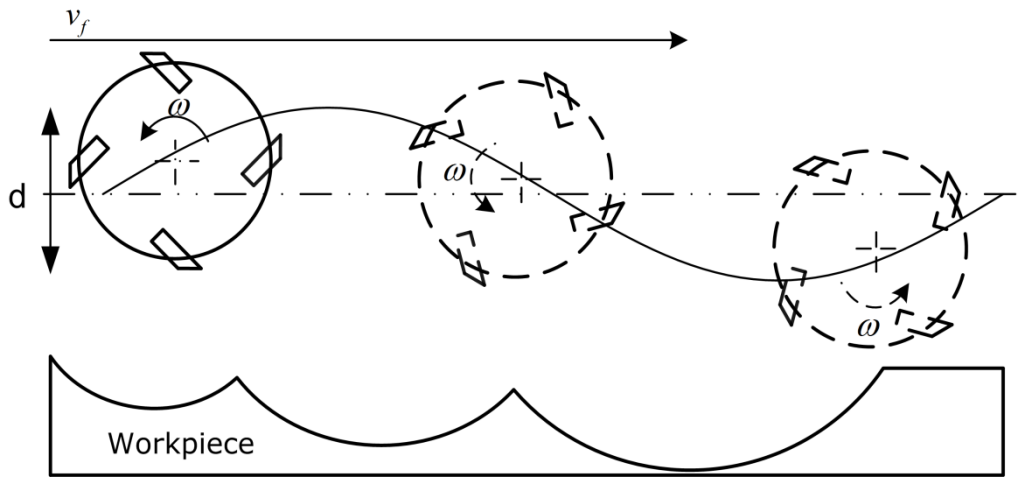


Figure 3.6 Representation of the rotary machining process of timber

The overall final equations are given as follows:

$$x_{ij} = a_{ij}(t) + c_{ij}(t) + R_i.\cos(\omega_c t + \theta_o) \tag{3.25a}$$

$$y_{ij} = b_{ij}(t_2) + R_i.\sin(\omega_c t + \theta_o) \tag{3.25b}$$

where

- *i = 1,2,3* ..... total number of knives on the cutterhead (*N*)
- *j = 1,2,3* ..... total number of cutterhead revolutions required to simulate the repeating patterns (*K)*
- *t* is a linearly spaced time vector between 0 and half of the period of revolution ($\frac{T}{2}$)
- t_2 is a linearly spaced time vector between t_{start} and t_{end} of each knife, as given in Equation 3.17
- $a_{ij}(t)$ is a matrix representing the instantaneous distance moved by the workpiece for the jth cutterhead revolution of the ith knife, calculated from Equation 3.19
- $b_{ij}(t_2)$ is a matrix representing the instantaneous vertical vibration signal for the jth cutterhead revolution of the ith knife, calculated from Equation 3.22
- $_{cij}(_{t2})$ is a matrix representing the instantaneous horizontal vibration signal for the jth cutterhead revolution of the ith knife, calculated from Equation 3.23
- θ_o is the initial angular displacement (*rad*) of the cutterhead w. r. t the positive x-axis (Cartesian coordinate). This value should always be set to π
- ω_c is the angular speed of the rotating cutterhead *(rad/s)*
- R_i is the radius of each knife, *i (mm)*
- x_{ij} and y_{ij} are matrices describing the path traced by the ith knife during the jth revolution of the cutterhead.

Inputs to the Model

- Number of knives on the cutterhead, *N*
- Radii of the cutting knives, $R = [R_1 \ldots R_N]$
- Workpiece feed speed, v_f
- Cutterhead angular speed, ω_c

- Cutterhead vibration amplitude, d
- Frequency of cutterhead vibration, ω_{osc}
- Parameter to set the position of the imbalance relative to the positive vertical axis, ψ

3.5 Extraction of the Surface Profile

Since the whole knife tip paths do not form the resultant profile, there is the need to extract the portions form the surface profile out of the whole knife tip paths. This process has been identified by the previous researchers as the most complicated part. It is done here by using a robust algorithm to compute the exact point of intersection between two adjacent knife tip paths. The data points below the points of intersection are then used to form the resultant surface profile.

By using the intersection of two successive knife tip paths, the assumption is that the resultant surface is an all-knife finish, which is not always the case. During the cutting process, the cuttermarks formed by some knives can be totally removed by the following knives. This can occur if there are proud knives or vibration of the cutterhead. There are some critical values of the vibration amplitude above which some knives cut the timber but do not produce any visible cuttermarks on the resultant surface profiles. Thus, a computational algorithm is first used to select each knife tip path having at least one point as the lowest value in y_{ij} for all x_{ij}.

Let x_1 and y_1 be equal-length vectors of at least two points representing the first curve, and similarly, x_2 and y_2 represent the adjacent curve. An algorithm which approximates the point of intersection from the actual data in the input vectors was used initially. The algorithm is such that for each point i, in x_1 and y_1, a loop is made through all points j, in x_2

and y_2 in order to find the point where $x_{1j} \geq x_{2j}$ and $y_{1j} \geq y_{2j}$. The first point to satisfy these criterions is then taken to be the point of intersection.

Even though its implementation is simple and fast, its limitation is that its accuracy depends on how closely *x* and *y* are sampled. The exact value at the point of intersection can only be obtained if a sampled data falls on that point. Consequently, the knife tip paths represented by the discrete sample points cannot provide accurate results in this case. The effect of this drawback is seen in Figure 3.7 where adjacent curves overlap after the extraction procedure.

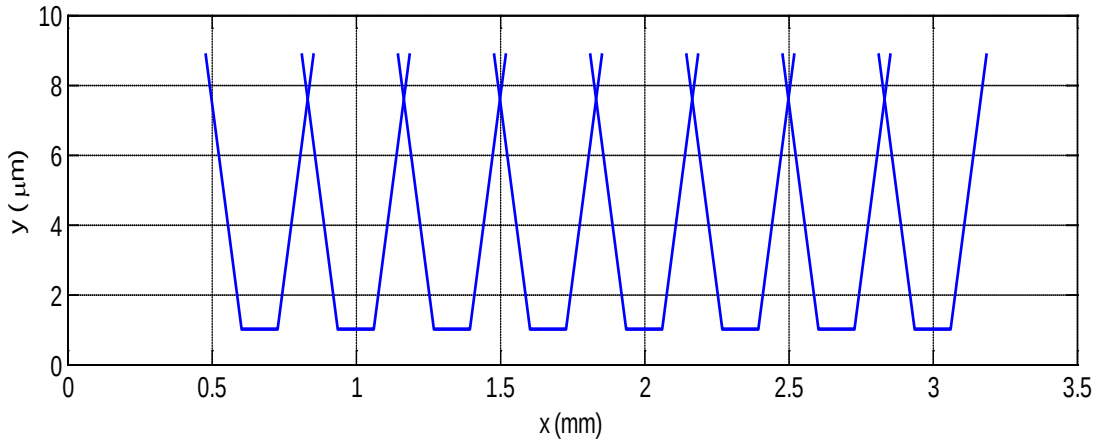


Figure 3.7 Effects of coarse sampling of the cutterhead movement

The limitation of the above algorithm led to the use of a more accurate method, which is explained below.

Given two line segments L_1 and L_2, where L_1 = (x_{11}, y_{11}) to (x_{12}, y_{12}) and L_2 = (x_{21}, y_{21}) to (x_{22}, y_{22}). Four equations with four unknowns can be generated as follows:

$$x = x_{11} + (x_{12} - x_{11}).S_1 \qquad (3.26a)$$

$$x = x_{21} + (x_{22} - x_{21}).S_2 \quad (3.26b)$$

$$y = y_{11} + (y_{12} - y_{11}).S_1 \quad (3.26c)$$

$$y = y_{21} + (y_{22} - y_{21}).S_2 \quad (3.26d)$$

- *(x, y)* is the point of intersection of L_1 and L_2
- S_1 is the distance from the starting point of L_1 to the point of intersection relative to the length of L_1
- S_2 is the distance from the starting point of L_2 to the point of intersection relative to the length of L_2.

The values of S_1 and S_2 are used to determine whether L_1 and L_2 intersect at *x* and *y* or not. If $0 \leq S_1 < 1$ and $0 \leq S_2 < 1$, then the two line segments intersect at *(x, y).* In principle, the solutions to the above equations should be found for every pair of line segments in the input vectors x_1, y_1, x_2, y_2. However, there can be quite a large number of points so a simple preliminary check is performed first in order to eliminate the line segment pairs that could not possibly cross. The check looks at the smallest enclosing rectangles for each line segment pair to see if there is an overlap. If there is an overlap, the values of S_1 and S_2 are computed to check if the line segments intersect before computing the values of *x* and *y*. This check eliminates all the line segment pairs except that of the actual point *(x, y)*, where the two lines intersect.

The way the above equations calculate the point of intersection between two adjacent curves is illustrated in Figure 3.8. The solutions to the equations are the values of *x* and *y*.

For the surface profile to be accurately generated without overlaps, the values of x_{12} and x_{21} are replaced by x. Similarly, the values of y_{12} and y_{21} are replaced by y.

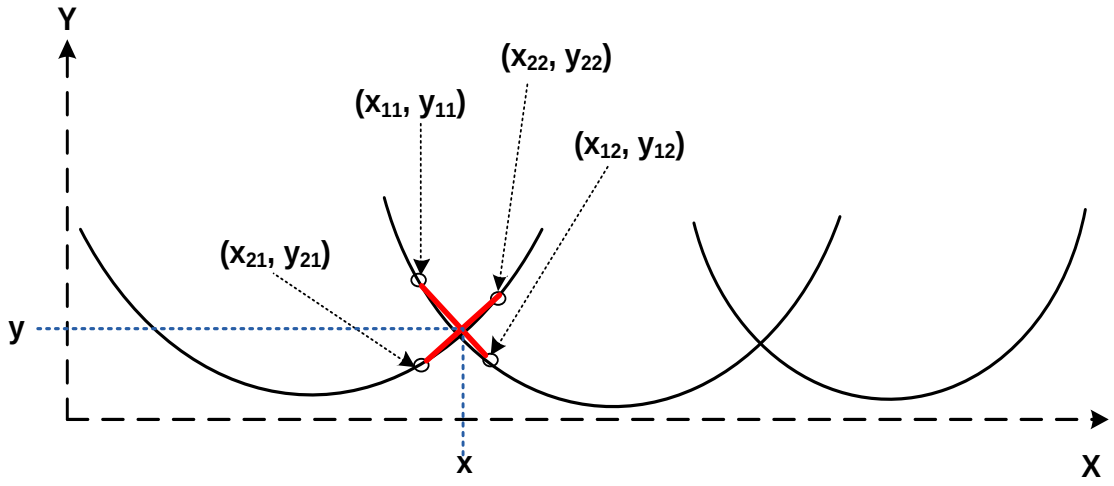


Figure 3.8 Calculating the point of intersection between two adjacent curves

After selecting the data sets below the points of intersection of adjacent curves, only a small fraction of the data points in each curve eventually form the resultant profile. This is because the time taken by each knife to travel through the length of each cuttermark (time of cutter engagement) is insignificantly short compared to the time taken by the cutterhead to make one revolution.

The effect of generating the surface profile from such few data points is also shown in Figure 3.7. Many sample points for each knife tip path are required to provide smooth curves for the surface profile after the extraction. This is a major problem earlier pointed out by Maycock (1993) and Brown (1999). The downside of having such large data points is that the performance of the surface extraction procedure is greatly affected.

An effective way of going round this problem is to reduce the number of sample points for each knife tip path, and then use cubic spline approximation to draw a smooth curve around the few remaining data points (Hynek, 2004). The cubic spline interpolation is a piecewise continuous curve, passing through each of the data points. An example of the knife tip paths and the extracted surface profile is shown in Figure 3.9.

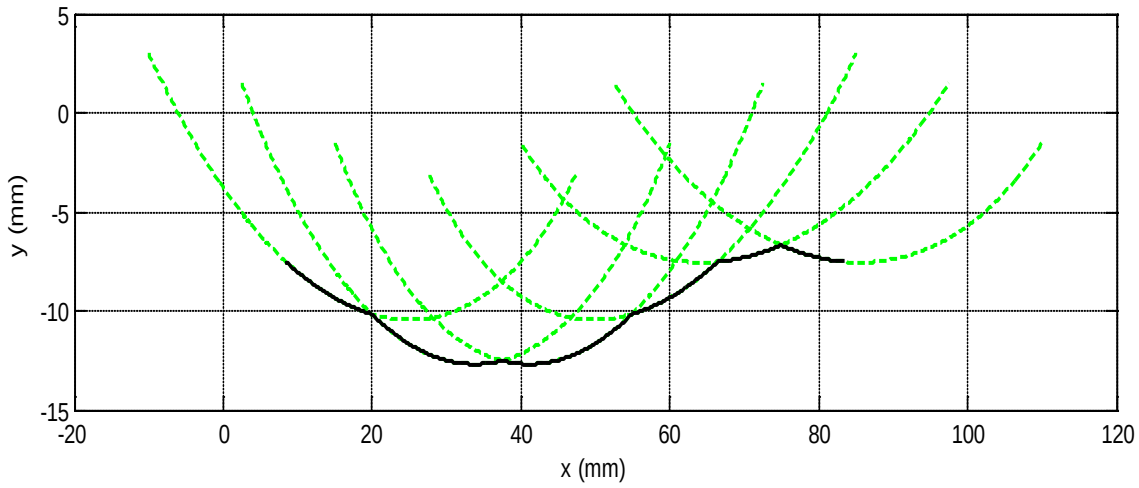


Figure 3.9 Knife tip paths and the extracted surface profile

Since the *x* and *y* coordinates of the points of intersection are known, the exact height *h*, and width *w*, of each cuttermark can be extracted from the surface profiles without the need for further analysis (Figure 3.10).

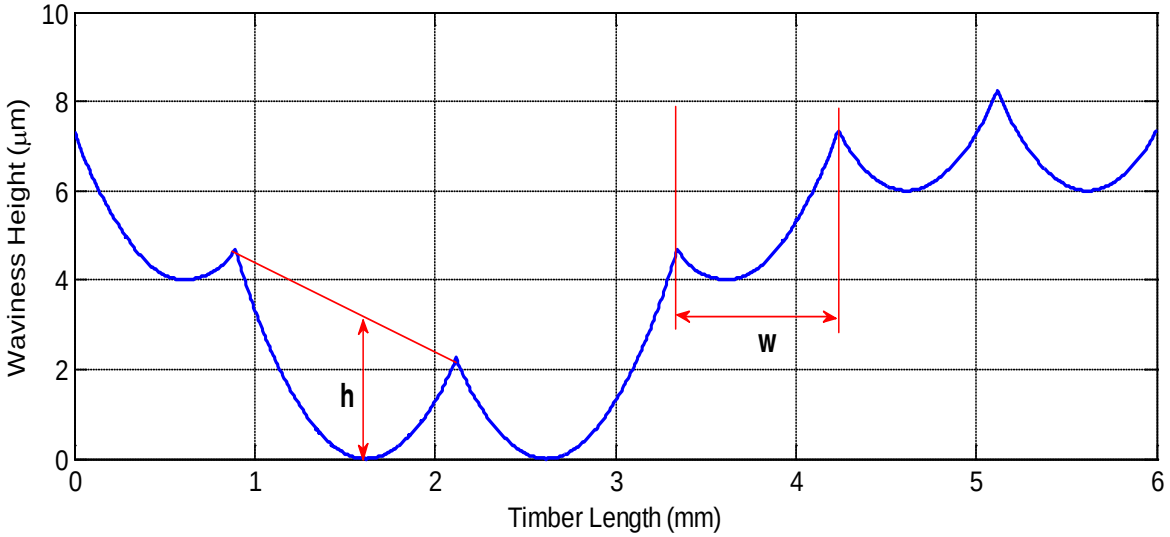


Figure 3.10 Extraction of cuttermarks height and width

3.6 Depth of Cut Consideration

The depth of cut in wood machining is usually about 500μm or greater in order to avoid push off or rubbing of the cutting edge on the timber workpiece (Jackson, 1986). Since this value is far greater than the maximum peak-to-peak height of the cuttermarks, the depth of cut could be justifiably neglected in formulating the simulation algorithm. Nevertheless, the effect of the depth of cut, which is smaller than the maximum peak-to-peak height of the cuttermarks, is also taken into consideration.

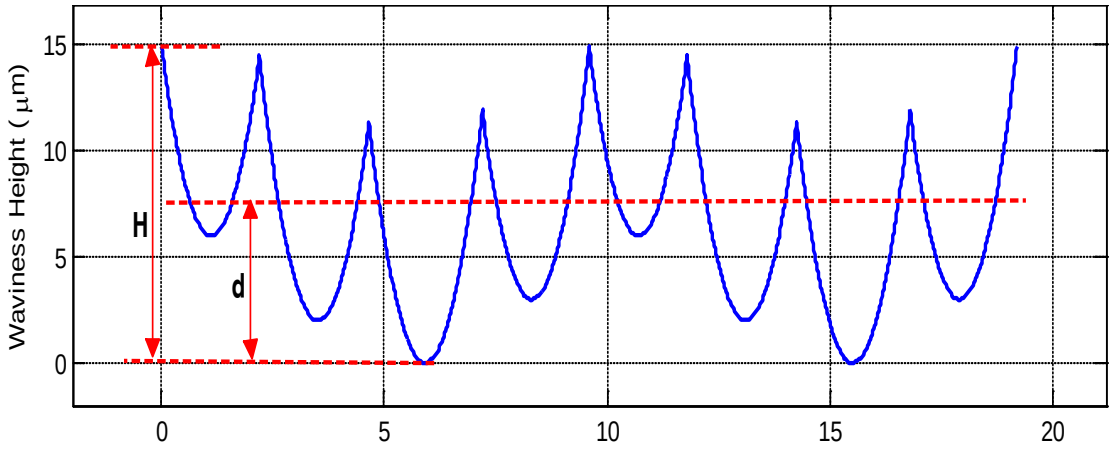


Figure 3.11 Depth of cut consideration

With reference to Figure 3.11, the depth of cut, d_c, does not have any effect on the surface profile if its value is greater than or equals to the peak-to-peak height, H. However, if d_c is less than H as shown, then all the data points above that line are replaced with the value of d_c according to equation 3.27. The effect of a depth of cut value of $10\mu m$ on Figure 3.9 is shown in Figure 3.12.

$$y_{ij} = \begin{cases} d_c, & d_c < H \\ y_{ij}, & d_c \geq H \end{cases} \tag{3.27}$$

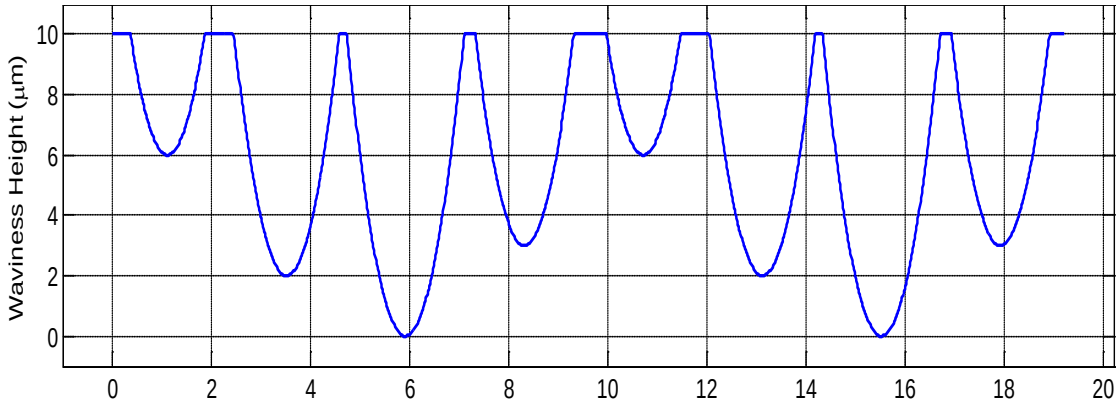


Figure 3.12 Effect of small depth of cut

3.7 Simulation Examples

Some examples of typical waviness profiles are synthesised in this section using the ECAT. The results are compared with those of the generalised circular arc theory in order to show that the circular arc theory could also be used as a general-purpose simulator. Secondly, the comparison is done in order to provide a base reference for the ECAT.

Example 1

The first example is a six-knife finish without any defect. The machining parameters used are $N = 6$, $R = [70, 70\ 70, 70, 70, 70]$ mm, $v_f = 768$mm/s and $\omega = 4800$rpm. The surface profiles generated using the generalised circular arc theory and the ECAT are shown in Figure 3.13. The surface has been simulated for two cutterhead revolutions. The widths and heights of the cuttermarks, which have been extracted as explained in section 3.5, are shown in Table 3.1.

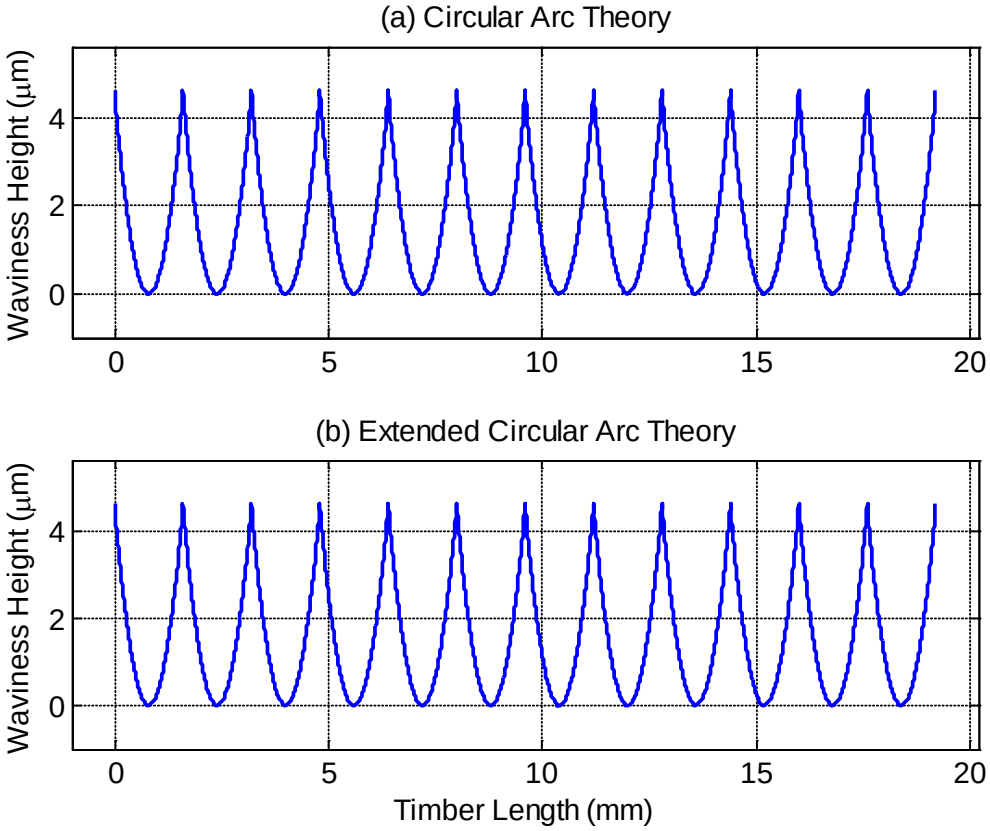


Figure 3.13 Six-knife finish without any defect

Table 3.1 Surface waviness assessment for example 1

	Circular Arc Theory		Ext. Circular Arc Theory	
	w(mm)	*h(μm)*	*w(mm)*	*h(μm)*
Knife 1	1.60	4.60	1.60	4.40
Knife 2	1.60	4.60	1.60	4.40
Knife 3	1.60	4.60	1.60	4.40
Knife 4	1.60	4.60	1.60	4.40
Knife 5	1.60	4.60	1.60	4.40
Knife 6	1.60	4.60	1.60	4.40

The data in Table 3.1 confirm the point made in Hynek (2004) that the actual waviness height is between 2-5% lower than the height of the idealised surface. If the height of each cuttermark is computed from Equation 3.2, the value that would be obtained is 4.6μm. This is exactly the value obtained for the circular arc theory. For the ECAT, the height is about 4.4% lower than that of the circular arc theory height.

Example 2

The second example shows the effect of proud knives on surface finishes. The machining parameters used are $N = 6$, $R = [70, 70\ 70.003, 70, 70.002, 70]$ mm, $v_f = 768$mm/s and $\omega = 4800$rpm. From the specified knife radii, the third and fifth knives are longer than the other four by $3\mu m$ and $2\mu m$ respectively. As can be seen in Figure 3.14, the proud knives produce deeper cuttermarks than the rest of the knives. The two algorithms produce similar waviness patterns apart from the expected slight differences in the cuttermark heights.

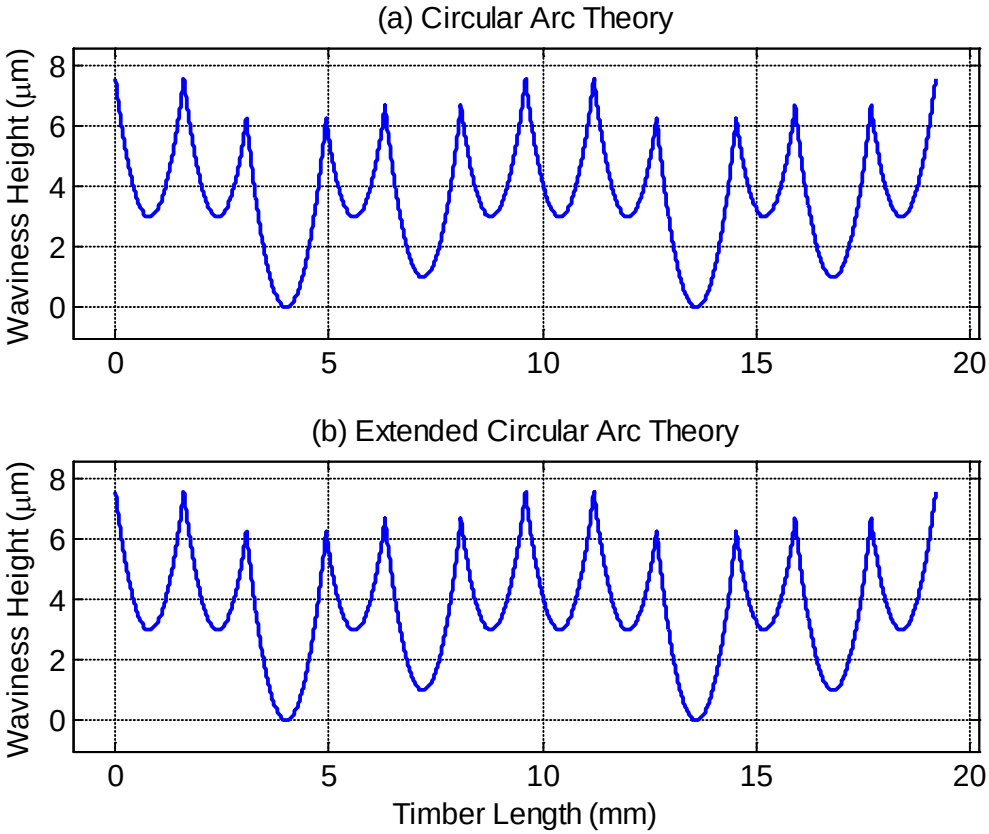


Figure 3.14 The effect of proud knives

Table 3.2 Surface waviness assessment for example 2

	Circular Arc Theory		Ext. Circular Arc Theory	
	w(mm)	*h(μm)*	*w(mm)*	*h(μm)*
Knife 1	1.60	4.60	1.60	4.40
Knife 2	1.47	3.90	1.46	3.70
Knife 3	1.86	6.30	1.87	6.10
Knife 4	1.38	3.50	1.37	3.30
Knife 5	1.77	5.70	1.78	5.50
Knife 6	1.51	4.20	1.51	4.00

Effects of Vibration

The following examples show the effect of spindle vibration during the machining process. There is a slight difference in the initial cutting conditions between the generalised circular arc theory and the ECAT. The positions of the first knives relative to the positions of the resultant mass imbalances are shown in Figure 3.15. In order to have a common basis for comparing the results of the two algorithms, the value of ψ needs to be set to $-\pi/2$.

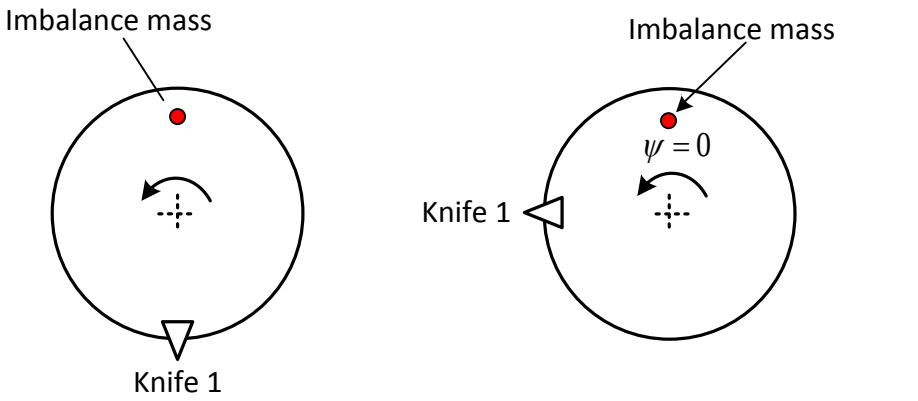


Figure 3.15 Initial cutting conditions of the cutterhead

Example 3

The third example is a two-knife finish having superimposed vibration at once every revolution of the cutterhead. This type of waviness defect is usually as a result of the cutterhead mass imbalance, which causes the cutterhead to vibrate at the frequency equal to the spindle rotational speed (Jackson, 1986). The machining parameters are $R = 75mm$, $N = 2$, $v_f = 150mm/s$ and $\omega = 3000rpm$, and the vibration amplitude is $3\mu m$. Figure 3.16 shows the surface waviness generated using the generalised circular arc theory and the ECAT. The waviness quality assessment is shown in Table 3.3.

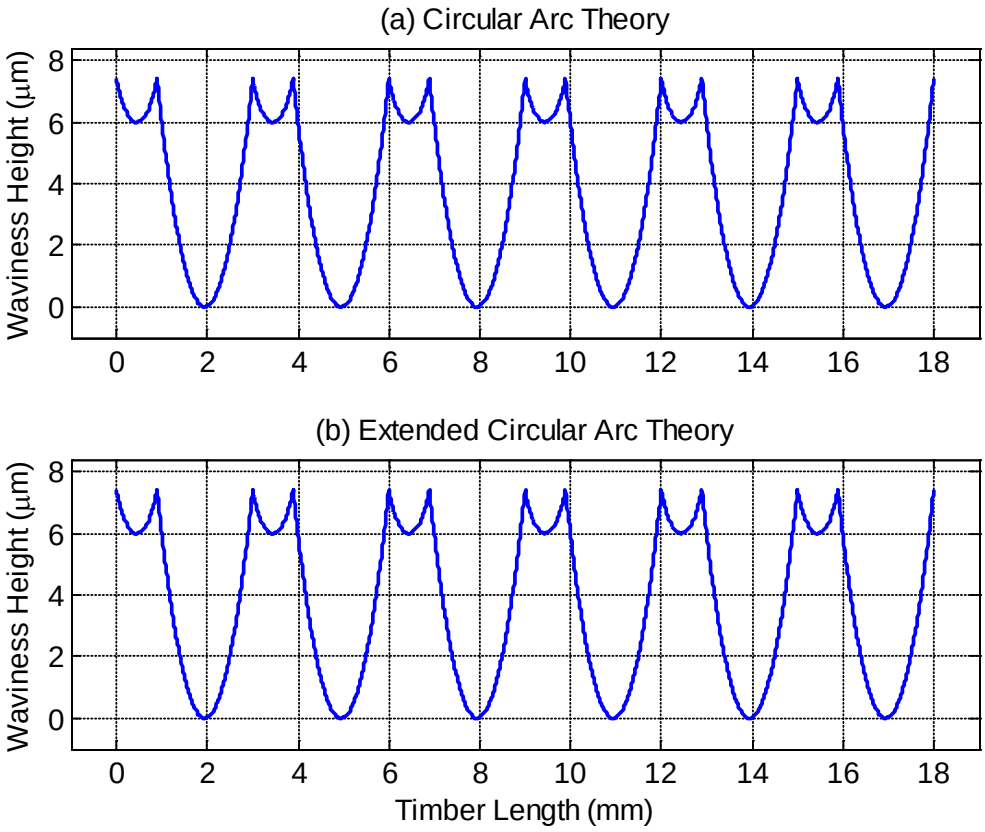


Figure 3.16 The effect of once per revolution vibration on two-knife finish

Table 3.3 Surface waviness assessment for example 3

	Circular Arc Theory		Ext. Circular Arc Theory	
	w(mm)	*h(μm)*	*w(mm)*	*h(μm)*
Knife 1	0.94	1.60	0.93	1.60
Knife 2	2.06	7.60	2.07	7.60

The expected width of the cuttermarks for a non-defective surface is 1.5mm but the cutterhead vibration has caused non uniform cuttermarks to be produced. This is because one knife is always cutting when the cutterhead is at the lowest vertical position and the other diametrically opposite knife is cutting when the cutterhead is at the highest position. The vibration amplitude is significant compared to the expected cuttermarks height and that is why the effect of the vibration is very evident.

Example 4

The fourth example (Figure 3.17) is that of a four-knife finish having the same superimposed vibration at once every revolution of the cutterhead. The machining parameters are $R = 60mm$, $N = 4$, $v_f = 300mm/s$ and $\omega = 3000rpm$. The vibration amplitude is $4\mu m$. The pitch and height expected from these machine settings for a perfect surface are $1.5mm$ and $3.7\mu m$ respectively. The waviness assessment for this defect is shown in Table 3.4.

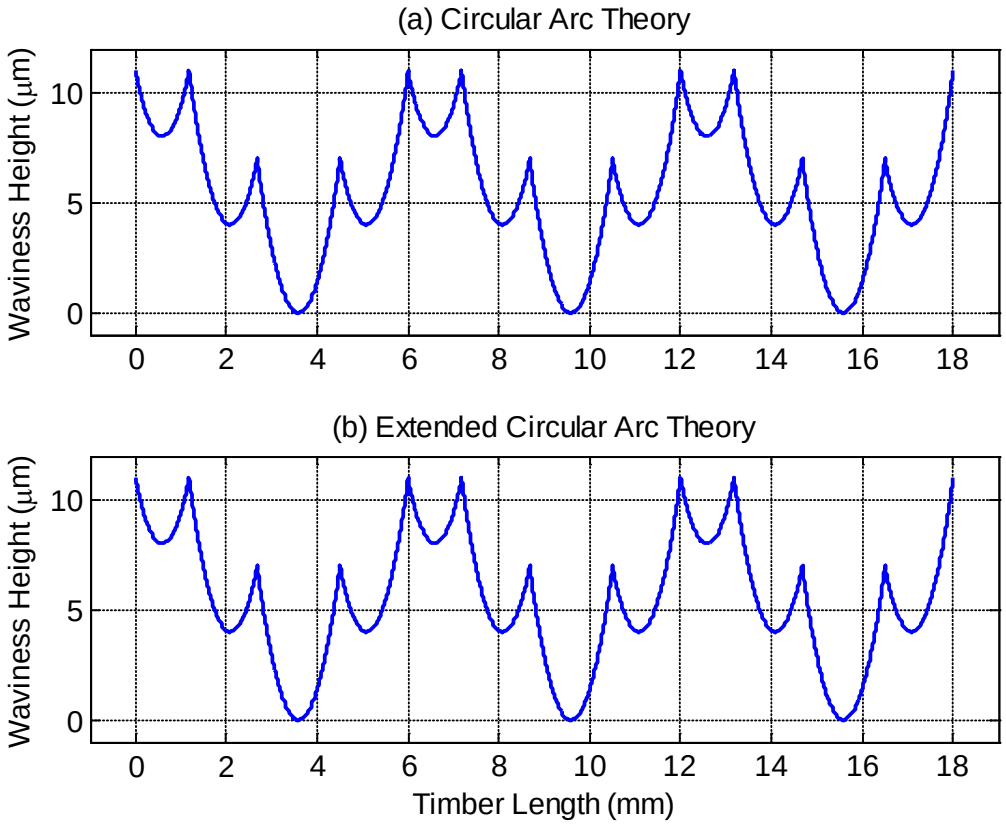


Figure 3.17 The effect of once per revolution vibration on four-knife finish

Table 3.4 Surface waviness assessment for example 4

	Circular Arc Theory		Ext. Circular Arc Theory	
	w(mm)	*h(μm)*	*w(mm)*	*h(μm)*
Knife 1	1.18	3.00	1.17	2.90
Knife 2	1.50	5.00	1.50	4.80
Knife 3	1.82	7.00	1.83	6.80
Knife 4	1.50	5.00	1.50	4.80

Example 5

The fifth example shown in Figure 3.18 is a six-knife finish with combination of proud knives and vibration occurring at twice per revolution of the cutterhead. The machining parameters are $R = [65, 65.001, 65, 65.003, 65, 65]mm$, $N = 6$, $v_f = 468mm/s$ and $\omega = 3600rpm$. The vibration amplitude is $3\mu m$. The corresponding pitch and height for a non-defective surface are $1.3mm$ and $3.3\mu m$ respectively. The surface waviness assessment for this defect is shown in Table 3.5.

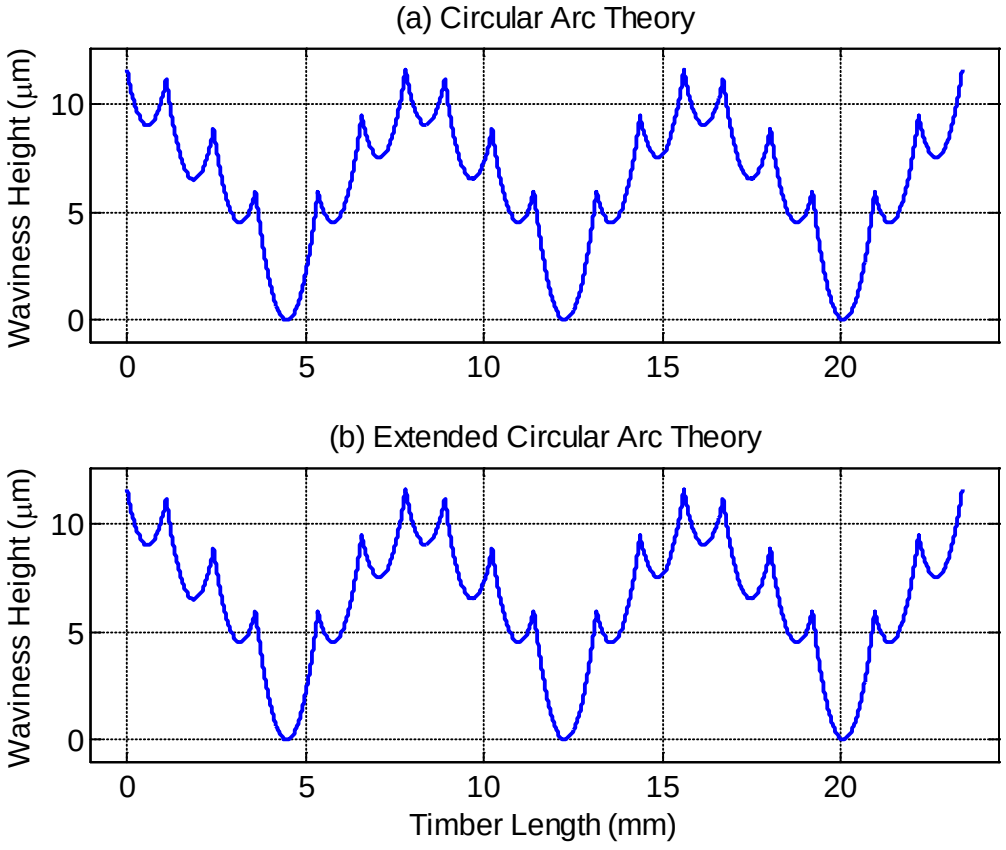


Figure 3.18 The effect of vibration and proud knives on six-knife finish

Table 3.5 Surface waviness assessment for example 5

	Circular Arc Theory		Ext. Circular Arc Theory	
	w(mm)	*h(μm)*	*w(mm)*	*h(μm)*
Knife 1	1.10	2.40	1.10	2.30
Knife 2	1.32	3.50	1.32	3.40
Knife 3	1.17	2.90	1.17	2.80
Knife 4	1.75	6.00	1.76	5.80
Knife 5	1.22	3.20	1.22	3.10
Knife 6	1.23	3.00	1.23	2.90

3.8 Summary and Conclusions

In this chapter, a generalised model for the existing circular arc theory has been developed so that expressions would not have to be derived for each defect case. This transforms the circular arc approximation method to a general-purpose simulator, which can easily be used to investigate the effects of combinations of one or more factors. Its only major limitation is that it does not represent the actual kinematics of the process.

A new simulation model for synthesising the surface profile produced by the rotary machining process of timber, known as ECAT, has also been developed. The algorithm models the instantaneous kinematics of the cutting process by using the equations of a circle with time-varying centre coordinates. The improvement offered by the new simulation model over the most recent one (Hynek, 2004) are as follows. Firstly, it allows easy extraction of the cuttermarks widths and heights without the need for further processing. Secondly, it allows easy variation of the position of the resultant mass imbalance (initial vertical position of the cutterhead), which is a very important requirement for simulating the effect of cutterhead vibration. Most notably, there is no any other general-purpose simulation model with such direct inputs and simple analytic expressions. This new algorithm is utilised more extensively in chapter five to generate synthetic data for the purpose of defect characterisation on planed timber surfaces.

4 Dynamic Wood Surface Profile Measurements

Traditionally, workpiece samples are measured after machining in order to assess the quality of their surface finishes. The primary disadvantage of the post-machining inspection is that corrections cannot be made in real-time if the surface quality is lower than the desired quality. The increasing demand for higher quality products in wood machining necessitates the need for an in-process surface profile measurement system. Therefore, the focus of this chapter is on dynamic wood surface profile measurements using a machine vision technique known as photometric stereo (PS). The online surface quality inspection can provide feedback information for the secondary closed-loop control of the machining process (Figure 1.6).

4.1 Background

PS is a technique used to recover the shape (surface orientation) and reflectance properties of an object from multiple images captured in a fixed spatial location but under different illumination directions. A special case of the PS method in which the shape of an object is estimated from a single image is known as shape from shading (SFS). In principle, conventional photometric stereo (CPS) technique is only applicable to static objects because it requires that the object position remains fixed with respect to the imaging system during the acquisition of the photometric images. That is, the pixel corresponding to a location in one image must correspond to the same location in the other images. The so-called correspondence problem now arises if the object is subjected to movements during the acquisition of the successive image pairs. Although the PS technique is widely used in computer vision, it has not been able to cross into the domain of industrial surface inspection where movement of samples has limited its application (Farooq et al., 2005).

Earlier investigations carried out by Yang (2006) showed that PS and SFS techniques can be used to measure wood surface profiles. In that research, two-image PS and one-image SFS methods were implemented for assessing the cuttermarks on static planed wood surfaces. In the case of static samples, the need to match the two images before applying PS algorithm would not arise because the workpiece remains in the same position when the image pairs are captured.

SFS technique would be more suitable for dynamic surface profile measurements because there is no need to match images since it utilises a single image of the workpiece. However, its consistency and reliability is questionable as reported by Yang (2006). Generally, one of the assumptions made by SFS technique is that the surface to be measured has uniform reflectance properties (albedo). It is uncertain whether the reflective properties of wood are such that the albedo is constant or varies within a small range that it effects could be neglected. Yang (2006) recommended that an appropriate technique should be used to recover the point-by-point albedo of wood samples in order to address this uncertainty.

Therefore, the work reported in this chapter involves the following:

- Use of a three-image PS technique to recover the surface reflectance properties of some selected wood samples
- Extension of PS technique to the measurements of moving wood samples

4.2 Theory of Photometric Stereo and Shape from Shading

The fundamental theory that underpins the application of PS and SFS techniques to the shape and albedo recovery of wood is the assumption that wood exhibits Lambertian (diffuse) reflectance. Although total reflection from polished wood surfaces usually comprises of both specular and diffuse reflection, unfinished wood exhibits approximately diffuse reflectance because of its heterogeneous and anisotropic nature (Maristany et al., 1992). The geometry of the Lambertian surface reflectance function is shown in Figure 4.1.

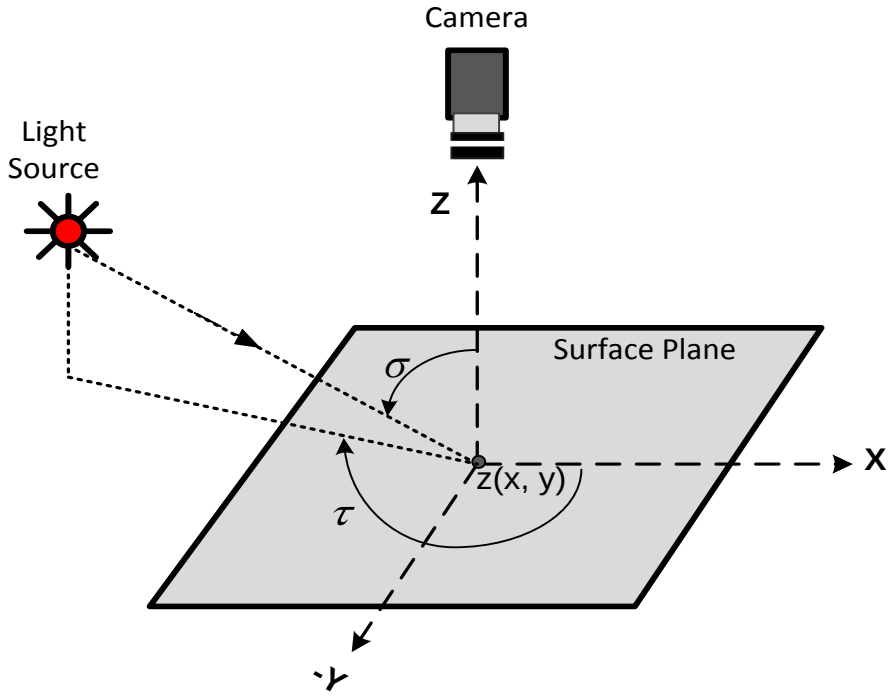


Figure 4.1 Geometry of the generalised Lambertian surface photometric function

where

- The *XY* plane is coincident with the object surface and the *Z* axis is perpendicular to the object surface
- The *Z* axis is aligned with the viewing direction

- τ is known as the azimuth or tilt angle of the light source. It is the angle between the *X* axis and the light path, measured in the *XY* plane
- σ is known as the zenith or slant angle of the light source. It is the angle between the light path and the camera direction.

According to Lambert's law, the reflection from a point (*x, y*) on a Lambertian surface is given by:

$$I(x,y) = I_o \rho(x,y) \left(\frac{-p(x,y)\cos\tau\sin\sigma - q(x,y)\sin\tau\sin\sigma + \cos\sigma}{\sqrt{(p^2(x,y) + q^2(x,y) + 1)}} \right) \qquad (4.1)$$

where

- *I(x, y)* is the intensity reflected at the point *(x, y)*
- I_o is the intensity of the incident light
- *ρ(x, y)* is the point albedo; it is the fraction of incident light that is being reflected from the point *(x, y)*
- *p* and *q* define the gradient of the surface at any local point in the *x* and *y* directions respectively.

4.2.1 Surface Albedo Recovery using PS

There are three unknowns in in Equation 4.1. Hence, by utilising three separate images that are acquired under different illumination directions, it is possible to generate a set of three simultaneous equations for finding unique solutions to the equation. The following albedo recovery technique is adapted from Smith (2001), in which Equation 4.1 is expressed by the following matrix equation:

$$\begin{bmatrix} I_1 \\ I_2 \\ I_3 \end{bmatrix} = I_o \rho \begin{bmatrix} s_{1x} & s_{1y} & s_{1z} \\ s_{2x} & s_{2y} & s_{2z} \\ s_{3x} & s_{3y} & s_{3z} \end{bmatrix} \begin{bmatrix} n_x \\ n_y \\ n_z \end{bmatrix} \quad (4.2)$$

where I_1, I_2, and I_3 are the intensity values of the three images, ρ is the unknown surface albedo, (n_x, n_y, n_z) are the unknown components of the local surface normal, and (s_1, s_2, s_3) are unit vectors describing the locations of the light sources. Equation 4.2 can be re-written in a more concise notation as follows:

$$I = I_o \rho \, [s] \, n \quad (4.3)$$

$$\eta = \rho I_o = |[s]^{-1} I| \quad (4.4)$$

I is the image intensity vector, $[s]$ is the light source direction matrix, n is the surface normal component vector and η is known as the composite albedo. For $[s]^{-1}$ to exist, the three light sources and the surface location of interest must not lie in the same plane (non-coplanar). It is very essential to position the lights at different locations that are distinct from one another. All the light sources must also contribute to the illumination of the observed surface one at a time.

4.2.2 Surface Gradients Recovery using PS

Ideally, a rotary planed wood surface does not have cuttermarks height variation along the Y axis, i.e. $q(x, y) \cong 0$. For this reason, the three-dimensional surface topography can be represented by a two-dimensional surface profile (Jackson et al., 2007). Equation 4.1 then reduces to the following equation:

$$I(x) = I_o \rho(x) \left(\frac{-p(x) \cos\tau \sin\sigma + \cos\sigma}{\sqrt{(p^2(x) + 1)}} \right) \tag{4.5}$$

If an object is illuminated from two distinct locations, the surface reflectance will be the same but the reflectance map will be different (Jain et al., 1995; Smith, 2001). Suppose that two lights having approximately equal intensities are located at the same zenith angle σ, but at different azimuth angles $\tau_1 = 0^o$ and $\tau_2 = 180^o$ (Figure 4.2), then the following equations can be obtained from Equation 4.5:

$$I_1(x) = I_o \rho(x) \left(\frac{-p(x) \cos\tau_1 \sin\sigma + \cos\sigma}{\sqrt{(p^2(x) + 1)}} \right) \tag{4.6a}$$

$$I_2(x) = I_o \rho(x) \left(\frac{-p(x) \cos\tau_2 \sin\sigma + \cos\sigma}{\sqrt{(p^2(x) + 1)}} \right) \tag{4.6b}$$

By substituting the values of τ_1 and τ_2, and then dividing equation 4.6a by equation 4.6b:

$$p(x) = \frac{I_2(x) - I_1(x)}{I_2(x) \cos\tau_1 - I_1(x) \cos\tau_2} \cdot \frac{1}{\tan\sigma} \tag{4.7}$$

Consequently, only two images are required to compute the gradient of the surface. The images are first converted into intensity profiles using the column-wise averaging technique described in Yang (2006) as shown in Figure 4.3. The intensity profile is calculated from the following equation:

$$I(j_{col}) = \left(\sum_{i_{row}=1}^{m} I(i_{row}, j_{col}) \right) / m \qquad (4.8)$$

where $I(i_{row}, j_{col})$ is the intensity value of the pixel at the i_{row}^{th} row and the j_{col}^{th} column of the image matrix, and m is the number of rows in the matrix. The intensity profiles for the two images are then substituted for $I_1(x)$ and $I_2(x)$ in Equation 4.7 to calculate $p(x)$.

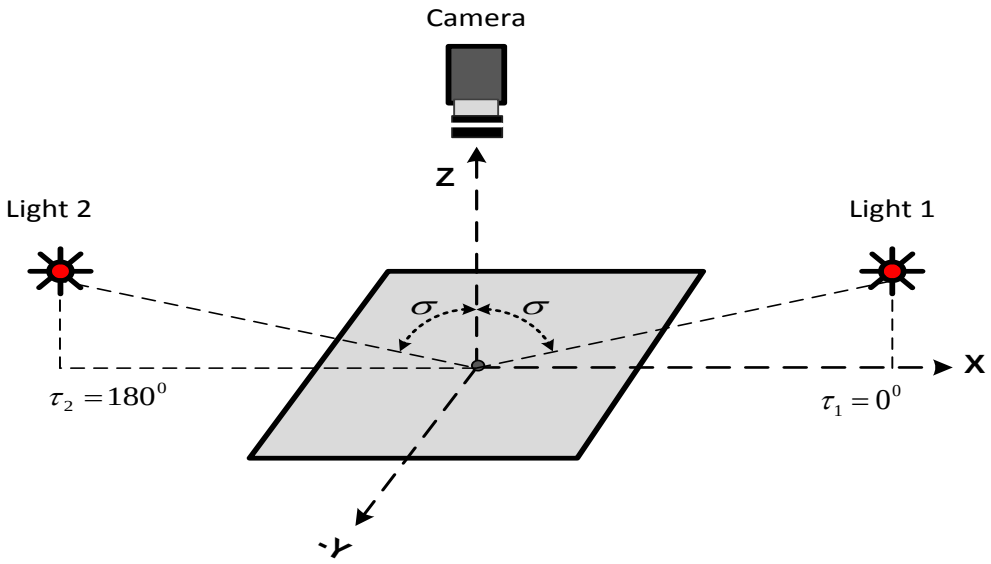


Figure 4.2 Schematic of the 2-image photometric stereo setup

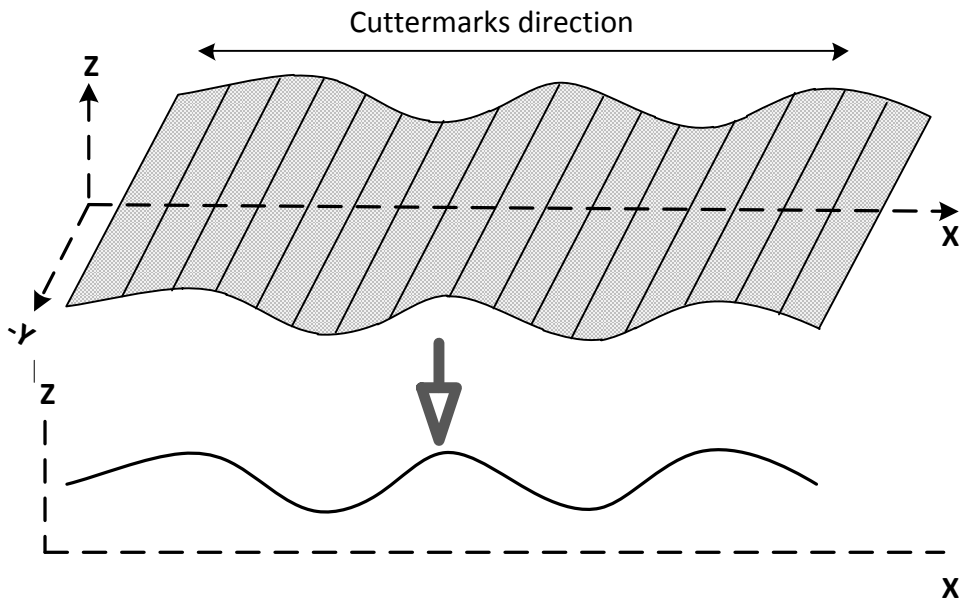


Figure 4.3 Conversion from 3D to 2D profile by column-wise averaging (Yang, 2006)

4.2.3 Surface Gradients Recovery using SFS

The central problem in SFS is the difficulty in finding a unique solution to Equation 4.1 using one image. The problem has been simplified in this case by the assumption that the cuttermarks height only varies in one direction. Surface smoothness constraint and an assumption of constant albedo for wood are used to further simplify the problem.

A smooth surface is characterised by slowly varying gradients. Since the cuttermarks heights are in micrometre range, it can be assumed that the surface is smooth enough so that *p(x) << 1*. Hence, $\sqrt{(p^2(x)+1)} \approx 1$. The other main assumptions are those of constant albedo and uniform illumination at every point on the surface. With these assumptions, the effects of the incident intensity and albedo are neglected. Therefore, Equation 4.5 further reduces to the following equation:

$$I(x) = (-p(x)\cos\tau\sin\sigma + \cos\sigma) \tag{4.9}$$

The equation for calculating the gradient of the surface profile along *x*-direction is obtained as follows:

$$p(x) = \frac{\cos\sigma - I(x)}{\cos\tau \sin\sigma} = \frac{1}{\cos\tau \tan\sigma} - \frac{I(x)}{\cos\tau \sin\sigma} \quad (4.10)$$

where *I* is a row vector obtained from the column-wise averaging of the image intensity.

4.2.4 Height Recovery from the Surface Gradients

Integration of the gradient data is required to transform the data into height. The integration may be performed using either local or global approaches. Though local techniques are easy to implement and computationally efficient, the local nature of the calculations and the propagation of errors make them to be more susceptible to noise (Gullon, 2003). Since the imaging system can pick up wood chips and other sources of noise during the acquisition of the images, a global integration approach is implemented as described in Frankot and Chellappa (1988).

4.3 Camera Calibration

Camera lenses are not perfectly manufactured in practice. The shape of the lenses can lead to radial (barrel or pincushion) distortions of the pixel locations in the images. The effect of distortion is that a perfectly straight line in the object coordinate appears bent in the image. Tangential distortions can also arise due to the lenses being imperfectly aligned with the image plane during the assembling process (Bradski and Kaehler, 2008).

Significant lens distortions will definitely affect the results of the column-by-column averaging of the image intensity data shown in Figure 4.3. It is very critical that the

variation of the cuttermarks across the feed direction should be maintained in the images; otherwise the column-wise averaging cannot be used to accurately convert the 3-D profile to a 2-D profile. In order to eliminate the effect of lens distortions, the images have to be corrected before applying the averaging technique. The distortions can be corrected according to Brown's model (Brown, 1971) as given by the following equations:

$$x_u = x_d + \bar{x}(k_1 r^2 + k_2 r^4 + k_3 r^6) + p_1(r^2 + 2\bar{x}^2) + 2p_2\bar{x}\bar{y} \qquad (4.11a)$$

$$y_u = y_d + \bar{y}(k_1 r^2 + k_2 r^4 + k_3 r^6) + 2p_1\bar{x}\bar{y} + p_2(r^2 + 2\bar{y}^2) \qquad (4.11b)$$

in which

$$\bar{x} = x_d - x_o, \qquad \bar{y} = y_d - y_o$$

$$r = \sqrt{[(x_d - x_o)^2 + (y_d - y_o)^2]}$$

where

(x_d, y_d) is the original location of the distorted point

(x_u, y_u) is the new location of the corrected point

(x_o, y_o) is the principal point of the image

k_1, k_2 and k_3 are coefficients of the 2nd, 4th and 6th order radial distortion respectively

p_1 and p_2 are the coefficients of tangential distortion.

Only the second order radial distortion component is required for lenses with narrow field of view (FOV). Even for cameras with standard FOV, it is often not necessary to estimate

the distortion coefficients beyond the 4th order because radial distortions are primarily dominated by low order components (Zhang, 1999). The tangential components of distortion can also be justifiably neglected because most currently manufactured lenses do not have imperfection in centring (Zhang, 1999). The principal point could also be assumed to be located at the centre of the image sensor. Consequently, the only required parameter is k_1.

The distorted images are then corrected using a reduced version of Equation 4.11 given as:

$$x_u = x_d + \bar{x}k_1r^2 \qquad (4.12a)$$

$$y_u = y_d + \bar{y}k_1r^2 \qquad (4.12b)$$

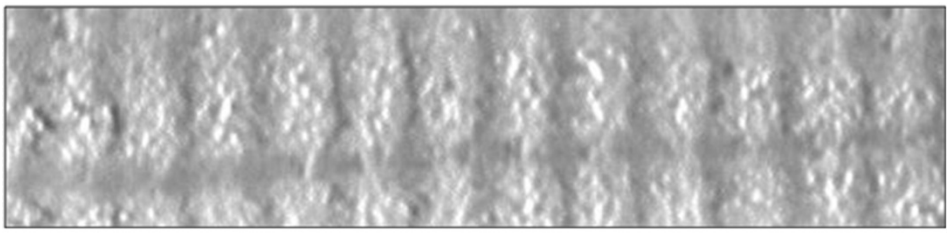
A camera calibration procedure is required to estimate the intrinsic parameters, k_1. The details of the camera calibration procedure are explained in Appendix A.

4.4 Determination of the Optimum Light Source Positions

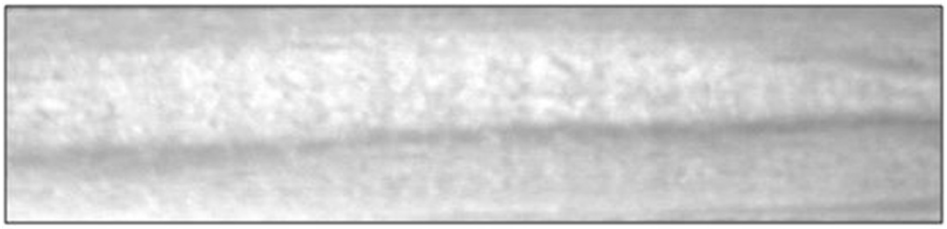
The success of most machine vision techniques depends on the setup of the illumination sources. In theory, the PS and SFS techniques require that the light sources be distant point light sources so that uniform illumination across the surface area can be obtained. This requirement cannot be met due to space restrictions and the desire for compact design. Therefore, collimated light emitting diodes (LEDs) are used so that this requirement could be approximately met. Although rays from collimated lights spread out gradually as they propagate, the divergence is usually minimal.

The effects of positioning the light sources at small or large zenith angles have been reported by Yang (2006). Theoretically, any angle of incidence should give the same results (Equation 4.7 and Equation 4.10). However, if the angle of incidence is too close to 90^0, the illumination will produce shadowy surfaces. Meanwhile, Lambert's law does not apply to shadowy surfaces. Small angles of incidence (0^0 - 30^0) also reduce the contrast of the images, thereby reducing the amount of cuttermarks' information that can be revealed. The optimum angle of incidence is found to be within the range of 80^0 - 85^0.

Further experiments have been carried out in this research to determine the optimum azimuth angles of the light sources. These experiments are necessitated by the fact that the eventual goal is to integrate the machine vision system with a wood planer test rig whose construction might not allow the lights to be located at some particular positions. Generally, the only requirement for the locations of the light sources in terms of azimuth angle is that the light sources should not be coplanar. However, it has been observed that only the projections where the light rays are directly perpendicular to the cuttermarks (0^o and 180^o) contribute greatly to the performance of the proposed surface recovery methods. Images of a machined pine, captured with light sources positioned at azimuth angles of 0^o and 90^o are shown in Figure 4.4. The cuttermarks (pitch = 2.5mm) are more visible in Figure 4.4a compared to Figure 4.4b. This indicates that the further the light sources are positioned away from azimuth angles of 90^o or 270^o, the better the illumination.



(a) Illuminated from azimuth angle of 0^o



(b) Illuminated from azimuth angle of 90^o

Figure 4.4 Images of wood obtained from different lightening directions

4.5 Recovery of Wood Surface Reflectance Properties (Albedo)

Yang (2006) made some comparisons between the profiles obtained using PS and SFS methods for nine different samples of wood. The results of these comparisons show that there can be up to about 98% correlation between the SFS and PS profiles for some wood samples, whereas, the correlation can be as low as 8% for some other wood samples. This suggests that the SFS technique is unreliable, unpredictable and inconsistent, and has called to question the validity of the uniform albedo assumption for wood samples. In order to address this doubt, a 3-image PS technique is used to recover the albedo of wood at every pixel location in the image.

As earlier derived in section 4.2.1, three images of a surface are required to completely recover the albedo at every point. Planed wood samples are illuminated by three light sources located at the same zenith angle $\sigma = 80^o$, but at different azimuth angles $\tau_1 = 0^o$, $\tau_2 = 150^o$, and $\tau_3 = 180^o$. Three images are then captured with each of the lights on while

keeping the other two off. The images shown in Figures 4.5, 4.6 and 4.7 are for a Beech sample with 2mm cuttermarks width. It is worth mentioning that the imaging system could still pick up the cuttermarks even at azimuth angle of 150^o. The albedo at each point in the surface is then recovered by solving Equation 4.4.

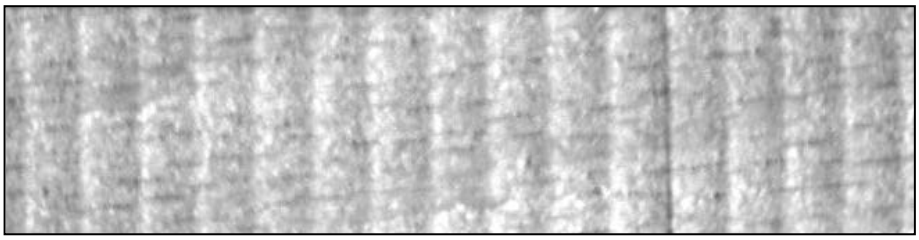


Figure 4.5 Beech sample captured with light source at azimuth angle of 0^0

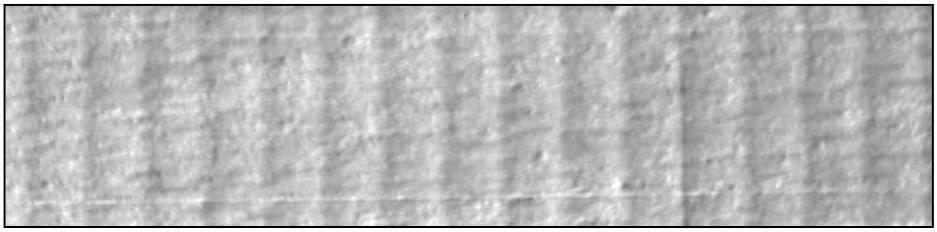


Figure 4.6 Beech sample captured with light source at azimuth angle of 150^0

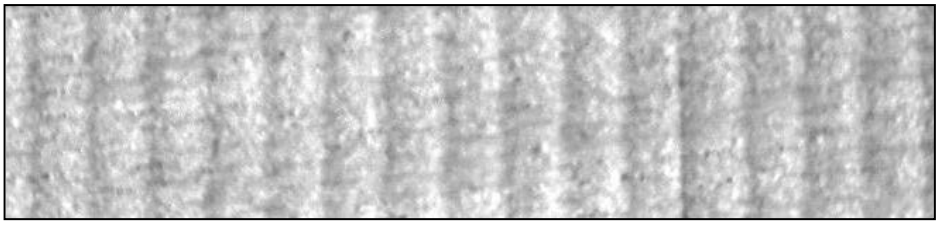


Figure 4.7 Beech sample captured with light source at azimuth angle of 180^0

The solution to Equation 4.4 is a matrix, which contains the composite albedo of each pixel point on the surface. The composite albedo is a parameter used to describe the product of the incident light intensity and the surface albedo at a particular point. This parameter is used because the intensity of the incident light is not known so it is difficult to separate it

from the albedo. Since the light sources are collimated thereby validating the assumption of uniform illumination, the difference in the reflected intensity at every point on the surface will be due to only the albedo and the topography of that point.

Standard deviation of the composite albedo data is used to measure the uniformity of the wood surface albedo. In order for the standard deviation to be meaningful, the composite albedo is first scaled so that all the values are fitted between 0 and 1. This is achieved by dividing all the elements in the composite albedo matrix by the maximum value in the matrix. The interpretation is that, the closer the standard deviation is to 0, the more the uniformity of the albedo.

Two samples of four different types of wood are used in the experiment. The standard deviations of the scaled composite albedos and the correlation between PS and SFS profiles of the different samples are shown in Table 4.1. Comparisons between the PS and the SFS profiles for sample 1 and 8 are shown in Figure 4.8 and Figure 4.9 respectively. The correlation coefficients are computed using the *corr2* function in MATLAB according to the following equation:

$$r = \frac{\sum_m \sum_n (A_{mn} - \bar{A})\,(B_{mn} - \bar{B})}{\sqrt{(\sum_m \sum_n (A_{mn} - \bar{A})^2)\left((\sum_m \sum_n (B_{mn} - \bar{B})^2)\right)}} \tag{4.13}$$

where

- A and B are vectors representing the PS and SFS profiles respectively
- $\bar{A}$ and $\bar{B}$ are the mean values of the elements in A and B respectively

Table 4.1 Albedo uniformity for various wood samples

Sample	Wood Species	Cuttermark Width (mm)	Standard Deviation of Scaled Composite Albedo	Correlation between PS and SFS Profiles (%)
1	Beech	2.5	0.0666	95.6
2	Beech	2.0	0.1242	91.6
3	Ramin	2.0	0.3346	69.5
4	Ramin	2.0	0.5234	51.7
5	Oak	2.5	0.2723	82.2
6	Oak	2.0	0.3615	67.9
7	Spruce	2.0	0.2765	81.3
8	Spruce	2.0	0.2314	84.5

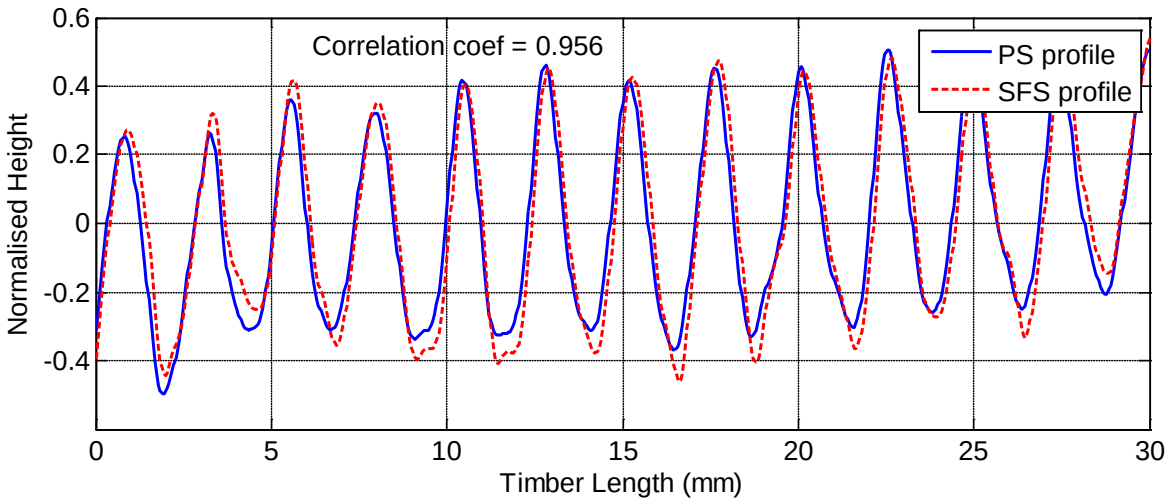


Figure 4.8 PS and SFS profiles of a Beech sample with 2.5mm cuttermarks

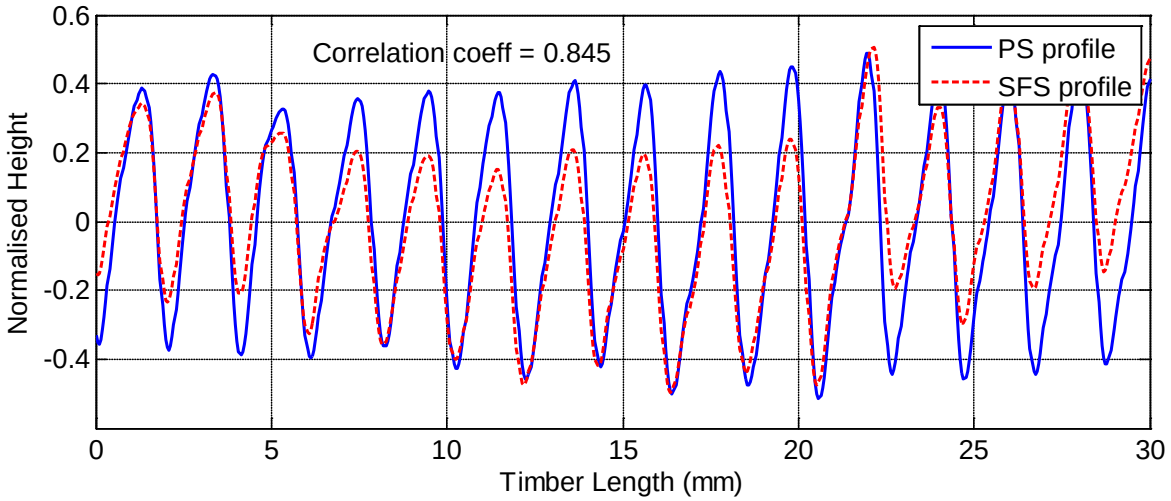


Figure 4.9 PS and SFS profiles of a Spruce sample with 2mm cuttermarks

The results in table 4.1 provide some explanations to the variable correlation between the SFS and the PS profiles. The correlation between the PS and SFS profiles reduces as the standard deviation of the albedo increases. It is now clear that the assumption of uniform albedo made by the SFS algorithm is not always valid for wood surfaces. The point-by-point albedos are highly variable, even for the same wood species. The random albedo values can be attributed to the heterogeneous and anisotropic material nature of wood. Since it is now clear that the SFS technique, which would have been more suited for dynamic measurement, is not reliable, it becomes necessary to adapt the PS technique to moving wood samples.

4.6 Dynamic Photometric Stereo (DPS)

The key to the application of PS technique to dynamic surface assessments is the ability to register the images. Optical flow computation is commonly used to estimate the motion of objects between two successive image frames, which are taken at different times. This would have provided a means of matching the images. The drawback is that image matching through optical flow computation is only successful if the illumination direction

is fixed, so that a linear approximation of the reflectance map can be applicable (Hatzitheodorou et al., 2000). Since the direction of the illumination is being changed during the acquisition of the image pairs, optical flow method is not suitable.

Photometrically disparate image pairs cannot be easily and reliably registered unless external means of estimating the displacements between the images are devised. The method used in this research is to determine the pixel correspondence between successive image pairs through the use of an incremental encoder. The encoder is used to measure the position of the workpiece at the time when the acquisition of each image is triggered. The displacements between successive image pairs are then calculate as follows:

Suppose that the first and second images are triggered when the workpiece is at position e_1 and e_2 respectively, the linear displacement between the image pair is given as:

$$l = e_2 - e_1 \tag{4.14}$$

The displacement in pixels can then be calculated as follows:

$$d_{pixel} = S_R \times l \tag{4.15}$$

where S_R is the spatial resolution of the camera in pixel per millimetre and l is linear displacement of the workpiece in millimetres.

4.6.1 Test Rig Setup

A variable-speed conveyor system has been constructed to simulate a real industrial machining environment for the in-process wood surface inspection (Figure 1.5). Theoretically, the test facility is capable of measuring moving samples up to the speed of 2m/s (Yang, 2006). The conveyor belt is equipped with a rotary encoder to measure the distance over which the sample has moved between successive image shots. A 659 x 493 pixel digital camera with an IEEE 1394 FireWire interface is connected to a PC so as to capture the images of the moving surface in real-time. The camera has been carefully aligned perpendicularly to the conveyor belt surface. The illumination sources are red collimated LEDs.

A proximity sensor is used to detect the moving sample when it is within the camera view. The camera is then hardware triggered by the proximity sensor with each of the two lights on and the other light off. The PC is setup to wait for the two image frames from the camera via the FireWire interface using MATLAB Image Acquisition Toolbox. The interconnections between the various components of the system are shown in Figure 4.10. The corresponding positions of the belt (in counts) when the image capture are triggered are also recorded and transmitted to the PC through RS232 serial communication protocol. This tight synchronisation, including the camera triggering, is achieved using a PIC18F458 microcontroller. Since the camera triggering is hardware based, the image acquisition is immediate and the camera latency is deterministic.

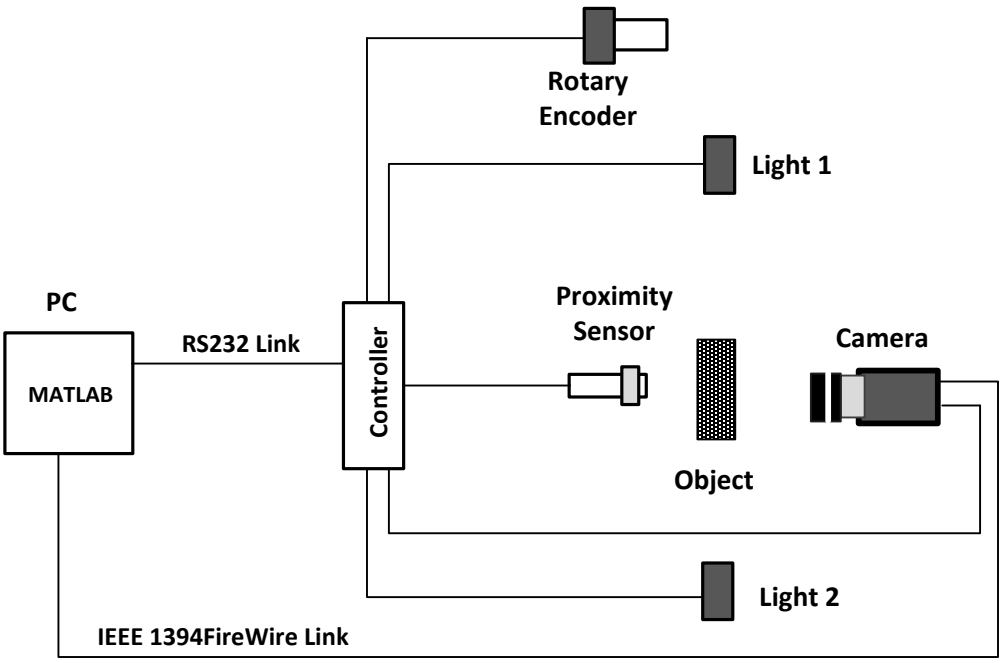


Figure 4.10 Interconnections between the components of the machine vision test rig

The displacement between the image frames is calculated according to Equation 4.15 in order to establish pixel correspondence. The conversion factor from counts to pixel has been estimated through experimentation (0.2425pixel/count). A black cross was printed on a white paper and then pasted on a wood sample. The displacements of the cross centre between successive image frames in pixels and encoder counts were then used to determine the conversion factor.

4.6.2 Challenges with the DPS

There are a number of difficulties that are potentially associated with the application of the proposed technique to moving samples. The major ones being skewing and motion blur within the image frames. Commercial cameras have two types of shutters namely, rolling shutters and global shutters. In the rolling shutter, portions of the objects are exposed to light at different moments in time by scanning horizontally or vertically across the frame. If the wood sample is moving in the horizontal direction during the exposure and the

shutter is rolling in the vertical direction, the cuttermarks might become skewed in the final image. This occurrence is illustrated in Figure 4.11.

Similarly to the radial distortion problem introduced by camera lenses, the averaging of the 3-D profile in order to generate a 2-D profile will not give the correct results if the skewness is significant. In that sense, a camera with a global shutter is a better choice for the in-process cuttermarks' measurement.

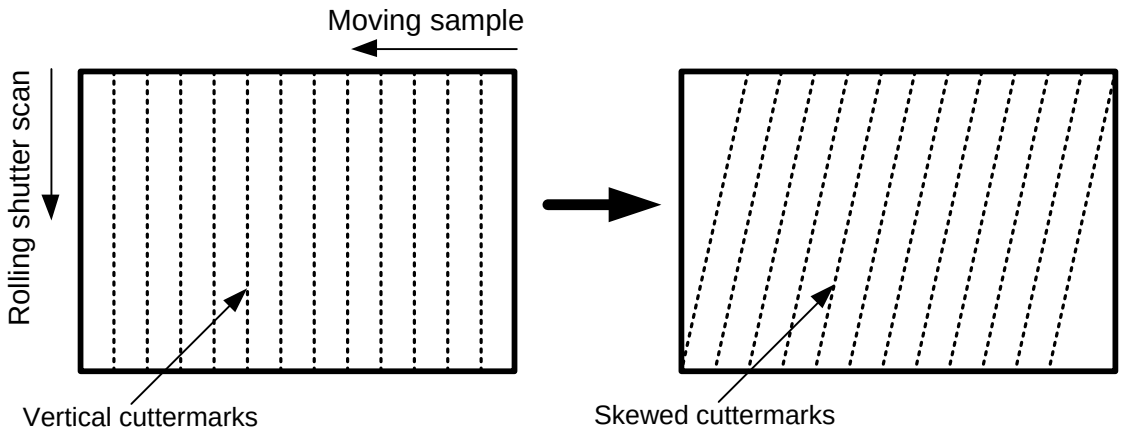


Figure 4.11 Skewed cuttermarks due to the rolling shutter effect

As opposed to the rolling shutter, the global shutter exposes the entire frame to light at the same time. It eliminates the problem of image skewness, but any motion of the sample during the frame capture would now result into image blurring. Blur will occur if the exposure time is long enough so that the sample can move during one shutter cycle. The problem of motion blur could limit the speed at which the wood sample can be measured. The problem can be minimised by using a short exposure time (increase shutter speed) as any motion will be frozen in time, resulting in images with less blur. However, sufficient light might not reach the image sensor if the exposure time is too short, thereby causing the

images to be dark. The problem could also be minimised by using high speed cameras and brighter illumination sources.

4.7 Experimental Results

Some wood samples were measured using the test rig. Dynamic surface measurements were done for samples moving at the speed of 50mm/s. Measurements at faster speeds could not be achieved on the current test rig because of motion blur and jerky movements of the conveyor belt. In order to assess the accuracy of the dynamic surface profile measurements, results obtained are compared with those of the static PS. The static PS measurement is used as the baseline reference since its effectiveness has been established in Yang (2006) by comparing it results with those from a laser profilometer. The comparisons between the static and the dynamic profiles are shown in Figure 4.12 and 4.13 for Beech and Oak samples respectively. The Beech sample is a single-knife finish while the Oak sample is a two-knife finish with one proud knife. The vision-based system does not provide absolute height information so the heights have been normalised.

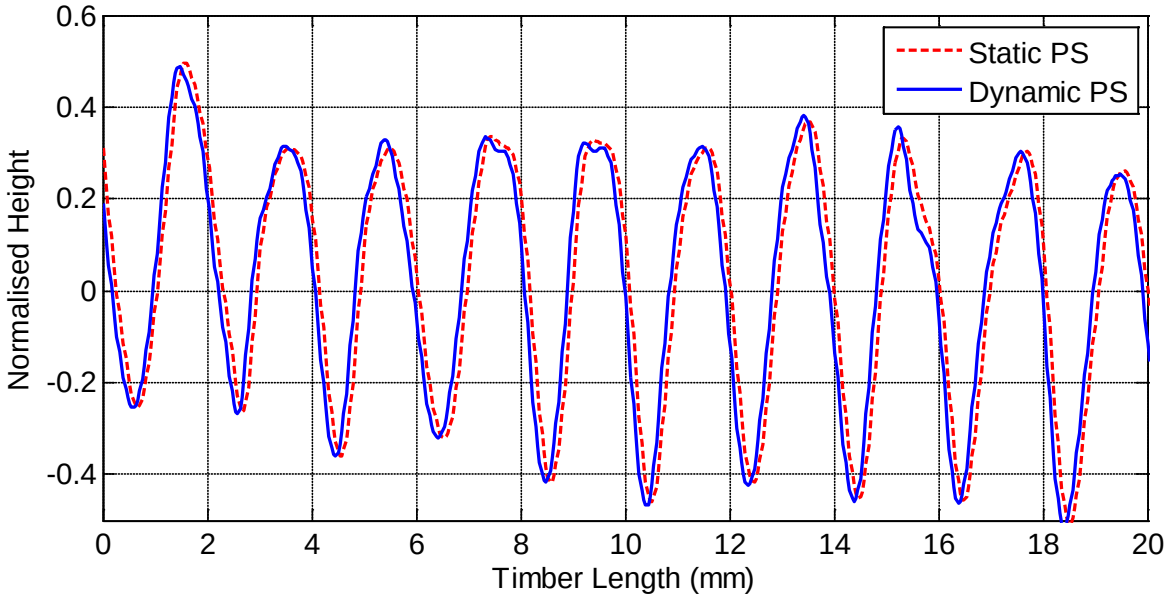


Figure 4.12 Static PS profile vs. Dynamic PS profile for Beech sample

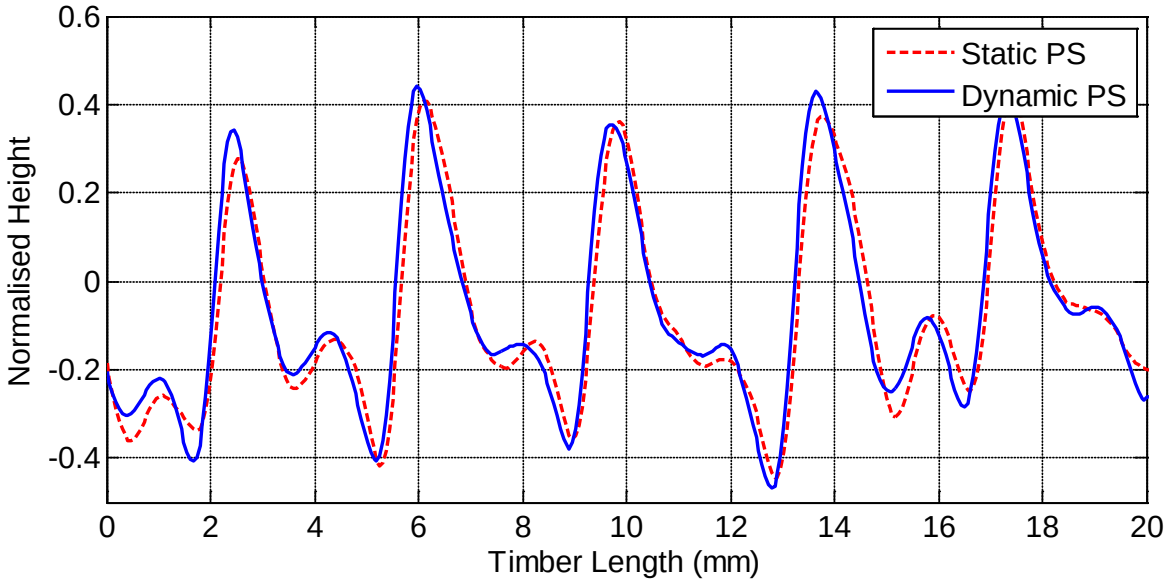


Figure 4.13 Static PS profile vs. Dynamic PS profile for Oak sample

The correlation coefficients between the surface profiles obtained using the static and the dynamic PS techniques are given in Table 4.2. The results show that the dynamic PS surface profiles compare well with those of the static PS.

Table 4.2 Percentage correlation between static and dynamic surface profile measurements for some selected wood samples

Sample	Wood Species	Cuttermarks Width (mm)	Correlation (%)
1	Beech	2.0	96
2	Oak	2.0	94
3	Ramin	2.5	93
4	Spruce	1.5	87
5	Beech	2.5	96
6	Meranti	2.5	91

Apart from motion blur and image skewness, the conveyor belt slippage is another potential source of errors in matching the photometric image pair. Under this situation, the actual wood sample movement will be different from the rotary sensor readings.

Considering the fact that any matching method employed will be subject to some errors, it is necessary to investigate the robustness of the dynamic PS technique to marginal image mismatches. This is done by comparing the surface profile extracted from perfectly matched images with the profiles extracted from manually mismatched images. Comparisons between the profiles obtained from the perfectly matched images and those of 8 and 15 pixels mismatched images are shown in Figure 4.14 and 4.15 respectively.

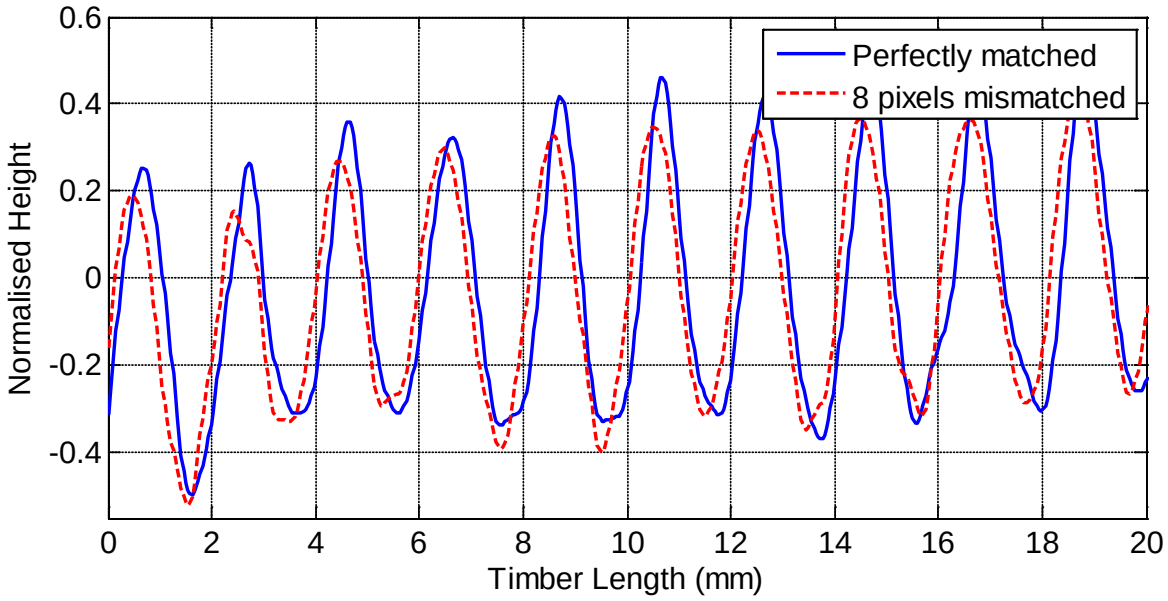


Figure 4.14 Perfectly matched and 8 pixels mismatched surface profiles

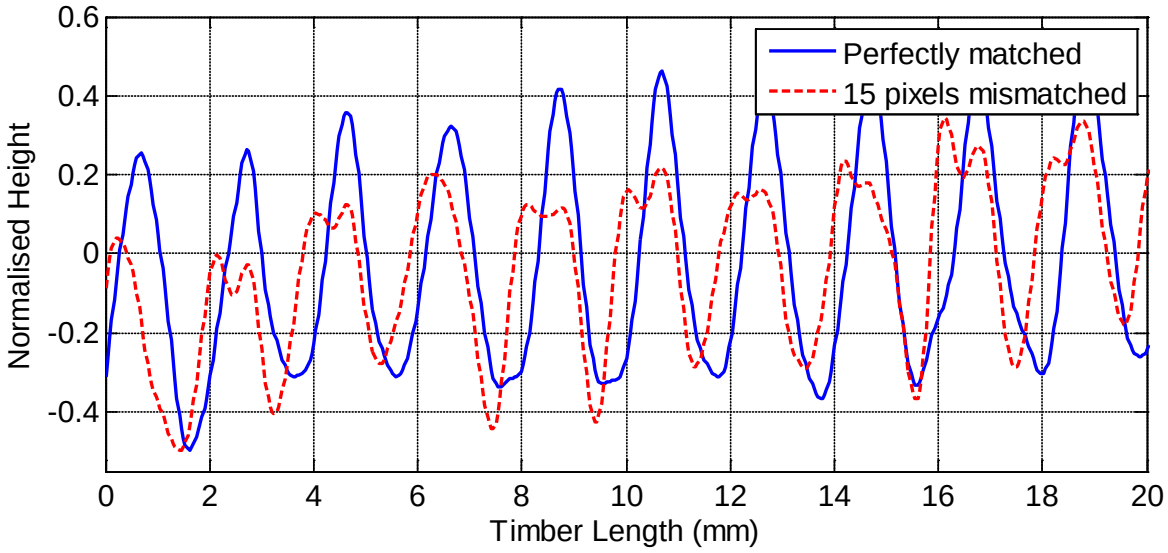


Figure 4.15 Perfectly matched and 15 pixels mismatched surface profiles

The correlation between the perfectly matched surface profile and the 8 pixels mismatched profile is about 87%. There is only about 56% correlation between the perfectly matched profile and the 15 pixels mismatched profile. Based on these values, a mismatch up to about eight pixels could still produce acceptable results. This means that the dynamic PS approach is robust to minimal matching errors. The tolerance limit will actually depend on the sizes of the cuttermarks and the spatial resolution of the images.

4.8 Summary and Conclusions

Research interests in the development of surface profile measurement systems for wood have increased over the years. Earlier investigations carried out by Yang (2006) reveal that some machine vision techniques demonstrate great practical potential for the inspection of planed wood surfaces. In that research, PS and SFS methods were implemented for the assessment of cuttermarks on static wood samples. The main challenge with the PS method is the determination of pixel correspondence between the image pairs if the workpiece is in motion. A novel approach has been used in this chapter to match the images through the

use of an incremental encoder. Experiments performed on a test rig designed to simulate a real machining environment show that the approach can be used for real-time dynamic wood surface quality inspection.

The SFS technique does not have the correspondence problem because it uses a single image of the wood surface. Based on the results obtained by Yang (2006), its consistency and reliability is questionable. It is uncertain whether the assumption of constant albedo made by the algorithm is valid or not for wood. In order to address this uncertainty, a 3-image PS method has been used in this chapter to recover the point-by-point albedo of some selected wood samples. Results obtained show that the assumption of constant albedo is not always valid for wood samples. The point-by-point albedos are highly variable even for the same wood species. The random albedo values can be attributed to the heterogeneous and anisotropic material nature of wood.

5 Characterisation of Defects on Planed Timber Surfaces

Surface waviness is the key parameter used in determining the quality of the finish produced by the rotary planing process of timber. There has been a great deal of research work in the area of both offline and in-process surface profile measurements of machined timber. However, these efforts are more beneficial if reliable defect detection and diagnosis tools that employ the waviness data are developed. Such tools will assist the operators to easily infer the machine deficiencies that produce particular waviness defects on the workpiece surface. Therefore, the purpose of this chapter is to create two novel approaches for the analysis and characterisation of defects on rotary planed timber surfaces. Due to the difficulty in generating a large amount of real surface profile data, the techniques are developed using synthetic data generated using the new simulation algorithm created in chapter three.

5.1 Introduction

The current practice in the woodworking industry makes use of accumulated visual a-priori knowledge of the waviness patterns observed by an operator under known machining conditions. The experienced operator then characterises any new waviness defect pattern based on this knowledge. Indeed, the operator must be very experienced in order to identify the cause of the defects to any degree of certainty. The problem with this approach is that it is subjective and the amount of information that can be extracted through visual examination of the measured surface profile signal is limited. Moreover, it only provides offline information about the defect-indicating patterns on the surface, which makes it unsuitable for real-time control of the machining process.

Two different methods are explored in the examination of the defect characteristics of planed timber surfaces. The first method is known as the Empirical Mode decomposition (EMD). The key ability of this method is that it can be used to decompose any complicated signal into a finite number of smaller signals called Intrinsic Mode Functions (IMFs). Each of the IMFs has physical and mathematical meanings. Analysis of the surface profile data using this method (combined with a-priori knowledge of some of the machining parameters) reveals valuable information about the signature of the cutterhead vibrations.

The EMD has been used in many applications including fluid mechanics (Huang et al., 1999), vibration signal analysis (Peng et al., 2005), image processing (Liu et al., 2004), and analysis of financial data (Huang et al., 2003). However, the application of this method to manufacturing operations is rare. So far, no work has been found on the development of a defect detection and diagnosis tool for machined wood surfaces. Therefore, this work is considered to be a novel contribution to the wood machining industry.

The second method investigated is known as the Principal Component Analysis (PCA). It involves a mathematical procedure that is used to transform a number of possibly correlated variables into a smaller number of uncorrelated variables called principal components. The principal components account for most of the variance in the observed variables. Analysis of the planed wood surface profile data using this method also shows that each defect case has uniquely defined principal components irrespective of the machining parameters. A-priori knowledge of the principal components for each defect can be used as criterion variables for predicting the nature of the structural vibration.

A knowledge-base is developed through principal component analysis of a number of synthetic surface profiles. A suitable neural network is then designed to represent the human reasoning mechanism. It is shown through simulation and practical considerations that the developed technique can effectively replace the human experts. This work is completely novel and is a worthy contribution to the woodworking industry.

It is relatively more straightforward to characterise defects due to cutterhead inaccuracy compared to those of structural vibration. The difference between the minima of the cuttermarks will reveal the knife run outs. The greatest challenge has been to characterise defects arising from structural vibration. In the case of vibration, the waviness patterns are highly variable as they depend on the relative engagement of the first knife at the start of the cutting process. This means that a particular vibration signature can give rise to variable waviness patterns even with the same machining parameters. Such possible occurrence makes it more difficult for an operator to characterise the defects. Therefore, focus is placed on only the most common vibration defect cases.

5.2 Empirical Mode Decomposition

The goal of EMD is to decompose a complex time series signal into a finite number of Intrinsic Mode Functions (IMFs) through an iterative sifting process. The IMFs are complete, adaptive and almost orthogonal representations of the analysed signal, which provide information about the different oscillatory modes that are present in the signal. A signal must satisfy two criteria to be an IMF. Firstly, the number of extrema and the number of zero crossings must either be equal or differ at most by one. Secondly, the mean of the envelope defined by the local maxima and the envelope defined by the local minima

must be zero. Given these two definitive requirements, the sifting process for extracting the IMFs from the surface profile data is described as follows (Huang et al., 1998):

1. Given the surface signal *x(l),* the first step is to identify all local extrema in the data
2. Once the extrema are located, all the local maxima are connected by a cubic spline approximation to create the upper envelope $e_{upper}(l)$. The local minima are similarly connected to produce the lower envelope $e_{lower}(l)$
3. The mean *m(l),* of the upper and lower envelope values is computed to generate the mean profile data.

$$m(l) = \frac{e_{upper}(l) + e_{lower}(l)}{2} \tag{5.1}$$

4. The difference between the original signal and the mean profile is computed

$$d(l) = x(l) - m(l) \tag{5.2}$$

5. Steps 1-4 are repeated for *d(l)* until the resulting signal satisfies the criteria of an IMF. This first IMF is designated as $c_1(l)$.

The procedure is illustrated in Figure. 5.1, 5.2 and 5.3 using a simulated surface profile of a four-knife cutterhead having waviness defect of once per revolution vibration. Figure 5.1 shows the data in solid line, and the upper and lower envelopes in the dashed lines. Figure 5.2 shows the data in solid line and their mean in dashed line. Figure 5.3 is the difference between the data and the local mean as given by equation 5.2.

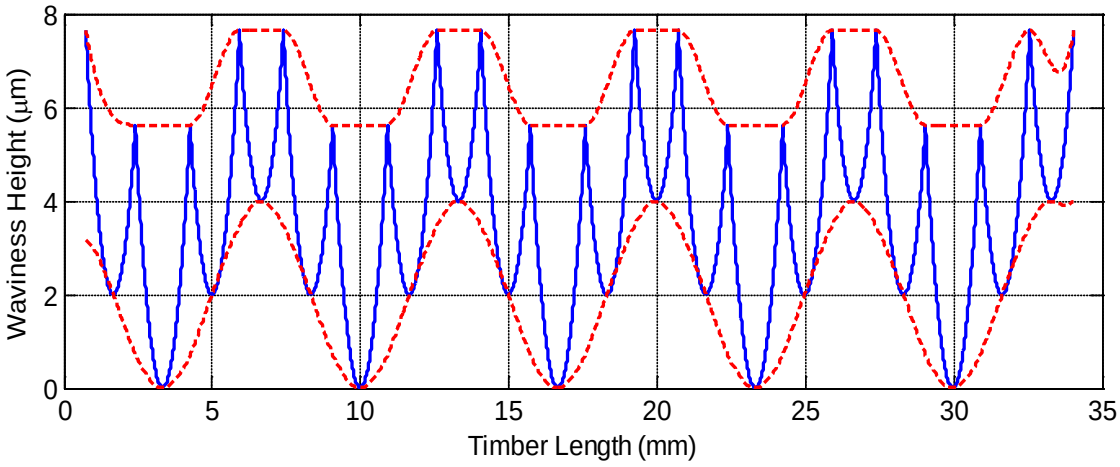


Figure 5.1 The data with the upper and lower envelopes

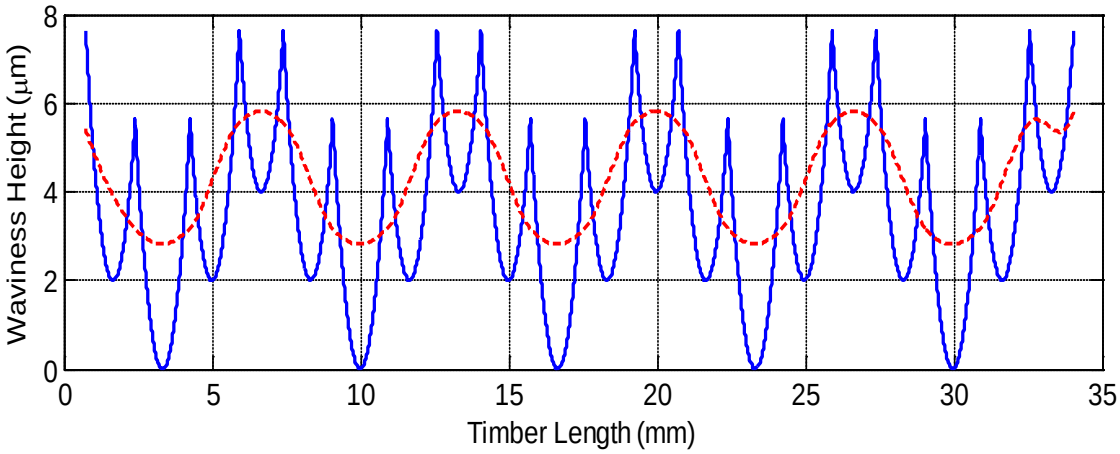


Figure 5.2 The data with the mean of the upper and lower envelopes

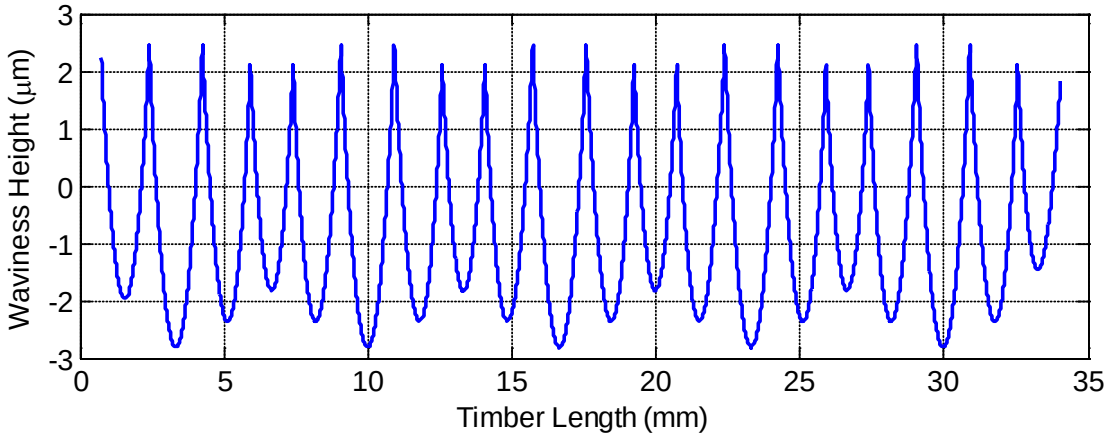


Figure 5.3 The difference between the data and the mean of the envelopes

In order to guarantee that the IMF components retain enough physical meanings of both amplitudes and frequency modulations, a criterion has to be determined for the sifting process to stop. Over-sifting will produce smooth amplitude IMF components with the physical meanings all sifted away. Therefore, there is a trade-off between producing incorrectly defined IMFs due to insufficient sifts to remove all the riding waves (under-sifting), and producing less physically meaningful IMFs (over-sifting).

Two different stoppage criterions were proposed by Huang et al. (1998). The first one is similar to the Cauchy convergence test in which the sifting process is stopped when the standard deviation (SD) computed from two consecutive sifting processes is smaller than a pre-determined value. A typical value for SD as given by the original author is between 0.2 and 0.3. The second criterion, which is implemented in this case, is based on a number called the S-number. It is defined as the number of consecutive siftings when the numbers of zero crossings and extrema are equal or at most differing by one. The sifting process is stopped if for S consecutive times, the numbers of zero crossings remain the same and are equal or at most differ by one. A value of 3 is selected for the S-number.

The first IMF $c_1(l)$, is removed from the original data to obtain the first residue

$$r_1(l) = x(l) - c_1(l) \tag{5.3}$$

Since the residue can still contain longer period components of the data, it is treated as the new data and then subjected to the same sifting process as described above. Normally, the sifting process is stopped finally when the residue, r_n, becomes a monotonic function from which no IMF can be extracted, or when it becomes so small that it is less than a

predetermined value of substantial consequence. However, only the first 2 IMFs are considered to be significant for the defect characterisation. At the end of the sifting process, the signal *x(l)*, can be expressed as follows:

$$x(l) = \sum_{i=1}^{2} c_i(l) + r_2(l) \tag{5.4}$$

5.2.1 Physical Significance of the IMFs

In order to fully verify the effectiveness and limitations of the EMD method, it is applied to a number of simulated waviness defect cases using the algorithm developed in chapter three. The first 3 cases have the same machining parameters given in Table 5.1. A careful observation of the IMFs for the machining conditions reveals that the first and second IMFs have physical meanings. The first IMF is effectively the expected theoretical waviness patterns if there is no defect, and the second IMF is directly related to the errors present in the machining process.

Table 5.1 Machining Parameters for EMD

Parameter	Symbol	Value	Unit
Number of knives	N	4	--
Cutting speed	ω	3000	rpm
Feed speed	v_f	600	mm/s
Cutter radius	R	75	mm

Case 1

The first case is that of a surface without any defect (uniform cuttermarks). The original surface profile, the first IMF and the second IMF are shown in Figure 5.4. It can be seen clearly that the peak-to-peak amplitude of the first IMF is the same as that of the original

signal and they both have the same wavelength. This shows that the first IMF is close to the non-defective surface profile. The second IMF is a straight line at zero indicating that there is no overriding wave apart from the one due to the kinematics of the cutting process.

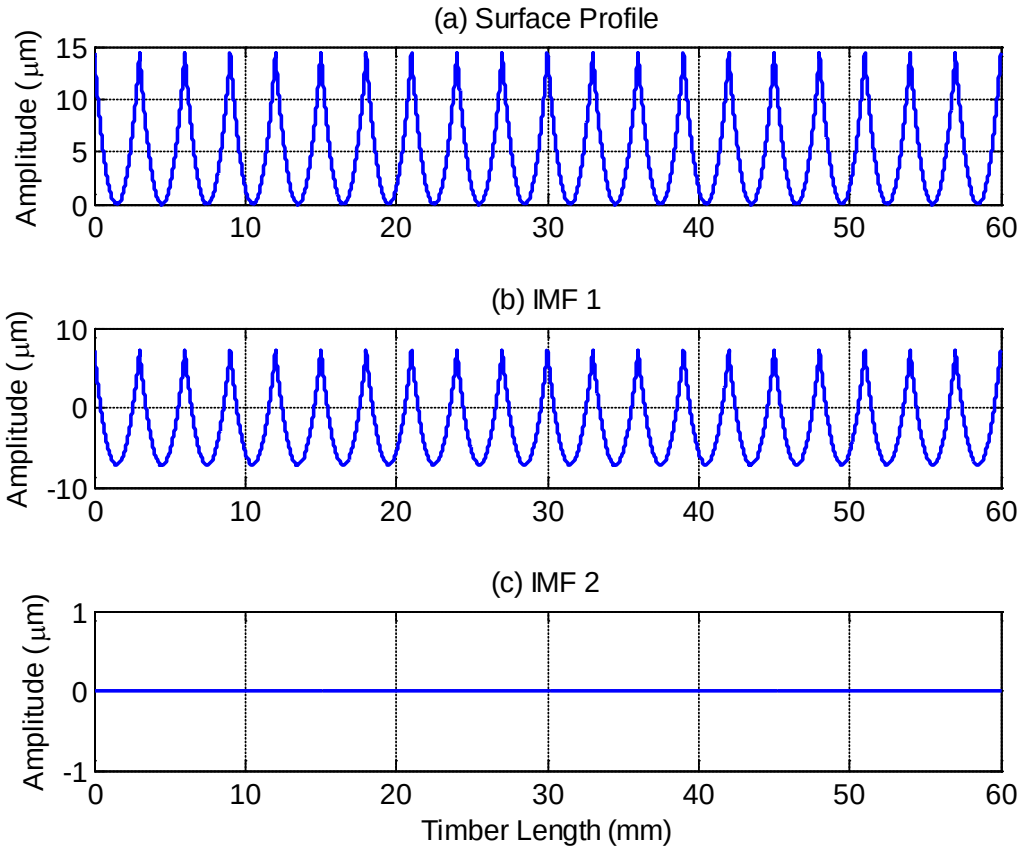


Figure 5.4 Case 1: (a) The original surface profile; (b) The first intrinsic mode function; (c) The second intrinsic mode function

Case 2

The second case shown in Figure 5.5 is that of a surface with a superimposed cutterhead oscillation of 3μm at once per revolution of the cutterhead. This type of waviness defect is usually as a result of the cutterhead mass imbalance, which causes the cutterhead to vibrate at the frequency equal to the spindle rotational speed (Jackson, 1986). The surface is simulated for 5 revolutions of the cutterhead (5 x 4 = 20 cuttermarks).

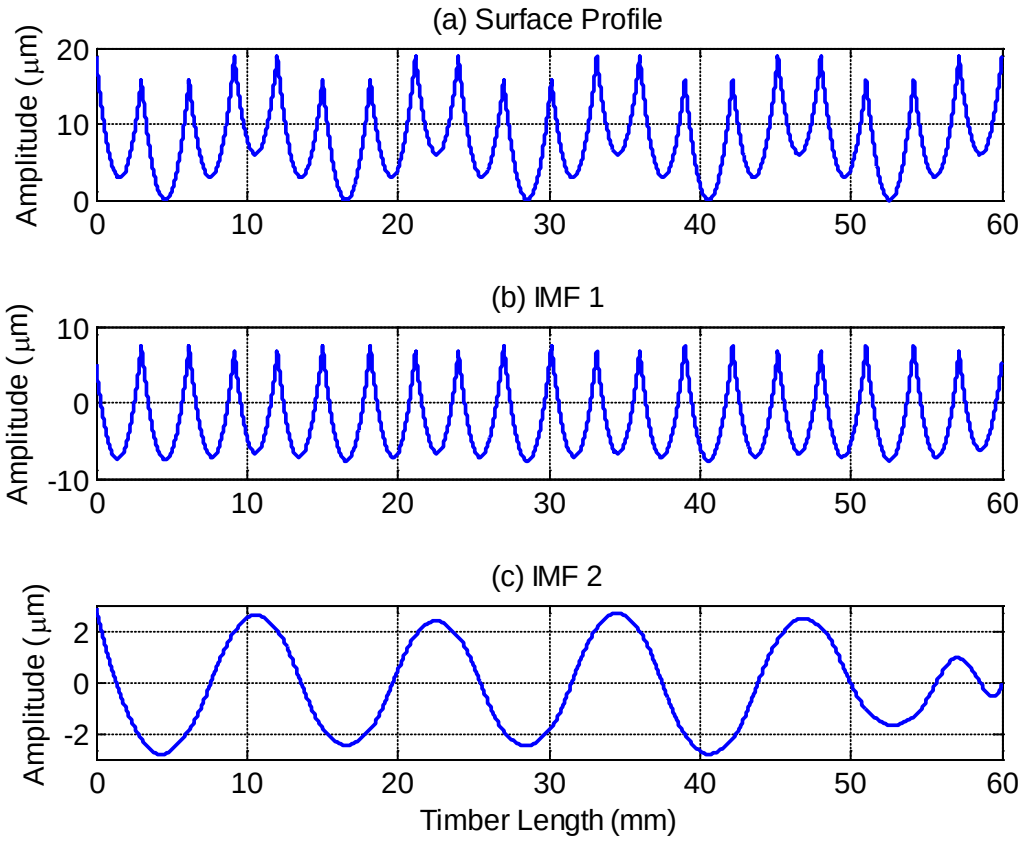


Figure 5.5 Case 2: (a) The original surface profile; (b) The first intrinsic mode function; (c) The second intrinsic mode function

The second IMF (Figure 5.5c) has an average amplitude of about 3μm and there are approximately 5 peaks in the waveform. Since the original surface profile is simulated for 5 revolutions of the cutterhead, it clearly indicates that there is an oscillation of about 3μm occurring at once per revolution of the cutterhead. The average value of the peak-to-peak amplitudes and the wavelengths of the first IMF (Figure 5.5b) are approximately the same as the expected waviness height and pitch for a defect-free surface.

Case 3

The third example is shown in Figure 5.6. It is similar to the second example except that in this case, the oscillation occurs at twice per revolution of the cutterhead. This type of defect can either be caused by misalignment between the outboard bearing and the spindle housing, which produces a significant increase in the first harmonic of the spindle rotational frequency; or in occasions where the spindle support structure exhibit natural frequencies at approximately twice the spindle rotational speed (Jackson, 1986).

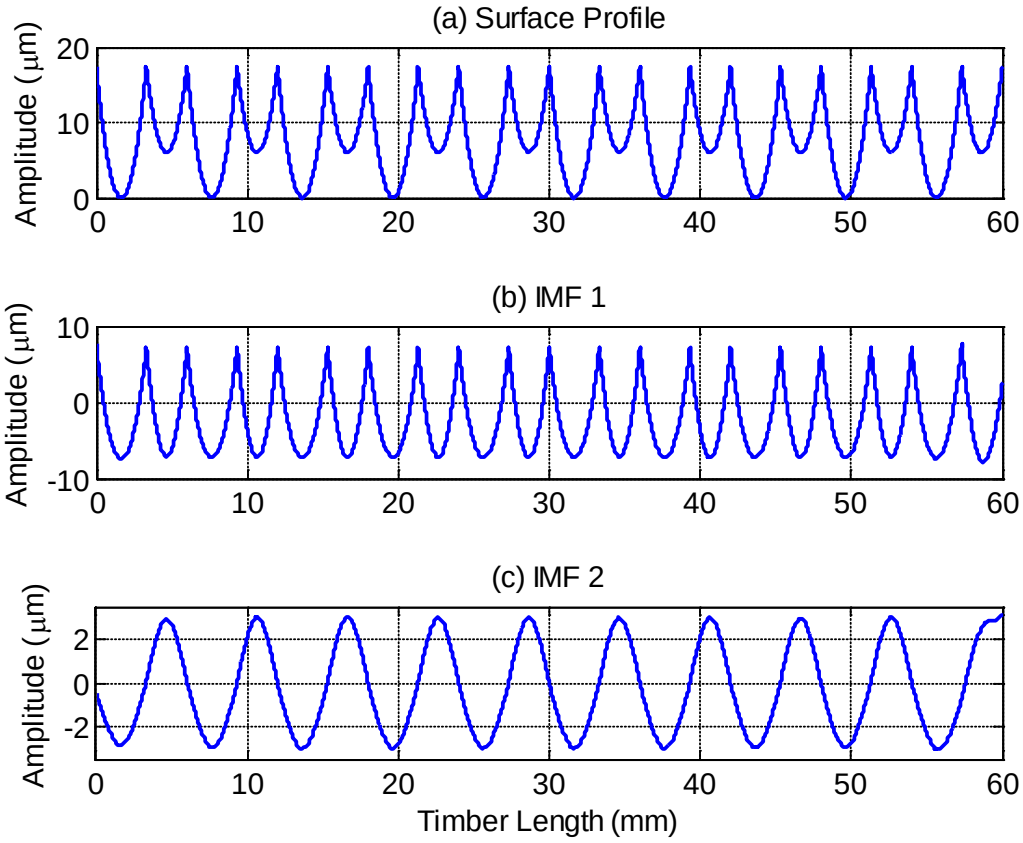


Figure 5.6 Case 3: (a) The original surface profile; (b) The first intrinsic mode function; (c) The second intrinsic mode function

It can be seen that the second IMF (Figure 5.6c) is the defect signal. It also has an average amplitude of about 3µm just as in the second example. The only difference is that there are approximately 10 peaks in the waveform, indicating that there are two peaks in one revolution of the cutterhead. Average values of the peak-to-peak amplitudes and the wavelengths of the first IMF (Figure 5.6b), are also approximately the same with the theoretical waviness height and pitch of the non-defective surface.

Case 4

Another common waviness defect, which is also observed during the wood planing process, is that of a superimposed cutterhead vibration occurring once every two revolutions of the cutterhead. This phenomenon can be observed in cases where the cutterhead spindle is running at twice the speed of the spindle drive motor via a 2:1 belt drive. The effect of the motor imbalance forces can be amplified by structural resonances and cause the cutterhead to vibrate at the motor's frequency (Jackson, 1986). This defect is also simulated for a single-knife finish with the same vibration amplitude of 3µm. The surface is generated for 10 revolutions of the cutterhead. The feed speed and cutting speed are 100mm/s and 3000rpm respectively. EMD method is also able to recover the vibration signal from the surface profile data as shown in Figure 5.7c.

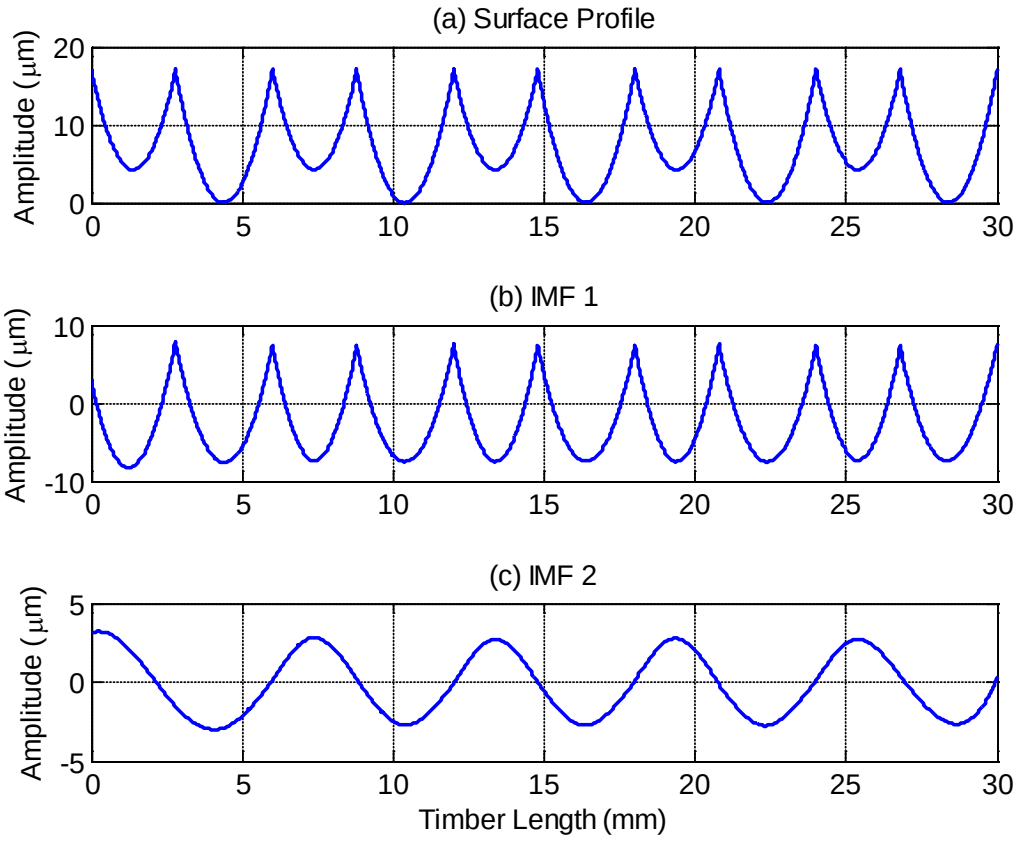


Figure 5.7 Case 4: (a) The original surface profile; (b) The first intrinsic mode function; (c) The second intrinsic mode function

5.2.2 Apriori Knowledge Requirements

In practice, it might not be possible to know the number of cutterhead revolutions that are embedded in a measured surface profile data. Therefore, knowledge of some of the machining parameters is required to predict the vibration frequency. If the cutting speed and the feed speed are known, then the number of oscillations per cutterhead revolution can be calculated as given by the following equations:

Let the wood surface be measured from position p_a, to position p_b, along the timber surface. Then, the measured length s, is given by:

$$s = p_b - p_a \tag{5.5}$$

The time it takes to travel that length during the cutting process, *t*, is:

$$t = \frac{s}{v_f} \tag{5.6}$$

Period of the cutterhead revolution, *T*, is given as:

$$T = \frac{1}{\omega} \tag{5.7}$$

If the number of peaks in the recovered vibration signal is designated as $N_{p,}$ then the number of displacements per cutterhead revolution is given by:

$$d_{rev} = \frac{T \times N_p}{t} \tag{5.8}$$

5.3 Comparisons between EMD and Fourier Analysis

Since Fourier analysis has become a common way of analysing signals, it is worth comparing the two methods. There are some practical defect conditions where characterisation based on Fourier spectral analysis will fail. In the case of waviness defects caused by cutterhead vibration, there are some critical values of the vibration amplitudes above which the cuttermarks produced by one knife can be completely removed by the following cutting knife. When this occurs, some knives will not have any effect on the resultant surface profile. Thus, defect characterisation based on the combination of apriori knowledge of the number of cutting knives with the frequency components of the surface

profile signal will fail completely. An example of such case is synthesised as shown in Figure 5.8 using the machining parameters stated in Table 5.1.

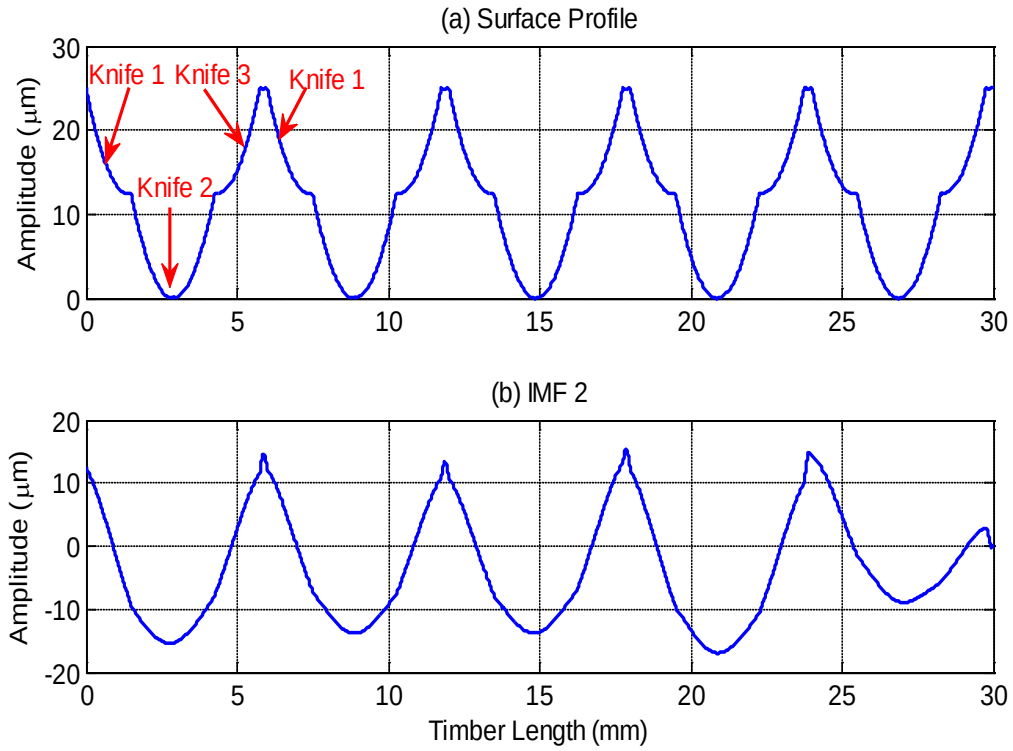


Figure 5.8 Waviness defect produced by extreme values of the vibration amplitude

The surface profile is that of a four-knife finish, with superimposed vibration of 13µm at once per revolution of the cutterhead. As seen in Figure 5.8a, the surface exhibits a three-knife finish due to the large vibration amplitude, making the other knives to completely remove the cuttermarks produced by the fourth knife. Fourier spectral analysis of the surface profile will produce wrong results in this case since it will be based on apriori knowledge of four knives. However, EMD method could still recover the vibration signal from the surface profile. The vibration signal is shown in Figure 5.8b (IMF 2).

Fourier analysis is also limited because a particular vibration signature can give rise to variable frequency components depending on the position of the imbalance mass. Figure 5.9 shows two surface profiles produced by the same once per revolution vibration condition (4μm amplitude) but the resultant imbalance mass is located at different positions. Clearly, the frequency components are different and there are a number of these variations that can be observed in practice (Jackson, 1986). As a result, the frequency spectrum cannot be used for any deterministic characterisation of the defects. EMD is still able to recover the vibration from the surface profiles as seen in Figure 5.10.

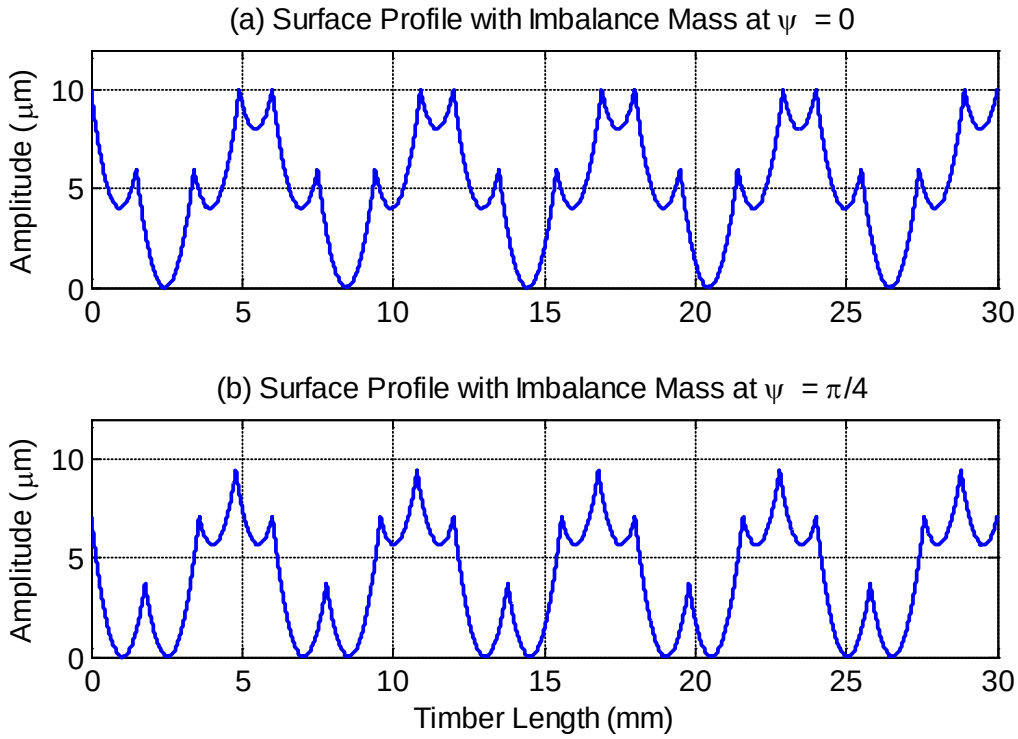


Figure 5.9 Defects caused by varying imbalance mass positions

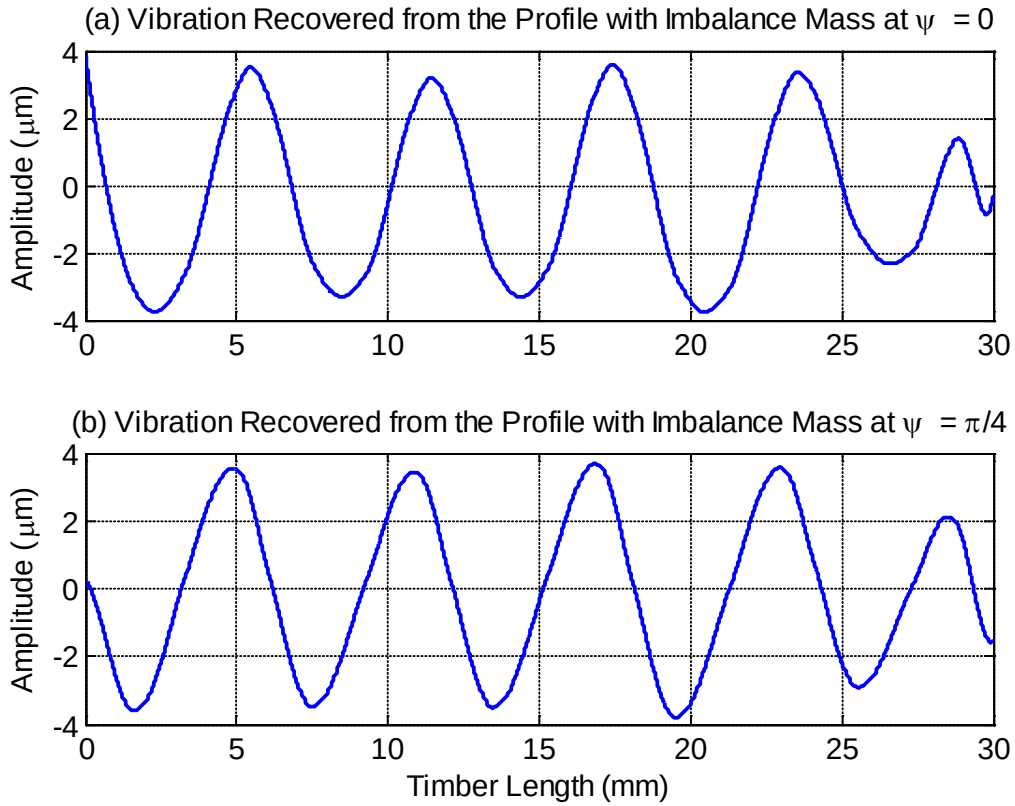


Figure 5.10 Vibration recovered from profiles with varying imbalance mass positions

5.4 Principal Component Analysis Method

Principal Component Analysis (PCA is a variable reduction procedure used to generate smaller number of artificial variables from a number of observed variables. The goal of PCA is to transform a complex dataset of higher dimension into an alternative dataset of a smaller dimension while retaining as much as possible of the variations present in the original dataset. The lower dimensional data are known as *principal components* (Abdi and Williams, 2010).

In mathematical terms, PCA is defined as a linear orthogonal transformation of a data from a higher dimensional space to a lower dimensional space such that the variances of the data lie on the principal components (Jolliffe, 2002). The principal components are the

eigenvectors of the covariance matrix of the original data corresponding to the largest eigenvalues.

5.4.1 Procedure for Applying PCA

The PCA is only appropriate for finding variations between two or more measured variables. The upper and lower envelopes of the surface profiles are taken to be two separate variables. The PCA is able to reduce the envelopes into a smaller dimension. A careful observation of the reduced data reveals that the absolute values of the principal component coefficients remain fairly constant for a particular type of defects irrespective of the machining parameters. Interestingly, the coefficients are distinct from one defect to the other. For example, the principal component coefficients of a once per revolution vibration are different from those of a twice per revolution vibration.

The procedure for extracting the principal components, which starts off the same way as the EMD, is described as follows:

1. Given the surface profile *x(l)*, the first step is to identify all the local extrema in the data set between each successive pair of zero crossings

2. Once the extrema are located, all the local maxima and minima are connected by a cubic spline approximation to create the upper envelope $e_{upper}\ (l)$ and lower envelope $e_{lower}(l)$

3. Let the upper and lower envelopes be two observed variables of the same sizes *x*, and *y*. The empirical means of two variables are computed to give $\bar{x}$ and $\bar{y}$ respectively

4. The mean of each of the variables is then subtracted from all the data points in each variable to generate new variables with zero mean. This procedure, which is known as mean centering, is necessary to ensure that the first principal component represents the direction of maximum variance between the upper and lower envelopes. Without mean centering, the first principal component might correspond to the mean of the data instead (Miranda et al., 2008)

$$x_m = x - \bar{x} \qquad (5.9a)$$

$$y_m = y - \bar{y} \qquad (5.9b)$$

5. x_m and y_m are combined to form matrix X, where each of the variables is a column in the matrix. The covariance matrix of X is then computed. The covariance is a measure of the degree of linear relationship between the two variables

6. The final step is to calculate the eigenvectors and eigenvalues of the covariance matrix. The eigenvectors are the principal components of the data set. The columns of the eigenvectors are then re-arranged in the order of decreasing eigenvalues. This gives the principal components in order of their significance.

The mathematical procedure for computing the principal components of a dataset can be found in relevant texts, or by using the *princomp* command in MATLAB.

5.4.2 Significance of the Principal Components

The principal components represent the variation between the lower and the upper envelopes of a surface profile. In order to fully verify the effectiveness and limitations of PCA, the principal components are computed for a number of simulated waviness defect cases. Machining parameters for the simulations have been carefully selected to cover a wide range of variations that can occur in practice. At the start of the cutting, the first knife is aligned with the negative x-axis and ψ is used to set the position of the resultant imbalances forces relative to the positive y-axis. That is, the vertical position of the cutterhead is at the positive peak when $\psi = 0$. Although the tests were done for two, four, six, eight and ten knives, only those of four-knife, six-knife and ten-knife finishes are presented for illustration.

A few examples of simulated waviness defects caused by structural vibration and their corresponding principal component coefficients are presented as follows. It has been assumed that the cutters are accurately grinded and jointed, thus any irregular waves are due to the structural dynamics only. That is, there are no errors due to the cutterhead geometry. PCA reduces the surface profiles to a 2-by-2 matrix, which represents the variation between the lower and upper envelopes. It was found that the diagonals of each of the 2-by-2 matrices are exactly the same, so only the first column of the matrix is displayed in the tables.

Case 1: Four-Knife Finish with Once Per Revolution Vibration

A simulated waviness pattern for a four-knife finish with a once per revolution vibration is shown in Figure 5.11. The principal component coefficients are shown in Table 5.2.

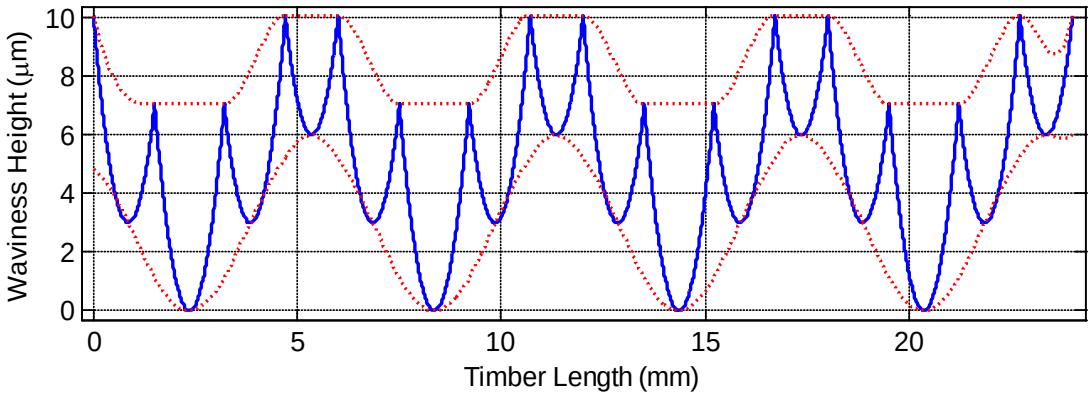


Figure 5.11 Four-knife finish with once per revolution vibration defect

Table 5.2 Principal components for four-knife finish with once per revolution vibration

Cutting Speed (rev/min)	Feed Speed (mm/s)	Knife Radius (mm)	Vibration Amplitude (mm)	Principal Components
3000	300	50	0.003	0.5105, 0.8599
3000	400	60	0.006	0.5108, 0.8597
3000	500	70	0.008	0.5113, 0.8594
2800	450	65	0.005	0.5119, 0.8590

It has been mentioned earlier that the waviness patterns produced by fixed machining parameters and vibration signature can vary depending on the position of the resultant imbalance mass. In order to fully verify the robustness of the PCA to these variations, it is applied to the once per revolution vibration condition having different initial cutter engagement positions. The parameters used and their corresponding principal components are as given in Table 5.3. The waviness patterns for each of the initial cutter engagement values are shown in Figure 5.12, 5.13, 5.14 and 5.15. The machining parameters are fixed to the ones in the first row of Table 5.2.

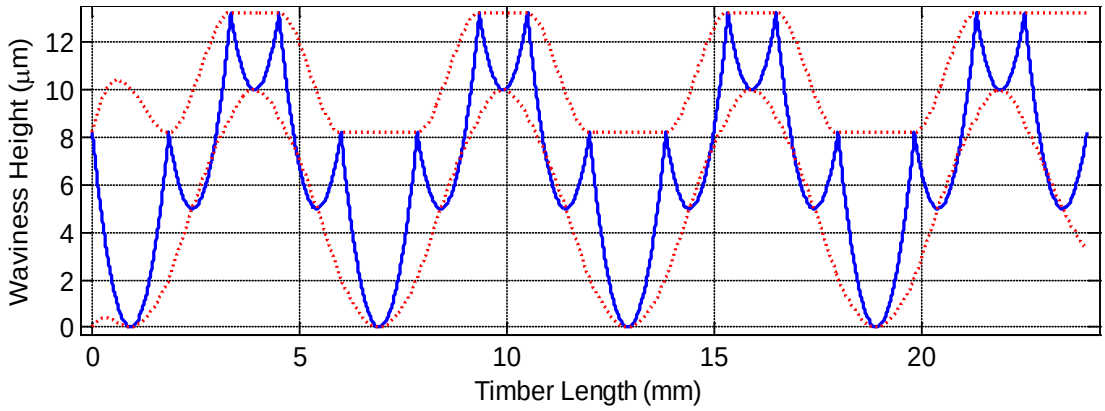


Figure 5.12 Four-knife finish with once per revolution vibration defect ($\psi = \pi/2$)

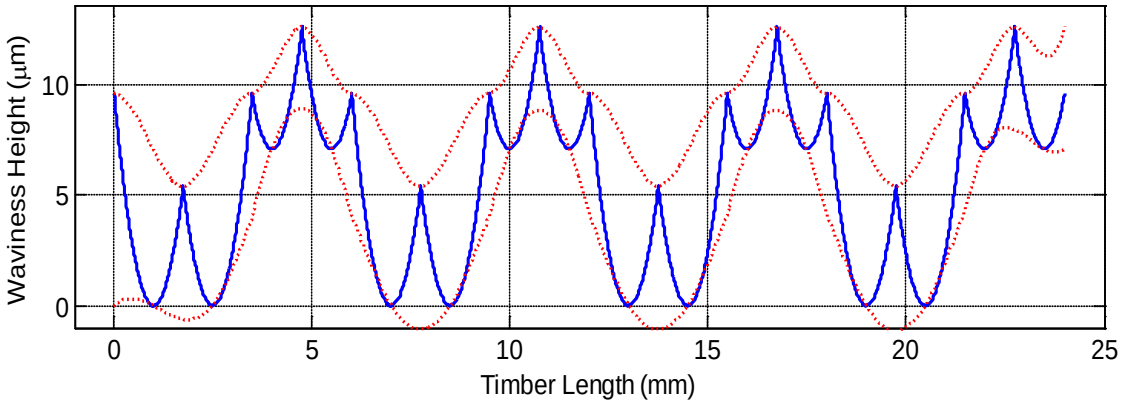


Figure 5.13 Four-knife finish with once per revolution vibration defect ($\psi = \pi/4$)

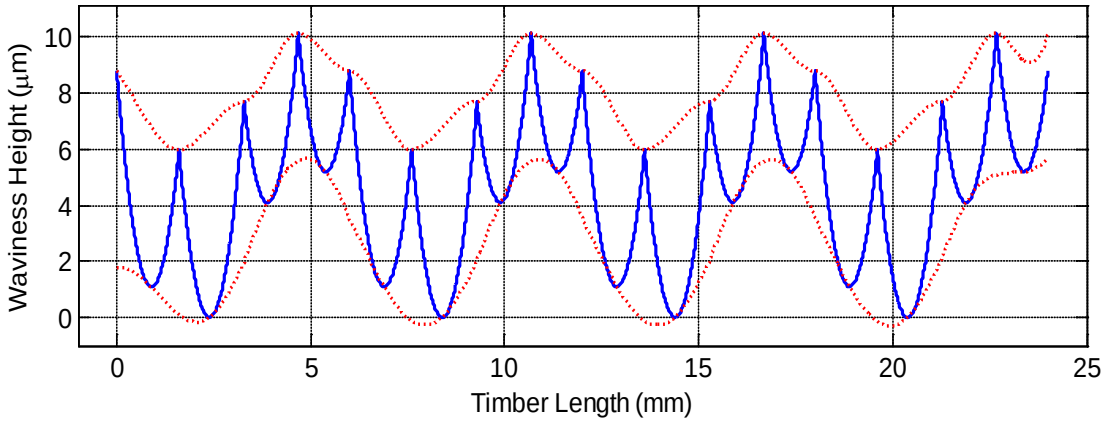


Figure 5.14 Four-knife finish with once per revolution vibration defect ($\psi = \pi/6$)

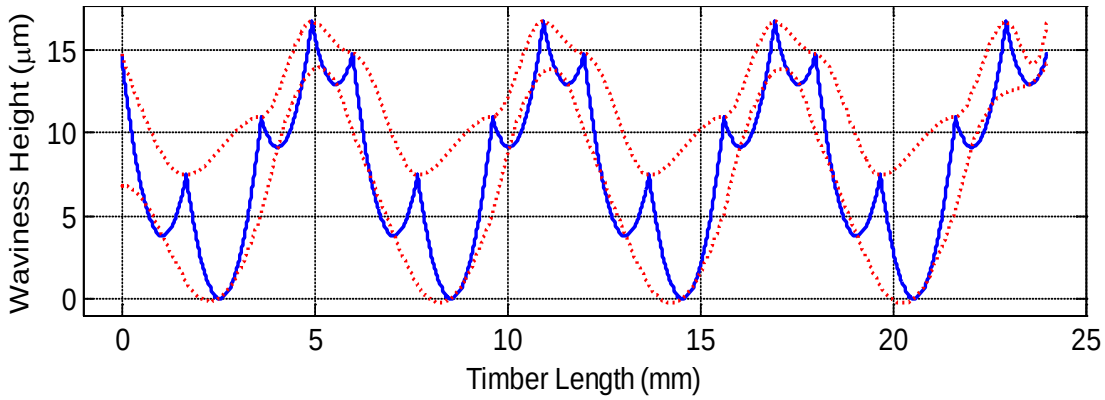


Figure 5.15 Four-knife finish with once per revolution vibration defect ($\psi = \pi/8$)

Table 5.3 Principal components for four-knife finish with once per revolution vibration at varying imbalance positions

Vibration Amplitude(mm)	ψ (radians)	Principal Components
0.005	$\pi/2$	0.5050, 0.8631
0.005	$\pi/4$	0.5252, 0.8510
0.003	$\pi/6$	0.5279, 0.8493
0.007	$\pi/8$	0.5200, 0.8542

As seen from the figures, the waviness patterns are completely different due to the variation in the position of the resultant imbalance masses. Nevertheless, the principal component coefficients remain reasonably close as seen in Table 5.3. This indicates that PCA is not sensitive to the variation in the frequency components resulting from variations in the positions of the mass imbalance. As will be seen in the following cases, the coefficients only change significantly if the frequency of the cutterhead vibration changes.

Case 2: Four-Knife Finish with Twice Per Revolution Vibration

A waviness defect pattern caused by twice per revolution vibration, where the cutterhead is aligned with its maximum positive amplitude at the start of the cutting cycle ($\psi = 0$), is shown in Figure 5.16. The principal component coefficients are presented in Table 5.4.

They are completely different from the ones in Table 5.2 and Table 5.3. This is simply because of the difference in the frequency of cutterhead vibration.

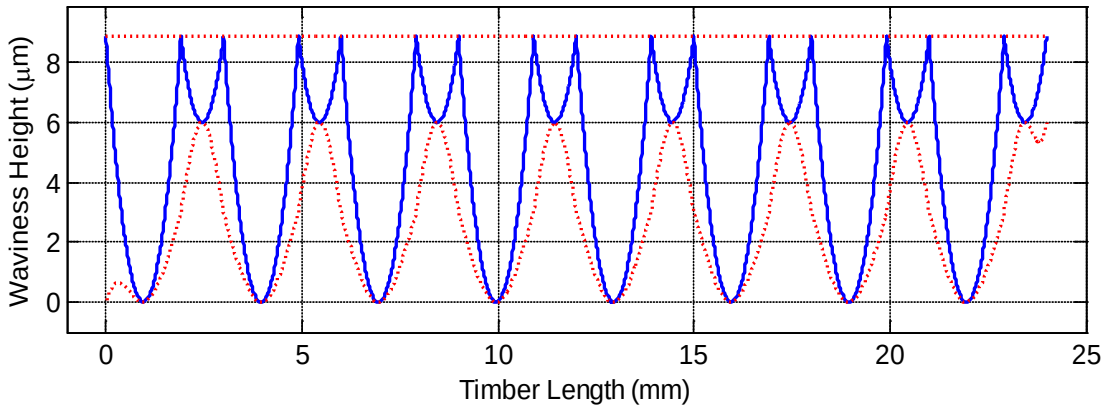


Figure 5.16 Four-knife finish with twice per revolution vibration defect

Table 5.4 Principal components for four-knife finish with twice per revolution vibration

Cutting Speed (rev/min)	Feed Speed (mm/s)	Knife Radius (mm)	Vibration Amplitude (mm), ψ (rad)	Principal Component
3000	300	50	0.003, 0	0, 1
3000	400	60	0.006, π/2	0, 1
3000	500	70	0.004, π/4	0, 1
2800	450	65	0.005, π/8	0, 1

Case 3: Four-Knife Finish with Once Per Two Revolutions Vibration

Another common waviness defect is caused by superimposed vibration occurring once every two revolutions of the cutterhead. Figure 5.17 is a sample waviness pattern produced by such vibration signature. The principal components are shown in Table 5.5.

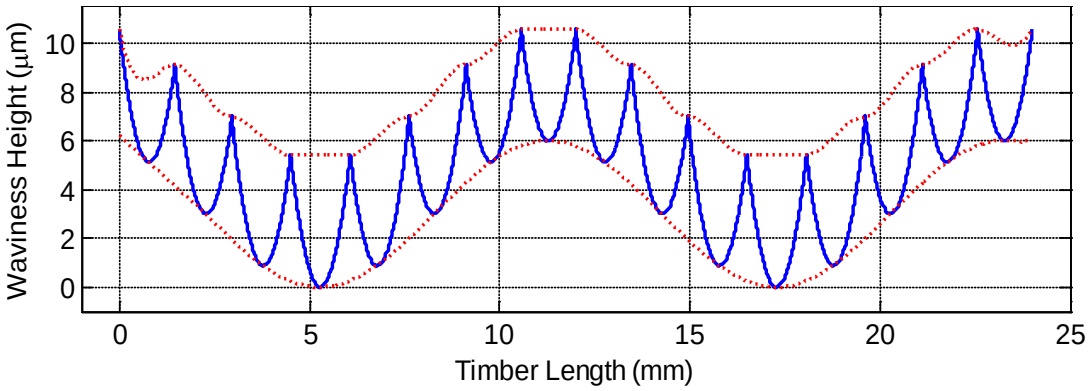


Figure 5.17 Four-knife finish with once per two revolutions vibration defect

Table 5.5 Principal components for four-knife finish with once per two revolutions vibration

Cutting Speed (rev/min)	Feed Speed (mm/s)	Knife Radius (mm)	Vibration Amplitude (mm), ψ (rad)	Principal Component
3000	300	55	0.003, 0	0.6490, 0.7608
3000	400	60	0.006, π/2	0.6737, 0.7390
3000	500	65	0.002, π/8	0.6634, 0.7483
2800	450	75	0.005, π/10	0.6599, 0.7513

Case 4: Six-Knife Finish with Once Per Revolution Vibration

The trend followed by the principal components for the defects caused by cutterhead vibration in a six-knife finish has also been examined. A sample theoretical surface produced by a once per revolution vibration effect is shown in Figure 5.18. The position of the imbalance mass has been varied as shown in Table 5.6 in order to investigate the robustness of PCA to variations in the frequency components of the surface profiles.

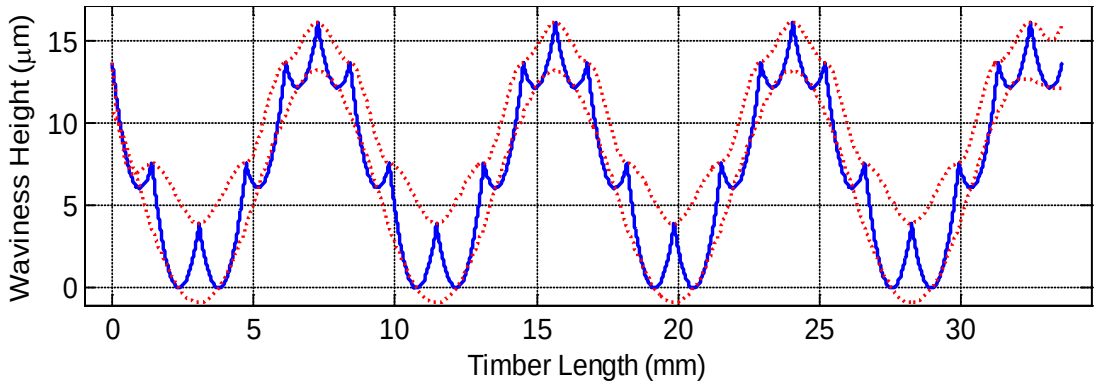


Figure 5.18 Six-knife finish with once per revolution vibration defect

Table 5.6 Principal components for six-knife finish with once per revolution vibration

Cutting Speed (rev/min)	Feed Speed (mm/s)	Knife Radius (mm)	Vibration Amplitude (mm), ψ (rad)	Principal Component
2500	350	60	0.007, 0	0.6348, 0.7727
2500	400	65	0.004, π/2	0.6172, 0.7868
2500	450	55	0.008, π/4	0.6407, 0.7678
2500	500	70	0.003, π/10	0.6419, 0.7668

Case 5: Six-Knife Finish with Twice Per Revolution Vibration

Two Surface profiles produced by six-knife finish with superimposed twice per revolution vibration are shown in Figures 5.19 and 5.20. The values of ψ for the first and second profiles are 0 and π /10 respectively. It is worth noting that the frequency components are completely different due to difference in the value of ψ (imbalance position).

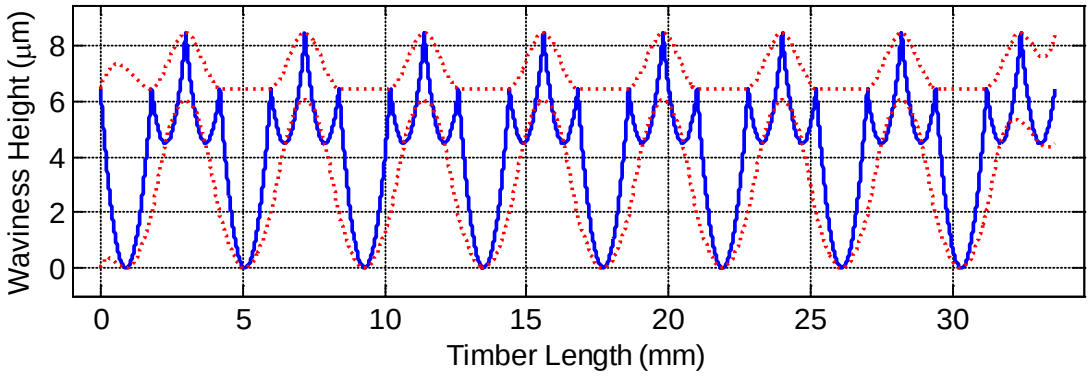


Figure 5.19 Six-knife finish with twice per revolution vibration defect ($\psi = 0$)

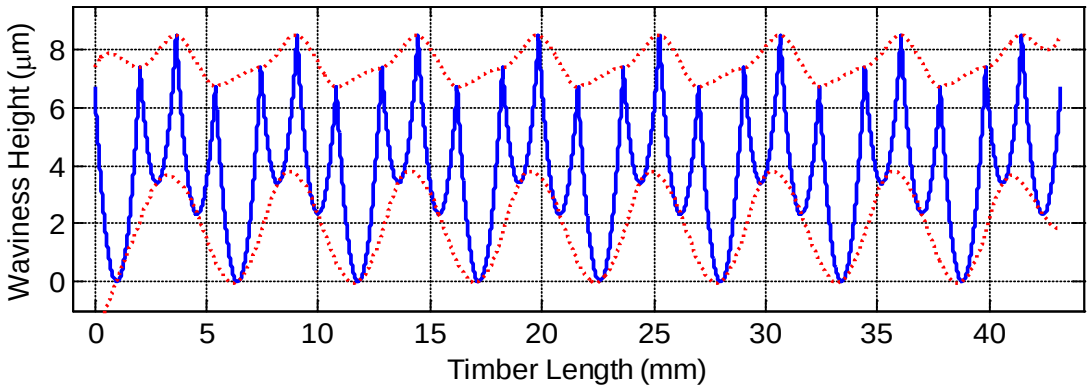


Figure 5.20 Six-knife finish with twice per revolution vibration defect ($\psi = \pi/10$)

Table 5.7 Principal components for six-knife finish with twice per revolution vibration

Cutting Speed (rev/min)	Feed Speed (mm/s)	Knife Radius (mm)	Vibration Amplitude (mm), ψ (rad)	Principal Component
2500	350	60	0.003, 0	0.3286, 0.9544
2500	400	65	0.004, $\pi/2$	0.3355, 0.9420
2500	450	55	0.002, $\pi/4$	0.3518, 0.9361
2500	500	70	0.001, $\pi/10$	0.3476, 0.9376

As presented in Table 5.7, the principal component coefficients for six-knife finish also have deterministic values for the twice per revolution case. Based on the above results, it is

concluded that the principal component analysis can be used to generate a-priori knowledge for identifying the types of vibration defect in a surface profile. After some tests, it was observed that as the number of knives increases, the principal component coefficients for the once per revolution vibration and once per two revolutions vibration become similar. This occurrence is shown in Table 5.8 and Table 5.9 for ten-knife finish. In effect, it becomes increasingly difficult to classify the defects separately based on the coefficients. However, if the average of the lower and upper envelopes is taken as an additional variable to the PCA (Figure 5.21), then there will be more coefficients for making more distinct classifications. With three signals, the principal component coefficients are nine in number (3-by-3 matrix).

Table 5.8 Principal components for ten-knife finish with once per revolution vibration

Cutting Speed (rev/min)	Feed Speed (mm/s)	Knife Radius (mm)	Vibration Amplitude (mm), ψ (rad)	Principal Component
2500	600	65	0.005, 0	0.6853, 0.7283
2500	600	65	0.003, $\pi/4$	0.6833, 0.7301
2500	600	65	0.008, $\pi/2$	0.6749, 0.7379

Table 5.9 Principal components for ten-knife finish with once per two revolutions vibration

Cutting Speed (rev/min)	Feed Speed (mm/s)	Knife Radius (mm)	Vibration Amplitude (mm), ψ (rad)	Principal Component
2500	600	65	0.005, 0	0.7005, 0.7136
2500	600	65	0.003, $\pi/4$	0.7024, 0.7118
2500	500	65	0.008, $\pi/2$	0.7005, 0.7136

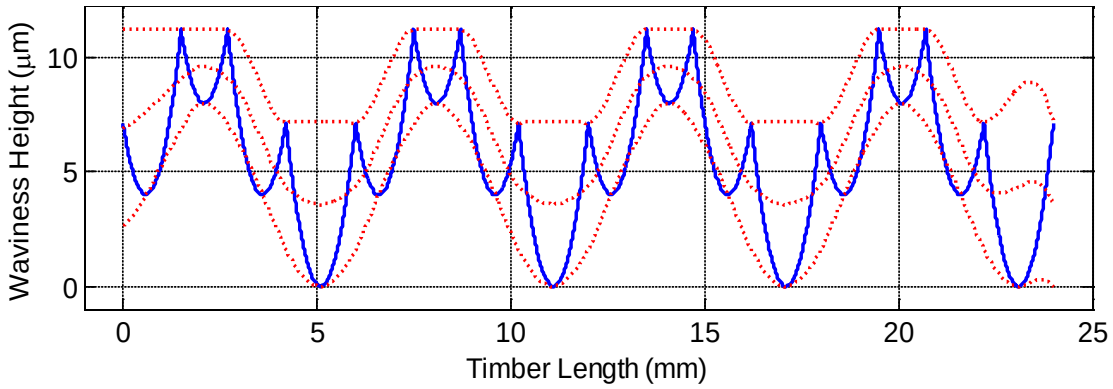


Figure 5.21 The upper, lower and average envelops of a surface profile

5.4.3 Classification of the Principal Components

The goal of PCA is only to extract relevant features from the surface profiles so the analysis can be simpler. With three signals (envelopes), the original data is reduced to a 3-by-3 matrix containing the principal components. There is still the need to classify the defects based on the principal components. A number of pattern classification algorithms are available for this purpose but a *Kohonen competitive neural network* is used here because it is simple and suitable for the task.

The network uses a competitive learning algorithm, which is a form of unsupervised training, to learn how to classify presented input vectors. After the training, a new input vector is assigned to the closest out of the fixed number of possible classes. The function of the network is to assign a new set of principal components to the class of defect they belong to, based on the training set in which the defect groupings are already established.

The structure of the network is shown in Figure 5.22. The network contains two layers of nodes, namely, an input layer and a mapping (output) layer. There are nine nodes in the input layer, each corresponding to each of the principal component coefficients in the 3-by-3 matrix. The three nodes in the output layer represent the once per revolution vibration,

twice per revolution vibration, and once per two revolutions vibration, in an order which is determined after the training process.

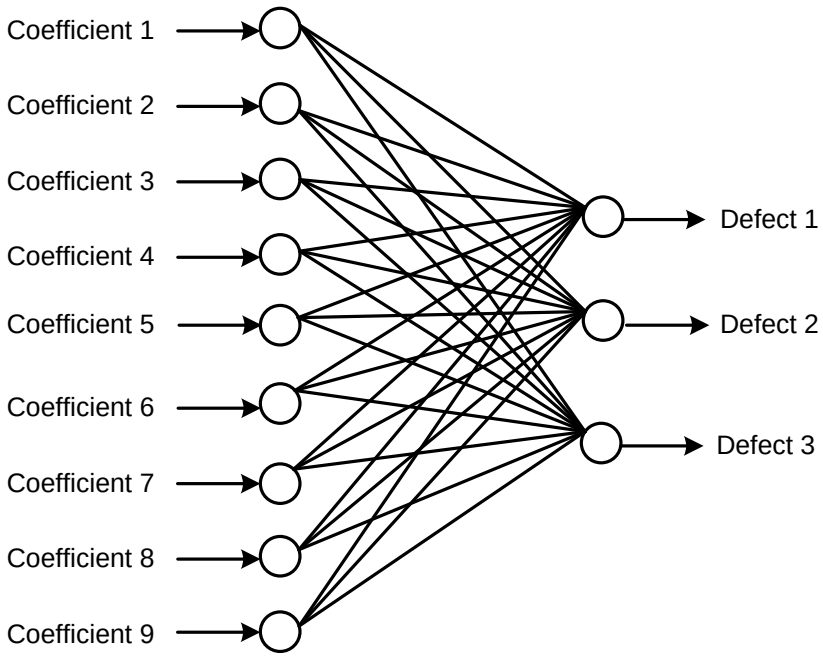


Figure 5.22 Structure of the competitive neural network

All the nodes in the input layer are fully connected to the nodes in the mapping layer. The matrix *W* is the weight of the connections between the input and the output nodes.

$$W = \begin{bmatrix} w_{11} & w_{12} & w_{13} \\ w_{21} & w_{22} & w_{23} \\ \vdots & \vdots & \vdots \\ w_{n1} & w_{n2} & w_{n3} \end{bmatrix} \quad (5.10)$$

where $n = 9$. The weights are first initialised to some random numbers between 0 and 1. This creates a structure for the neural network, which is then trained to do the classification job using the competitive learning algorithm.

During the training, each of the input vectors *x*, from the training data set is presented to the network. The output node whose weight vector is the closest to the input vector wins the competition and outputs 1, while the other nodes output 0. The closeness is measured in terms of the Euclidean distance between the input vector and the weight vector. The weights of the winning node are then adjusted so as to minimise the Euclidean distance. Supposing that the k^{th} node wins, the elements of the k^{th} column of the weight matrix are adjusted according to the Kohonen learning rule (Curry and Morgan, 2004)**,** given by the following equation:

$$w_k(t+1) = w_k(t) + \alpha[x - w_k(t)] \tag{5.11}$$

where α is the learning rate. As a result of the update, the node whose weight vector is closest to the input vector becomes closer to the input vector. The effect of this is that the winning node is empowered more to win the competition the next time it is presented with a similar input vector, and less likely to win when presented with a different input vector. As more inputs from the training sets are presented to the network, the weights of the wining nodes are adjusted towards the input vectors.

A training set of 600 records was generated by varying the vibration signature and the machining parameters supplied to the surface simulation algorithm. The principal component analysis was then performed on each of the surface profiles as described in section 5.4.1. The competitive neural network was created and trained using the *newc* and *train* commands available in the MATLAB neural network toolbox. After about 500 iterations, the network has learnt to classify every cluster of similar principal component

coefficients as the same defect. When a new set of principal components is subsequently presented to the trained network, the winning node is used to infer the nature of the defect.

5.5 Considerations for Practical Applications

EMD and PCA techniques have been applied to perfectly simulated surfaces. However, real machined surfaces usually contain irregularities as a result of both the machining process and the anatomy of the wood specimen (Gurau et al., 2007). A planed timber surface is characterised by its roughness and waviness. The surface roughness is associated with the timber anatomical structure while the surface waviness is due to the kinematics of the machining process. A perfectly generated surface profile with additive normally distributed random noise is used to simulate a profile with both texture and waviness features. A plot of the simulated noisy profile is shown in Figure 5.23.

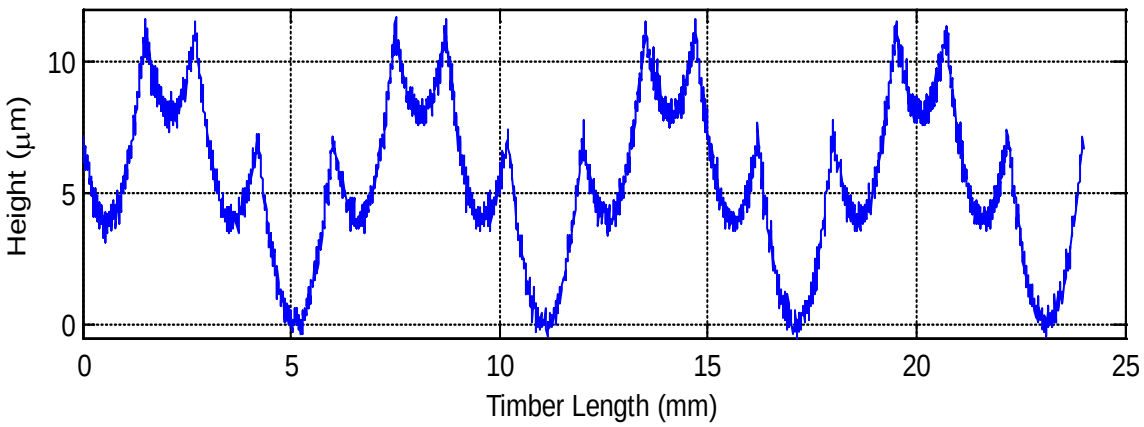


Figure 5.23 The simulated noisy surface profile

In order for the surface waviness to be properly characterised, the roughness components need to be filtered out from the surface profile data before applying any of the two techniques. A low-pass Gaussian filter can be used for this purpose because it has good roll-off capability with low amplitude distortion and phase shift. It is also the

recommended filter by International Standard Organisation for surface profile metrology in ISO 11562:1996 (Geometrical Product Specifications – Surface texture: profile method - metrological characteristics of phase correct filters). The standard specifies how to separate the long and short wave contents of a surface profile. The kernel of the filter has the shape of a Gaussian density. The discrete mathematical representation of the Gaussian filter as given in ISO 11562:1996 is expressed as follows:

$$S_k = \frac{\Delta x}{\beta \lambda_c} exp\left[-\pi \left(\frac{k\Delta x}{\alpha \lambda_c}\right)^2\right] \tag{5.12}$$

where Δx is the sample spacing with which the surface is measured, λc is the cut-off wavelength of the filter, and β is a constant defined as

$$\beta = \sqrt{\frac{\log 2}{\pi}} = 0.4697 \tag{5.13}$$

A Gaussian filter with a cut-off wavelength of 0.1mm is applied to the noisy surface profile and the resultant profile is plotted alongside the filtered profile in Figure 5.24. Clearly, the filter is able to remove the shorter wavelength components from the noisy profile without any significant amplitude roll-off or phase shift. The correlation between the filtered and the original signal is computed to be 97%.

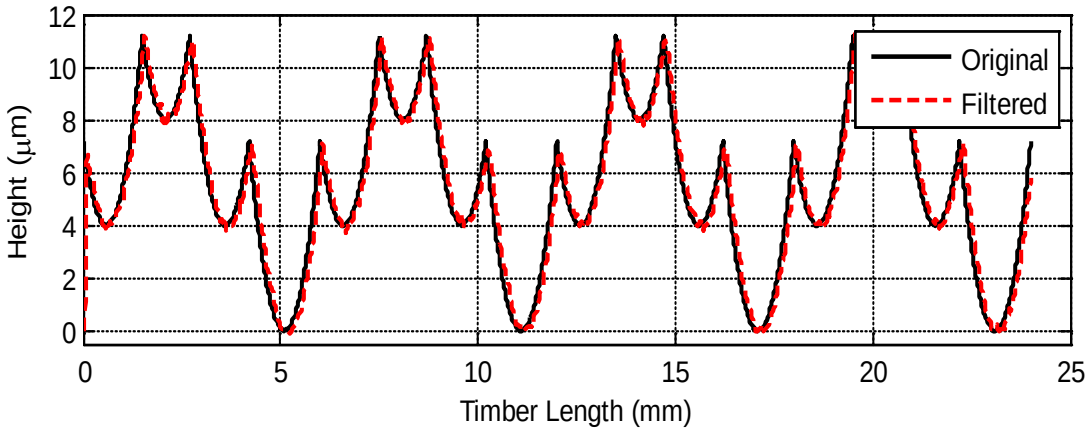


Figure 5.24 The original and the filtered surface profiles

5.6 Summary and Conclusions

In this chapter, two novel approaches for characterising the waviness defects on planed timber surfaces using EMD and PCA techniques have been developed. The main focus has been placed on characterising only the defects caused by structural vibration because it is relatively more straightforward to characterise the defects arising from cutterhead inaccuracy without any rigorous analysis.

It is shown that EMD can recover cutterhead vibration signature from measured surface profile if information about some of the machining parameters is available. In comparison with Fourier analysis, it is also shown that EMD will perform better under general conditions where the Fourier analysis is likely to fail.

In the intelligent approach, a knowledge-base is first developed through principal component analysis of the surface profiles generated by known defect conditions. A competitive neural network is then designed to represent the human reasoning mechanism for subsequent identification of unknown defects. It is shown through simulation that the developed technique can effectively replace a human expert in terms of identifying the

vibration signature. The limitation of PCA compared to EMD is that it does not give any information about the amplitude of vibration.

For all the defect cases considered, it is assumed that the cutters are accurately grounded and jointed. That is, there are no significant defects due to cutterhead inaccuracy. However, waviness defects might arise from the combination of both structural dynamics and cutterhead inaccuracy in a practical multi-knife finish. Characterisation of such defects remains a challenge as it is difficult to separate the influence of the two conditions. A form of real-time sensitivity test, whereby subtle changes are introduced during the machining process, is required to identify the influence of each condition. This is a subject of major investigations carried out in Chamberlain (2012).

The two techniques have been applied to simulated data. Real wood surface profiles will contain irregularities such noises and roughness components. Necessary considerations for practical applications of the two techniques on real timber surfaces have been discussed. Further work needs to be done in terms of the application of the techniques to real data.

6 Test Rig Characterisation and System Identification

The wood planing machine that is shown in Figure 1.4 is a newly upgraded version of the one originally designed by Hynek (2004). After the upgrade, some tests were performed to ensure that the system produces the desired performances under operating conditions. The details of these tests are presented in this chapter. Furthermore, the adaptive control system designed in chapter seven for the high performance machining system is based on the modal control approach, which requires that the dynamic model of the spindle system and the piezoelectric actuators be available in form of mathematical equations. The details of the experimental system identification procedure used to develop the dynamic models of the test rig are also presented in this chapter.

6.1 Sensors and Actuators Arrangement

An overhung arrangement has been chosen for the spindle unit by the original designer (Hynek, 2004) mainly because of its simplicity. The spindle is supported by two angular contact ball bearings arranged in face-to-face configuration as shown in Figure 6.1. The back bearing is fixed in the spindle unit housing. The front bearing is fitted in a ring, which is being supported by four piezoelectric actuators. Additional support is provided by four flexural hinges, which also retain the front ring in axial direction. Therefore, the control of the spindle displacement is achieved by moving the front bearing. The spindle is displaced in the desired direction by applying voltage on the corresponding actuator. Two eddy current sensors, which are 90^o apart, are used to measure the spindle displacement in the plane perpendicular to its rotational axis. The sensors are aligned with the actuators in axial direction but rotated by 45^o with respect to the actuators as depicted in Figure 6.1.

It is necessary to transform the eddy current sensor readings to the actuator coordinate system because the directions of the sensor measurements are different from the directions in which the actuators act on the spindle. The following directional cosine matrix is used to perform the transformation:

$$\begin{bmatrix} x_a \\ y_a \end{bmatrix} = \begin{bmatrix} \cos(\varphi) & -\sin(\varphi) \\ \sin(\varphi) & \cos(\varphi) \end{bmatrix} \begin{bmatrix} x_s \\ y_s \end{bmatrix} \tag{6.1}$$

where x_a, y_a are the spindle displacements in the actuator coordinate system, and x_s, y_s are the displacements measured in the sensor coordinate system.

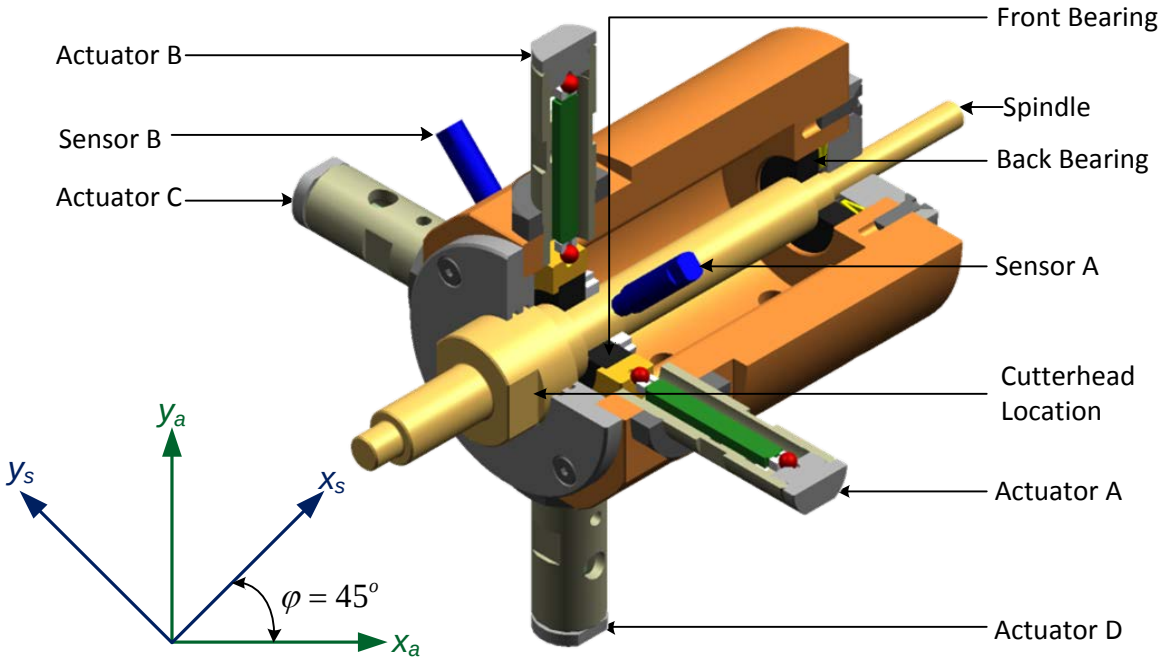


Figure 6.1 Actuators and sensors arrangement on the smart spindle unit

The eddy current sensors and the actuators are collocated at the front bearing so that the spindle movement can be measured at the point where it is being actuated. This is advantageous for feedback control implementation. The slight disadvantage is that the

spindle displacement is not measured at the point where the cutterhead is located. It has been shown in Hynek (2004) and Elmas (2008) that the tool tip displacement is proportional to the front bearing displacement up to the first resonance frequency of the spindle unit (first vibration mode at 500Hz). At higher frequencies, the tool tip displacement cannot be estimated by considering only the spindle geometry as the dynamic characteristics of the spindle also come into play. It is indeed shown in Hynek (2004) that the tool tip displacement and the front ring displacement are in opposite direction at the second vibration mode of the spindle.

The first resonance frequency of the spindle unit with a four-knife cutterhead of mass 293g attached to it is about 500Hz. This is well above the maximum excitation frequency range of the smart wood planing machine (100Hz). Consequently, the displacement at the cutterhead location is calculated from the geometry of the spindle unit (Figure 6.2).

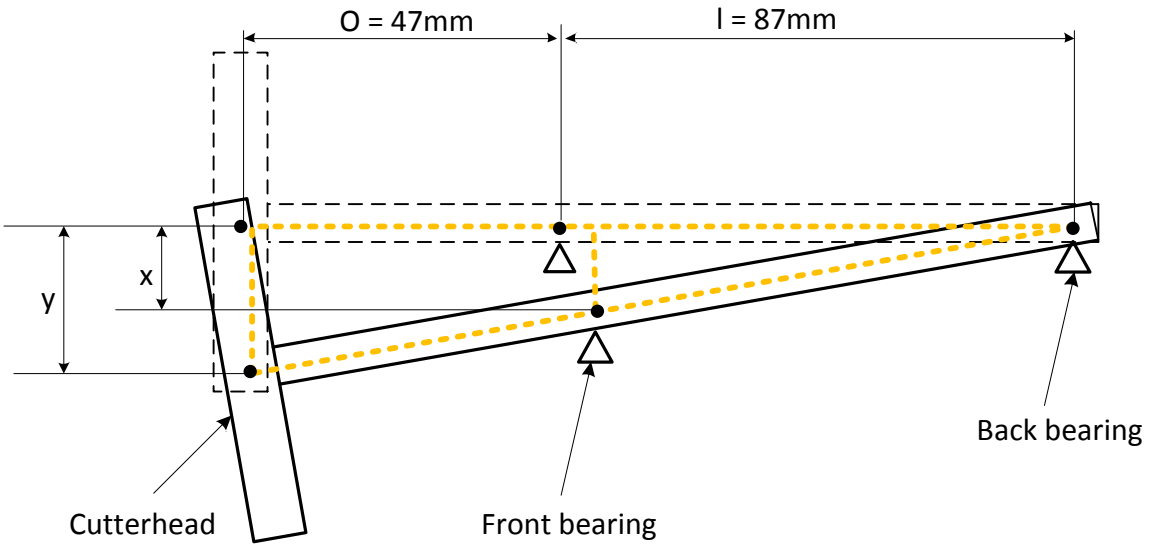


Figure 6.2 Geometry of the spindle unit

$$\frac{y}{o+l} = \frac{x}{l} \tag{6.2}$$

The dimensions of the spindle were extracted from Hynek (2004). Based on the geometric relationships, the displacement at the cutterhead location is approximately 1.54 times the displacement at the front bearing. In order to experimentally verify the above theoretical calculations, a digital dial test indicator (DTI) is placed on the cutterhead (Figure 6.3). The specifications of the DTI are given in appendix D. Voltage inputs are applied to the piezoelectric actuators in the vertical axis (B and D). The displacements at the front bearing and at the cutterhead position are then measured with the eddy current sensors and the DTI respectively. The readings obtained are recorded in Table 6.1.

Table 6.1 Spindle displacements measurement

Voltage	Sensors Reading, *x*	DTI Reading, *y* (μm)	*y/x*
40	5.30	7	1.32
75	10.00	13	1.30
76	10.05	13	1.29
107	14.30	18	1.26
124	16.50	20	1.21
-80	-10.70	-13	1.22
-83	-11.06	-14	1.27
-116	-15.44	-19	1.23
-117	-15.60	-19	1.22

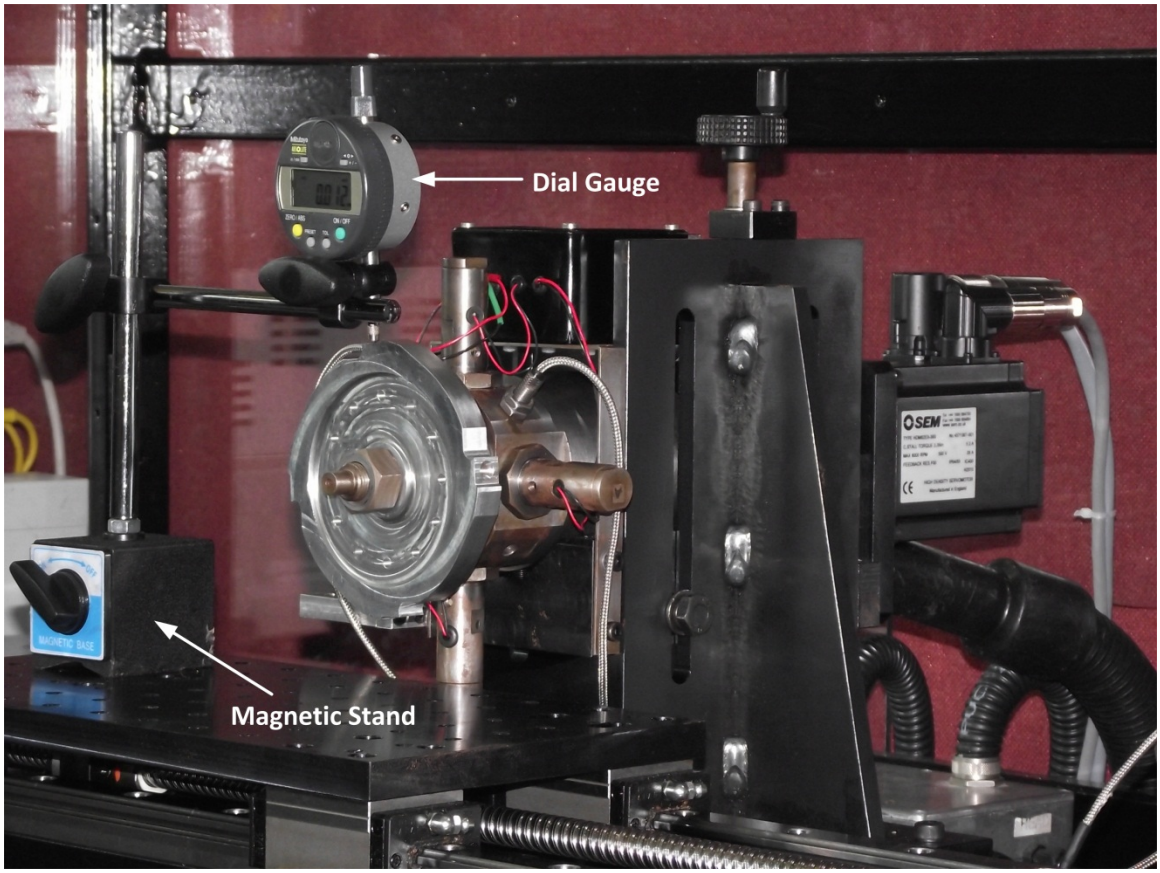


Figure 6.3 Experimental setup for the spindle displacement measurements

The values in Table 6.1 show that the measured displacement at the cutterhead location is different from what would be obtained from the theoretical calculations. The average displacement at the cutterhead location (measured with the dial gauge) is about 1.26 times the displacement at the front bearing. This difference could be attributed to errors in the eddy current sensors calibration. Eddy current sensors are very sensitive to the target thickness, the target materials and the way they are being mounted. Therefore, there might have been slight errors in the original determination of the sensors calibration factor. The difference could also be attributed to the much lower resolution of the DTI (1µm) compared to that of the eddy current sensors (up to 0.1µm).

6.2 Spindle Support Operation

The overall mechanical support for the spindle in the vertical axis is depicted in Figure 6.4. The two piezoelectric actuators on each of the axis are arranged in push-pull configuration. Each of the actuators is mechanically modelled as an infinite stiffness pusher and a spring (k_p = 14N/μm) connected in series. The support stiffness of the flexural hinges is also represented by a spring (k_s = 2N/μm). The effective stiffness of the actuator and the support is 16N/μm since they can be modelled as two springs in parallel connection.

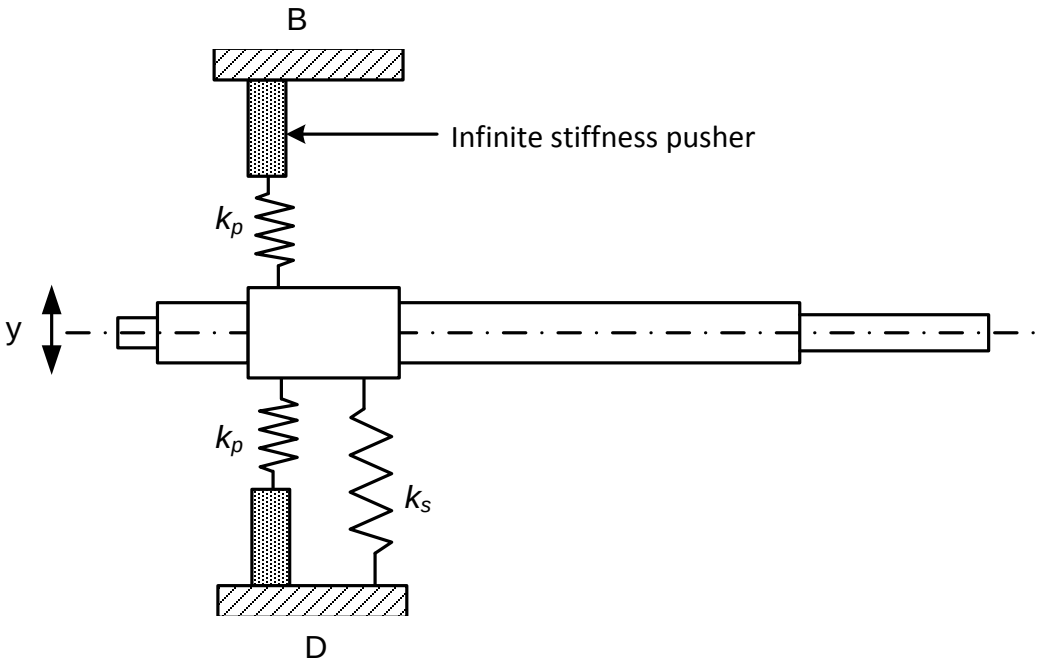


Figure 6.4 Mechanical supports for the spindle

Some tests have been performed in order to estimate the amount of vibration caused by imbalance forces in the system. The spindle is rotated at different speeds and its vibration in the vertical plane is measured using the eddy current sensors. A sample plot of the spindle vibrations is shown in Figure 6.5. The signal was sampled at the rate of 10 kHz while running the spindle at the speed of 3000rpm (50Hz). The same tests are also

performed with a cutterhead of mass 293g attached to the spindle. Table 6.2 shows the vibration amplitudes at the different rotational speeds.

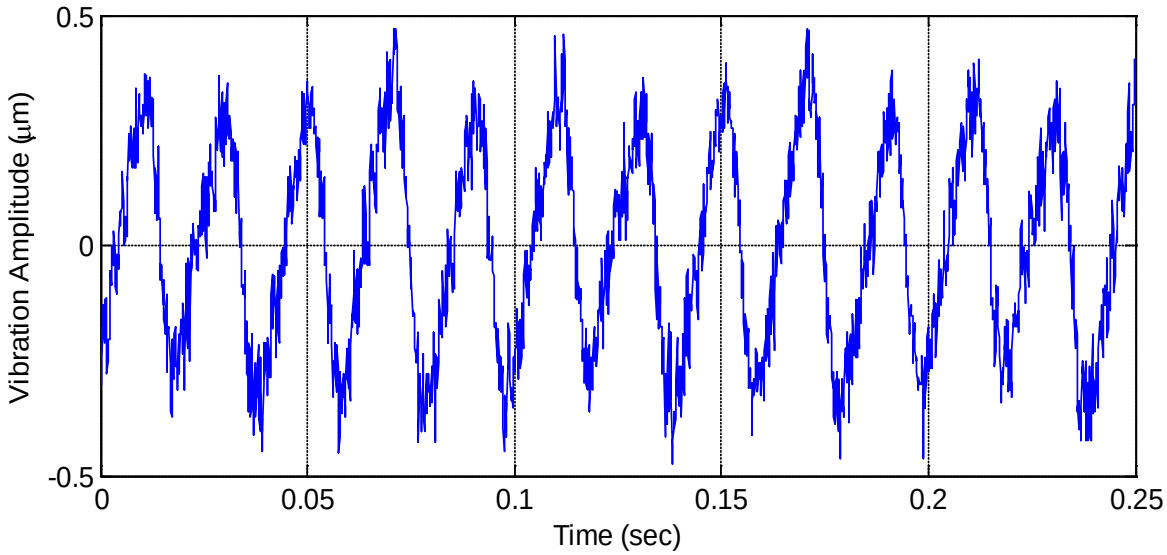


Figure 6.5 Vibration of the spindle rotating at 3000rpm

Table 6.2 Spindle vibrations due to mass imbalance

Speed (RPM)	Amplitude (µm) Spindle Only	Amplitude (µm) Spindle + Cutterhead
600	0.31	0.31
1000	0.32	0.33
1500	0.35	0.36
2000	0.36	0.37
3000	0.38	0.39
4000	0.41	0.42

The results in the above table show that there is no significant mass imbalance in the system. This is desirable because the less the spindle vibration, the better the surface finish. Although the actual vibration amplitude at the point where the cutterhead is located is about 1.2 times the measured values, the maximum amplitude of 0.5 µm will not introduce any significant defects into the surface finish. The amount of imbalance mass that must be

present in the system for the spindle to deflect by a given amplitude can be calculated according to the following equation:

$$F = kX = me{\omega_c}^2 \tag{6.3}$$

where:

F is the imbalance force/deflection force (N)

k is the effective stiffness of the actuators and the support (16 N/μm)

X is the spindle vibration amplitude (μm)

m is the resultant imbalance mass (kg)

e is the radial position of the resultant mass imbalance (m)

ω_c is the spindle rotational speed (rad/s)

From simple calculations, an imbalance of about 162g-mm must be present in order to deflect the spindle by 1μm (at the front bearing) when it is rotated at the speed of 3000rpm. It should be noted that the above formula is only guaranteed to hold at speeds well below the first resonance frequency of the system (500Hz). It is also assumed that the damping in the system is negligible.

6.3 Characteristics of the Piezoelectric Actuators

The static and dynamic characteristics of the spindle system including the piezoelectric actuators have been thoroughly investigated by Hynek (2004) and Elmas (2008). Detailed mathematical models of the actuators were also derived. The only test that is necessary in this research is to determine the voltage-displacement characteristics of the spindle actuation system. This understanding will help to achieve a better control of the spindle.

The experiments reported in this thesis are only on the actuators along the vertical axis (B, D) because the control system to be designed does not operate along the feed direction. The main interest is to control the spindle centre position along the vertical axis. This is because the spindle vibration and tooling inaccuracy are in the micrometre range while the width of each cuttermark is in the millimetre range. Therefore, these factors do not have any significant effects along the feed direction. Their effects are more influential on the vertical axis because the heights of the cuttermarks are in the micrometre range.

The voltage-displacement characteristics of the spindle actuation system have been determined experimentally by measuring the spindle response to a low frequency triangular input signal of 5V/s. Such a low frequency has been chosen in order to avoid the influence of the system dynamics on the response of the spindle. The magnitude of the voltage is gradually increased from 0 to 150V at an incremental step of 5V. The motion is reversed in a similar manner. The responses of the spindle for the two actuators (B and D) are shown in Figure 6.6 and Figure 6.7 respectively.

It is evident from the two figures that the piezoelectric actuators exhibit highly nonlinear behaviour due to their inherent hysteretic characteristics. The hysteresis, which is within the range of 10-12%, has led to non-repeatability of the spindle responses upon reversal of motion. The hysteresis depends on the direction of recent motion performed by the actuator, which makes it difficult to model and control the piezoelectric actuators. This nonlinearity is often neglected in modelling the actuators so that the theory of linear dynamic systems can be used for analysis and control. From a practical point of view, the hysteresis presents a limitation for an open-loop control of the spindle. This is the motivation for the hybrid closed-loop control system designed in chapter seven.

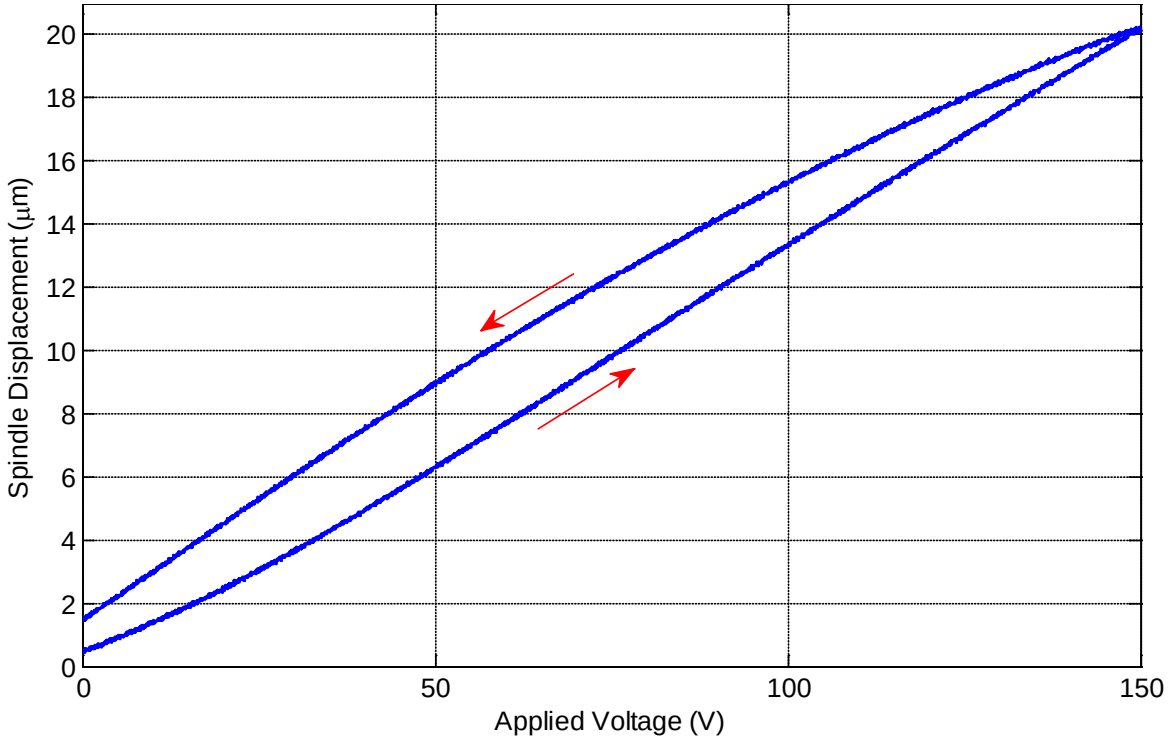


Figure 6.6 The hysteresis curves for piezoelectric actuator B

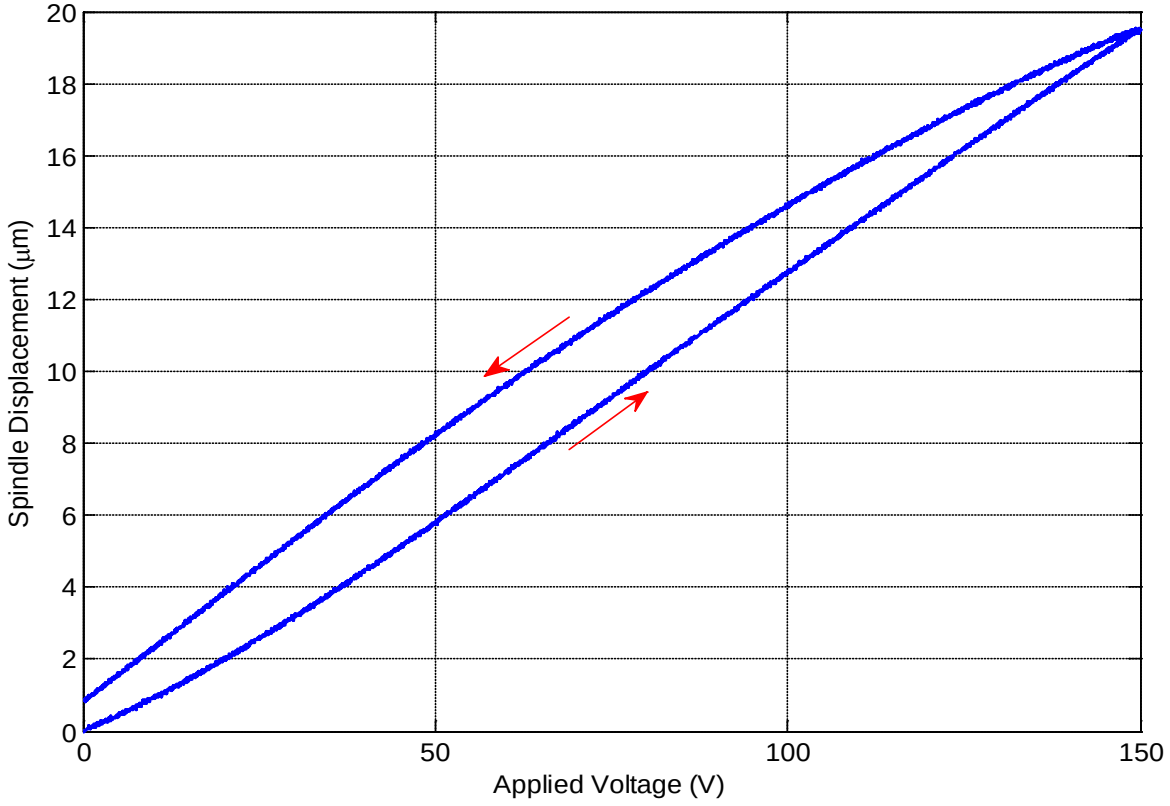


Figure 6.7 The hysteresis curves for piezoelectric actuator D

Some other tests were also performed to determine the response time of the spindle actuating system. It is necessary to perform these tests so as to have an idea of the cutting speed and the TIR that the actuators can cope with when the controller designed in chapter seven is in operation. Step inputs of 20V, 40V, 60V and 80V are applied on actuator A. The responses of the spindle are shown in Figure 6.8. The responses are sampled at a frequency of 10 kHz.

The response time of the actuators is estimated to be approximately 1ms. Interestingly, it is found that this time does not change as the voltage increases. That is, it takes the same time for the piezoelectric actuator to displace from zero to any final value. Nowadays, there are piezoelectric actuators with extremely faster responses (sub millisecond). However, the 1ms response time is still sufficient to operate the test rig at cutting speed of about 5000rpm for a four-knife cutterhead according to the data shown in Table 8.1. Some other tests were also performed to determine the overall lag in the system. It was found that there is about 2ms lag in the system.

6.4 Feed and Cutting Motors Tests

In rotary wood machining, the pitch of the cuttermarks depends on the workpiece feed speed and the cutting speed (Equation 3.1). It is therefore very important that the actual speed of the cutting motor and the feed table be constant and exactly as set by the operator in order to obtain the desired waviness. The feed and cutting motors installed on the upgraded wood planer test rig both have built-in feedback speed control via the digital controllers. The motors are controlled internally using PID algorithm with tuneable gains. Therefore, it is expected that their speeds will remain constant to a reasonable degree during the machining process.

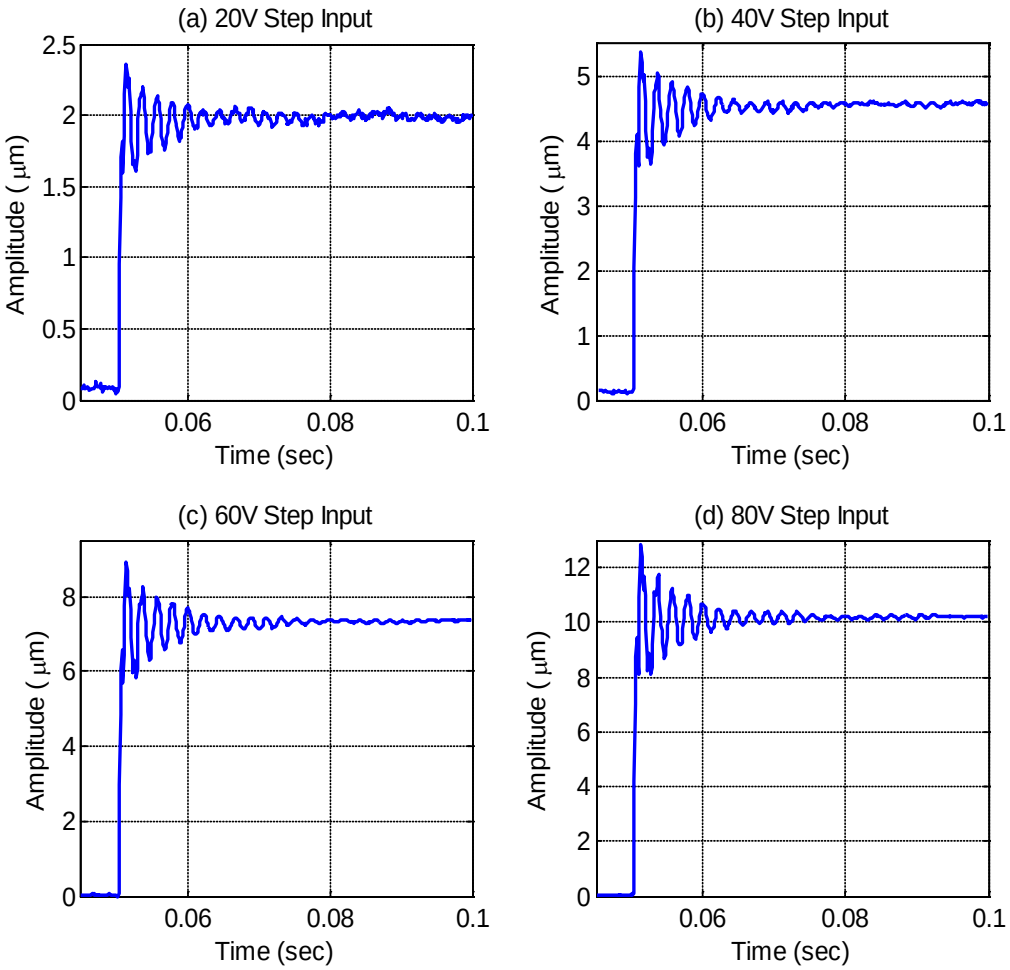


Figure 6.8 Spindle responses to step voltage inputs

The maximum speed rating of the feed motor is 8000rpm. A ball screw of 16mm diameter with a lead of 10mm is used to translate the rotational motion of the feed motor to the linear motion of the table. In theory, the feed motor could drive the table up to the speed of 1333.33mm/s with the ball screw. However, the table could not be driven faster than 500mm/s (3000rpm) without causing the whole system to vibrate and also slightly whirling the ball screw. Nevertheless, cutting tests could still be performed at spindle speed up to 5000rpm for a four-knife cutterhead aimed at producing cuttermarks of 1.5mm pitch.

In order to determine the acceleration of the feed motor, the motor is rotated at 3000rpm and its speed is logged through the built-in encoder. The speed is sampled at the rate of 200Hz as the motor digital controller could not cope with faster sampling rate. The speed-time graph of the feed motor is shown in Figure 6.9.

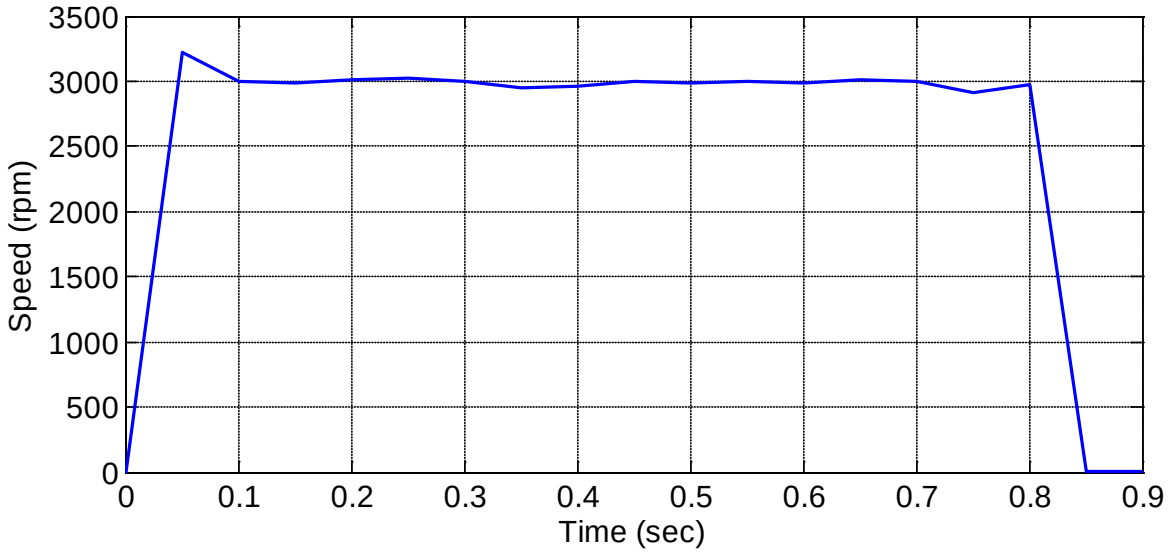


Figure 6.9 Speed-time graph of the feed motor

Looking at the speed-time graph, the motor is able to accelerate from zero to the required speed of 3000rpm (500mm/s) in 50ms or less. From Newton's law of motion, the corresponding acceleration of the feed table is 10000mm/s^2. The travel distance between the starting point of the feed table and the point where the cutting knives engage with the workpiece is about 90mm. The table is able to accelerate from rest to the speed of 1341.6mm/s within the 90mm distance. This means that the motor acceleration is more than what is required for the test rig to be operated at its maximum speed.

6.5 Plant Modelling

6.5.1 Background

Mathematical models of dynamic systems can be developed either analytically or experimentally. The analytical approach is based on the application of well-known basic physical laws (first principles). This approach is known as *modelling* and does not involve any experimentation on the actual system. The models developed through the first principles technique are generally termed as *white-box* models.

The second approach, which is based on measured input-output data from the system, is known as *system identification*. In some cases where the structure of the system is so complex that it is difficult to derive models analytically, experimental techniques have been shown to be quite effective (Ljung, 2002). In processes for which experimental input-output data are available, the main objective of the system identification is to develop a model that represents the best possible approximation of the measured data. Models that are developed using this approach are known as *black-box* models.

The two common techniques for system identification are the nonparametric and parametric estimation methods (Karray and De Silva, 2004). The goal of nonparametric system identification is to obtain the model of a system under the assumption that its dynamics is linear and time-invariant. Parametric system identification on the other hand is effective for online modelling of systems whose parameters are subject to dynamic changes. For more detailed explanation of the system identification technique, reference could be made to Ljung (1999), in which the theory is extensively covered. This text is the foundation upon which the System Identification Toolbox in MATLAB is built.

Generally, the main drawback of the system identification technique is that it can only be used when the plant to be modelled exists physically. In contrast, the analytical modelling technique has the advantage of being usable at the early stages of design. This is very helpful if the control system is to be simulated before committing resources into building physical prototypes. The experimental approach towards deriving mathematical models is adopted in this research for two reasons. The first one is that the plant to be controlled has already been designed and built. Secondly, one of the objectives of this research is to design an adaptive controller for the test rig. Models used for adaptive control algorithms are mostly derived through the experimental technique.

The spindle of the wood planer test rig has earlier been modelled by Hynek (2004) using finite element (FE) method. The primary advantage of this method is that it could be used in the design phase to simulate the dynamic behaviour of the final system. However, the parameters of the system such as the spindle dimensions and bearing damping must be known in order to obtain a fairly accurate model of the system.

Although some of the required parameters such as the spindle dimensions can be measured, there are still some parameters that cannot be easily obtained. A typical example is the determination of the damping characteristics of the spindle system. It is difficult to determine the damping in the bearings supporting the spindle unit. Sources of damping include but not limited to the front and back bearings, spindle material damping and piezoelectric actuator damping, and it is almost impossible to separate the contribution of each source. The so called white-box models are usually overly complicated from the control design viewpoint.

Another challenge in FE modelling is that the dynamic response of the model can differ from that of the actual system due to the use of inadequate number of elements or unrealistic boundary conditions. For any FE model to be used with confidence, it is always necessary to tune the model using the parameters obtained from experimental tests so that the modelled response closely fits the experimental output data.

Elmas (2008) later performed observability and controllability tests of the derived FE model from Hynek (2004) and reported that the model is neither observable nor controllable. Consequently, a grey-box model, which combined the structure of the finite-element model with measured input-output data, was developed by Elmas (2008) for implementing an active vibration control system on the wood planing machine. The FE model provided a structure for the overall model while the input-output data was used to tune the parameters in order to provide a better match with the experimental data.

In the current research where adaptive control of the machining process is desired, building the mathematical models of the system using the modelling approach is not practicable. Consequently, an approach that does not assume any prior first principles model of the spindle and the piezoelectric actuators is pursued. The entire model of the test rig is built from input and output signals from the test rig. The only requirement in this case is that the appropriate model order describing the dynamics of the system should be selected.

.

6.5.2 System Identification and Parameter Estimation

The optimal tracking controller for the test rig requires that the system be represented in a linear time-invariant state-space form. The state-space model represents the relationship between the inputs, outputs and state variables of the physical system as a set of first-order differential or difference equations. The discrete-time representation of the state-space model of a noisy plant is defined by the following difference equations:

$$x(t + T_s) = Ax(t) + Bu(t) + Fe(t) \qquad (6.4a)$$

$$y(t) = Cx(t) + e(t) \qquad (6.4b)$$

where:

x is the state vector [x_1, x_2, ... x_n]

y is the output vector [y_1, y_2, ... y_q]

u is the input vector [u_1, u_2, ... u_p]

A is the state matrix (n by n)

B is the input matrix (n by p)

C is the output matrix (q by n)

F is the stochastic noise coefficient matrix (n by q)

T_s is the data sampling interval

n is the order of the model, p and q are number of inputs and outputs respectively.

The approach earlier used by Hynek (2004) and Elmas (2008) was to develop separate models of the spindle unit and the piezoelectric actuators. The mechanical part of the spindle unit, which consists of the spindle itself and the associated support structures, was modelled as a rotor system using the finite element method. A linear model of the actuator system was also created based on the electromechanical behaviour of the piezoelectric actuators and the driving amplifiers. The two models were then combined together to form a state-space model of the test rig. Parameters such as the stiffness and capacitance of the actuators, driving amplifier output impedance need to be accurately determined in order to obtain a good model. Although some of these parameters can be obtained from datasheets, there are still some parameters that are unknown.

The overall aim of the system identification procedure is to estimate the values of matrices *A, B, C, D* from measured data, without actually going into the details of the physical principles guiding the behaviours of the spindle assembly and the piezoelectric actuators. Therefore, the parameters of the plant components (e.g. damping, spindle dimensions, actuator stiffness, and amplifier impedance) and the underlining mathematical relationships are not required. This approach creates a "black-box" model in which only the inputs and outputs of the model have physical meanings, while the internal state variables do not have any physical meanings. The following basic steps are involved in the identification procedure:

- Measurements of the system's response to an input signal
- Estimation of the state, input and output matrices of the model
- Evaluation of the estimated model quality

6.5.3 Input-Output Data Collection

Frequency response testing is used to determine the dynamic characteristics of the planer rig and also generate data for the system identification procedure. Quantitative knowledge of the frequencies associated with the structural resonances will aid in understanding the spindle vibration at certain cutting speeds, and also allow for intelligent evaluation of the final control system.

The excitation signal used in this experiment is a linear sine-sweep. The sine-weep signal has been chosen mainly because it makes it possible to excite the various resonances of the spindle unit. The frequency response measurement readily provides information about the natural frequencies and the amount of damping in the system. The magnitude of the sine-sweep signal applied to the piezoelectric actuators is limited to 25V in order to avoid excessive vibration of the spindle, which could potentially damage the actuators.

The frequency of the sine-sweep signal ranges from 0 – 1 kHz. Such a low frequency range has been used because the voltage amplifiers have limited bandwidth. According to the datasheet for the driving amplifiers, the bandwidth of the amplifiers is just above 800Hz. Elmas (2008) performed some tests to determine the bandwidth of the amplifiers using an oscilloscope and reported that it is 1424Hz at 3db. The amplifiers exhibit amplitude roll-off at higher frequencies. Nevertheless, the chosen frequency range (0-1KHz) is still enough to excite the dominant resonances within the maximum operating speed range of the cutting motor, which is 6000 rpm (100 Hz).

The rate of change of frequency used is 0.5 kHz/sec. A higher frequency rate of 0.8 kHz/sec has earlier been used in Hynek (2004) and Elmas (2008) in order to limit the

length of time spent in resonant regimes. Meanwhile, it is demonstrated in Hynek (2004) that half of the frequency rate (0.4 kHz/sec) will deliver up to 4% more accuracy in the amplitude and 1% in resonant frequency. This has informed the 0.5 kHz/sec value used in this research. The selection of the sweep parameters is a trade-off between accuracy and subjection of the actuators to potentially damaging levels of vibration.

A number of other test signals, such as the impulse signal, could be used to excite the system. The impulse excitation is useful because its energy comprises of continuously distributed portions of all possible excitation frequencies. The major drawback of the impulse excitation is that it does not allow a precise control of the excitation frequency range. Although this is not a problem for frequency response testing, it could affect the accuracy of the model obtained through the system identification. This is because the actual input signal to which the plant responds must be used for the identification. Meanwhile, the bandwidth limitations of the amplifiers might cause the actual input to the piezoelectric actuator to be different from the desired input. For this reason, the impulse excitation is not used for the system identification.

The sine-sweep excitation signal is applied to the spindle through the piezoelectric actuators and the spindle response is measured using the eddy current sensors mounted on the test rig. In order to obtain a good model of the system, it is essential that the input signal should excite the important dynamics of the system. Also, the data must be measured at appropriate sampling intervals, within a sufficiently long time to capture the important time constants. The input and output variables are recorded at a uniform sampling frequency of 1 kHz to obtain two discrete-time vectors of the following form:

$$u_{meas} = [V(T_s), V(2T_s), V(3T_s), V(4T_s), \ldots\ldots V(NT_s)] \quad (6.5a)$$

$$y_{meas} = [y(T_s), y(2T_s), y(3T_s), y(4T_s), \ldots\ldots y(NT_s)] \quad (6.5b)$$

where T_s = 0.001s and NT_s is the time of the last sampling. The sweep test was performed for four different configurations of the spindle unit. The first one was performed with no cutterhead attached to the spindle unit. The second one was with a cutterhead of mass 106g attached to the spindle. The third and fourth were performed with cutterheads of masses 190g and 293g respectively. The time-domain responses of the spindle to the sweep signal are shown in Figures 6.10, 6.11, 6.12 and 6.13 respectively. At the frequency rate of 0.5 kHz/sec, it will take 2sec for the bandwidth to sweep from 0 to 1 kHz. The duration of each of the tests is 6sec, meaning that the responses repeat every 2sec.

All the tests were performed while the spindle was stationary (non-rotating) since it has been demonstrated in Lauffer et.al (1998) and Hynek (2004) that spindle rotation does not generally have any significant influence on the dynamics of plants. The sweep signal was applied to the actuators on the vertical axis only (B and D). The identification of the spindle unit in the horizontal direction is not that critical because the cutterhead inaccuracy compensation and the vibration control system are implemented on the vertical axis only.

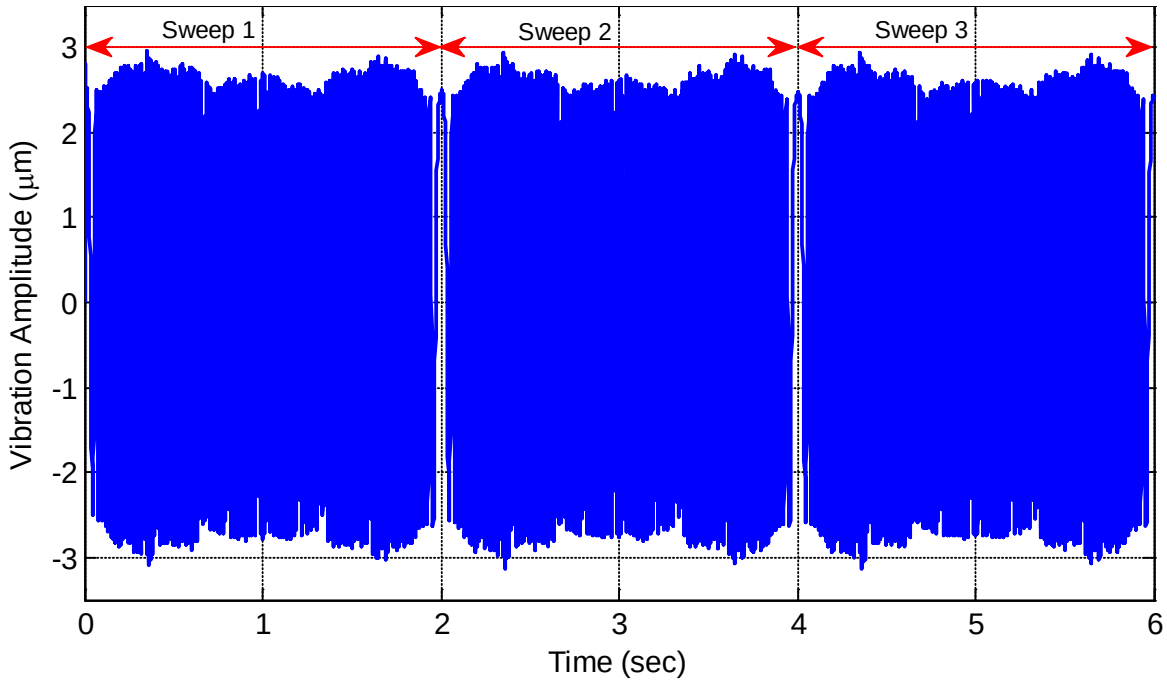


Figure 6.10 Time-domain response: spindle without cutterhead

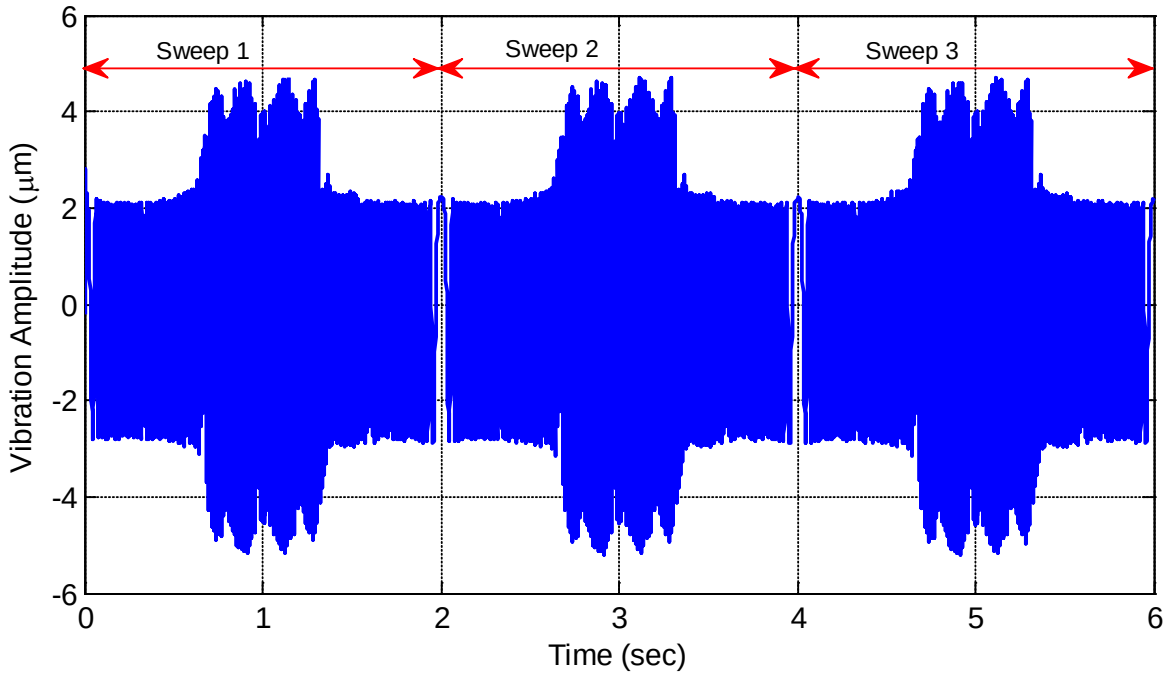


Figure 6.11 Time-domain response: spindle with cutterhead of mass 106g

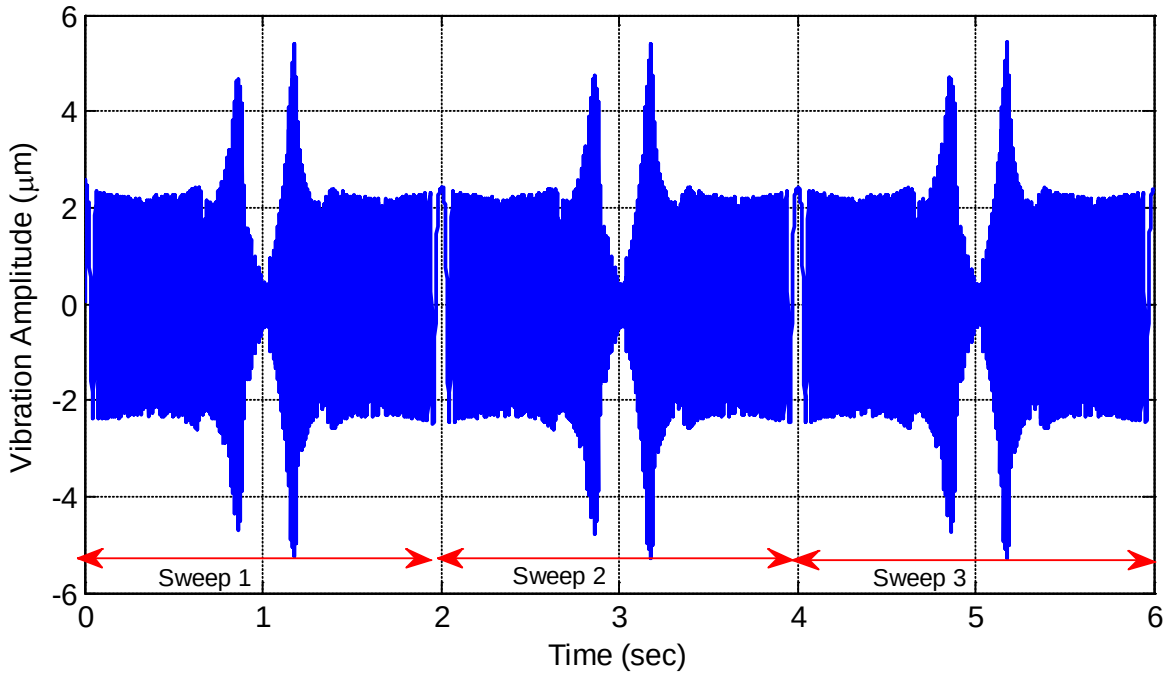


Figure 6.12 Time-domain response: spindle with cutterhead of mass 190g

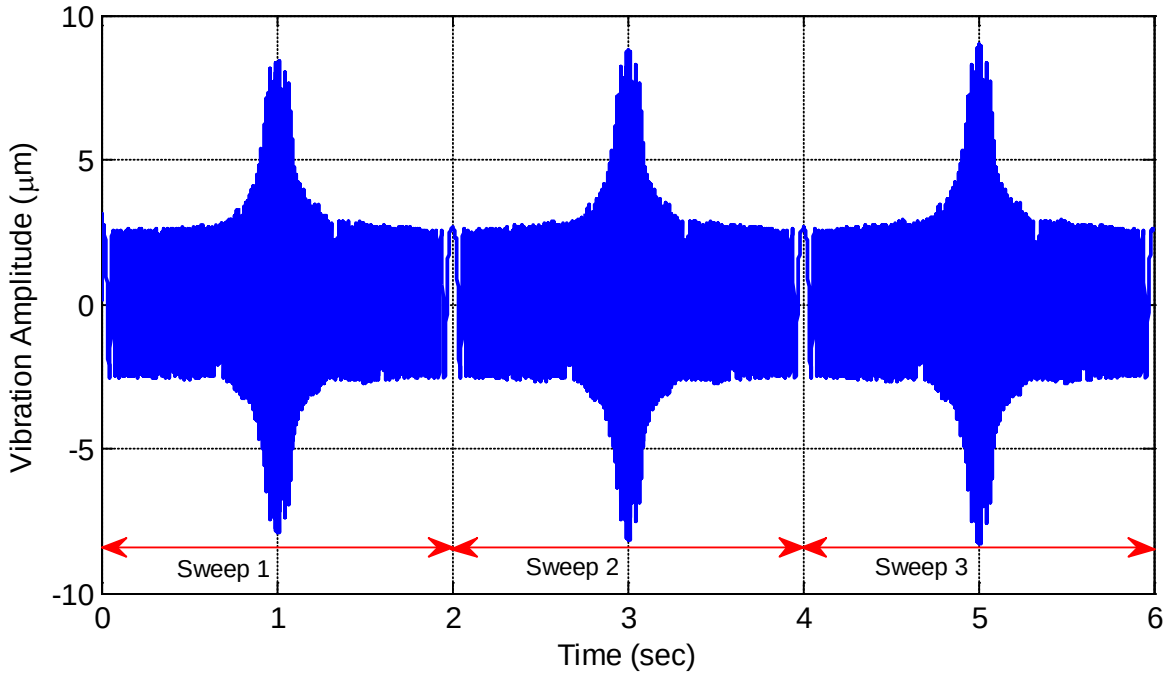


Figure 6.13 Time-domain response: spindle with cutterhead of mass 293g

The planer rig spindle responses to a sweep frequency input signal have been shown in the above figures for different masses of cutterheads. The variation in cutterhead masses substantially influences the dynamic behaviour of the system. The practical implication of this is that if different cutterheads from the one used to develop the original FE models are mounted on the spindle, then the whole FE modelling process must be repeated for each of the new cutterheads. Another situation that might also necessitate a repeat of the modelling activities is if the piezoelectric actuator and the voltage amplifiers are changed. Clearly, experimental system identification and parameter estimation is needed to easily cope with any changes in the dynamics of the system.

The frequency response of the spindle with the cutterhead of mass 293g is obtained from the envelope of the time-domain response. This envelop is then considered to be the frequency response approximation when plotted against frequency. The resultant frequency response for the spindle unit configuration, obtained from the signal in Figure 6.13, is shown in Figure 6.14. As seen in the figure, the first natural frequency of the spindle unit configuration is around 500Hz. The frequency response functions could not reveal higher vibration modes because the bandwidth of the voltage amplifiers is not high enough to excite such resonances.

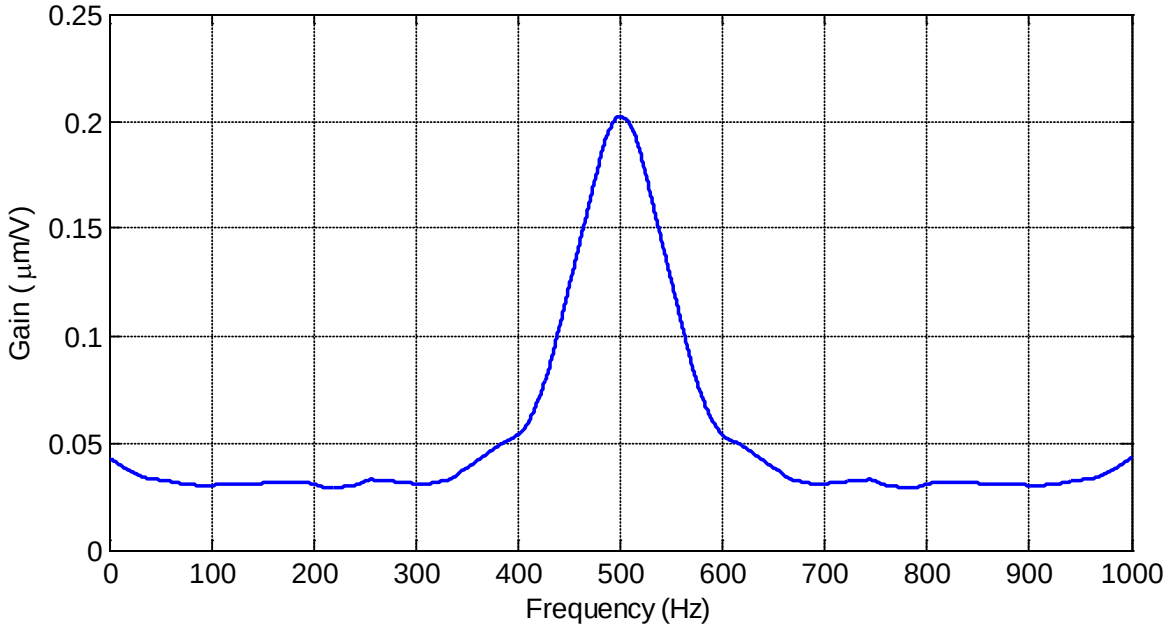


Figure 6.14 Frequency response function: spindle with cutterhead of mass 293g

6.5.4 Model Parameters Estimation and Validation

The MATLAB System Identification Toolbox is used to estimate the state-space model matrices from the measured input-output data (u_{meas} and y_{meas}). The toolbox uses an algorithm known as the prediction-error minimisation (PEM) method (Ljung, 2002) to estimate the model parameters through minimisation of the following objective function:

$$V = \frac{1}{M}\sum_{t=1}^{M}\frac{1}{2}e^2(t) \tag{6.6}$$

where *e(t)* is the difference between the measured output and the predicted output of the estimated model. The PEM first finds an initial estimate of the model using the subspace method and then iteratively varies the parameter values along a specific direction as to as minimise the objective function (Ljung, 1999). The objective function depends on the number of data samples *M* and the estimated model becomes more accurate for larger

values of *M*. This is the reason why the duration of the excitation is 6sec rather than the 2sec that is required to sweep the frequency from 0 to 1 kHz.

The most important parameter to be selected in estimating the model is the model order. The suitable model order that is enough to capture the essential dynamics of the plant must be determined. This is done here by comparing the output of the estimated model with the output of a validation data set. The data acquired from the test rig during the excitation is split into two parts, half of which is used for estimating the model and the other half for validating the model. During the model validation, the input signal from the validation data set is used as the input to the model. The predicted output of the identified model is then compared with the measured output in the validation data set. The comparisons between the estimated output and the corresponding measured output are shown in Figures 6.15, 6.16 and 6.17 for 2^{nd}, 4^{th}, and 6^{th} order models respectively. These plots are for the dynamic model of the spindle unit with the cutterhead of mass 293g mounted on it.

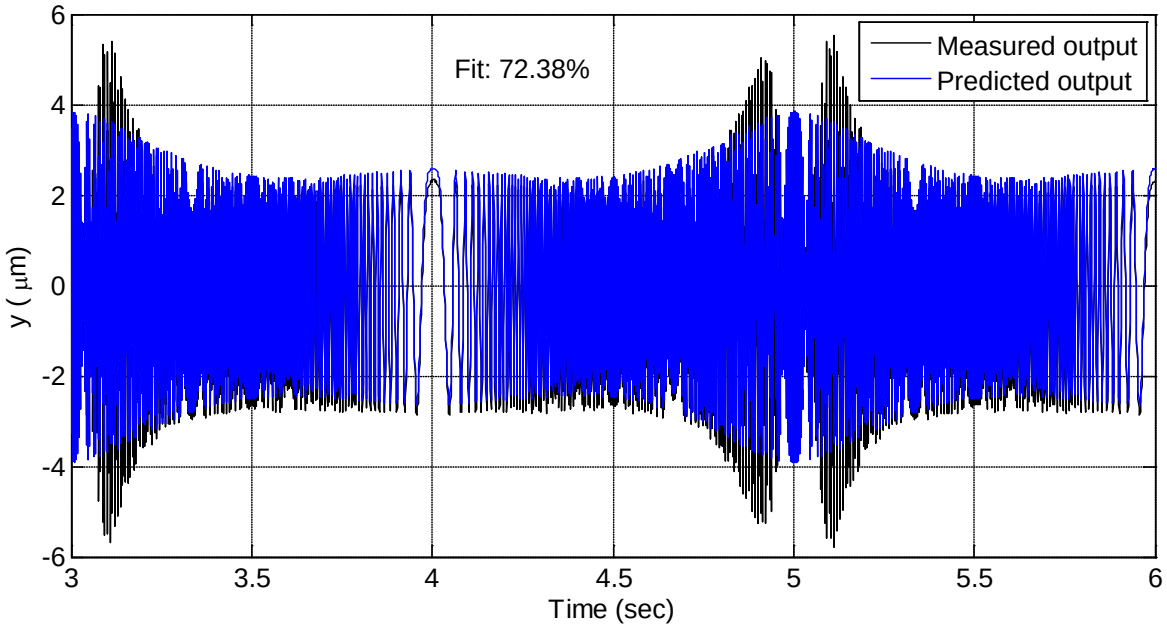


Figure 6.15 Measured and predicted outputs for second order model

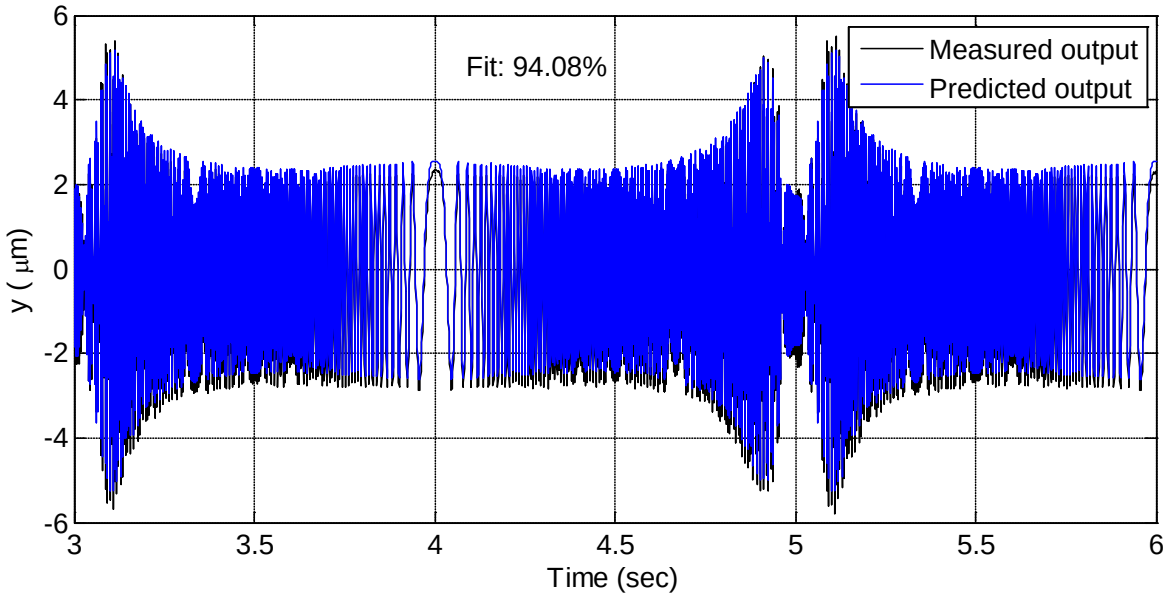


Figure 6.16 Measured and predicted outputs for fourth order model

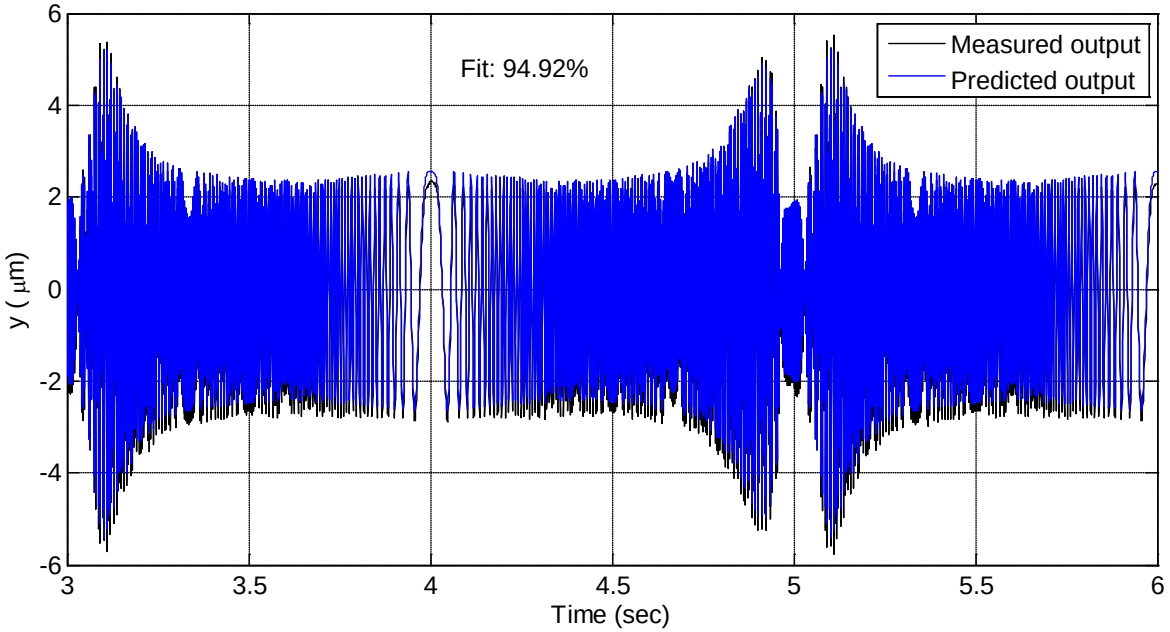


Figure 6.17 Measured and predicted outputs for sixth order model

From the calculations, there is 21.7% increase in correlation between the measured and predicted outputs when the model order is increased from two to four. However, there is only about 0.84% increase in accuracy when the model order is increased from four to six. Anything from six and above does not provide any significant improvement. In order to

find a good balance between the model accuracy and the computational requirements of the final control system, the 4^{th} order model is selected. The computational requirement increases considerably for every small increase in the model order, and therefore a higher order than necessary should be avoided. It is worth mentioning that Hynek (2004) and Elmas (2008) have earlier modelled the test rig using a 6^{th} order state-space model. However, the 4^{th} order model is considered to be a better balance between the model accuracy and computational requirements. The numerical parameter values for the estimated discrete-time state-space model are given in Appendix B. It should be noted that this numerical values do not have any physical meanings.

6.6 Summary and Conclusions

This chapter is focused mainly on the development of mathematical models of the wood planer test rig from measured data. The experimental approach is known as system identification. The overall aim of the system identification procedure is to obtain state-space models of the plant without actually going into the details of the physical principles guiding the behaviours of the spindle assembly and the piezoelectric actuators.

The planer test rig has been modelled by the previous researchers using finite element (FE) method. The primary advantage of the FE method is that it could be used in the design phase to simulate the dynamic behaviour of the final system. However, the parameters of the plant components (e.g. damping, spindle dimensions, actuator stiffness, and amplifier impedance) and the underlining mathematical relationships are required in order to obtain a fairly accurate model of the system. One of the problems with the FE approach is that it is time-consuming and often times produce less accurate results.

The system identification approach does not assume any prior first principles model of the spindle and the piezoelectric actuators. Only the input-output data from the test rig are required to estimate the state-space model of the plant. The main requirements are that the inputs applied to the system must excite its important dynamics and the appropriate model order describing the dynamics of the system must be selected. Therefore, a sine-sweep with frequency ranging from 0 – 1 kHz is used to excite the plant and a 4^{th} order model is found to be sufficient for describing the plant dynamics. The accuracy of the 4^{th} order state-space model is found to be within 94-96% after validation.

The main advantage of the system identification is simplicity. Secondly, one of the objectives of this research is to design an adaptive controller for the wood planing machine. Models used for adaptive control algorithms are mostly derived through the experimental technique. In practical terms, the experimental method is the most pragmatic approach because the plant to be modelled exists physically.

7 Optimal Controller Design for the Active Machining System

In rotary wood planing, structural vibration and tooling inaccuracy have been identified to be the primary causes of poor surface quality and material wastage. The need to minimise the undesirable effects of these factors in real-time cannot be overemphasised. Therefore, the focus of this chapter is to design a suitable closed-loop adaptive control system for the smart wood planing machine. The primary objective of the control system is to compensate for the cutting tool inaccuracy and also reject the effect of process disturbances such as vibration and cutting forces.

7.1 Principles of the Cutter Run out Compensation

Defects arising from cutterhead inaccuracy typically occur in multi-knife finish operations. It is a common occurrence for the cutting edges on the cutterhead to have different radii due to the difficulties in grinding and setting them to a very high level of precision. Even the use of the best available precision tools and techniques would still produce a total indicated run out (TIR) within the range of 5-10μm (Jackson, 1986). The TIR is the difference between the longest and the shortest knife on the cutterhead. A TIR value of less than 1μm will be required to produce an acceptable finish but this is not technically feasible at a reasonable price using mechanical methods (Jackson et. al, 2002).

The proposed technique for compensating for the cutterhead inaccuracy is to adjust the cutterhead vertical position in such a way that all the knife tips are at the same level when passing through their lowest positions. The technique is described as follows:

It is assumed that there are N number of cutters on the cutterhead, each with radius R_1, R_2 ..... R_N. One of the cutters is taken to be the reference. If the reference knife has a radius of R_s, then the respective error of each knife i, relative to the reference knife is given as:

$$e_i = R_i - R_s \tag{7.1}$$

The idea is to displace the cutterhead vertically by a value of e_i within an angular rotation where the i^{th} knife produces visible cuttermarks on the timber surface. The cutterhead is then moved downward outside this angular movement. The whole movement is depicted in Figure 7.1. The effect of the vertical displacement is that it changes the effective radius of each knife to that of the reference knife, thereby serving the same radius adjustment purpose as the mechanical jointing process.

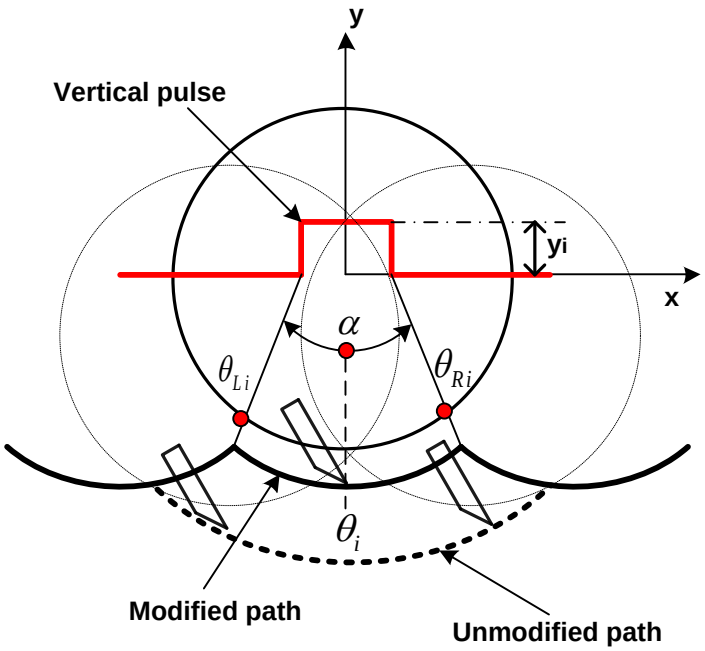


Figure 7.1 Principle of the cutterhead inaccuracy compensation

There is a very short time window within which the vertical displacement pulse must take place. The pulse width is the time *t* required by the reference knife to machine one cuttermark, which is expressed as follows (Hynek, 2004):

$$t = \frac{p}{v_c + v_f} \tag{7.2}$$

$$v_c = \omega_c R_s \tag{7.3}$$

where v_f *(mm/s*) is the workpiece feed speed and ω_c *(rad/s)* is the cutterhead angular speed. Taking the absolute angular position of the cutterhead at the lowest point of each knife tip to be θ_i, the vertical pulse must be synchronised with the rotation of the cutterhead such that it is applied when the angular position of the cutterhead is at least between θ_{Li} and θ_{Ri}. Any displacement of the cutterhead outside this angle will not influence the surface profile because the surface machined by the knife outside this angle will be removed by either the subsequent knives or the same knife during subsequent revolutions.

$$\theta_{Li} = \theta_i - \frac{\omega_c t}{2}, \qquad \theta_{Ri} = \theta_i + \frac{\omega_c t}{2} \tag{7.4}$$

$$\beta = |\theta_{Li} - \theta_{Ri}| = \omega_c t \tag{7.5}$$

The angle between θ_{Li} and θ_{Ri} is very small ($\beta \approx 1.5^o$) for typical values of *R = 75mm* and *p = 2mm*. Therefore, the dynamic response requirement of the actuator increases with the cutting speed. Figure 7.2 shows a graph of the pulse width with respect to the cutting speed for *R = 75mm*, *N= 4* and *p = 2mm*.

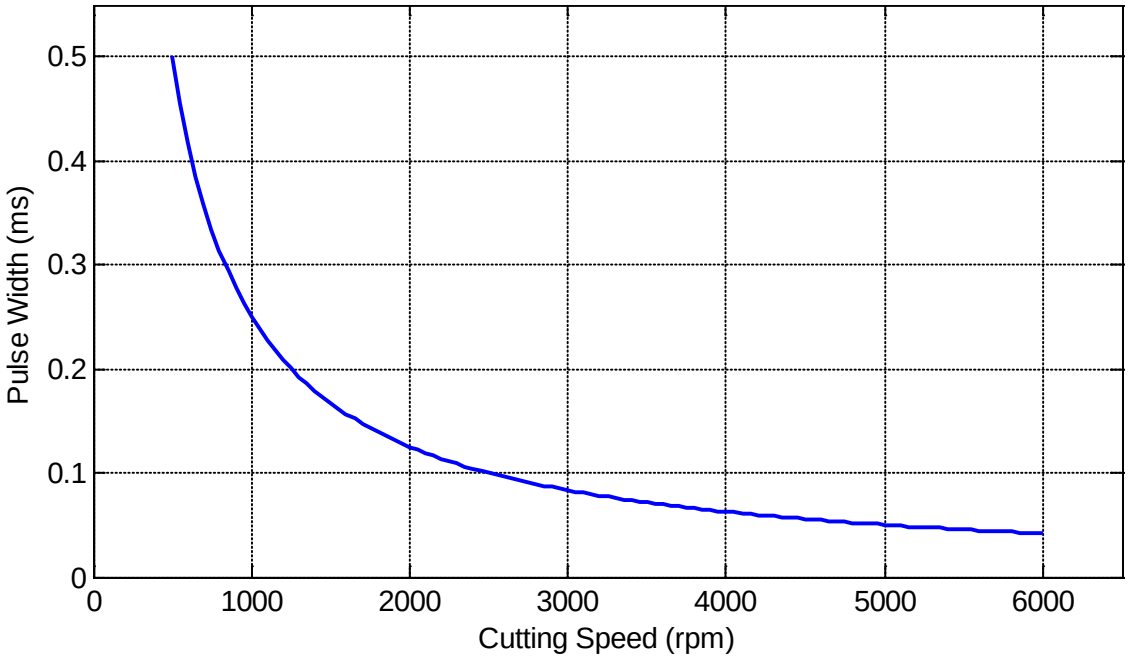


Figure 7.2 Relationship between pulse width and cutting speed

The magnitude of the vertical pulse signal for each knife is expressed as follows:

$$y_i(\theta) = \begin{cases} e_i, & if\ \theta\ \in (\theta_{Li}, \theta_{Ri}) \\ 0 & if\ \theta\ \notin (\theta_{Li}, \theta_{Ri}) \end{cases} \tag{7.6}$$

For practical purposes, the width of the vertical pulse could be increased beyond θ_{Li} and θ_{Ri}. This serves a dual purpose of accommodating any error in the measurement of θ_i and also gives reasonable time for any transient responses to settle before the cutters reach the region where they produce visible cuttermarks on the workpiece. The limit to which the pulse width can be increased depends on the number of knives on the cutterhead. For example, the angle between θ_{Li} and θ_{Ri} can be increased up to 90^o for a four-knife cutterhead and only about 30^o for a twelve-knife cutterhead.

7.2 Structure of the Proposed Control System

A controller is needed to implement the cutterhead inaccuracy compensation and also suppress the vibration of the spindle. A Linear Quadratic Gaussian (LQG) tracking controller with integral action (also known as a setpoint tracker) is chosen because it attempts to provide the best possible performance using the least amount of control effort (Tewari, 2002). Apart from its optimality, it is also stable and robust to process disturbances and measurement noise. The LQG design technique is normally used in applications where the control objective is to drive the output of the plant to zero (regulator). Some additional measures need to be taken in order to use the LQG technique for tracking purposes.

The conventional LQG design technique has been used by Elmas (2008) to implement an active vibration control system on the wood planing machine. As opposed to the regular-type LQG controller whose goal is to regulate the spindle position around zero, the proposed servomechanism-type controller ensures that the vertical position of the spindle tracks a desired reference path. The goal here is to drive the error between the spindle output and the reference path to zero. If the setpoint is a constant zero signal, the controller will attempt to regulate the position of the spindle around zero. In such a case, the LQG tracking controller is effectively functioning as an active vibration control system.

The LQG design technique is based on the modal control strategy, which requires the dynamic mathematical model of the plant. The majority of processes have stochastic characteristics where the parameters of the system may change over time. For example, the dynamic characteristics of the whole spindle unit could be altered if the cutterhead mounted on the spindle is replaced with another one of a different mass (as seen in chapter

six). Therefore, an adaptive control strategy is required for the system to maintain optimal behaviour according to the desired performance specifications. The FE modelling approach used in Elmas (2008) is not suitable for the adaptive control of the system. Apart from the improved control objective (vibration and cutter inaccuracy compensation), the design of a knowledge-based adaptive control strategy in this research is another significant improvement over the work done by Elmas (2008).

The problem with feedforward-only control is that the exact amount of control effort that is needed to provide a desired response must be known and all disturbances acting on the plant must be accurately measured and accounted for. However, unknown disturbances are always present in any real process. A feedback loop is required to suppress the effects of any unmeasured disturbances or disturbances that cannot be accurately predicted.

The proposed control system combines a disturbance feedforward control loop with the feedback LQG control scheme. A simple feedback control mechanism alone may not meet extra high tracking performance requirements, especially in the presence of large disturbances and when there is a long delay between the plant output measurements and the firing of the actuators. Significant improvements in the tracking performance can be obtained if some of the process disturbances can be measured and fed forward into the control loop, so that corrective actions can be initiated in advance before they affect the system's response. This combined configuration takes advantage of the fact that some of the process disturbances can be measured and compensated for before they affect the process output, thereby improving the performance of the overall control system. The structure of the combined control mechanism is shown in Figure 7.3.

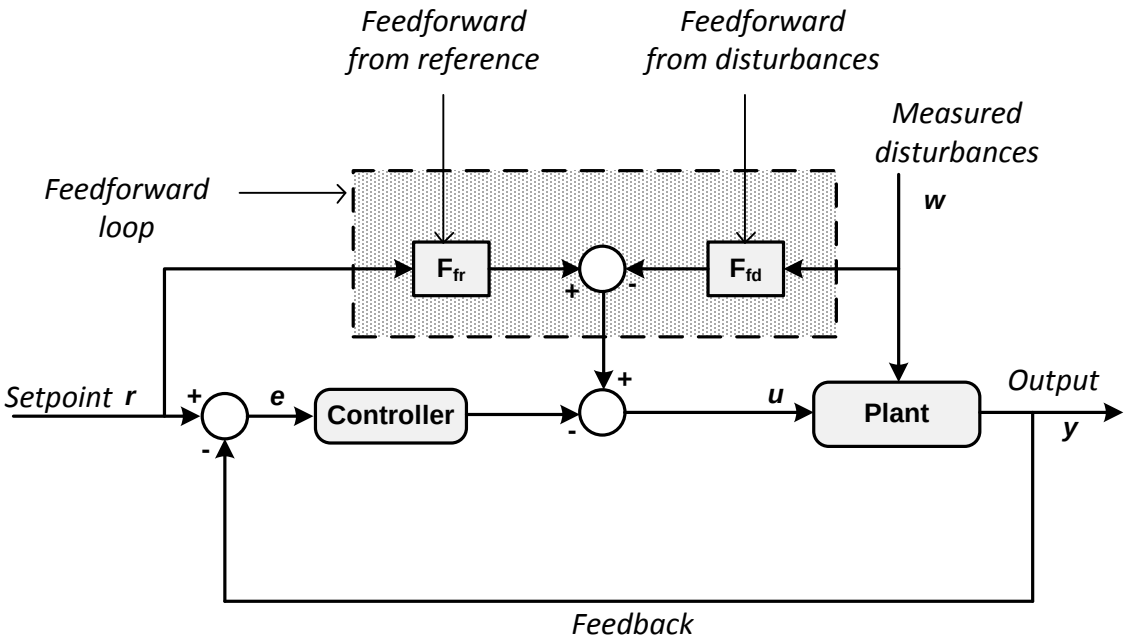


Figure 7.3 Control system with both feedforward and feedback control

The idea of combining both feedforward and feedback schemes is inspired by Seborg et al. (2004) where a PID feedback controller is combined with disturbance feedforward compensation in order to control the temperature of a continuously stirred tank reactor. An LQG controller is more suitable for this research because the planer rig has been modelled as a fourth order system. PID controllers are generally not capable of delivering sufficient performance for high-order systems (Astrom and Hagglund, 1995).

The operation of the hybrid controller is that when the spindle unit is to be oscillated, a proportional amount of control effort is generated by the feedforward loop based on apriori knowledge of the static knife run outs, static gain of the piezoelectric actuators and the anticipated effects of measurable disturbance inputs (vibration). This feedforward mechanism alone might in some cases be able to track the reference setpoint, however, it lacks robustness. In addition to that, it cannot be used to directly specify the controller response requirements in terms of rise time, overshoot and settling time.

Large tracking errors could result from inaccurate knowledge of the dynamic gain of the piezoelectric actuators, the hysteresis of the piezoelectric actuator, and any unknown disturbances acting on the plant. The feedback information from the eddy current sensors is then used to generate any increase or decrease in the combined controller output that is required to minimise the error between the setpoint and the actual spindle position. The hybrid control scheme provides a more stable and responsive control system.

7.3 The Optimal Control Problem

The purpose of the optimal controller design is to realise a system with practical components that will provide desirable time-domain operating performances. The design of the tracking controller typically consists of three steps. In the first step, the feedback gains are computed based on the assumption that all the state variables are available for measurement. However, a full-state feedback is not practicable because it is not always possible to measure all the state variables with sensors. In fact, the state variables of the model obtained through the black-box system identification procedure do not have any physical meanings and therefore cannot be measured with sensors. An observer needs to be incorporated. The second step is therefore to design an optimal observer (Kalman filter) for estimating the state variables, which are not directly measured as outputs. The final step is to combine the separately designed optimal tracking controller and the Kalman filter to form a compensator. The compensator generates the control effort to the plant based upon the estimated state variables.

7.3.1 Optimal Tracking Controller Design

In most texts, optimal control design expressions are in terms of differential equations. However, such continuous time expressions cannot be applied in this case because a digital computer is used to implement the control system on the plant. The eddy current sensor readings and the voltage applied to the actuators are discrete in nature. Therefore, the state-space models of the plant obtained through the system identification are also discrete rather than being continuous. Consequently, a digital form of the LQG compensator is used.

Consider a linear time-invariant system described by the following state-space equations:

$$x(k+1) = \ Ax(k) + Bu(k) \qquad (7.7a)$$

$$y(k) = Cx(k) \qquad (7.7b)$$

The parameters are as earlier defined in equation 6.4. The requirement is to design a control system with satisfactory transient response and the steady state output of the plant should be equal to an arbitrary reference signal. This requirement can be more easily achieved if the control law makes use of both the nominal state vector and the integral of the error between the reference and actual output (Young and Willems, 1972). Therefore, the integral of the error is used as an additional state variable to form an augmented state vector. The position of the spindle *y(k),* is compared with the reference set-point value *r(k),* and the error is passed through an integrator. The output of the integrator is given as:

$$i(k) = \sum_{k=0}^{N} r(k) - y(k) \ = \sum_{k=0}^{N} r(k) - Cx(k) \qquad (7.8)$$

The augmented state vector $\hat{x}$ is given as follows:

$$\hat{x}(k) = \begin{bmatrix} x(k) \\ i(k) \end{bmatrix} \tag{7.9}$$

The state equation for the augmented system is given as (Young and Willems, 1972)

$$\hat{x}(k+1) = \underbrace{\begin{bmatrix} A & 0 \\ -C & 0 \end{bmatrix}}_{\hat{A}} \hat{x}(k) + \underbrace{\begin{bmatrix} B \\ 0 \end{bmatrix}}_{\hat{B}} u(k) \tag{7.10a}$$

$$y(k) = \underbrace{[C \quad 0]}_{\hat{C}} \hat{x}\,(k) \tag{7.10b}$$

An optimal control law that includes feedback of both the nominal states variables and the added state variable is formulated as follows:

$$u(k) = -K\hat{x}(k) = K \begin{bmatrix} x(k) \\ i(k) \end{bmatrix} \tag{7.11}$$

The gain *K* is calculated so that the control law minimises the objective function given by equation 7.12. The objective function defines the trade-off between tracking performance and the control effort.

$$J(0,N) = \sum_{k=0}^{N} \hat{x}^T\,(k).Q.\hat{x}(k) + u^T(k).R.u(k) \tag{7.12}$$

where:

$\hat{x}^T$ is the transpose of the augmented state vector

u^T is the transpose of the input vector

Q is a square, symmetric matrix called the state weighing matrix

R is a square, symmetric matrix called the control cost matrix

The augmented state feedback gain matrix *K* is calculated from the following equation:

$$K = R^{-1}.\hat{B}^T.M \tag{7.13}$$

where *M* is the solution to an algebraic Riccati equation, given by

$$0 = Q + \hat{A}^T.M + M.\hat{A} - M.\hat{B}.R^{-1}.\hat{B}^T.M \tag{7.14}$$

For the existence of a unique solution to equation 7.14, the plant (*A*, *B*) must be controllable, *Q* must be positive semi-definite ($\hat{x}^T Q\hat{x} \geq 0$) and *R* must be positive definite ($\hat{u}^T R\hat{u} > 0$). The augmented state feedback gain can be partitioned into

$$K = [K_x\ K_i] \tag{7.15}$$

The final control law, which also includes the reference signal feedforward, is written as:

$$u(k) = -[K_x\ K_i]\begin{bmatrix} x(k) \\ i(k) \end{bmatrix} + K_r r(k) \tag{7.16}$$

$$u(k) = -K_x x(k) - K_i i(k) + K_r r(k) \tag{7.17}$$

where K_x is the nominal state feedback gain, K_i is the steady state error integral gain and K_r is the reference signal feedforward gain.

7.3.2 Optimal Observer Design (Kalman Filter)

A full-state feedback cannot be used to design a control system based on the stochastic plant because the state vector *x(k)* cannot be predicted. A Kalman filter is required to estimate the state vector, based upon the output measurement *y(k)* and known input *u(k)*. The Kalman filter is an optimal observer, which minimises a statistical measure of the estimation error, $e(k) = x(k) - x_e(k)$. The goal of the Kalman filter is to provide an estimated state vector $x_e(k)$ so that the estimation error is brought to zero in the steady state. The Kalman observer design is adapted from (Tewari, 2002). Consider a stochastic noisy plant with the following discrete state-space representation:

$$x(k+1) = Ax(k) + Bu(k) + Fv \tag{7.18a}$$

$$y(k) = Cx(k) + z \tag{7.18b}$$

where *v* is the process noise vector, which may arise due to modelling errors such as neglecting nonlinearities or higher frequency dynamics, and *z* is the sensor measurement noise vector arising from sensor imperfections. For all practical purposes, it is assumed that *v* and *z* are discrete Gaussian white noises. The stochastic noise coefficient matrix, *F*, is also being estimated by the system identification procedure. The state-equation of the Kalman filter is written as follows:

$$x_e(k+1) = Ax_e(k) + Bu(k) + L[y(k) - Cx_e(k)] \tag{7.19}$$

where L is the Kalman filter gain matrix also called the optimal observer gain matrix. Being an optimal observer, the Kalman filter is a counterpart of the optimal tracking controller. However, while the tracking controller minimises an objective function based on system response and control effort, the Kalman filter is formed by minimising the covariance of the estimation error, $R_e=E[e(k), e^T(k)]$. The estimation covariance matrix R_e can be evaluated by solving the following algebraic Riccati equation:

$$0 = A.R_e + R_e.A^T - R_e.C^T.Z^{-1}.C.R_e + F.V.F^T \tag{7.20}$$

where A, F and C are the plant's state coefficient matrices, V is the process noise spectral density matrix, and Z is the measurement noise spectral density matrix. For the existence of a unique solution to equation 7.20, the plant with coefficient matrices A and C must be observable, V must be a positive semi-definite matrix, and Z must be a positive definite matrix (Tewari, 2002). The observability test is performed using the *rank* and *obsv* commands in MATLAB CST. The Kalman filter gain matrix is then calculated as follows:

$$L = R_e.C^T.Z^{-1} \tag{7.21}$$

7.3.3 Optimal Linear Quadratic Gaussian (LQG) Compensator Design

Having used the *principle of separation* to design the optimal tracking controller and the Kalman filter, the two are combined to form an optimal compensator for the plant. The final state-space realisation of the optimal compensator for tracking a reference signal in a noisy plant with the state-space representation of equations 7.18 is given by the following state and output equations:

$$x_e(k+1) = (A - BK_x - LC + LK_x)x_e(k) + Ly(k) \qquad (7.22a)$$

$$u(k) = -K_x x_e(k) - K_i i(k) + K_r r(k) \qquad (7.22b)$$

The schematic overview of the optimal LQG compensator is shown in Figure 7.4.

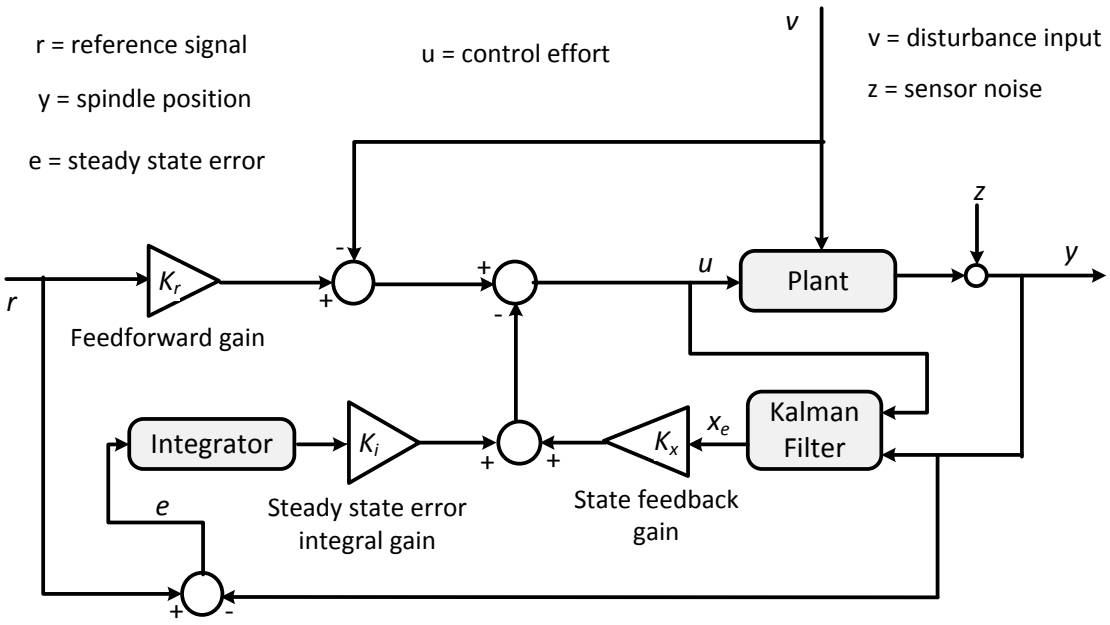


Figure 7.4 Structure of the LQG tracking controller with integral action

The control strategy allows trade-off between tracking performance and control effort, and also takes into account process disturbances and measurement noise. Generally, the optimal tracking controller and the Kalman filter can be selected to have desirable properties that are independent of one another because they are designed separately. The feedforward gain, K_r, the controller weighting matrices, Q and R, and the Kalman filter's spectral noise densities, V and Z, are the tuneable design parameters for the LQG tracking compensator. Hence, the desired closed-loop system's performance is obtained by suitably selecting the values of K_r, Q, R, V and Z.

It is not known apriori what values of Q and R will produce the desired closed-loop response. Therefore, some trial and error are required in selecting the appropriate values. The ratio between Q and R is the most important and not their actual values. If Q is greater than R, it means that it is more important to track the cutterhead reference signal than to minimise the amount of control input generated by the actuators, and vice-versa. As the value of Q is increased relative to R, the closed-loop poles (eigenvalues) are pushed deeper into the left-half plane, which is desired for the asymptotic stability of the tracking error dynamics. However, the limiting factor is that the physical actuating system must be able to generate the increasing amount of control effort. The locations of the closed-loop poles determine the performance of the tracking system, such as the rise time, maximum overshoot and the settling time.

The existence of a unique solution to the Riccati equation is only guaranteed if Q and R are positive semi-definite and positive definite respectively, and the plant is controllable. If the plant is not controllable, the control input generated using Equation 7.16 will not affect all the state variables of the plant. The controllability test is performed using the *rank* and *ctrb* functions in MATLAB Control System Toolbox (CST). In order to guarantee that Q and R are both positive definite, they are chosen to be of the forms, $Q = \alpha I_1 \; and \; R = \beta I_2$. I_1 and I_2 are identity matrices of size 5-by-5 and 1-by-1 respectively. It should be remembered that the identified state-space model of the plant is of the 4^{th} order and the integral of the tracking error is used as an additional state variable. That is why the size of I_1 is 5-by-5. The size of I_2 is 1-by-1 because the plant has a single input. The tuneable parameters then become the scaling values α and β for Q and R respectively. The optimal

state-feedback control law for the reference tracking loop is computed using the *lqi* function available in MATLAB CST.

In order to achieve the same performance in the compensated system as the corresponding full-state feedback system, the Kalman filter tuning parameters (*V* and *Z*) must be properly selected such that its eigenvalues do not dominate the closed-loop system (Tewari, 2002). As there is no control input cost associated with the Kalman filter, its eigenvalues can be pushed deeper into the left-half plane by increasing the value of *V* relative to *Z*. In other words, the dynamics of the Kalman filter can be made faster than that of the tracking controller without causing any problem.

However, it is not always advisable to push the poles too much into the left-half plane because of noise in the sensor measurements. If the sensor is noisy or inaccurate, the output measurement should not be trusted as much; therefore the Kalman filter gain matrix *L* should be low. The closed-loop system will be more sensitive to noise as the poles are moved deeper into the left-half plane. On the other hand, if the process noises are large, then a larger sensor correction is required to account for these disturbances. This is achievable with high values of the optimal Kalman filter gains (Rowley and Batten, 2008).

The noise spectral densities have to be selected such that the Kalman filter yields the best recovery of the full-state feedback dynamics. In order to guarantee that the two spectral densities are positive definite as required, they are chosen to be of the forms $V = \rho F^T F \; and \; Z = \gamma C C^T$ (Tewari, 2002). The scaling parameters ρ and γ are then fine-tuned through trial and error to get the desired response of the Kalman filter. The Kalman filter gain *L* is calculated using the *kalman* command in MATLAB CST.

7.4 Vibration Disturbance Feedforward Compensation

Although the LQG tracking controller designed in section 7.3 uses feedback information to reject process disturbances, it has been said that significant improvements in its performance would be obtained if the vibration disturbance could be suppressed in a feedforward manner before it has the chance to act on the spindle. This requires that the control system be able to gather early information about the vibration disturbance. The approach used to achieve this is explained below.

It has been shown in section 6.2 that there is not much vibration disturbance acting on the spindle. In order to generate greater imbalance forces, a block of mass weighing 116g was attached to the cutterhead at a radius of 35mm from the centre (4060g-mm) as shown in Figure 7.5. The spindle was rotated at the desired speed and its vertical vibration is measured using the eddy current sensors. This was done without any inputs from the piezoelectric actuators so that any displacement away from equilibrium would be due primarily to the mass imbalance or other sources of vibration acting against the stiffness of the piezoelectric actuators and flexural hinges. While sampling the eddy current sensors, the angular position of the spindle is also measured using the rotary encoder mounted on the spindle. This provides information about the position of the resultant mass imbalance.

A sample plot of the spindle vibration against its angular position is shown in Figure 7.6. The signals were acquired for duration of 60sec while rotating the spindle at the speed of 1500rpm. As seen, the additional mass imbalance has resulted into greater vibrations of the spindle compared to the ones given in Table 6.2.

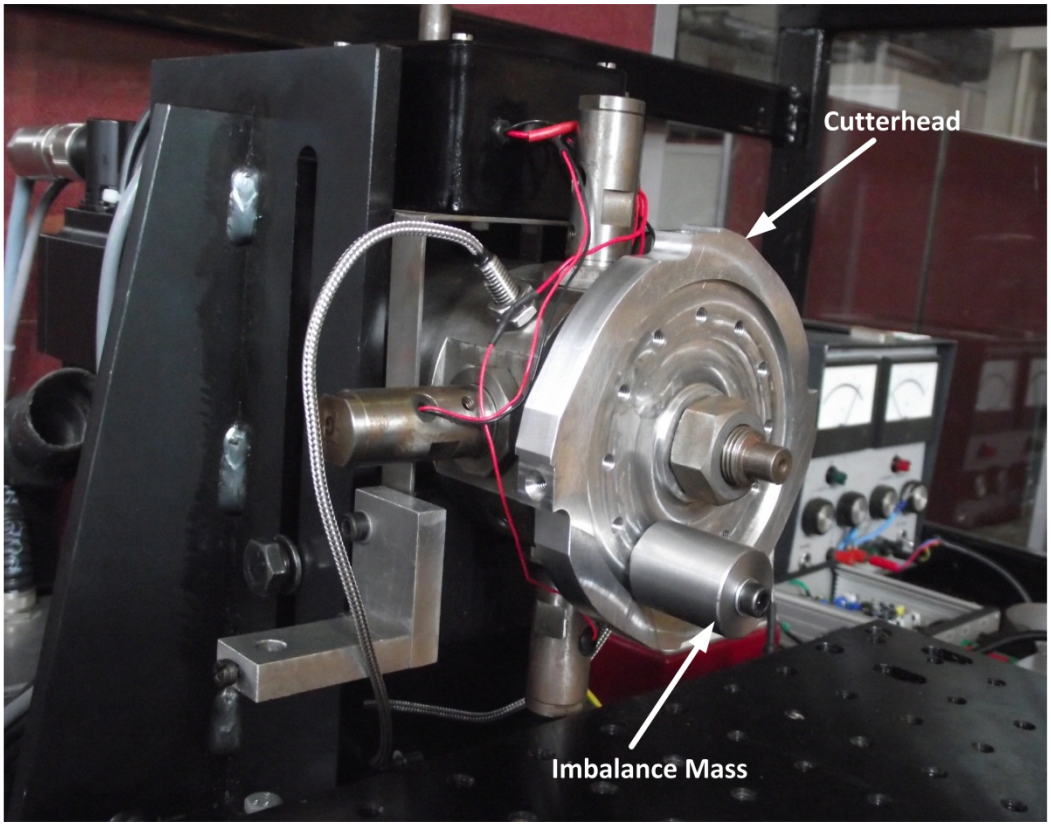


Figure 7.5 Cutterhead and the attached imbalance mass of 116g

In order to be able to generate the vibration signal, the vibration amplitude and the position of the imbalance have to be predetermined. The amplitude of vibration is estimated by computing the average of the positive peaks. The angular position of the spindle at the positive peaks, which is the position of the resultant mass imbalance, is also determined through averaging. For the plot shown in Figure 7.6, the vibration amplitude and the position of the resultant imbalance are approximately 5μm and 1.354 radians respectively. The spindle vibration is re-generated in real-time using the following equation:

$$y(t) = X\cos[\theta(t) - \theta_a] \tag{7.23}$$

where

$y(t)$ is the instantaneous vertical position of the spindle (μm)

X is the predetermined vibration amplitude (μm)

$\theta(t)$ is the instantaneous angular position of the spindle (rad)

θ_a is the predetermined angular position of the resultant imbalance mass (rad)

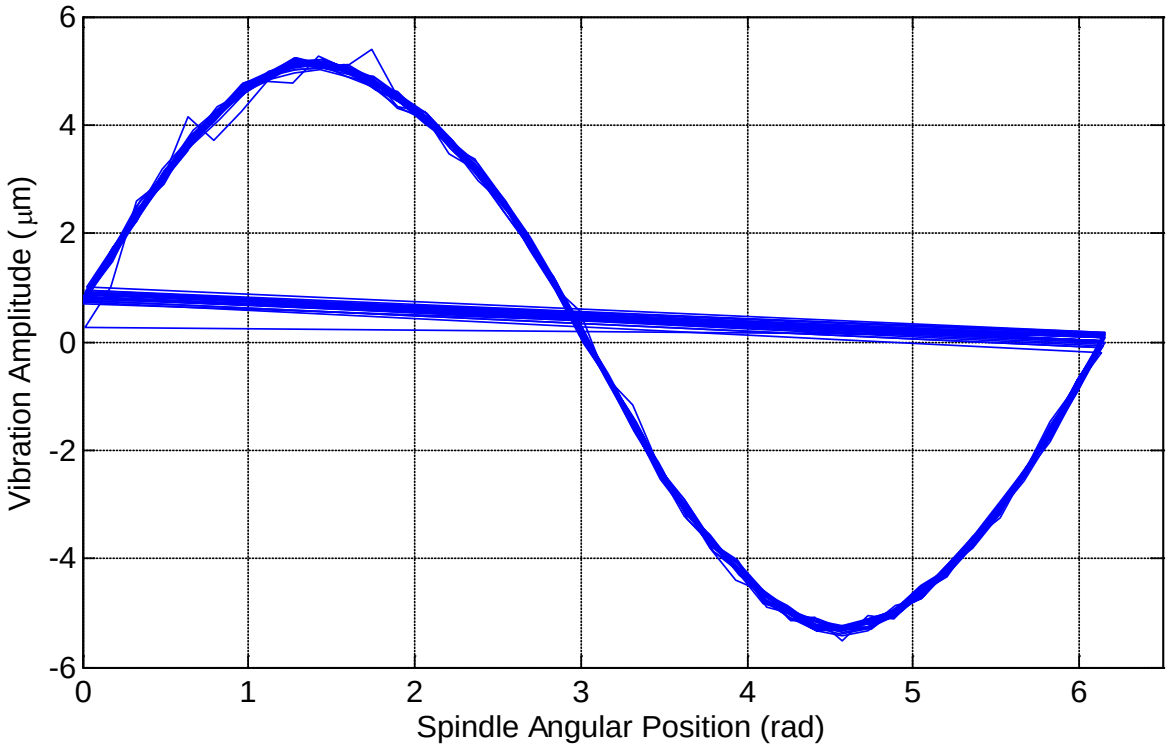


Figure 7.6 Spindle vibrations against angular positions of the spindle

A sample of the real-time spindle vibration and the re-generated vibration signal are shown in Figure 7.7. It should be noted that the vibration amplitude needs to be re-determined each time the cutting speed is changed. The position of the mass imbalance may also need to be re-determined if the cutterhead is removed and then mounted back on the spindle, or if the block of imbalance mass is attached to a different position.

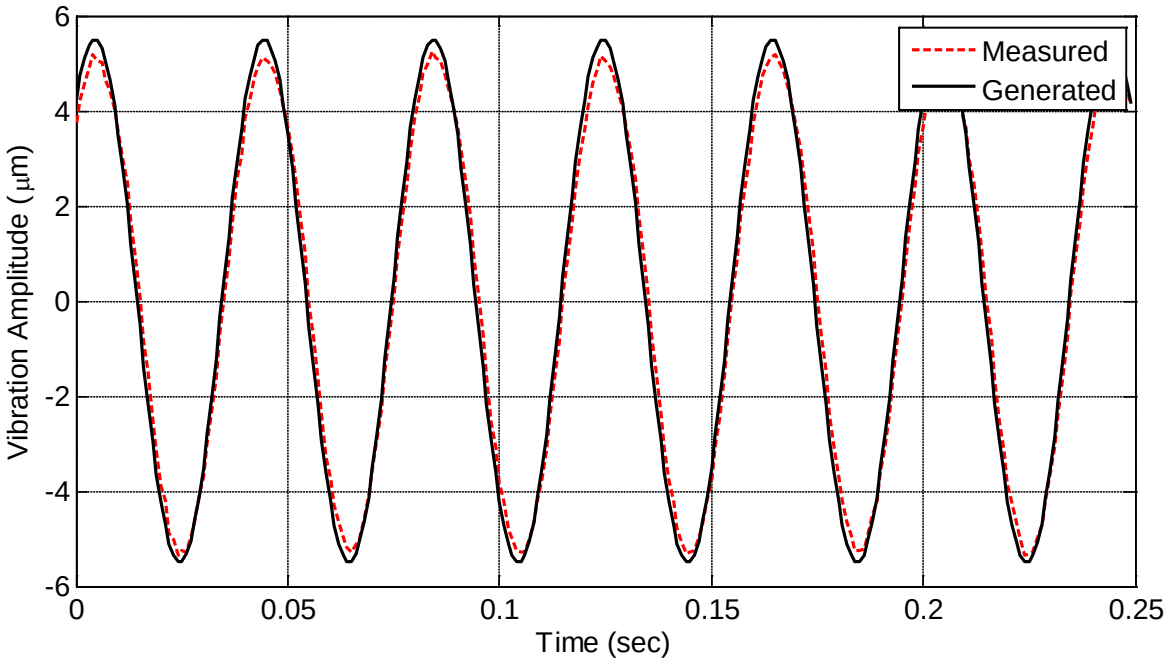


Figure 7.7 Real-time measured and generated spindle vibrations

For the feedforward compensation, the spindle vibration signal needs to be converted to the equivalent piezoelectric actuator voltage. This will usually be achieved by passing the vibration signal through an inverse model of the plant. The position of the spindle is the input to the inverse model and the actuator voltage is the output; so that when a new spindle position is given, it outputs the amount of voltage that would have been required to move the spindle to that position through the actuators.

Two approaches for developing the inverse model of the plant were explored. The first approach is to process the input-output data from the sine-sweep excitation using MATLAB SI toolbox. As opposed to the forward model, the position of the spindle is used as the input signal while the excitation voltage is the output signal. Unfortunately, the model obtained using this method did not represent the inverse behaviour of the plant.

The second method explored is neuro-fuzzy modelling, which has earlier been successfully used to model the hysteresis in shape memory alloy actuators (Razaeeian et al., 2008). The neuro-fuzzy model is able to capture the inverse behaviour of the plant including nonlinearities arising from the piezoelectric actuator hysteresis. The main limitation of the neuro-fuzzy model is its speed of response. It could not cope with spindle speed greater than 1000rpm. For these reasons, the static gain of the piezoelectric actuators is used to calculate the vibration disturbance input. The equation is given as follows:

$$u_d(t) = y(t)/G_s \tag{7.24}$$

$u_d(t)$ is the disturbance input (V)

G_s is the static gain of the piezoelectric actuator ($\mu m/V$)

The static gain is determined from the voltage-displacement characteristics of the spindle as earlier described in section 6.3. The final control law for compensating for the combined effects of cutterhead inaccuracy and vibration is then obtained by extending equation 7.17 as follows:

$$u(t) = -K_x x(t) - K_i i(t) + K_r r(t) - u_d(t) \tag{7.25}$$

The approach cancels out the spindle vibration through the introduction of a signal, which is 180^o out of phase with the process disturbance vibration.

7.5 Simulation and Rapid Control Prototyping

This section presents some simulation results as well as the experimental results obtained from real-time testing of the control system on the actual test rig.

7.5.1 Control System Simulation

The LQG control system was designed in Simulink. The plant model used for the simulation is that of the spindle with a cutterhead of mass 293g attached to it. The model output is made to track a particular reference signal and the simulation results are shown in the following figures. The reference signal is the setpoint that would be tracked by a four-knife cutterhead in order to implement the cutterhead inaccuracy compensation and vibration control strategy. The machining parameters used for the simulation are given in Table 7.1. Although the actual time of engagement of the cutters with the workpiece is very short, the pulse width has been increased to half of the knife-passing period.

Table 7.1 Machining parameters for control system simulation

Parameter	Value	Unit
Cutting speed	600	rpm
Cutter radius	[60, 60.015, 60.004, 60.009]	mm
Knife positions	[0, 90, 180, 270]	degrees

For the tracking responses shown in Figure 7.8 and Figure 7.9, the plant is modelled in such a way that there is no external disturbance acting on it. The only difference is that the steady state error integral gain K_i, has been set to zero for the response obtained in Figure 7.8. As seen in Figure 7.8, there is a small steady state error between the reference signal and the model output. The steady state error has been minimised by adding the integral action as seen in Figure 7.9.

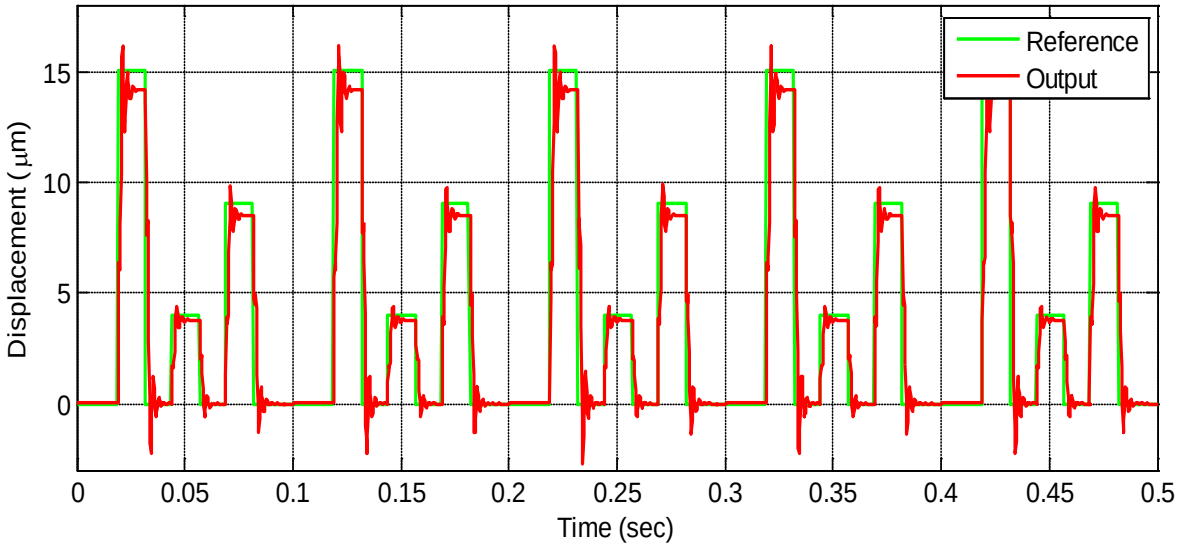


Figure 7.8 Tracking response obtained without integral action

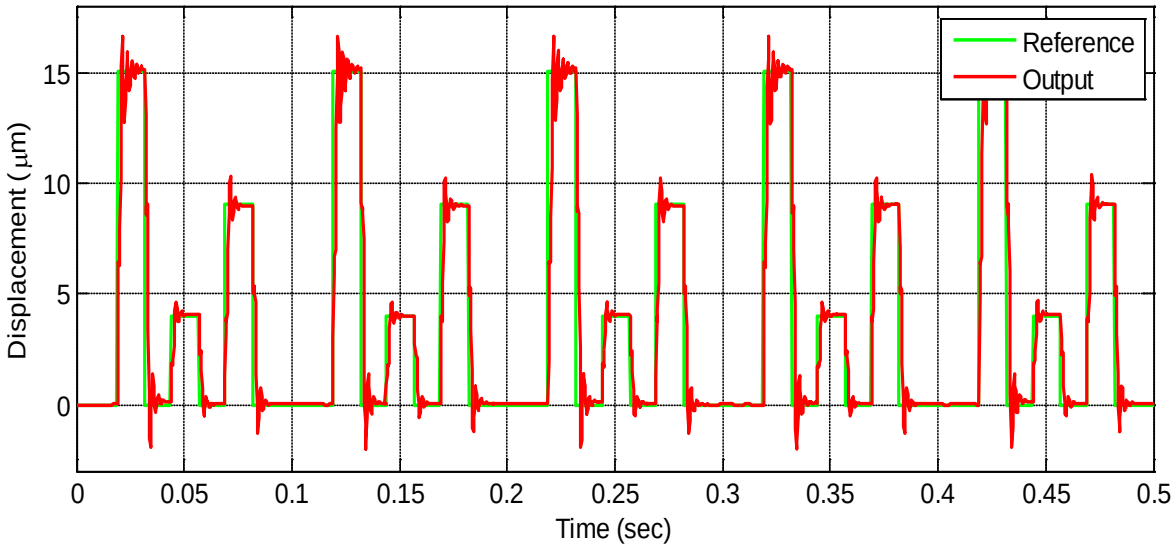


Figure 7.9 Tracking response obtained with integral action

Another thing that can also be seen in the above tracking responses is that there are overshoots and undershoots of up to about 13%. This is just the case of striking a balance between the response time and the overshoots/undershoots. Any attempt to minimise the overshoots/undershoots will result in a slower actuator response. As the cutting speed

increases, the faster the actuator response needs to be. However, this can only be achieved at the expense of the positive and negative overshoots.

For the tracking responses shown in Figure 7.10 and Figure 7.11, the plant is modelled such that there is an external vibration disturbance acting on it. The frequency of the vibration is the same as the cutting speed and its amplitude is 3µm. The vibration is treated as an unknown disturbance for the result obtained in Figure 7.10. That is, the vibration cannot be measured and compensated for in a feedforward manner. A careful observation of the plant output reveals that the controller has used feedback information to reduce the vibration amplitude to about 1µm (66.67%).

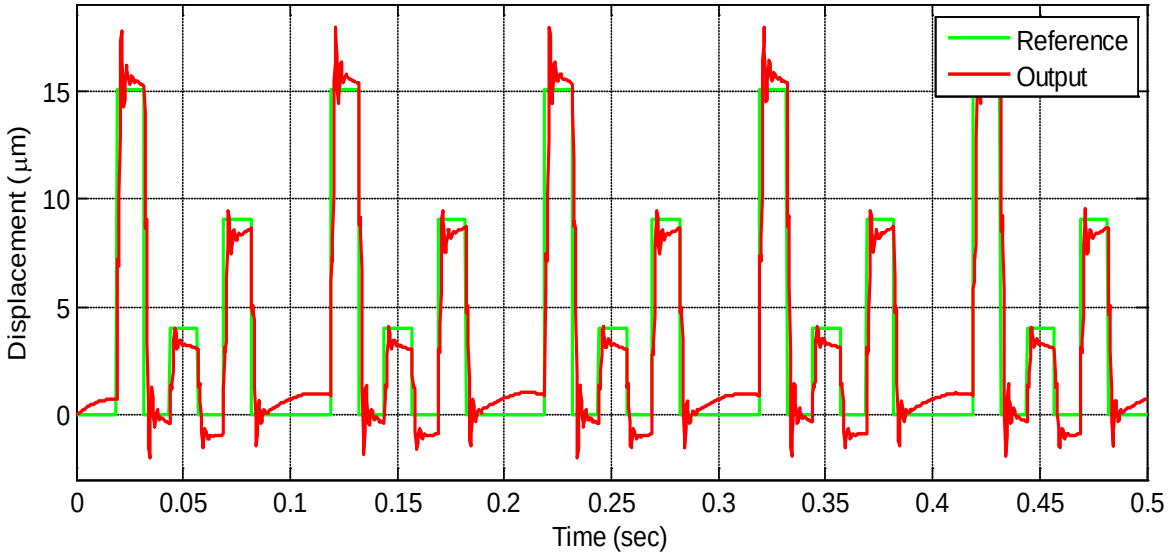


Figure 7.10 Tracking response for the plant with unknown vibration disturbance

As earlier envisaged, better rejection would be achieved if early information about the disturbance can be gathered and compensated for in advance. The vibration is treated as a known disturbance for the response shown in Figure 7.11. The feedforward loop has been able to minimise the vibration further, thereby providing a better tracking performance.

The performance increase provided by the feedforward loop will depend on how accurately the vibration disturbance can be predetermined.

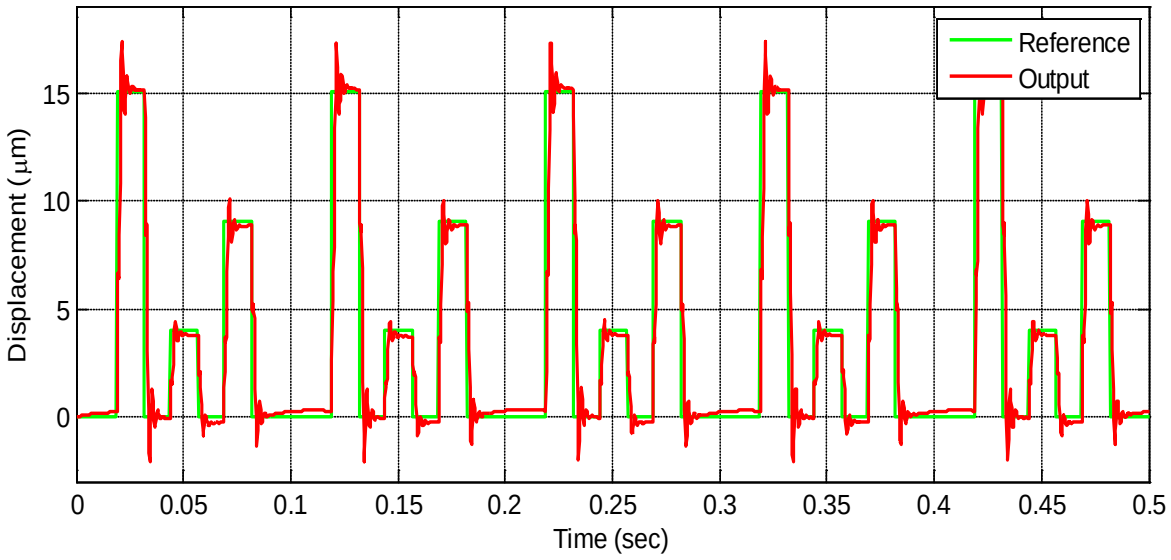


Figure 7.11 Tracking response for the plant with feedforward vibration compensation

7.5.2 Real-Time Testing Environment

A real-time rapid prototyping environment from MathWorks known as xPC Target is used to control the wood planing machine. The xPC Target enables direct execution of Simulink and Stateflow models on a control computer for real-time testing. After creating and testing the controller models in Simulink, Real-Time Workshop is used to compile the Simulink models to xPC Target kernel applications.

The xPC Target control machine is equipped with a data acquisition board (Humusoft MF614) through which it takes spindle orbit and angle of rotation data from the planing machine, and also applies control signals to the actuators. The xPC Target also provides an interface for real-time signal monitoring, parameter tuning and data logging from the control machine into the development machine. The control and development machines,

which have been assigned static IP addresses, communicate via the TCP/IP protocol. The real-time testing environment is shown in Figure 7.12.

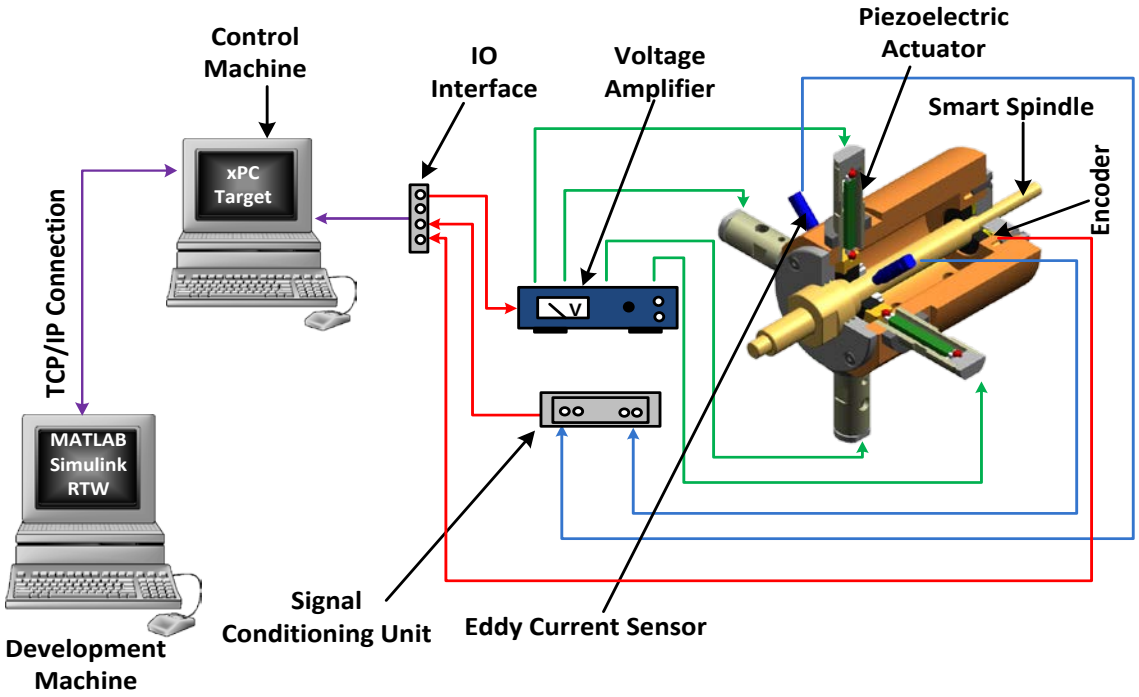


Figure 7.12 Schematic of the active wood machining control environment

7.5.3 Real-Time Controller Performance Test

The controller is tested in real-time by replacing the plant model in the Simulink application with the actual plant. The eddy current sensors provide the spindle position feedback and the control effort generated by the controller is used to drive the piezoelectric actuators through the voltage amplifiers. The reference signal is generated using Stateflow based on the real-time measurement of the angular position of the spindle position through the rotary encoder.

The encoder generates 2000 counts per revolution and an index pulse once every revolution. The index signal is generated by a special track which produces a pulse at a specific position on the spindle. Although the rotary encoder gives relative positions, the index pulse is used to establish a zero reference position for the spindle. Every time the controller operation is initialised, the spindle will need to be rotated by a revolution (at most) before the encoder can establish its absolute position.

The vertical position of the spindle is made to track some arbitrary reference signals. The first one is for a two-knife cutterhead rotating at the speed of 2000rpm. The angular positions of the first and second knife are 55 and 1055 encoder counts respectively. One knife is displaced upward by 18μm (Piezoelectric Actuator D) and the other is displaced downward by the same 18μm (Piezoelectric Actuator B). The pulse width is increased to the knife-passing period (15ms). The purpose of tracking this signal is to assess the performance of the controller when the system is operating under the condition that is well within the response capabilities of the actuators.

The response of the spindle to the reference signal is shown in Figure 7.13. The two signals are compared by computing their correlation coefficient using equation 4.13. There is 98.8% correlation between the reference signal and the spindle response. The good tracking response is an indication of two things. Firstly, it shows that the designed LQG controller with integral action performs very well for the setpoint tracking. Also, it indicates that the mathematical model obtained through the system identification is able to capture the important dynamics of the actual test rig. The state-space matrices were used to compute the controller and observer gains during the optimal control design. Therefore,

large mismatch between the derived plant model and the actual behaviour of the plant would have resulted into poor tracking responses.

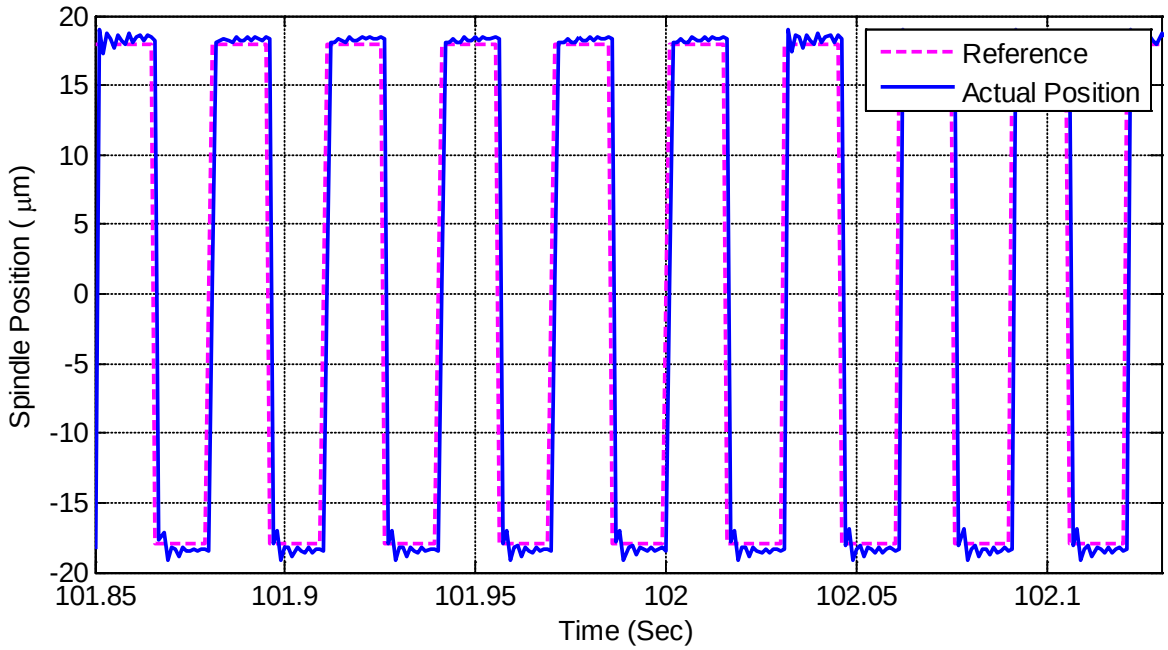


Figure 7.13 Tracking response of the spindle (2-knife cutterhead rotating at 2000rpm)

The second reference signal tracked by the spindle is the one that would be used to compensate for the inaccuracy in a four-knife cutterhead rotating at the speed of 1000rpm. The pulse width is half of the knife-passing period (7.5ms). The magnitudes of the pulses are 12µm, 8µm, 16µm and 0µm. The response of the spindle to this signal is shown in Figure 7.14. There is 96.8% correlation between the two signals.

The third reference signal is for the same four-knife cutterhead but the rotating speed has been increased to 3000rpm. The pulse width is the knife-passing period (5ms). The magnitudes of the pulses are 5µm, -10µm, 0µm and -7µm. The response of the spindle to this signal is shown in Figure 7.15 and their correlation is 94.8%.

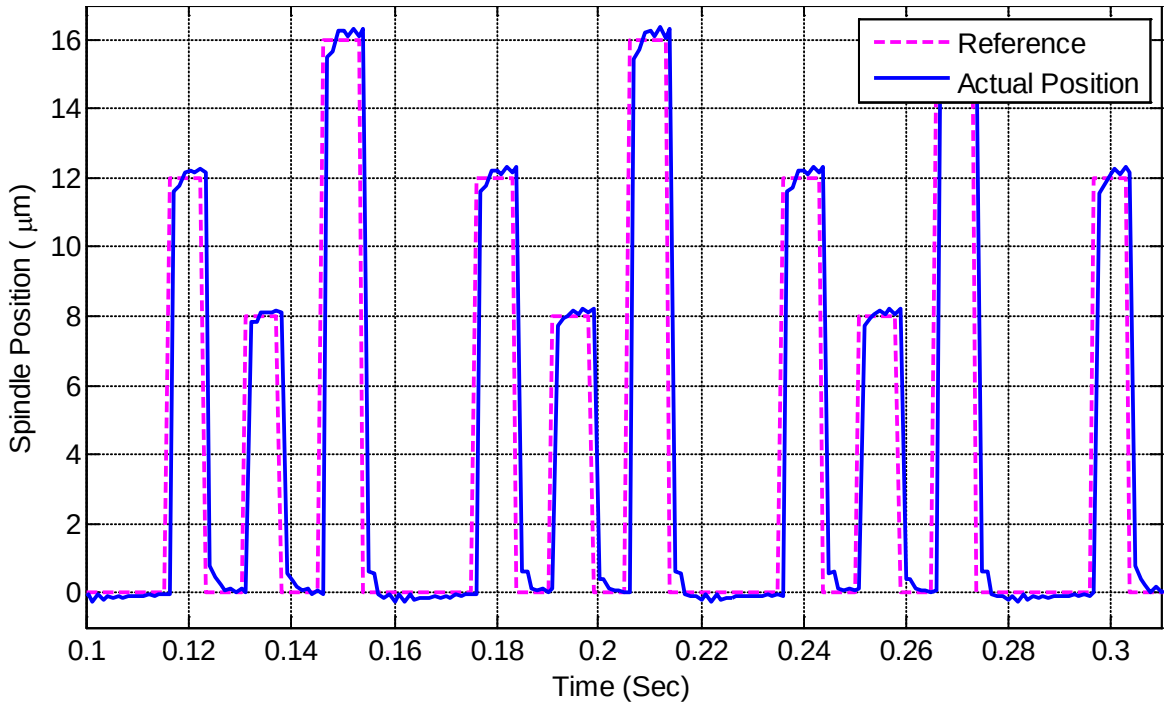


Figure 7.14 Tracking response of the spindle (4-knife cutterhead rotating at 1000rpm)

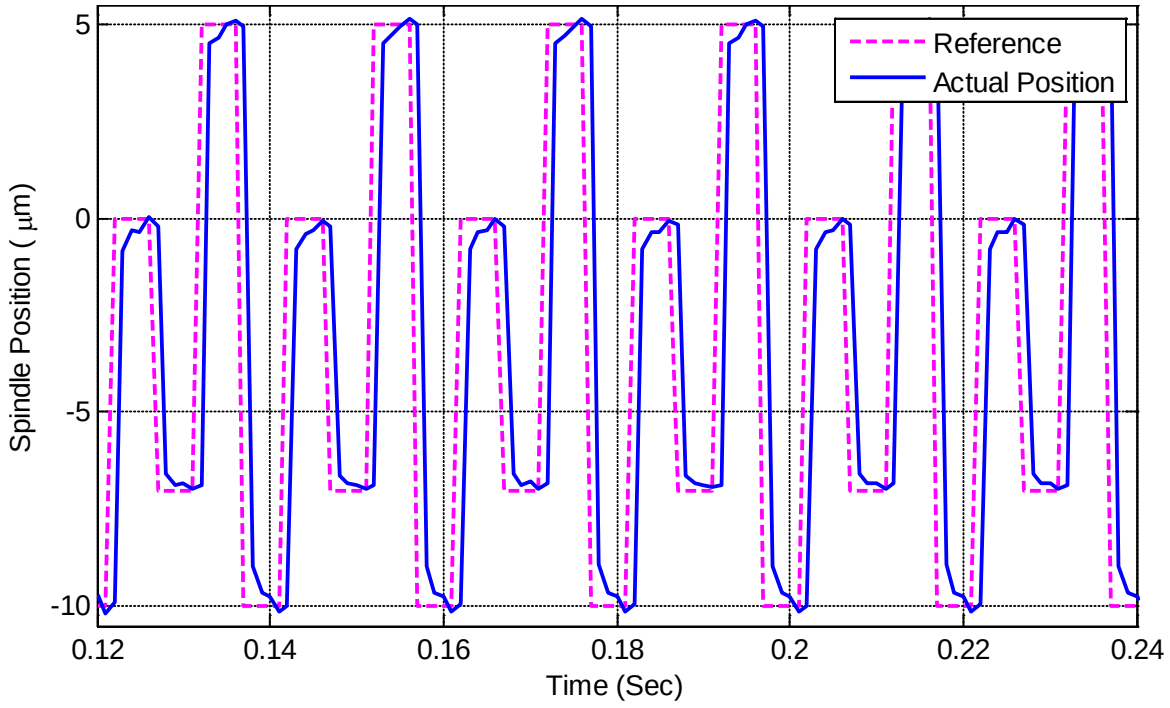


Figure 7.15 Tracking response of the spindle (4-knife cutterhead rotating at 3000rpm)

It should be mentioned that the above plots have taken into account the 2ms lag in the system. The tracking performance of the control system decreases slightly as the pulse width decreases as indicated by the correlation coefficients. This is because the time available for the actuators to respond is shorter. The use of the latest piezoelectric actuators, which have response time far below 1ms, could improve the performance of the system. The performance could also be improved by increasing the controller gains. As far as the cutterhead inaccuracy compensation is concerned, the main requirement is for the spindle to have been displaced by the desired magnitude before the cutting knives reach the region where they produce visible cuttermarks on the workpiece. This requirement is the criterion used to measure the performance of the controller in chapter eight.

The tracking responses presented so far were obtained without the additional imbalance mass attached to the cutterhead. Therefore, there were no significant vibration disturbances acting on the spindle. The only way to assess the performance of the control system in terms of vibration rejection is to introduce external disturbances on the spindle. This is achieved by attaching the imbalance mass to the cutterhead (Figure 7.5). It is worth mentioning that a shaker excitation could also be used to introduce disturbances at desired frequencies, which could be different from the frequency of the spindle rotation. The only drawback is that it will be difficult to use a shaker when the spindle is rotating.

The cutterhead (with the attached imbalance mass) was rotated at the speed of 1500rpm while its vertical position was made to track a zero reference signal (i.e. no cutterhead inaccuracy). The uncontrolled spindle response and the one controlled using the feedback control scheme are shown in Figure 7.16. The response obtained using the combination of the feedforward and the feedback control loop is also shown in Figure 7.17.

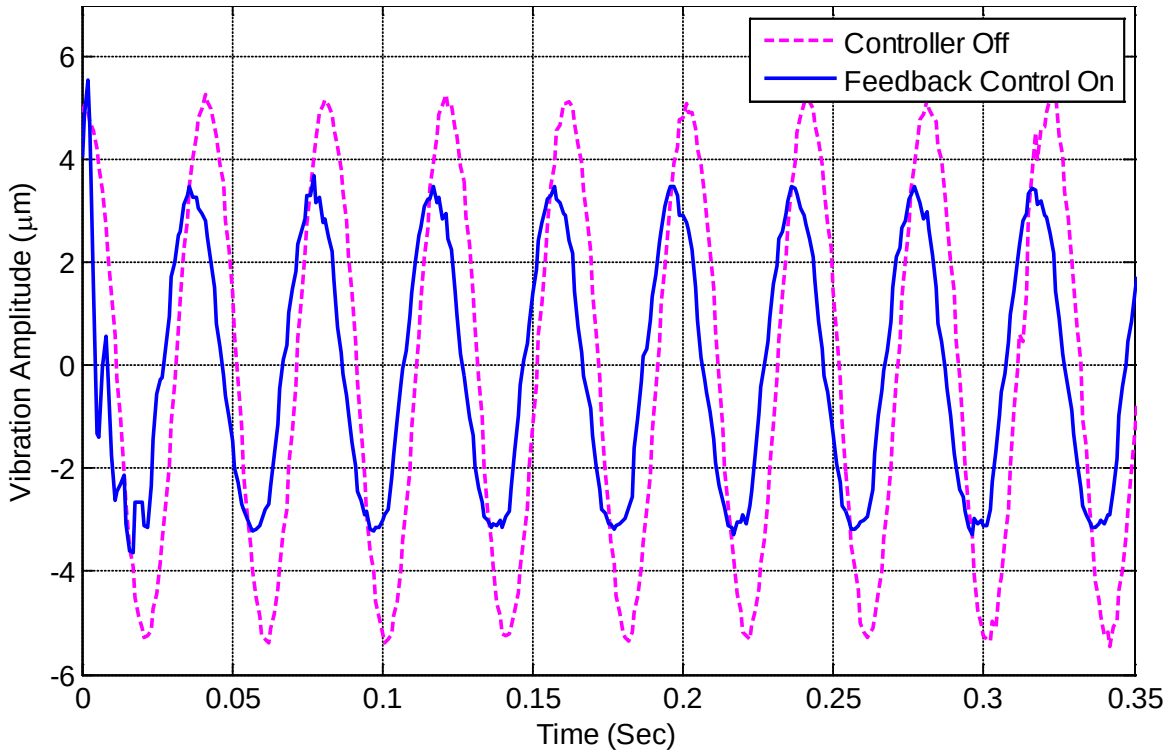


Figure 7.16 Comparison between uncontrolled and feedback-controlled vibration

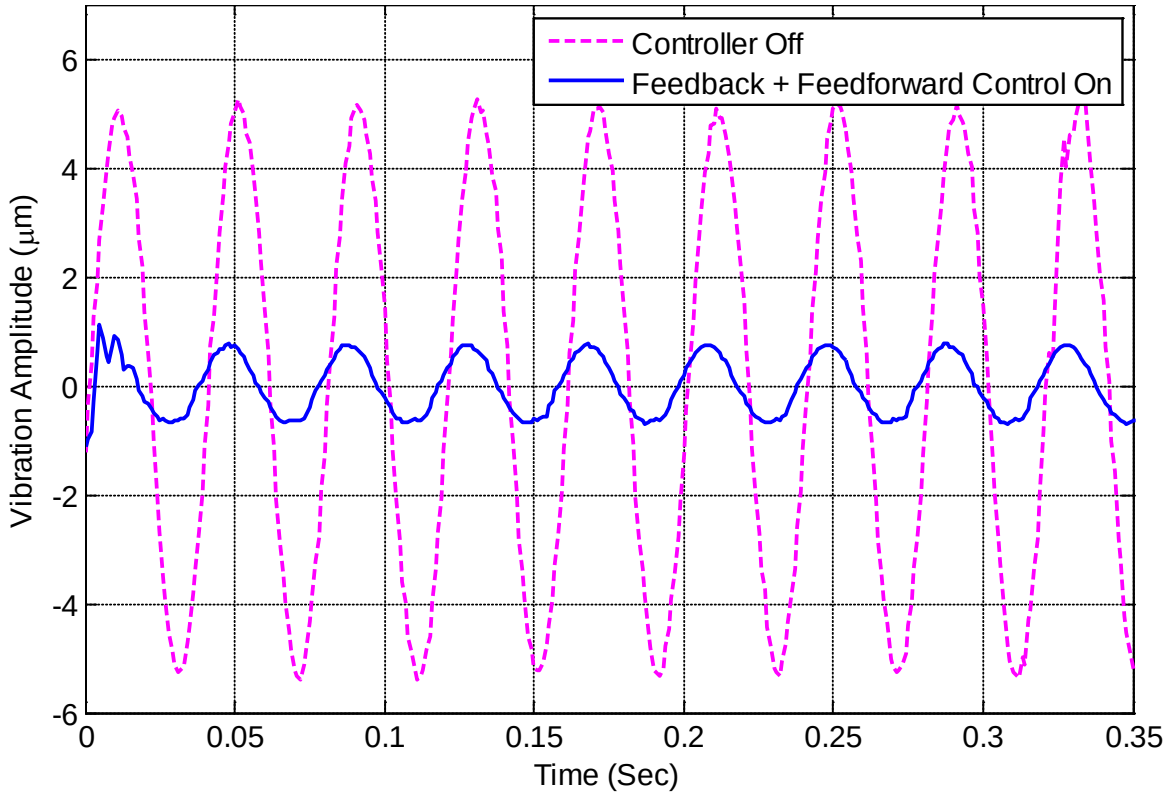


Figure 7.17 Comparison between uncontrolled and hybrid-controlled vibration

As seen in the above figures, the combined feedforward and feedback control scheme performs a lot better than the feedback-only control. The feedback-only controller minimises the vibration amplitude of the spindle from approximately 5µm to 3.5µm, which is about 30% reduction. In the case of the combined feedforward and feedback control, the vibration is further reduced by additional 52%, minimising the amplitude from 5µm to approximately 0.9µm (82%).

State-feedback optimal controllers generally have excellent robustness properties, including unknown disturbance rejection (Tewari, 2002). However, a Kalman filter has been included in the feedback loop because the state variables of the test rig could not be measured. The Kalman filter uses measurements of the plant's inputs and outputs, alongside its dynamic model, to estimate the state variables. This has drastically reduced the performance and robustness properties of the overall state feedback control because the vibration disturbance input is unknown to the Kalman filter. Although a technique known as loop transfer recovery could be used to recover some of the robustness of the full-state feedback (Tewari, 2002), it is only if the disturbances are known and rejected in advance that the divergence of the state estimation can be minimised.

Elmas (2008) reported that the LQG regulator provided good damping and stiffness properties (ca. 68% reduction) when the spindle was excited by an impulsive force through the piezoelectric actuators. Such high performance was obtained because the disturbance input that set the spindle on free vibration was known to the Kalman filter. If the excitation was from an external source (as it would be in practice) such as mass imbalance or cutting forces, then the observer would at least need to be augmented with the dynamic model of the disturbance in order to obtain any significant control performance.

Theoretically, the combined feedforward and LQG feedback control loop should be able to eliminate the vibration completely. However, this may not be achievable because of potential errors in the determination of the angular position of the resultant imbalance mass, and the system lag. Also, the dynamic gain of the piezoelectric actuators might be different from the static value used to convert the vibration signal to voltage.

The objective of the control system is to simultaneously compensate for cutting tool inaccuracy and also minimise the effect of vibration. In order to investigate this, the cutterhead (with the attached imbalance mass) was made to track a reference signal, which could be used to compensate for inaccuracy in a four-knife cutterhead having two proud knives. The spindle was rotated at the speed of 1000rpm and the imbalance produced a forced vibration of about 2.3µm without the vibration compensation. This superimposed vibration signal can easily be seen in Figure 7.18.

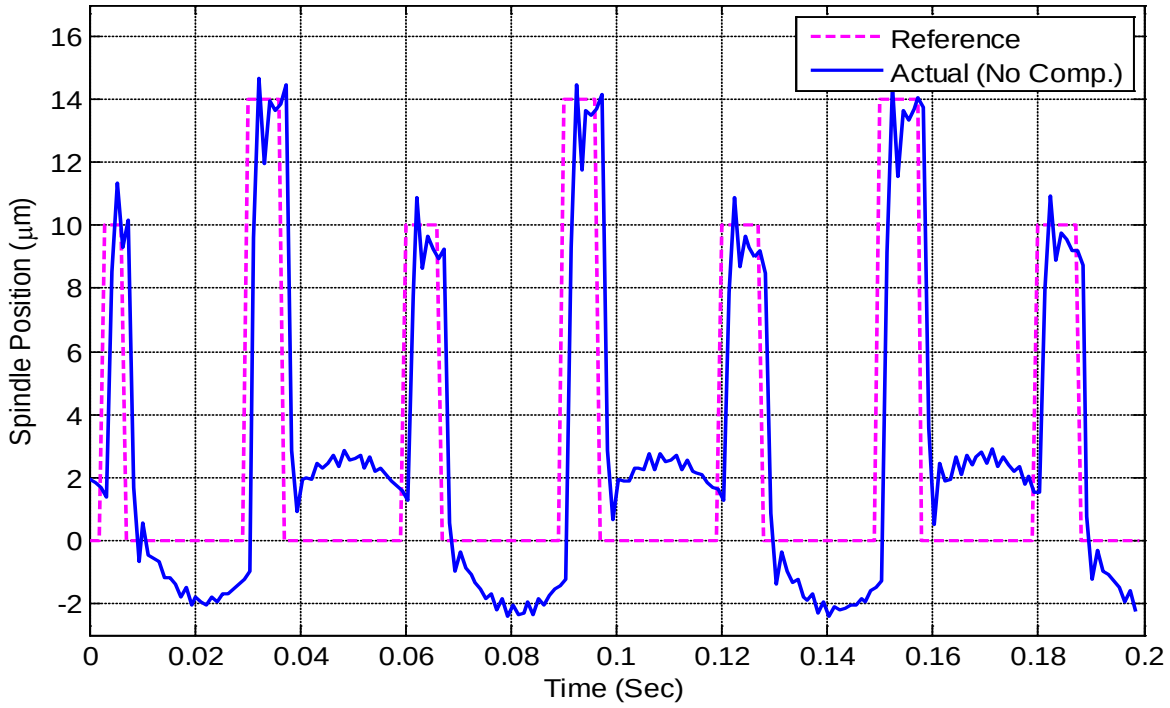


Figure 7.18 Tracking response obtained without vibration compensation

The hybrid vibration compensation was then activated and the result can be clearly seen in Figure 7.19. The vibration amplitude has been reduced to less than 1µm. Although the vibration could not be removed completely, a vibration amplitude of less than 1µm will not cause significant waviness defects.

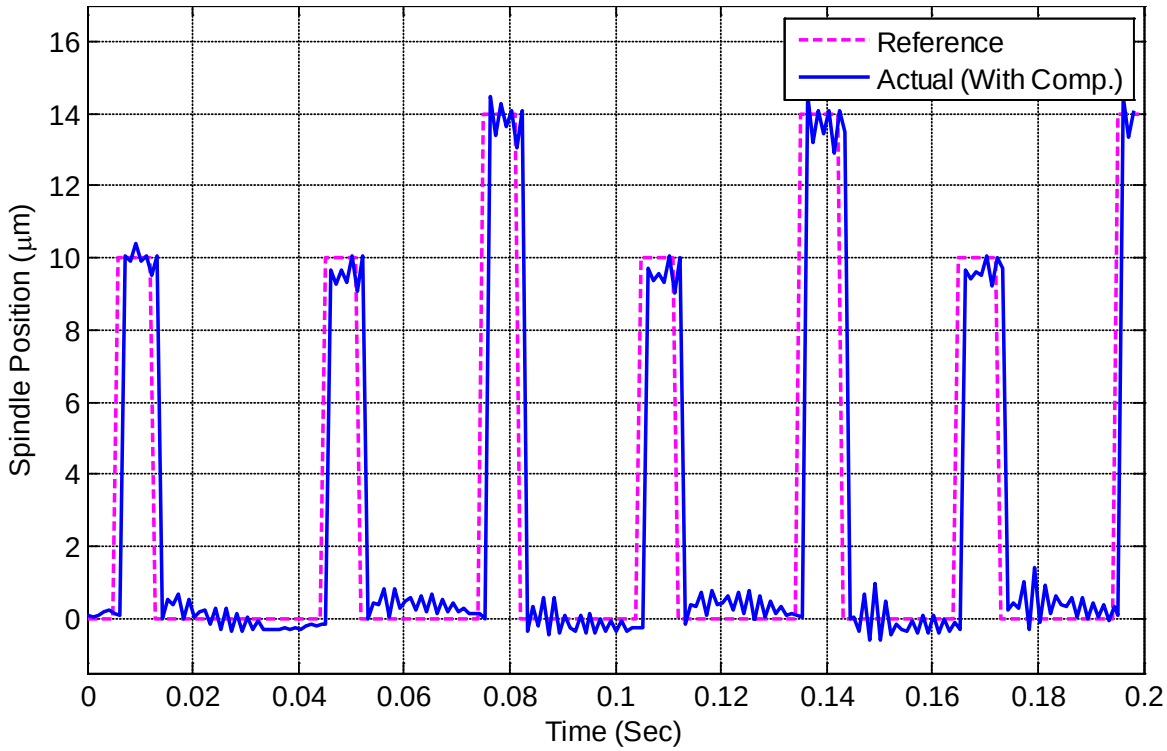


Figure 7.19 Tracking response obtained with hybrid vibration compensation

7.6 Knowledge-Based Adaptive Control Strategy

The optimal tracking controller has five tuning parameters. The parameters are the feedforward gain, K_r, the controller weighting matrices, Q and R, and the Kalman filter's spectral noise densities, V and Z. The tuning of the Kalman filter spectral noise densities is actually based on the sensor and process noises acting on the plant and not the internal dynamics of the plant. Once the appropriate Kalman filter parameters have been selected, it is not necessary to tune them as the process dynamics change. The parameters only affect the accuracy of the state variables estimation and do not have any direct effect on the

performance characteristics of the controller. Therefore, only the feedforward gain and the controller weighing matrices need to be adjusted during adaptive operation of the plant.

The ratio between Q and R is the most important parameter and not their actual values. This implies that one of them could be held constant while the other one is being adjusted. Only the Q matrix is tuned here for simplicity, leaving R to be constant. There are 25 elements in the Q matrix and this makes its full optimisation to be computationally intensive. Moreover, the requirement that matrix Q must be positive semi-definite puts significant constraints on its elements. As found in Tewari (2002), choosing the matrix to be of the form $Q = \alpha I$ will guarantee its semi-definiteness (where I is identity matrix). Consequently, only the feedforward gain K_r, and the scaling value α, are adjusted to cope with changes in the process dynamics and the machining parameters.

Typically, most adaptive control schemes involve recursive plant identification and controller parameter tuning while the system is in operation. This is the case with the MIAC schemes introduced in chapter two. For the wood planing machine, it could be rightly assumed that its dynamic parameters do not change significantly during the machining process. Although work done by Tseng et al. (2002) reveals that temperature variation can affect the internal dynamics of a spindle system, the effect is minimal. Therefore, an adaptive technique that does not require recursive system identification is proposed. The proposed technique can be taken to be a combination of the model identification adaptive control and the gain scheduling adaptive control.

In this approach, automatic system identification and controller optimisation are performed when requested by an operator. The identification is then switched off once the controller has been adjusted and it is then assumed that the parameters of the system remain fixed for all time throughout the following cutting operations. Hence, the system is controlled by fixed controller gains until a re-identification is specifically requested. The identification operation might also be performed automatically each time the machine is started. This approach allows focus to be placed on the actual tracking of the cutterhead pulse even at high cutting speed. Fully adaptive control schemes have further requirements in terms of data processing speed because of the frequent online identification. The design of the adaptive controller gain tuning system is reported in Chamberlain (2012).

The other aspect of the project investigated by Chamberlain (2012) is the development of a technique that can be used to provide a secondary control loop control for the machining process through real-time surface profile measurements. The reference position to be tracked by the spindle is generated based on the static run outs of the cutters. However, combinations of errors in the static run out measurements and the effect of structural dynamics (imbalance) might cause the dynamic run outs to be different from the statically determined values. The only way to detect such differences is by measuring and analysing the actual surface waviness produced by the machining operation. Necessary adjustments could then be made to the reference signal dynamically in order to produce consistently high quality surface finish. A new machine vision system, which works on the dynamic PS technique, has been designed and integrated with the wood planing machine. The overall test rig setup for the integrated wood machining system is shown in Figure 7.20.

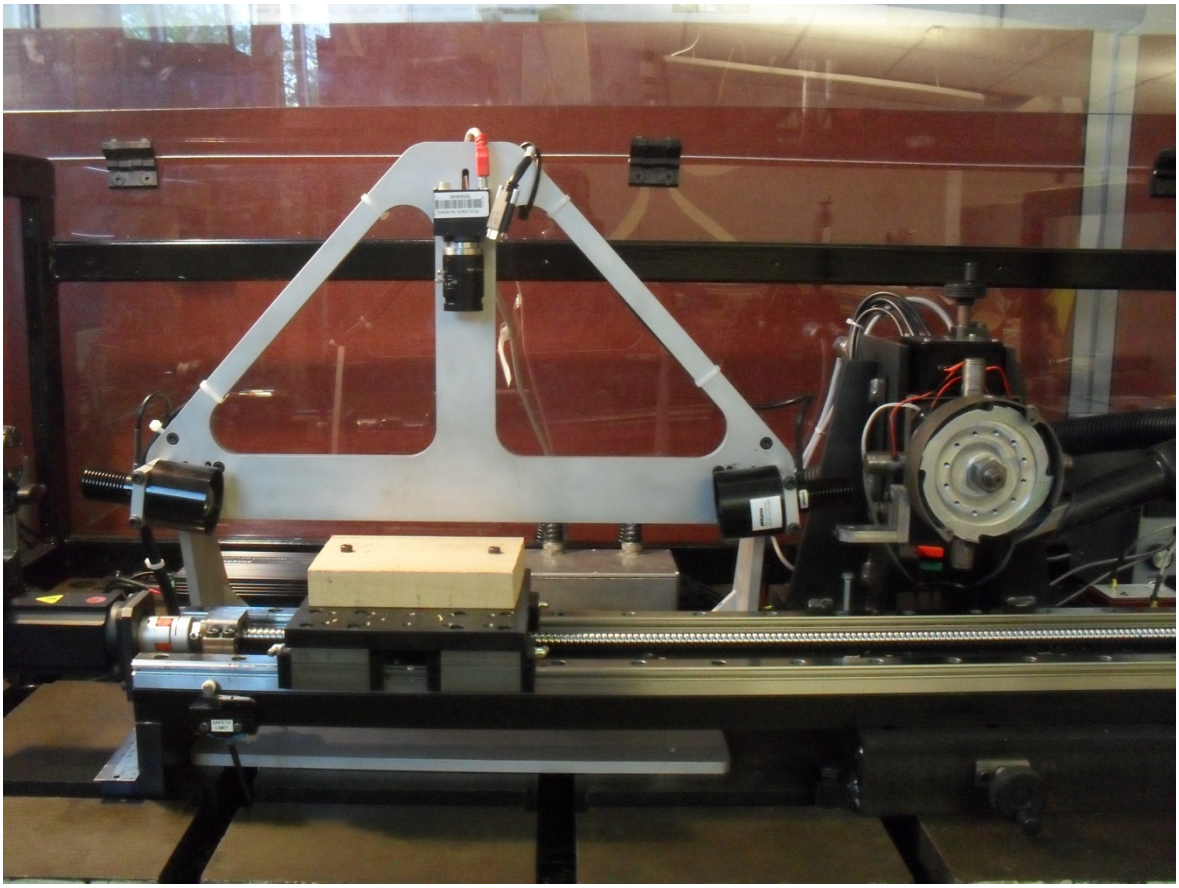


Figure 7.20 The integrated active wood machining system

Some of the problems mentioned in chapter four regarding belt slippage and jerky movements do no longer apply because the wood sample is mounted on the feed table, which is being moved by a ball screw. The collimated LEDs have also been changed to blue because blue light has a shorter wavelength than red. The camera resolution is 1294x964 pixels and it is connected to the PC through 1394b FireWire Interface. More details of the machine vision components can be found in Appendix E.

7.7 Summary and Conclusions

This chapter is focused on the design of an adaptive control system that is capable of compensating for the effect of cutterhead inaccuracy and spindle vibrations during the rotary wood planing process. The performance of the control system has been tested on the wood planing rig. The simulation and experimental results show that the combined LQG tracking controller and the feedforward vibration compensation are very effective in minimising the effects of both the spindle vibration and proud knives. The feedforward compensation should potentially cancel out the spindle vibration completely. However, this could not be achieved in practice possibly due to system lag.

If the effects of other factors that could affect the surface quality of the machined workpiece (timber material properties, cutter geometry) are neglected, then it could be concluded that the enhanced dynamic performance of the spindle would automatically lead to improved surface quality. Some woodcutting experiments have been performed in order to evaluate the influence of the high performance active machining on the resultant surface finish. The results of these experiments are presented in chapter eight.

8 Experimental Results and Discussions

This chapter presents the results of more detailed engineering tests performed on the planer rig in order to determine its closed-loop performance limits. Also, the overall aim of this research is to develop an integrated system that will aid automated production of higher quality wood surface finish. Therefore, machining experiments have been performed in order to investigate the effect of the developed compensatory approaches on the resultant surface finish. The results of these cutting experiments are also presented and discussed.

8.1 Planer Rig Closed-loop Performance Tests – Engineering Tests

The tests performed in order to determine the limit of the dynamic performance of the planer rig were in three stages. Firstly, the cutterhead was rotated at different speeds without any imbalance mass and the spindle was made to track an arbitrary reference signal. For practical reasons, trapezoidal pulse (Figure 8.1) trains were used instead of the rectangular pulses used in chapter seven. The specifications of the pulse trains are given in Table 8.1. The pulse trains are the ones that would be required to compensate for inaccuracy in a four-knife cutterhead having three proud knives with static run-outs of 6µm, 8µm and 5µm respectively. The comparisons between the reference signal and the spindle output are shown in Figure 8.2 to Figure 8.5. The knife-passing period is calculated from the following equation:

$$KP_{period} = \frac{1}{N.\omega} \tag{8.1}$$

where N is the number of cutting knives and ω (*rev/s*) is the cutting speed.

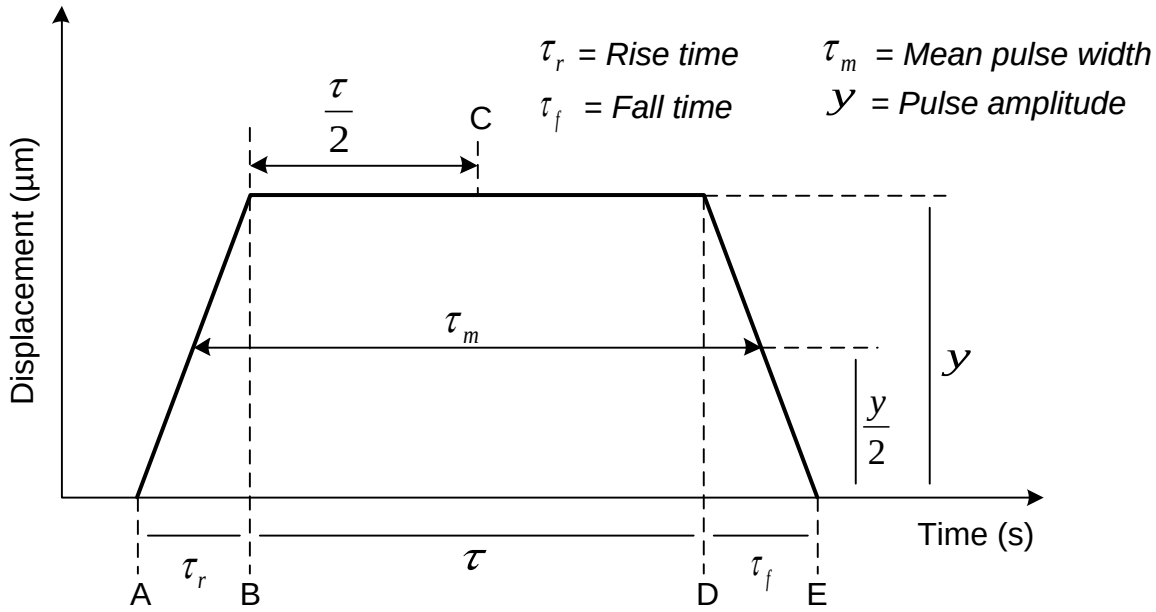


Figure 8.1 Trapezoidal pulse

Table 8.1 Reference spindle position specifications

Cutterhead Speed (rpm)	Knife-Passing Period (s)	Rise Time (s)	Fall Time (s)	Mean Pulse Width (s)	Pulse Amplitudes (µm)			
					1	2	3	4
2000	0.0075	0.001	0.001	0.004	6	8	5	0
3000	0.005	0.001	0.001	0.003	6	8	5	0
4000	0.00375	0.001	0.001	0.002	6	8	5	0
5000	0.003	0.001	0.001	0.002	6	8	5	0

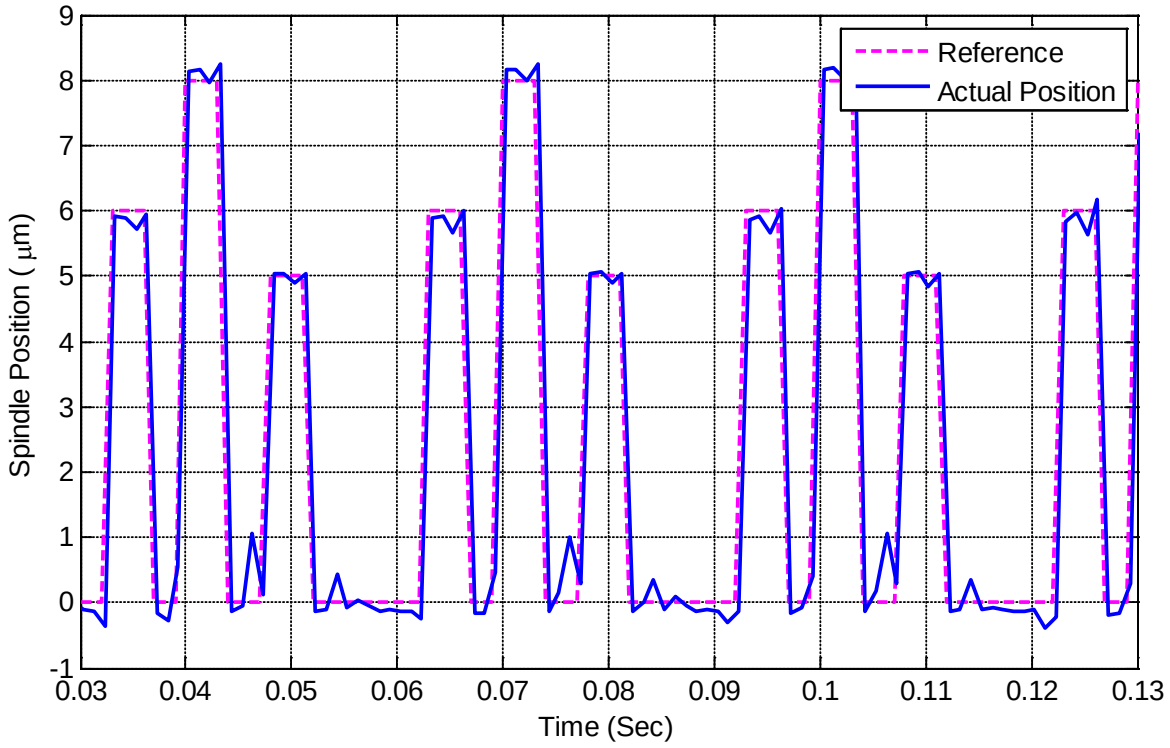


Figure 8.2 Tracking response of the spindle rotating at 2000rpm

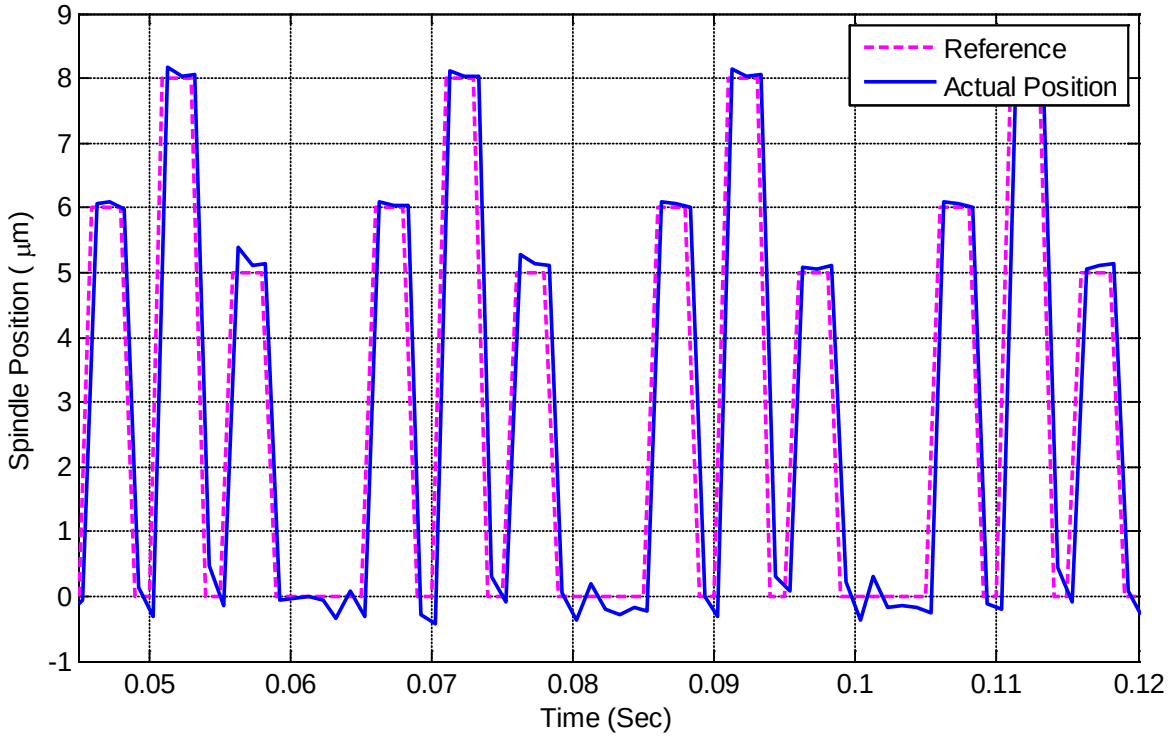


Figure 8.3 Tracking response of the spindle rotating at 3000rpm

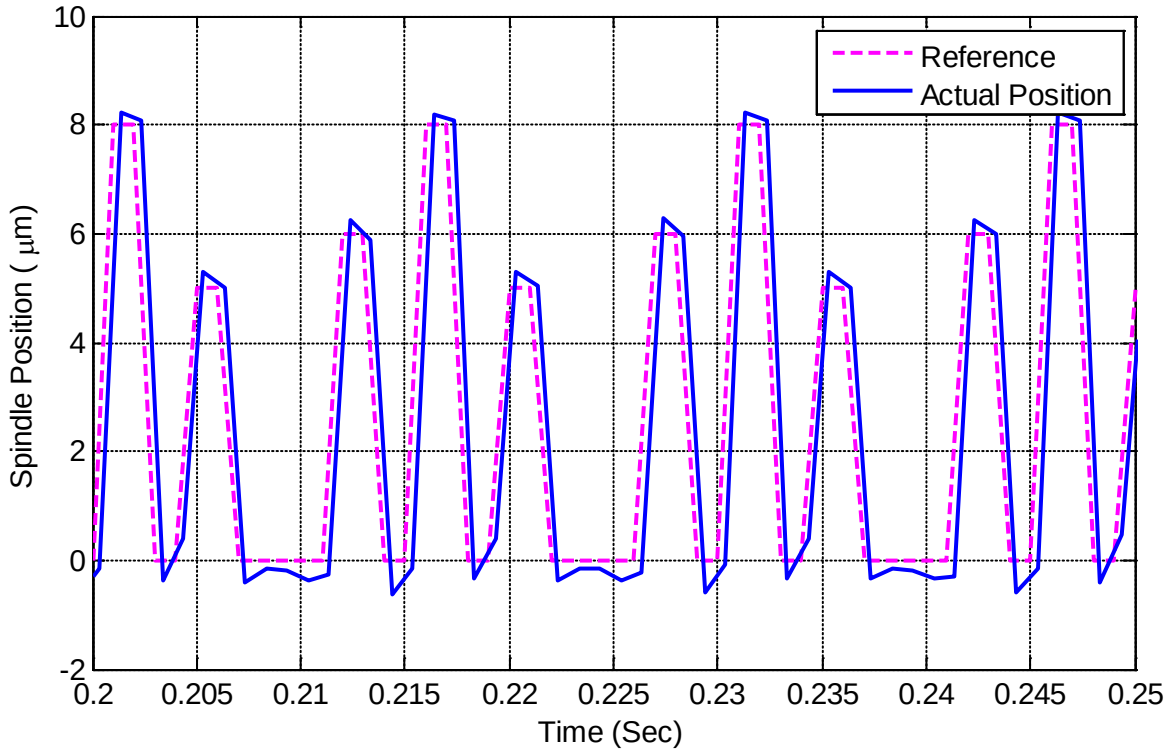


Figure 8.4 Tracking response of the spindle rotating at 4000rpm

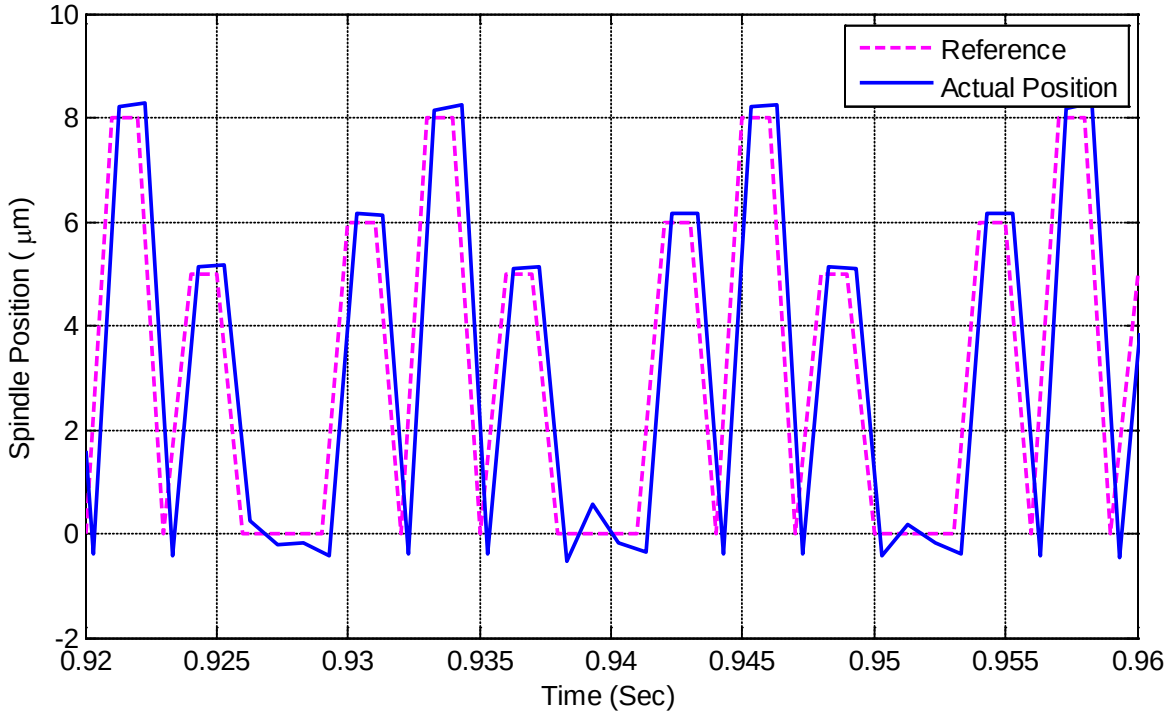


Figure 8.5 Tracking response of the spindle rotating at 5000rpm

Conventionally, the performance characteristics of reference tracking controllers are measured using the transient response parameters (rise time, overshoot, settling time) and the steady state error. However, these parameters are not considered to be the most suitable in this work. Instead, the performance criterion is chosen based on the objective of the active machining system, which is to keep the spindle at desired vertical positions when the cutters are within the angular positions where they produce visible cuttermarks on the workpiece. The positions of the spindle outside these regions do not have any effect on the surface finish. Therefore, the average percentage error between the reference positions and the actual positions of the spindle at the midpoints of the reference pulses (point C in Figure 8.1) is used to determine the performance of the controller. The efficiencies of the controller for the dynamic cutterhead inaccuracy compensation are shown in Table 8.2.

$$e_{avg} = \frac{\left|\frac{y_{ref}-y_{actual}}{y_{ref}}\right|_{pulse\ 1} + \left|\frac{y_{ref}-y_{actual}}{y_{ref}}\right|_{pulse\ 2} + \left|\frac{y_{ref}-y_{actual}}{y_{ref}}\right|_{pulse\ 3}}{3} \times 100 \quad (8.2)$$

Table 8.2 Controller efficiency for cutterhead inaccuracy compensation

Speed (RPM)	Pulse 1 Error (%)	Pulse 2 Error (%)	Pulse 3 Error (%)	Average Error (%)	Controller Efficiency (%)
2000	2.8	1.2	0.1	1.4	98.6
3000	0.1	0.1	4.0	1.4	98.6
4000	3.1	2.5	4.0	3.2	96.8
5000	3.3	2.6	4.1	3.3	96.7

The second stage of the experiments was performed while an imbalance mass of 21g was attached to the cutterhead at a radius of 35mm (735g-mm). The controller was then used to regulate the position of the spindle around zero. The uncontrolled and controlled vibrations

of the spindle at different rotating speeds are shown in Figure 8.6 to Figure 8.9. The effective performance of the controller is also presented in Table 8.3.

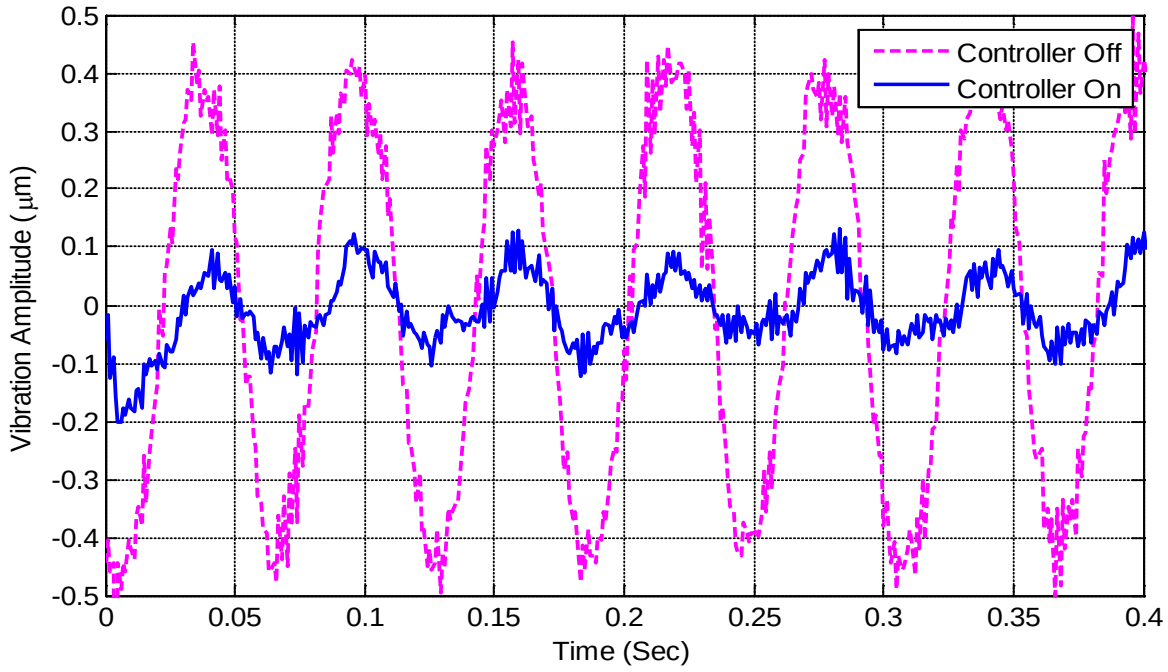


Figure 8.6 Controlled and uncontrolled vibration of the spindle rotating at 1000rpm

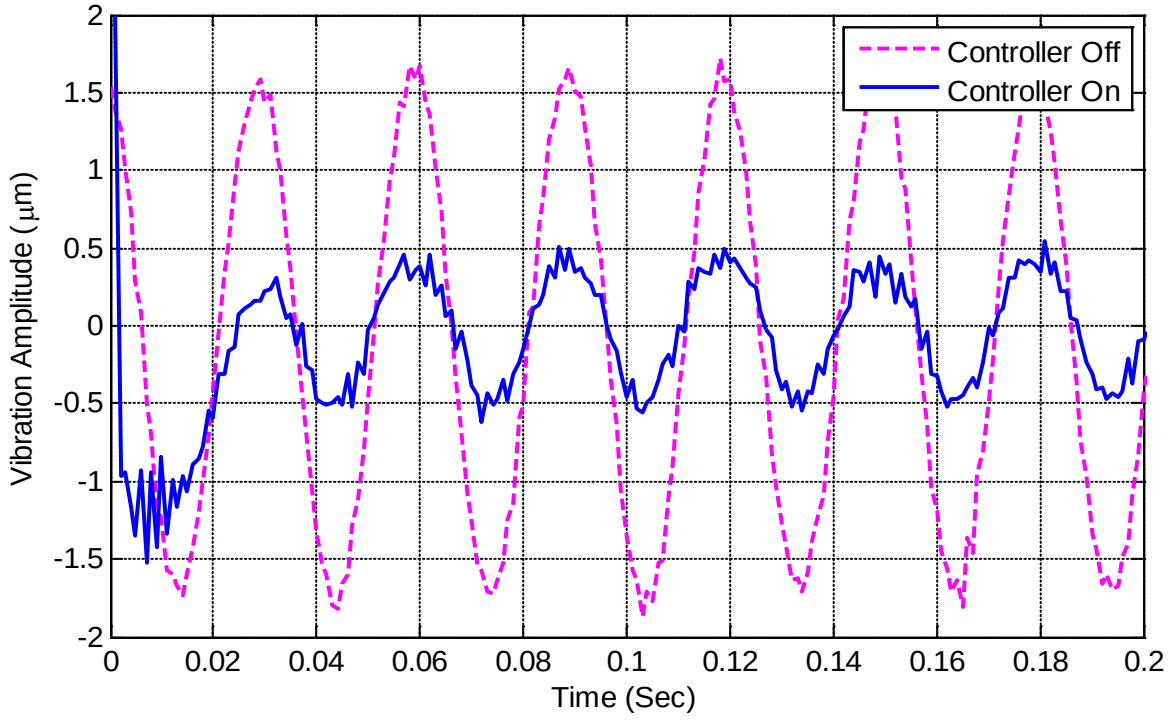


Figure 8.7 Controlled and uncontrolled vibration of the spindle rotating at 2000rpm

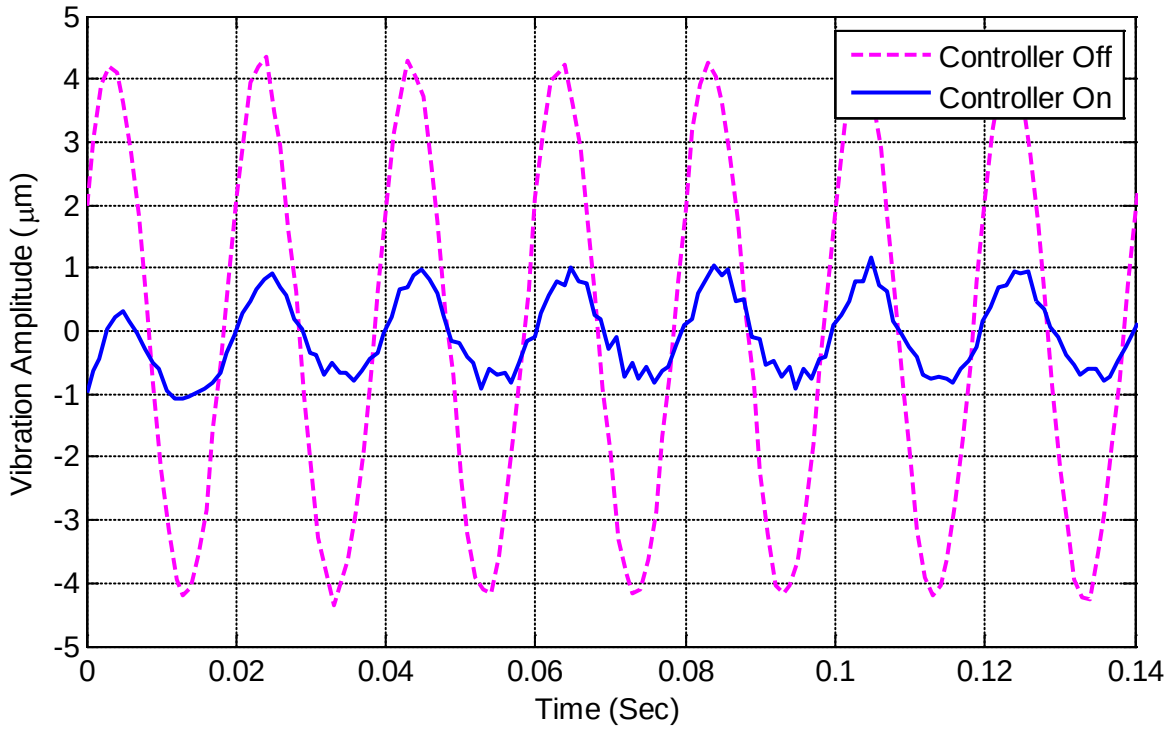


Figure 8.8 Controlled and uncontrolled vibration of the spindle rotating at 3000rpm

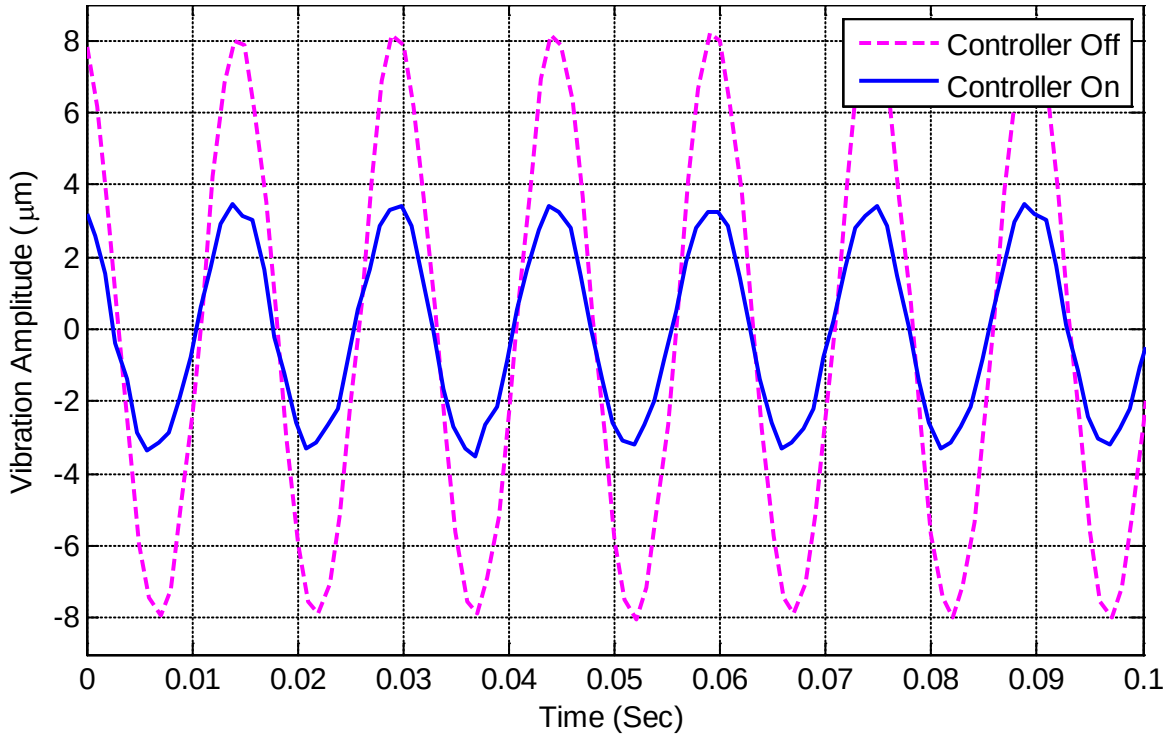


Figure 8.9 Controlled and uncontrolled vibration of the spindle rotating at 4000rpm

Table 8.3 Controlled and uncontrolled vibration amplitudes

Rotational Speed (rpm)	Imbalance Force (N)	Uncontrolled Vibration Amplitude (μm)	Controlled Vibration Amplitude (μm)	Vibration Reduction (%)
1000	8.06	0.45	0.09	80.0
2000	32.24	1.75	0.49	72.0
3000	72.54	4.12	0.90	78.2
4000	128.96	8.00	3.20	60.0

The results in table 8.3 show that the controller can provide up to 60% reduction in the spindle vibration amplitude when it is rotated at the speed of 4000rpm with the 735g-mm imbalance. It is also interesting to check how the actual uncontrolled vibration amplitudes of the spindle compare with the theoretical amplitudes computed using equation 6.3. These comparisons are made in Table 8.4. The results show that the amplitudes compare reasonably well especially at rotational speeds greater than 2000rpm.

Table 8.4 Theoretical and actual uncontrolled vibration amplitudes

Speed (rpm)	Theoretical Amplitude (μm)	Measured Amplitude (μm)	Percentage Difference (%)
1000	0.50	0.45	10.00
2000	2.00	1.75	12.50
3000	4.10	4.12	0.50
4000	8.06	8.0	0.75

The third stage of the experiments was performed with the same imbalance mass but the cutterhead was made to track non-zero reference signals. The comparisons between the reference signal and the spindle output for rotational speeds ranging from 1000rpm to

4000rpm at increment of 1000rpm are shown in Figure 8.10 to Figure 8.13. The effective performances of the controller are also presented in Table 8.5.

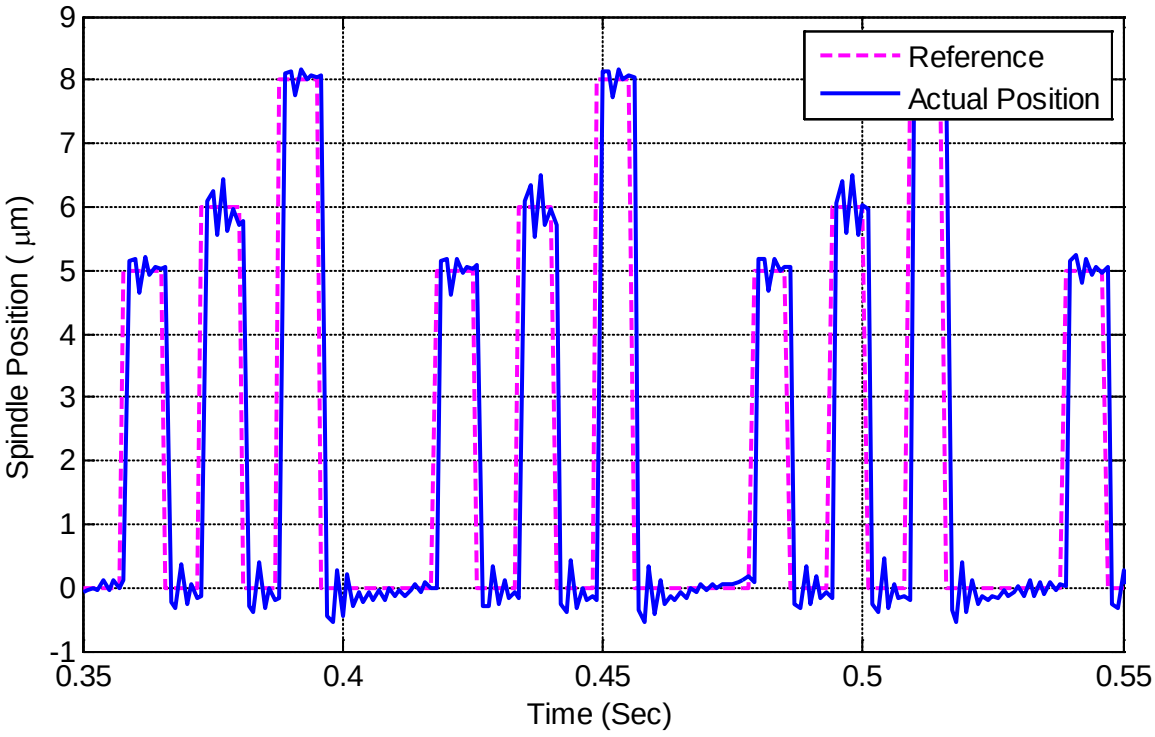


Figure 8.10 Tracking response of the spindle with imbalance mass at 1000rpm

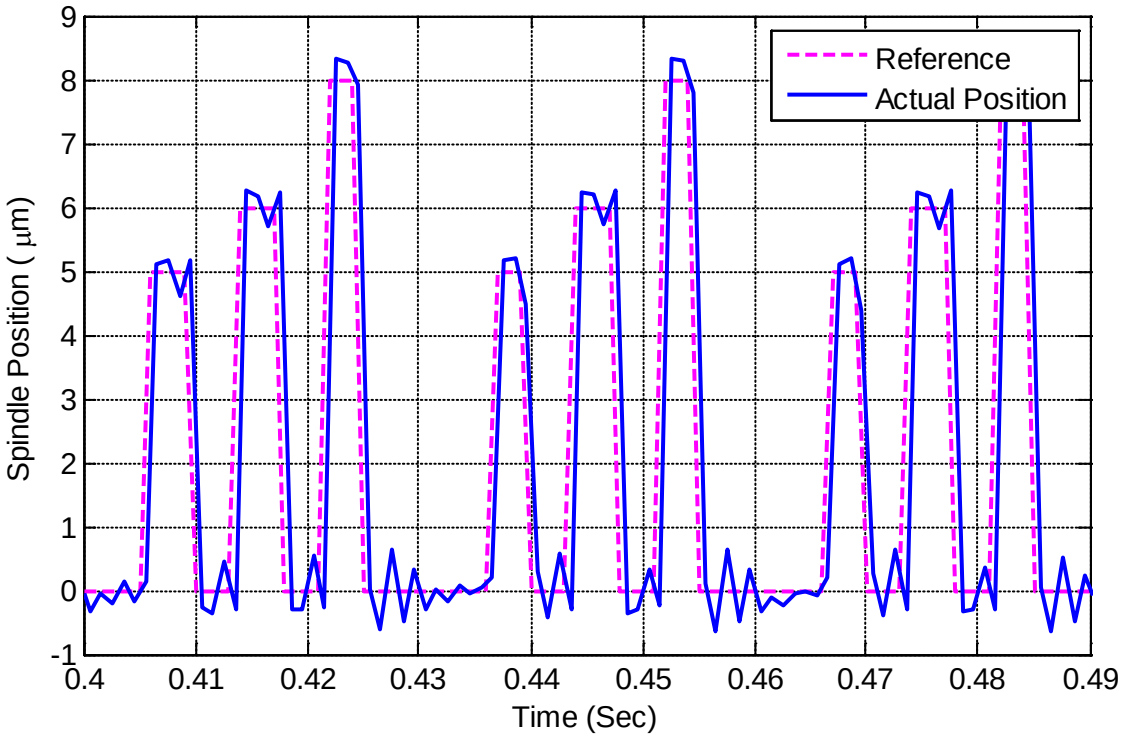


Figure 8.11 Tracking response of the spindle with imbalance mass at 2000rpm

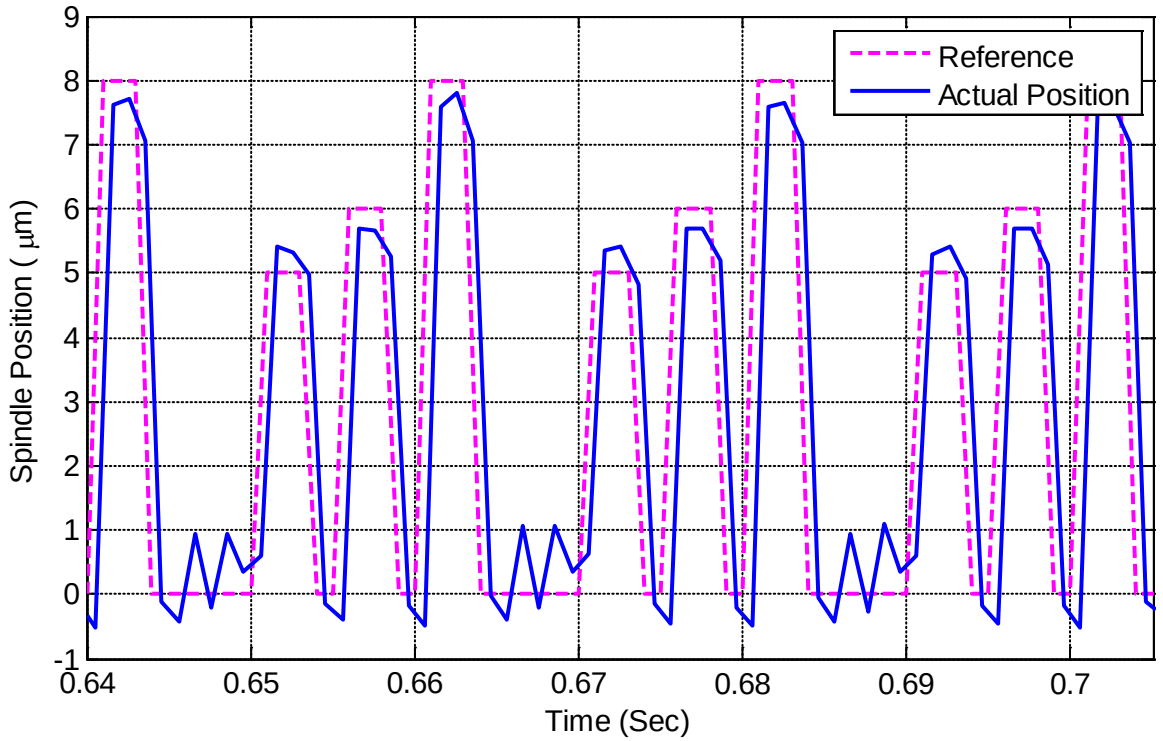


Figure 8.12 Tracking response of the spindle with imbalance mass at 3000rpm

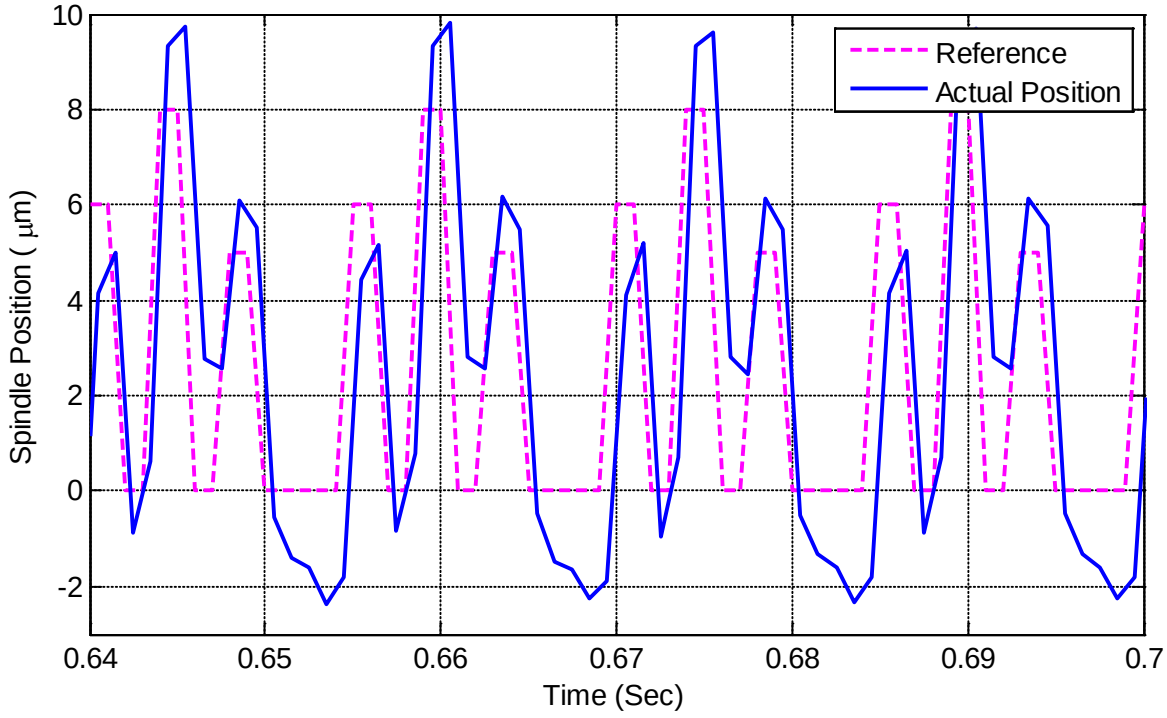


Figure 8.13 Tracking response of the spindle with imbalance mass at 4000rpm

Table 8.5 Controller efficiency for cutterhead inaccuracy and spindle vibration compensation

Speed (RPM)	Pulse 1 Error ((%)	Pulse 2 Error (%)	Pulse 3 Error (%)	Average Error (%)	Controller Efficiency (%)
1000	0.1	1.0	0.1	0.5	99.5
2000	2.1	3.1	5.0	3.4	96.6
3000	8.0	6.7	4.0	6.2	93.8
4000	30.0	22.5	20.0	24.2	75.8

8.2 Influence of cutterhead displacement on the surface form

The effectiveness of the proposed vertical cutterhead displacement depends on its magnitude and the time it is applied. The displacements must be synchronised with the knife positions in order to effectively compensate for the run outs. If there is any error in measuring the angular positions of the cutting knives, the efficiency of the proposed technique will be reduced. This requirement and the narrow pulse width place very strict response requirements on the actuation system. In order to minimise the strict actuator response requirements, the pulse width is increased to the maximum possible. The maximum possible angle within which the pulse must be applied is 360^{o} divided by the number of knives on the cutterhead. If the maximum possible angle is used, then the pulse width is mainly a function of the cutting speed and the number of knives (equation 8.1).

There is about 2ms lag in the test rig setup. This is not a problem if the pulse width is significantly longer than the 2ms. For shorter pulse width, the pulses must be triggered in advance so that they are synchronised with the knife positions.

There are two sets of apriori information that are required to implement the proposed vertical cutterhead oscillation technique. The first are the static run outs of the cutters and the other are the absolute angular positions of the spindle at the lowest point of each cutter. The values of the static run outs are measured while the cutterhead is mounted on the spindle in order to eliminate the effect of any misalignments between the centre of the cutterhead and the spindle centre.

The setup is the same as the one used for the spindle displacement measurements (Figure 6.3). One of the cutters is taken to be the reference cutter. The cutterhead is rotated by hand on to the dial test indicator until the highest point is registered on the reference cutter (maximum DTI reading). The DTI is then set to zero at this point. The run outs of the other cutters are then measured in a similar way relative to the reference cutter. The angular positions of the cutters are also predetermined using the encoder.

8.3 Wood Machining Experiments - Two-Knife Tests

A two-knife cutterhead with a nominal diameter of 120mm and a static TIR of 70µm was mounted on the spindle, after which the system identification was performed as explained in chapter six. Following the system identification, the controller parameters were tuned according to the desired time-domain performance characteristics. The run outs and the angular positions of the cutters are shown in Table 8.6.

Table 8.6 Angular positions and static run outs of the two cutting knives

Knife	Static run out (μm)	Angular Position (counts)
1	$y_1 = 0$	$\theta_1 = 83$
2	$y_2 = 70$	$\theta_2 = 1084$

The first two-knife cutting test was performed at a cutting speed of 1200rpm and a feed speed of 200mm/s. These parameters were chosen to produce 5mm waviness pitch. Although this is not a realistic waviness pitch, a shorter pitch would lead to a single knife finish due to the large 70μm radial difference between the two knives. The purpose of this first cutting experiment was to investigate the effect of the cutterhead inaccuracy compensation. The machining was done in two passes. The first was without the cutterhead inaccuracy compensation and the second was with the compensation. The surface profiles were measured with the machine vision system introduced in chapter four. The vision measuring system does not provide absolute height information, so the heights have been normalised. The uncompensated surface finish is shown in Figure 8.14. The effect of the proud knife can be seen in form of the light-deeper cuts (Figure 8.14).

During the controlled machining process, the shorter knife was displaced downward by 18μm at the front ring while the longer knife was displaced upward by the same 18μm. These displacements would compensate for a TIR of about 46μm at the cutterhead position. The compensated surface finish is shown in Figure 8.15. Clearly, the cutterhead inaccuracy compensation has improved the quality of the surface finish because the cuttermarks are more uniform.

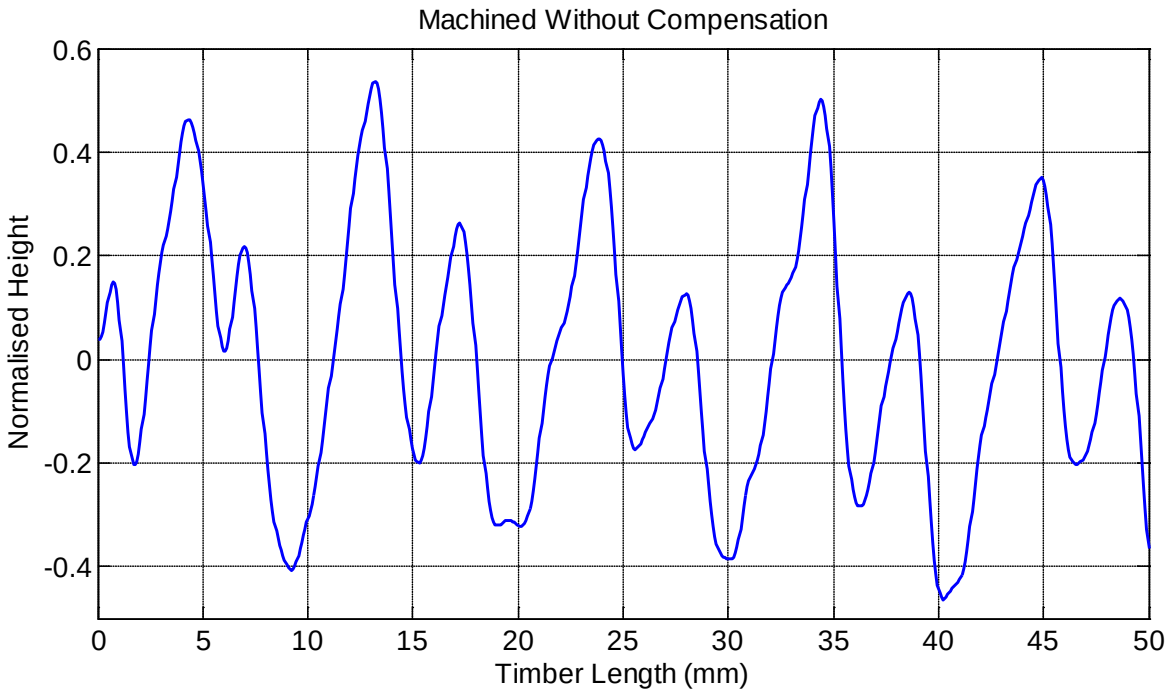


Figure 8.14 Two-knife test machined without compensation (Experiment 1)

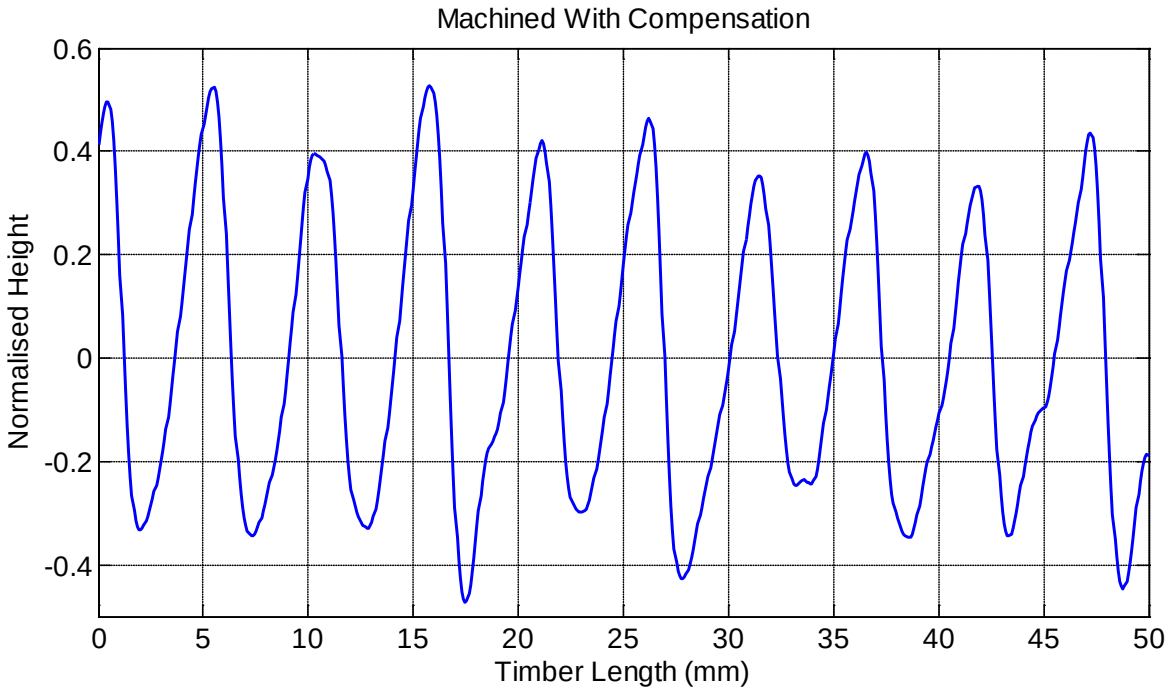


Figure 8.15 Two-knife test machined with compensation (Experiment 1)

Another set of experiments were performed at a cutting speed of 2400rpm and a feed speed of 240mm/s. The expected cuttermarks width for these parameters is 3mm. The uncompensated surface finish is shown in Figure 8.16. The 70µm difference between the cutting knives has resulted into a single knife finish because the cuttermarks produced by the shorter knife was completely removed by the longer one. The width of the cuttermarks is now twice as much as the expected pitch. The compensation was applied just as in the first experiment. The surface profile (Figure 8.17) shows clearly that the desired two-knife finish has been achieved with the compensation. The cuttermarks width has been reduced from 6mm to the expected 3mm, indicating that the two knives produced cuttermarks on the surface. Thus, the 70µm TIR that resulted into a single-knife finish has now produced a true double-knife finish when the compensation is applied.

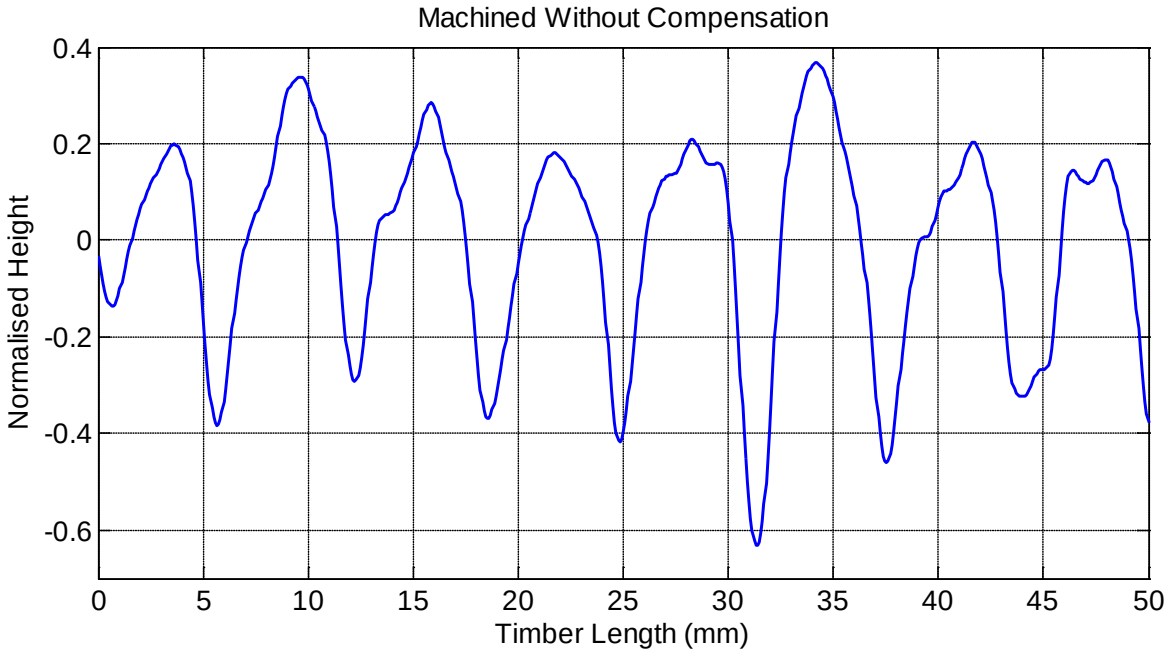


Figure 8.16 Two-knife test machined without compensation (Experiment 2)

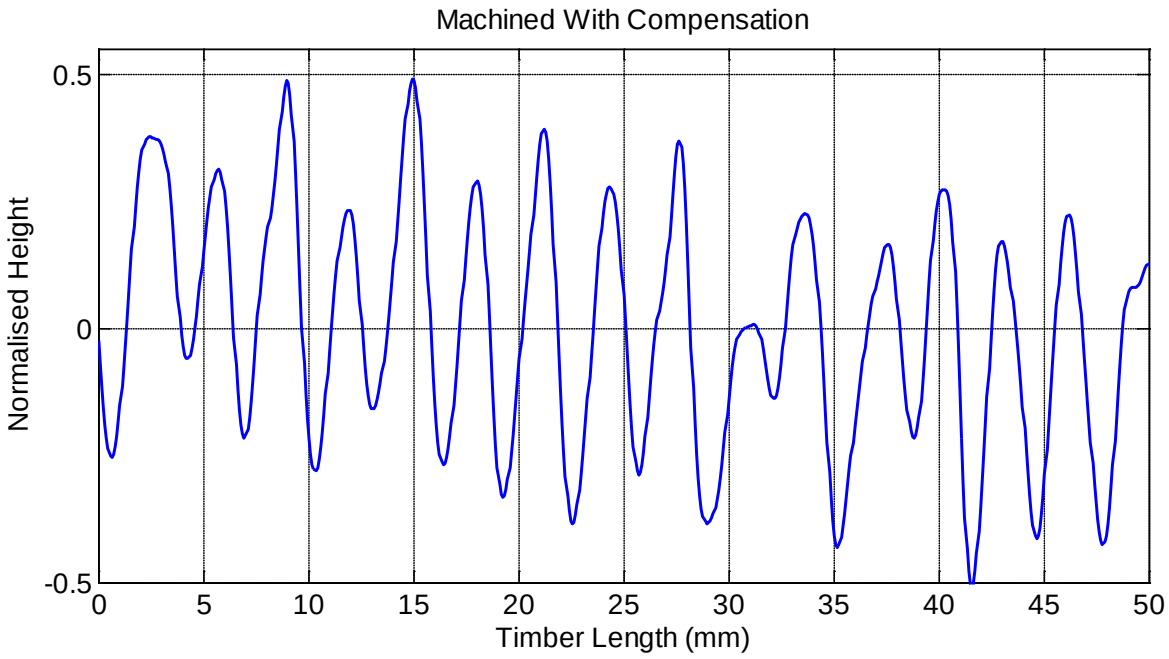


Figure 8.17 Two-knife test machined with compensation (Experiment 2)

8.4 Wood Machining Experiments - Four-Knife Tests

A four-knife cutterhead with a nominal diameter of 120mm was mounted on the spindle. The cutters were numbered from one to four in the clockwise direction, the first cutter being the reference on which the DTI was set to zero. The measured static run-outs and the angular positions of the cutters are given in Table 8.7.

Table 8.7 Angular positions and static run outs of the four cutters

Knife	Static run out (µm)	Angular Position (counts)
1	$y_1 = 0$	$\theta_1 = 60$
2	$y_2 = -12$	$\theta_2 = 560$
3	$y_3 = -2$	$\theta_3 = 1060$
4	$y_4 = 1$	$\theta_4 = 1560$

A steamed beech wood sample was machined without any compensation at the cutting speed of 1000rpm and feed speed of 133mm/s. These parameters were chosen to produce 2mm waviness pitch. The surface profile (Figure 8.18) was measured using the Alicona InfiniteFocus instrument (Appendix F). The Alicona was used because it gives absolute height values; therefore it is easier to correlate the heights of the cuttermarks with the static knife run-out measurements.

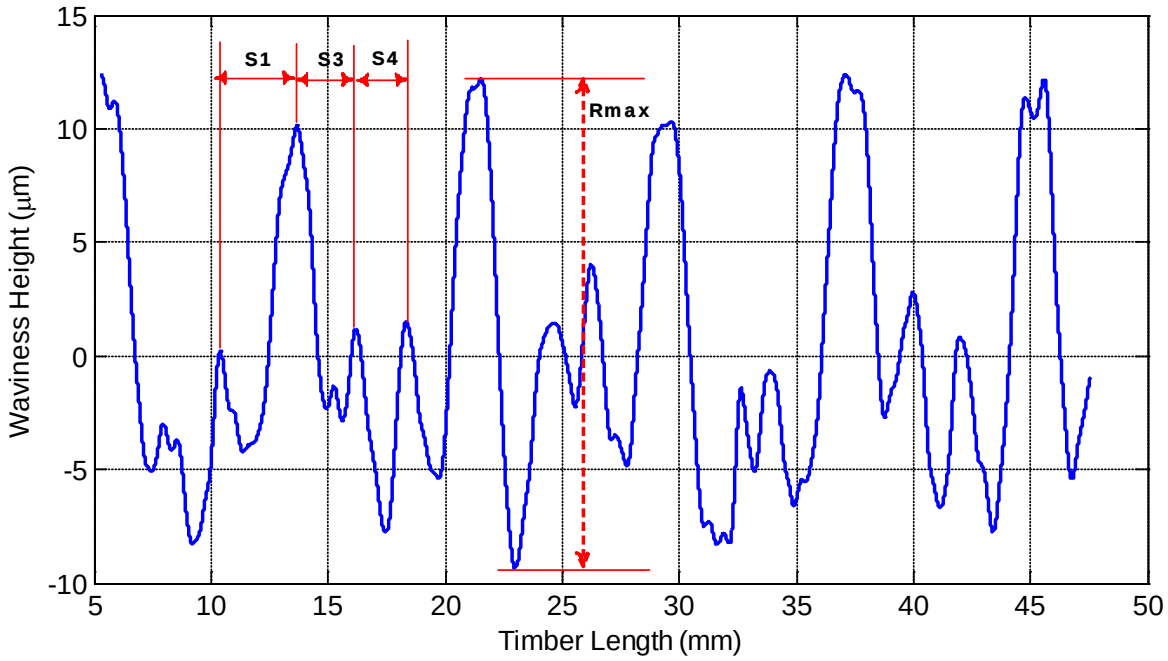


Figure 8.18 Four-knife test machined without compensation

The surface profile is almost a three-knife finish because of the 13µm TIR of the cutterhead. Although there are some variable differences in the heights of corresponding cuttermarks from one revolution to the other, the overall waviness pattern is in close agreement with the static run out measurements. In order to further validate the static run out measurements, the cutters were displaced downward by 14µm one at a time. It is expected that the surface finish should degrade further except for knife two, which is

considerably shorter than the rest. The resultant surface profiles for each of the knife displacements are shown in Figure 8.19 to Figure 8.22.

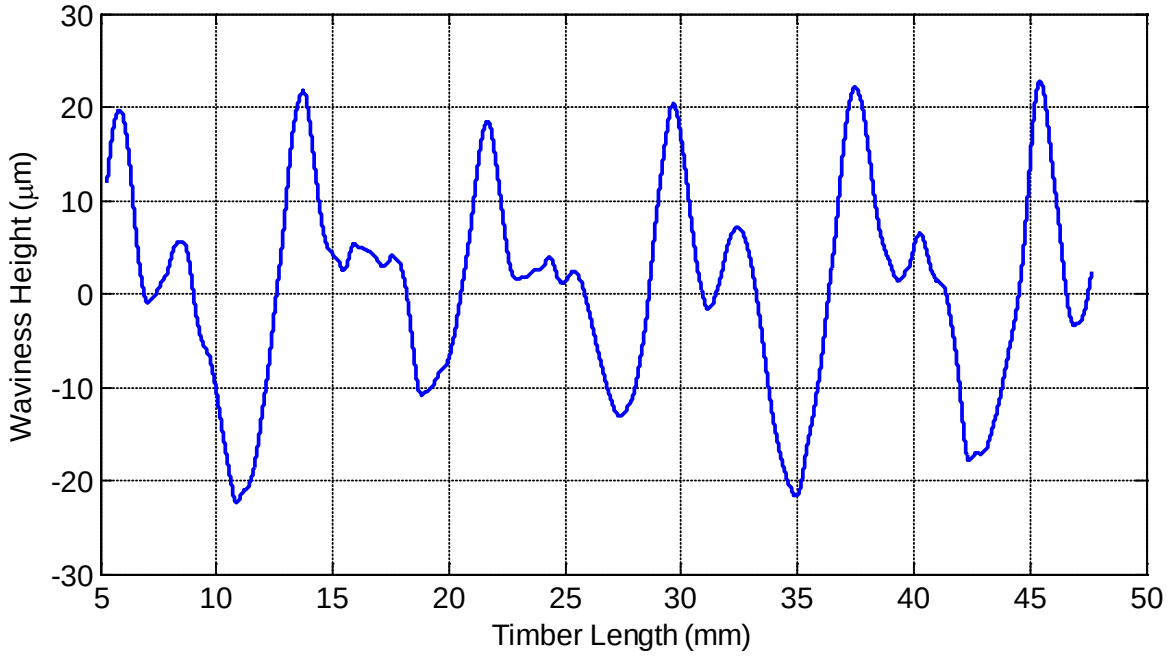


Figure 8.19 Four-knife test machined with 14μm downward displacement of cutter one

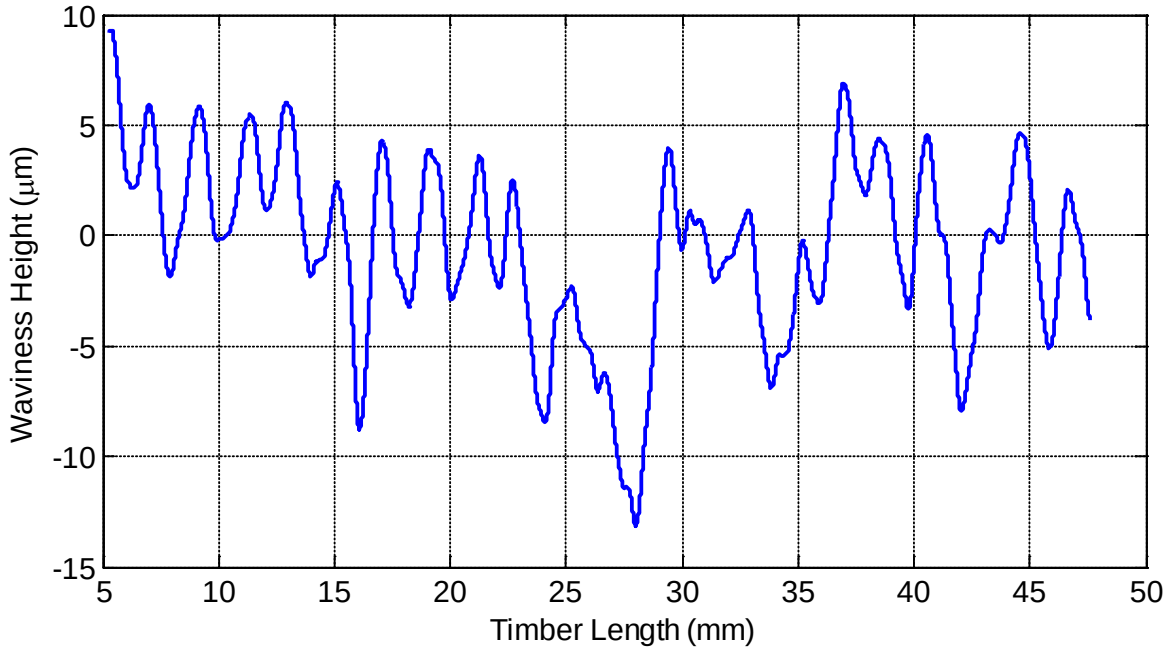


Figure 8.20 Four-knife test machined with 14μm downward displacement of cutter two

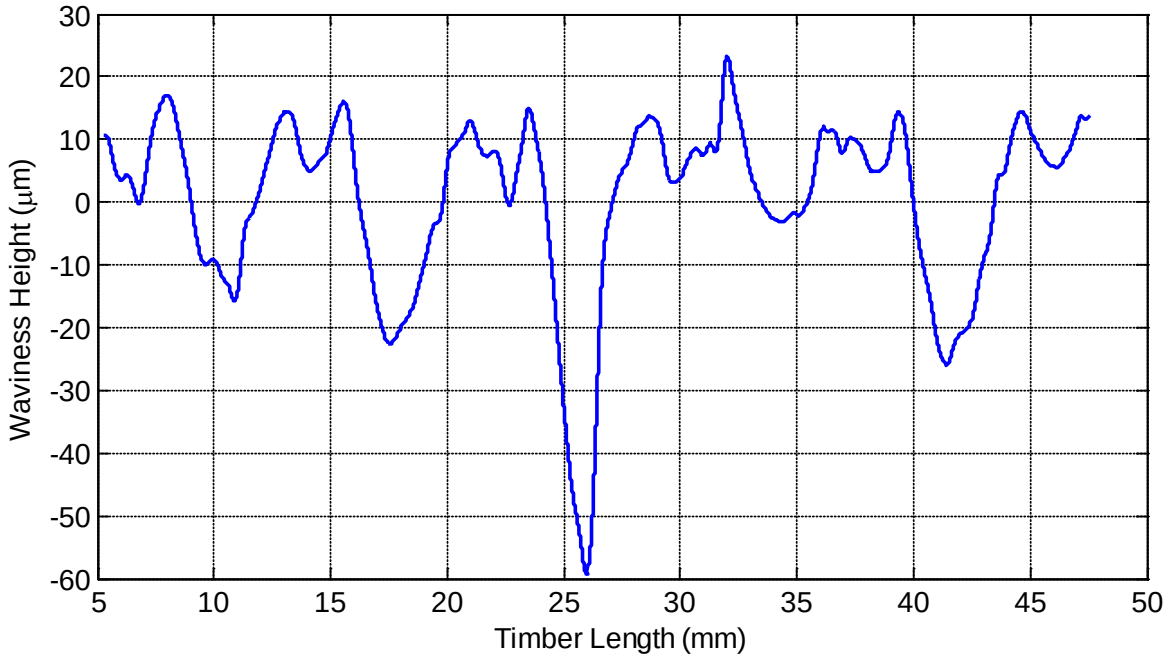


Figure 8.21 Four-knife test machined with 14µm downward displacement of cutter three

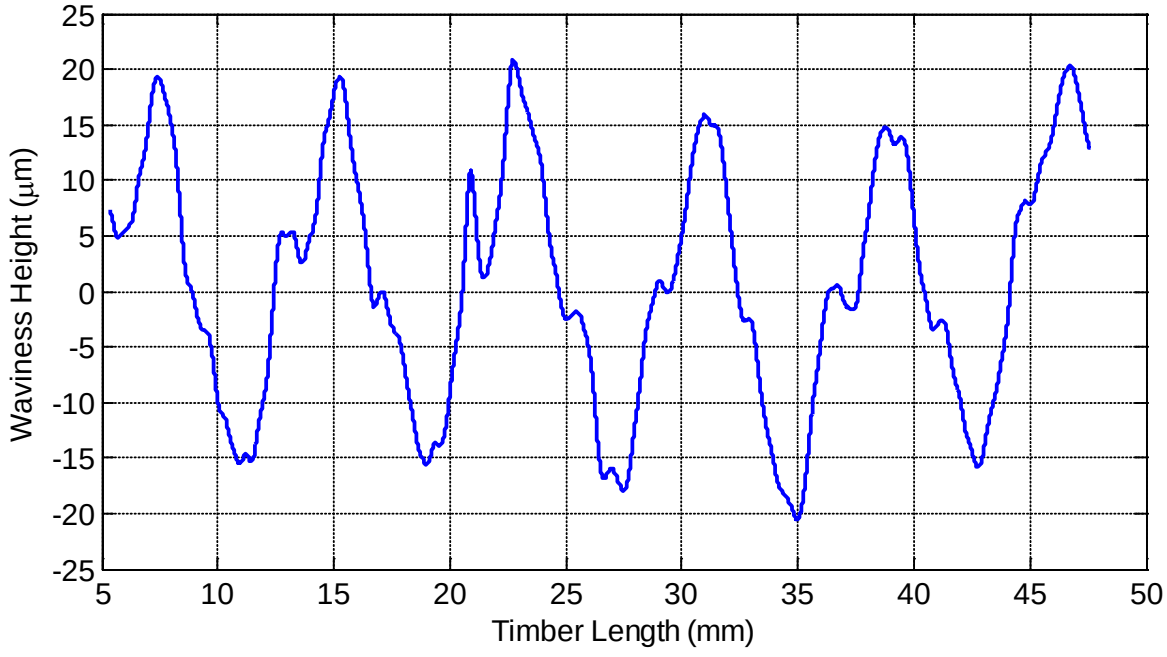


Figure 8.22 Four-knife test machined with 14µm downward displacement of cutter four

As seen in Figure 8.19 and 8.21, the surface profiles have become two-knife finishes. That of Figure 8.22 is almost a single-knife finish because the fourth knife is the longest and displacing it further down will increase the dynamic TIR. As expected, the profile in Figure 8.19 is the desired four-knife finish. This is evident from the number of cuttermarks per revolution (8mm timber length). These results confirm that knife two is the shortest as measured statically.

In order to compensate for the cutterhead inaccuracy, the cutterhead was displaced according to the static run out measurements. Cutter two and three were displaced downward by 12µm and 2µm respectively, and cutter four was displaced upward by 1µm. The surface profiles obtained at cutting speeds of 1000rpm and 4000rpm are shown in Figure 8.23 and Figure 8.24 respectively.

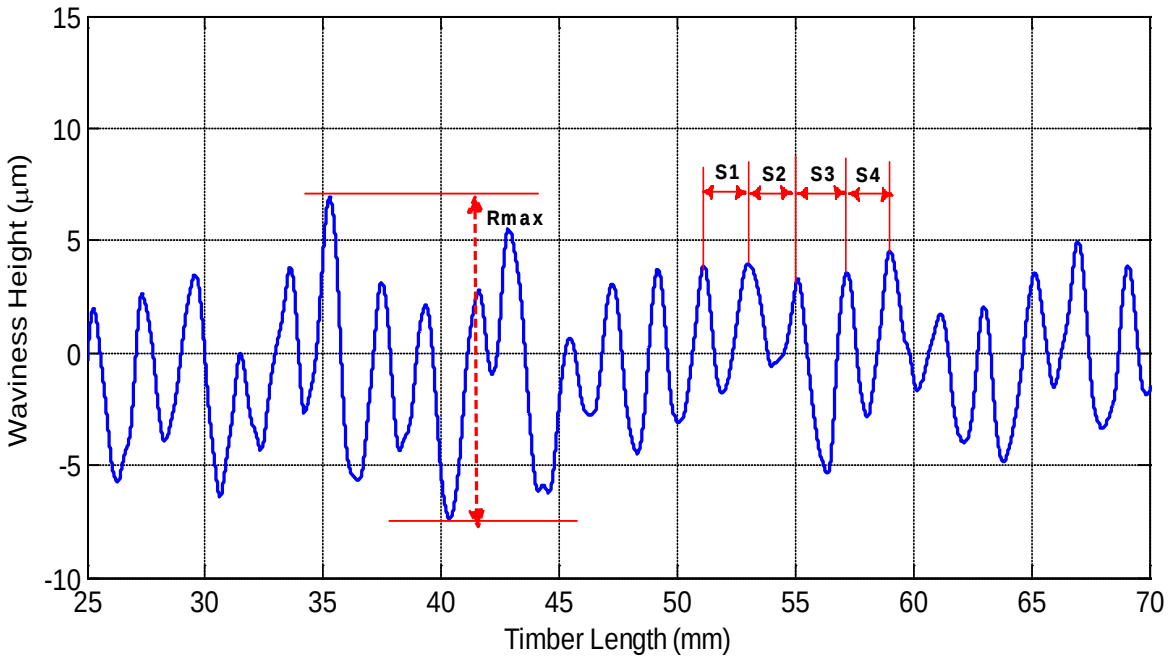


Figure 8.23 Four-knife test machined with compensation at 1000rpm

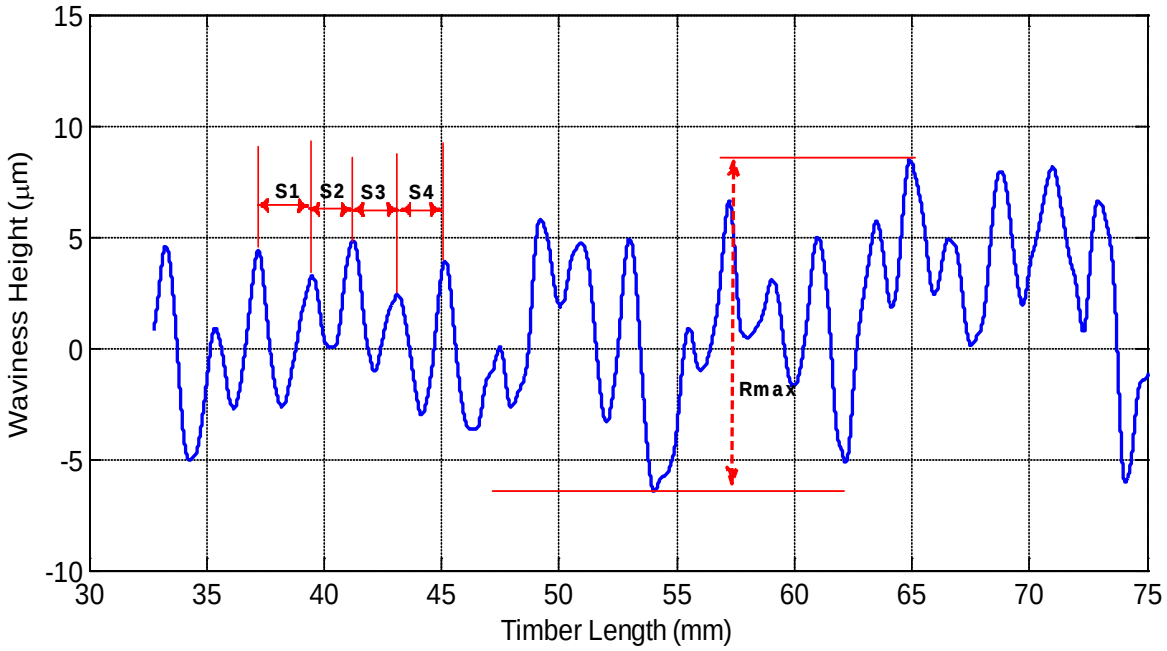


Figure 8.24 Four-knife test machined with compensation at 4000rpm

Although there are still visible cuttermarks heights variations in the compensated surface profiles, the scale is less than that of the uncompensated finish. This is evident from the maximum peak to valley heights of the profiles (R_{max}). Also, the surface profiles are clearly four-knife finishes compared to the three-knife finish seen in Figure 8.18. The standard deviation of the widths of the cuttermarks within a selected sample length (three cutterhead revolution) is used as the quality assessment parameter. The standard deviation is calculated as follows:

$$SD = \sqrt{\left(\frac{1}{N_c}\sum_{i=1}^{N_c}(S_i - \bar{S})^2\right)} \tag{8.2}$$

where

N_c is the number of cuttermarks (4 cutters x 3 revolutions)

$\bar{S}$ is the desired waviness pitch ($2mm$)

S_i is the width of the i^{th} cuttermark in the sample length

A low standard deviation indicates that the width of the individual cuttermarks tends to be very close to the desired pitch. Therefore, the lower the standard deviations, the higher the quality of the surface finish. The surface finish quality evaluation data for the surface profiles are shown in Table 8.8. Based on these values, the compensated surface finishes have higher quality ratings than the uncompensated finish.

Table 8.8 Surface finish quality evaluation

Surface Finish	R_{max} (µm)	Cuttermarks Width (mm)				SD (mm)
		S_1	S_2	S_3	S_4	
Uncompensated surface finish	20.95	3.37	0.00	2.50	2.12	1.26
Compensated surface finish at 1000rpm	13.82	1.90	2.15	2.08	1.88	0.13
Compensated surface finish at 4000rpm	14.58	2.17	1.80	1.94	1.98	0.25

Machining tests were also performed while the imbalance mass of 4060g-mm was attached to the cutterhead at the same angular position as knife four. The spindle was rotated at the speed of 1500rpm and the imbalance mass produce a forced vibration of about 7µm amplitude at the cutterhead position. This would effectively increase the dynamic TIR of the cutterhead from 13µm to 27µm.

A steamed beech wood sample was machined without any compensation at the feed speed of 200mm/s in order to aim at 2mm waviness pitch. The resulting surface profile is shown in Figure 8.25. The waviness pitch is about 8mm indicating that the profile is a single-knife finish. There is a clear similarity between the profile (Figure 8.25) and that of the 14µm downward displacement of knife four (Figure 8.22). This would be expected because the dynamic TIR of the cutterhead is 27µm in both cases. Another wood sample was machined

under the same conditions but the cutterhead inaccuracy and feedforward vibration compensation was applied during the machining operation. The resulting surface profile is shown in Figure 8.26.

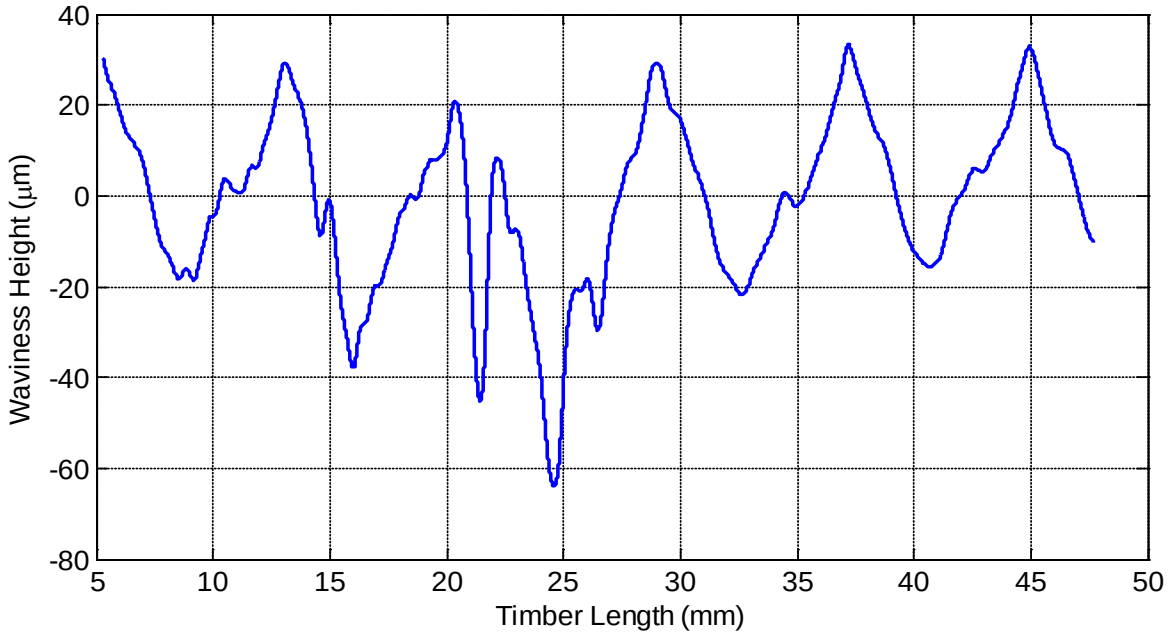


Figure 8.25 Four-knife finish with cutterhead inaccuracy and vibration defects

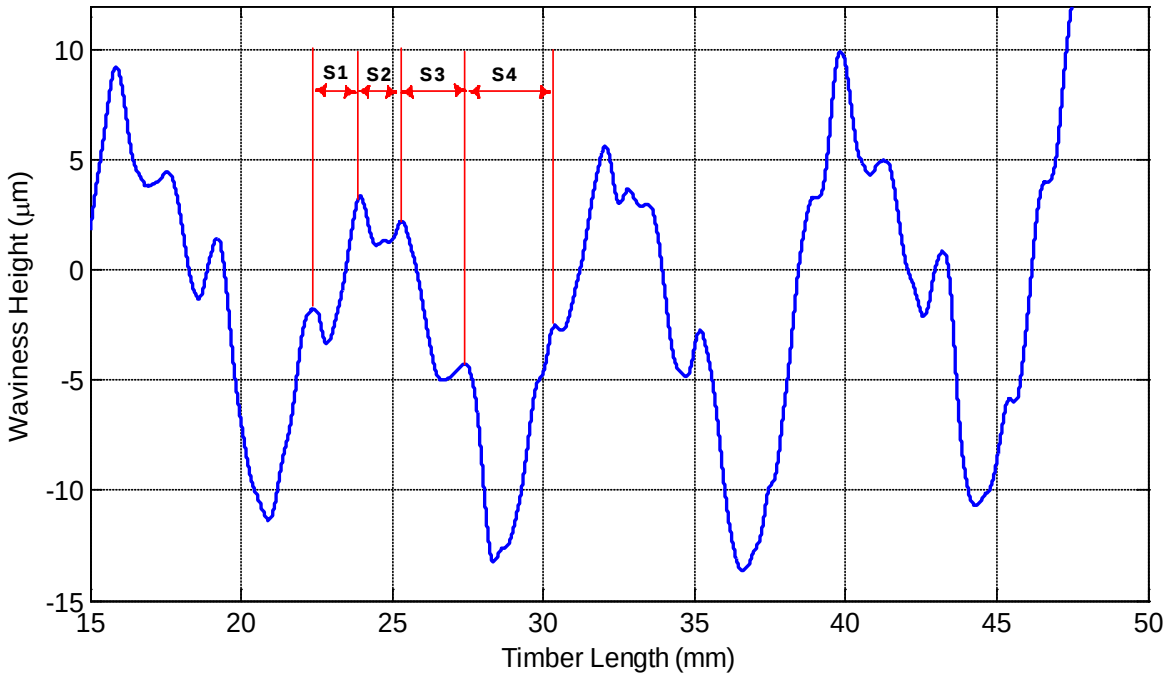


Figure 8.26 Four-knife finish with cutterhead inaccuracy and vibration compensation

The compensation was able to minimise the vibration to about 3μm according to the outputs of the eddy current sensors. As seen in Figure 8.26, the surface profile is a four-knife finish, having a pattern that is similar to the simulated effect of once per revolution vibration (Figure 3.15). The standard deviation of the widths of the cuttermarks in the uncompensated surface finish over three cutterhead revolutions is 3.46mm while that of the compensated surface finish is 0.64mm. These values also indicate that the compensated finish has much higher quality than the uncompensated finish.

There are some factors that could limit the level of the surface quality improvements achieved through the proposed cutterhead displacement technique. The first one is the precision of the static cutter run outs measurement. The repeatability of the TIR measurements is within 1-3μm. This could be due to the introduction of additional radial run outs when the cutterhead is rotated by hand. Since the cutterhead displacement is based on apriori knowledge of the static cutter run outs, imprecise measurements would limit the effectiveness of the applied compensation. Short term drift of the eddy current sensors is also another factor. The sensors could drift by ±2μm within a minute of clearing the offset. This would also affect the accuracy of the cutterhead displacement because the feedback loop relies on the eddy current sensors outputs.

9 Conclusions and Recommendations

9.1 Conclusions

A new machining technique and control architecture for improving the surface finish quality of rotary planed wood has been created in this thesis. The specific achievements in this thesis are as follows:

Surface Form Modelling

A generic simulation model called extended circular arc theory (ECAT) has been created for rotary wood planing process. The ECAT is suitable for simulating the effects of static and dynamic machine characteristics, such as cutter inaccuracy and forced vibration, on planed wood surfaces. The improvements provided by ECAT are as follows:

- The ECAT represents the kinematics of the machining process more accurately than the existing models
- It is shown that the ECAT is more flexible than the existing models because it allows easy variation of machining parameters, vibration signature, and position of the resultant mass imbalance, which is required for simulating the effects of cutterhead vibration
- The ECAT allows easy extraction of cuttermarks sizes without the need for additional processing as required by the existing algorithms.

Surface Profile Assessments

Application of photometric stereo (PS) and shape from shading (SFS) techniques to moving wood surface profile measurements has been investigated. The contributions made by this thesis are as follows:

- Extraction of the surface reflectance properties of wood: A three-image PS technique is used to recover the point-by-point albedo of some selected wood samples. It is shown that the albedo of wood is inconsistent, which is attributed to its anisotropic nature. This inconsistency in wood surface albedo makes SFS technique unsuitable for wood surface assessments because the principle of SFS is generally based on the assumption of constant and uniform albedo.

- Application of PS technique to moving wood samples: The major challenge in the application of PS technique to moving samples is how to determine pixel correspondence between photometric image pairs. The method designed in this thesis uses an incremental encoder to measure wood sample displacements between successive image pairs in order to establish pixel correspondence. Results obtained from the experiments performed on a test rig, which is designed to simulate a real machining environment, show that the approach is suitable for in-process surface quality inspection. The benefit of this work is that it provides direct feedback information on the machine output, which is used for real-time secondary control of the machining process.

Defects Characterisation

Two novel techniques for charactering defects on planed wood using empirical mode decomposition (EMD) and principal component analysis (PCA) have been developed. The techniques were applied to synthetic surface profile data generated using the ECAT simulation model. It is shown that EMD recovers cutterhead vibration signature from measured surface profile if the machining parameters are known. In comparison to Fourier

analysis, it is also shown that EMD will perform better under general conditions where Fourier analysis is likely to fail.

In the PCA approach, a knowledge-base is first developed through analysis of the surface profiles generated by known defect conditions. A neural network is then designed to represent the human reasoning mechanism for subsequent identification of unknown defects. It is shown that the technique can effectively replace a human expert in terms of identifying the frequency of cutterhead vibration. The limitation of PCA compared to EMD is that it does not provide the amplitude of cutterhead vibration.

Although the defect characterisation is not directly linked to real-time control of the machining process, it produced a software tool that can assist machine operators in inferring the causes of defects on planed timber surfaces.

Active Wood Machining

The current state of industrial wood planing machines indicates that the natural limits of purely mechanical design solutions have been reached. This led to the design of a new active machining technique for compensating for the dynamic effects of cutting tool inaccuracy and forced vibration in rotary wood planing. The technique is based real-time periodic optimization of cutting tool trajectory and active vibration control using eddy current displacement sensors and piezoelectric actuators. The specific work done involves the following:

- Identification of a wood planing machine in order to obtain its dynamic model
- Design of an adaptive Linear Quadratic Gaussian (LQG) tracking controller with integral action. The controller is used to implement the cutterhead inaccuracy compensation and also suppress spindle vibration
- Implementation of the LQG controller on the smart wood planing machine
- Engineering and wood cutting tests on the smart wood planing machine

Experimental results obtained from the smart wood planing machine using the developed monitoring and control system show improvements in the dynamic performance of the machine. Also, the surface profiles obtained from compensated machining operations have improved quality compared to the ones machined without compensation. The direct benefits of this mechatronic approach compared to the traditional mechanical solution to cutting tool inaccuracy (jointing) are lower tooling costs and higher machine performance.

9.2 Recommendations for Further Work

Two novel approaches for characterising the waviness defects on planed timber surfaces using the EMD and PCA techniques have been developed. The two techniques have been applied to synthetic data whereas real wood surface profiles contain irregularities such noises and roughness components. Further work needs to be done in order to investigate how well these techniques will perform on real wood samples. For all the cases considered, focus was placed on characterising the defects caused by structural vibration only. However, waviness defects might arise from the combination of both structural dynamics and cutterhead inaccuracy. Characterisation of such defects remains a challenge as it is

difficult to separate the influence of the two conditions. Further work needs to be done in this area also.

The precision and accuracy of the static cutter run outs measurements need to be increased. This could be achieved through the use of a non-contact measurement device instead of the dial test indicator, and efforts should be made to minimise the amount of radial run out introduced when rotating the spindle or cutterhead. The eddy current sensor drift needs to be checked further. The most likely cause of this problem is the signal conditioning unit.

The new vision system that is integrated with the wood planing machine is currently more suited for measuring static samples than dynamic samples. Basically, the mode of operation of the original test rig (Figure 4.10) needs to be replicated. Provision needs to be made for the camera to be hardware triggered so that the camera latency can be deterministic. Otherwise, it is almost impossible to consistently calculate the actual displacements between the photometric image frames.

References

Abdi, H. and Williams, L. J. (2010). "Principal component analysis". Wiley Interdisciplinary Reviews: Computational Statistics. 2 **(4)**, 433-459.

Adkins, C. A., Zhiming, H., Wong, B. W., Walcott, B. L. and Rouch, K. E. (1996). "Active vibration control using an electromagnetic absorber with two degrees of freedom", Proceedings of the IEEE on Bringing Together Education, Science and Technology, Tampa, FL, USA, April 11-14, 1996, pp. 175-178, ISSN 0-7803-3088-9.

Ahn, K. K. and Kha, N. B. (2007). "Internal model control for shape memory alloy actuators using fuzzy based Preisach model". Sensors and Actuators A. 136, 730 - 741.

Albertelli, Paolo (2008). High performance spindle design methodologies for high speed machining. Phd Thesis, Politecnico di Milano, Italy.

Al-Regib, E., Ni, J. and Lee, S. (2003). "Programming spindle speed variation for machine tool chatter suppression". International Journal of Machine Tools and Manufacture. 43, 1229-1240.

Astrom, K. and Hagglund, T. (1995). PID controllers: Theory, design and tuning, 2nd Edition edn, International Society for Measurement and Control.

Astrom, K. and Wittenmark, B. (1995). Adaptive control, 2nd ed. edn, MA: Addison-Wesley, Reading.

Belkharraz, A. I. and Sobel, K. (2007). "Simple adaptive control for aircraft control surface failures". IEEE Transactions on Aerospace and Electronic Systems. 43 **(2)**, 600-611.

Bradski, G. and Kaehler, A. (2008). Learning OpenCV: Computer vision with the OpenCV library, O'really Media Inc.

Bringier, B., Helbert, D. and Khoudeir, M. (2008). "The photometric reconstruction of a dynamic textured surface from just one color image acquisition". Journal of the Optical Society of America. 25 **(3)**, 566 - 574.

Brown, D. C. (1971). "Close-range camera calibration". 37 **(8)**, 855 – 866.

Brown, N. (1999). Modification of the rotary machining process to improve surface form. Phd Thesis, Loughborough University, UK.

Brown, N. and Parkin, R. M. (1999). "Improving wood surface form by modification of the rotary machining process - a mechatronic approach". Proceedings of the Institution of Mechanical Engineers, Part B, Journal of Engineering Manufacture. 213 **(3)**, 247-260.

Brown, N., Parkin, R. M. and Jackson, M. R. (2002). "Simulation of modified rotary timber machining process to improve surface form". Mechatronics. 12 **(3)**, 489-502.

Chamberlain, M. R. (2012). High level reasoning for intelligent control of a high performance production machine. Phd Thesis, Loughborough University, UK.

Chen, Y., Wang, X. G., Sun, C., Devine, F. and De Silva, C. W. (2003). "Active vibration control with state feedback in woodcutting". Journal of Vibration and Control. 9, 645 - 664.

Choudhury, S. K., Goudimenko, N. N. and Kudinov, V. A. (1997). "Online control of machine tool vibration in turning". International Journal of Machine Tools and Manufacture. 37 **(6)**, 801-811.

Clark, W. W. (2000). "Vibration control with state-switched piezoelectric materials". Journal of Intelligent Material Systems and Structures. 11 **(4)**, 263 - 271.

Corr, L. R. and Clark, W. W. (2001). "Energy dissipation analysis of piezoceramic semi-active vibration control". Journal of Intelligent Material Systems and Structures. 12, 729 - 736.

Curry, B. and Morgan, P. H. (2004). "Evaluating Kohonen's learning rule: An approach through genetic algorithms". European Journal of Operational Research. 154 **(1)**, 191 - 205.

Cus, F. and Zuperl, U. (2008). "Model reference adaptive force and surface roughness control in milling". Journal of Achievements in Materials and Manufacturing Engineering. 26 **(2)**, 179 - 182.

Cus, F., Zuperl, U., Kiker, E. and Milfelner, M. (2006). "Adaptive controller design for feedrate maximisation of machining process". Journal of Achievements in Materials and Manufacturing Engineering. 17 **(1-2)**, 237 -240.

Cyra, G. and Tanaka, C. (2000). "The effects of wood-fiber directions on acoustic emission in routing". Wood Science and Technology. 34 **(3)**, 237 - 252.

De Abreu, G. C. M., Teixeira, R. L. and Ribeiro, J. F. (2000). "A neural network-based direct inverse control for active control of vibrations of mechanical systems", Sixth Brazilian Symposium on Neural Networks, Rio de Janeiro, RJ, Nov. 22- 25, 2000, pp. 107 - 112, ISSN 0-7695-0856-1.

Denai, M. A., Palis, F. and Zeghbib, A. (2007). "Modelling and control of non-linear systems using soft computing techniques". Applied Soft Computing. 7 **(3)**, 728 - 738.

Denaud, L. E., Bleron, L., Ratle, A. and Marchal, R. (2007). "Online control of wood peeling process: Acoustical and vibratory measurements of lathe checks frequency". Annals of Forest Science. 64 **(5)**, 569 - 575.

Dohner, J. L., Lauffer, J. P., Hinnerichs, T. D., Shankar, N., Regelbrugge, M., Kwan, C., Xu, R., Winterbauer, B. and Bridger, K. (2004). "Mitigation of chatter instabilities in milling by active structural control". Journal of Sound and Vibration. 269 **(1-2)**, 197-211.

Ehmann, K. F. and Hong, M. S. (1994). "A generalised model of the surface generation process in metal cutting". Annals of the CIRP, International Institution for Production Engineering Research. 43 **(1)**, 483 - 486.

Elmas, S. (2008). Active vibration control and real-time surface profile monitoring system for a high performance machining process. Phd Thesis, Loughborough University.

Elmas, S., Islam, N., Jackson, M. R. and Parkin, R. M. (2011). "Analysis of profile measurement techniques employed to surfaces planed by an active machining system". Measurement. 44 **(2)**, 365 - 377.

Farooq, A. R., Smith, M. L., Smith, L. N. and Midha, S. (2005). "Dynamic photometric stereo for online quality control of ceramic tiles". Computers In Industry. 56, 918-934.

Frankot, R. T. and Chellappa, R. (1988). "A method for enforcing integrability in shape from shading algorithms". IEEE Transactions on Pattern Analysis and Machine Intelligence. 10 **(4)**, 439 - 451.

Gajate, A. M. and Guerra, R. E. H. (2009). "Internal model control based on neurofuzzy system for network applications. A case study on the high-performance drilling process". IEE Transactions on Automation Science and Engineering. 6 **(2)**, 367 - 372.

Ganguli, A., Deraemaeker, A., Horondica, M. and Preumont, A. (2005). "Active damping of chatter in machine tools - Demonstration with a 'hardware-in-the-loop' simulator", Proceedings of the Institute of Mechanical Engineers. Part I Journal of Systems and Control Engineering, vol. 219, pp. 359-369, .

Goodchild, R. (1963). "Investigating finish in rotary planing". Engineering. 1, 172-173.

Groeger, S., Dietzsch, M., Gerlach, M. and Jess, S. (2005). "Real mechanical profile- the new approach for nano-measurements". Journal of Physics. 13, 13-19.

Gullon, C. (2003). Height recovery of rough surfaces from intensity images. Phd Thesis, Heriot-Watt University, UK.

Gurau, L., Mansfield-Williams, H. and Irle, M. (2007). "Separation of processing roughness from anatomical irregularities and fuzziness to evaluate the effect of grit size on sanded European Oak". Forests Product Journal. 57 **(1-2)**, 110 - 115.

Haber, E. R., Alique, J. R., Alique, A. and Haber, R. H. (2005). "Controlling a complex electromechanical process on the basis of a neurofuzzy approach". Journal of Future Generation Computer System. 21 **(7)**, 1083 - 1095.

Hatzitheodorou, M., Karabassi, E. A., Papaioannou, G., Boehm, A. and Theoharis, T. (2000). "Stereo matching using optic flow". Real-Time Imaging. 6 **(4)**, 251 -266.

Heikkila, J. and Silvan, O. (1997). "A four-step camera calibration procedure with implicit image correction", Proceedings of the 1997 IEEE Computer Society Conference on Computer Vision and Pattern Recognition, San Juan, Puerto Rico, June 17-19, 1997, pp. 1106 – 1112, ISSN 0-8186-7822-4.

Hesselbach, J., Hoffmeister, H. W. and Loohb, T. (2007). "Process-integrated quality assurance in wood machining centres with the help of image processing". Journal of Production Engineering Research and Development. 1 **(1)**, 97 - 101.

Huang, N. E. (2000). "New method for nonlinear and nonstationary time series analysis: empirical mode decomposition and Hilbert spectral analysis", Proceedings of SPIE: Wavelet Applications VII, Orlando, FL, USA, April 26, 2000, vol. 4056, pp. 197-207, .

Huang, N. E., Shen, Z. and Long, S. R. (1999). "A new view of non linear water waves: The Hilbert spectrum". Annual Review of Fluid Mechanics. 31, 417-457.

Huang, N. E., Shen, Z., Long, S. R., Wu, M. C., Shih, H. H., Zheng, Q., Yen, N., Tung, C. C. and Liu, H. H. (1998). "The empirical mode decomposition and the Hilbert spectrum for nonlinear and non-stationary time series analysis", Proceedings of the Royal Society of London - Mathematical, Physical and Engineering Sciences , March, 8, 1998, vol. 454, pp. 903-995, .

Huang, N. E., Wu, M. L., Long, S. R., Shen, S. S., Qu, W. D., Gloersen, P. and Fan, K. L. (2003). "A confidence limit for the empirical mode decomposition and Hilbert spectral analysis", Proceedings of the Royal Society of London: Mathematical, Physical and Engineering Sciences, Sept. 8, 2003, vol. 459, pp. 2317-2345, .

Hynek, P. (2004). Wood surface form improvement by real-time displacement of tool trajectory. Phd Thesis, Loughborough University, Leicestershire, United Kingdom.

Iskra, P. and Hernandez, R. E. (2010). "Towards a process monitoring and control of a CNC wood router: development of an adaptive control system for routing white birch". Wood and Fiber Science. 42 **(4)**, 523 - 535.

Iskra, P. and Hernandez, R. E. (2009). "The influence of cutting parameters on the surface qualityof routed white birch and surface roughness prediction modelling". Wood and Fiber Science. 41 **(1)**, 28 - 37.

Iskra, P. and Tanaka, C. (2006). "A comparison of selected acoustic signal analysis techniques to evaluate wood surface roughness produced during routing". Wood Science and Technology. 40 **(3)**, 247 - 259.

Ismail, F., Elbestawi, M. A., Du, R. and Urbasik, K. (1993). "Generation of milled surfaces including tool dynamics and wear". Transactions - ASME Journal of Engineering for Industry. 115 **(3)**, 245 - 252.

Ismail, F. and Ziaei, R. (2002). "Chatter suppression in five-axis machining of flexible parts". International Journal of Machine Tools and Manufacture. 42 **(1)**, 115 - 122.

Jackson, M. R. (1986). Some effects of machine characteristics on the surface quality of planed and spindle moulded wooden products. Phd Thesis, Leicester Polytechnic, UK.

Jackson, M. R., Hynek, P. and Parkin, R. M. (2007). "On planing machine engineering characteristics and machined timber surface quality". Proceedings of IMechE Part E: Journal of Process Mechanical Engineering. 221, 17 - 32.

Jackson, M. R., Parkin, R. M. and Brown, N. (2002). "Waves on wood". Proceedings of Institution of Mechanical Engineers, Part B: Journal of Engineering Manufacture. 216 **(4)**, 475-497.

Jackson, M., Yang, D. and Parkin, R. (2007). "Analysis of wood surface waviness with a two-image photometric stereo method". Proceedings of IMecheE, Part I: Journal of Systems and Control Engineering. 222, 1091 - 1099.

Jain, R.C., Kasturi, R. and Shunck, B. G. (1995). Machine Vision, McGraw-Hill.

Jalili, N. (2002). "A comparative study and analysis of semi-active vibration control systems". Journal of Vibration and Acoustic. 124, 593-605.

Jolliffe, I.T. (2002). Principal components analysis, 2nd ed. edn, Springer, NY.

Karnopp, D., Crosby, M. and Harwood, R. (1974). "Vibration control using semi active forces generators". ASME Journal of Engineering for Industry. 96 **(2)**, 619-626.

Karray, F.O. and De Silva, C. (2004). Soft computing and intelligent systems design: Theory tools and applications, Pearson Education Limited, Harlow, Essex.

Lam, H. F. and Liao, W. H. (2001). "Semi-active control of automotive suspension systems with magnetorheological dampers", Proceedings of SPIE, Newport Beach, CA, USA, March 5th, 2001, vol. 4327, pp. 125-136, .

Lauffer, J. P., Regelbrugge, M. E., Dohner, J. L., Hinnerichs, T. D., Kwan, C. M., Lin, Y. and Xu, R. (1998). "Smart spindle unit for active chatter suppression of a milling machine: II. Dynamics and control", Smart Structures and Materials 1998: Industrial and Commercial Applications of Smart Structures Technologies, San Diego, CA, USA, March 03, 1998, vol. 3326, pp. 167 - 173, .

Lee, E. C., Nian, C. Y. and Tarng, Y. S. (2001). "Design of a dynamic vibration absorber against vibrations in turning operations". Journal of Materials Processing Technology. 108 **(3)**, 278 -285.

Lee, J. M., Choi, D. K., Kim, J. and Chu, C. N. (1995). "Real-time tool breakage monitoring for NC milling processes". CIRP Annals. 44 **(1)**, 59-62.

Lee, K. Y., Kang, M. C., Jeong, Y. H., Lee, D. W. and Kim, J. S. (2001). "Simulation of surface roughness and profile in high-speed end milling". Journals of Materials Processing Technology. 113 **(1-3)**, 410 - 415.

Lemaster, R. L., Lu, L. and Jackson, S. (2000b). "Use of process monitoring techniques on a CNC wood router. Part 2. Use of vibration accelerometer to monitor tool wear and workpiece quality.". Forests Product Journals. 50 **(9)**, 59 - 64.

Lemaster, R. L., Lu, L. and Jackson, S. (2000a). "Use of process monitoring techniques on a CNC wood router. Part 1. Sensor Selection". Forests Product Journal. 50 **(7)**, 31 - 38.

Lemaster, R. L. and Stewart, J. S. (1995). "Progress in evaluating surface quality using optical profilometer techniques", Proceedings of the 12th International Wood Machining Seminar, Kyoto, Japan, Oct, 1995, pp. 81-91, .

Li, H. and Zhao, D. (2006). "Control of structure with semi-active friction damper", 2006 IEEE International Conference on Fuzzy Systems, Vancouver, Canada, July 16-21, 2006, pp. 1584-1590, ISSN 0-7803-9488-7.

Liu, Y., Tao, G. and Joshi, S. M. (2009). "Modelling and model reference adaptive control of aircraft with asymmetric damage". Journal of Guidance, Control, and Dynamics. 33 **(5)**, 1500 - 1517.

Liu, Z., Wang, H. and Peng, S. (2004). "Texture segmentation using directional empirical mode decomposition", 2004 International Conference on Image Processing, Piscataway, US, 24-27 Oct, 2004, vol. 1, pp. 279- 282, ISSN 0-7803-8554-3.

Ljung, L. (2002). "Prediction error estimation methods". Circuits, Systems, and Signal Processing. 21 **(1)**, 11 - 21.

Ljung, L. (1999). System identification: theory for the user, 2nd Edition edn, Prentice-Hall, Inc.

Maristany, A. G., Lebow, P. K., Brunner, C. C., Butler, D. A. and Funck, J. W. (1992). "Classifying wood surface features using dichromatic reflection". Proceedings of the SPIE - The International Society of Optical Engineering. 1836, 56 - 64.

Maycock, K. M. (1993). The assessment of surface quality in planed and spindle moulded products. Phd Thesis, De Montfort University, UK.

Mei, D., Kong, T., Shih, A. J. and Chen, Z. (2009). "Magnetorheological fluid-controlled boring bar for chatter suppression". Journal of Materials Processing Technology. 209 **(4)**, 1861-1870.

Miranda, A. A., Borgne, Y. A. and Bontempi, G. (2008). "New routes from minimal approximation error to principal components". Neural Processing Letters. 27 **(3)**, 197-207.

Moheimani, S. O., Peterson, I. R. and Pota, H. R. (2004). "Emerging technologies for active noise and vibration control systems". Control Engineering Practice. 12, 987-988.

Norgaard, M., Ravn, O., Poulsen, N. K. and Hansen, L. K. (2000). Neural networks for modelling and control of dynamic systems: A practitioner's handbook, Springer-Verlag London Limited.

Parkin, R. M. and Jackson, M. R. (1996). "A mechatronic approach for analysis of timber surfaces". Mathematics and Computers In Simulation. 41 **(5-6)**, 445-450.

Peck, T. (2002). "The international timber trade". Forest Products Journal. 52 **(9)**, 10 -19.

Peng, Z. K., Tse, P. W. and Chu, F. L. (2005). "An improved Hilbert-Huang transform and its application in vibration signal analysis". Journal of Sound and Vibration. 286 **(1-2)**, 187-205.

Peter, N. K., Romstadt, D. L., Lizell, M. B. and Weyenberg, T. R. (1995). "Demonstration of an automotive semi-active suspension using electrorheleogical fluid". SAE Paper No. 950586.

Peters, C. C. and Cumming, J. D. (1970). "Measuring wood surface smoothness: A review". Forests Products Journal. 20 **(12)**, 40-43.

Pettersson, L., Hakansson, L., Claesson, I. and Olsson, S. (2001). "Active control of machine tool vibration in a CNC lathe based on an active tool holder shank with embedded piezo ceramic actuators", The 8th International Congress on Sound and Vibration, Hong Kong, China, Jul. 2-6, 2001, .

Ping, W., Baohua, C., Wenchao, X. and Hui, D. (2010). "The direct inverse-model control based on neural networks for inverts", 2010 International Conference on Measuring Technology and Mechatronics Automation, Changsha, China, March, 13-14, 2010, vol. 3, pp. 855 - 858, ISSN 978-1-4244-5001-5.

Qin, Y. and Park, S. S. (2005). "Robust adaptive control of machining operations", 2005 IEEE International Conference on Mechatronics and Automation, Niagra Falls, Ontario, July 29 - Aug 1, 2005, vol. 2, pp. 975 - 979, ISSN 0-7803-9044-X.

Qiu, J., Ji, H. and Zhu, K. (2009). "Semi-active vibration control using piezoelectric actuators in smart structures". Frontiers of Mechanical Engineering in China. 4 **(3)**, 242 - 251.

Ramaratnam, A. and Jalili, N. (2006). "A switched stiffness approach for structural vibration control: theory and real time implementation". Journal of Sound and Vibration. 291, 258 - 274.

Rashid, A. and Nicolescu, C. M. (2006). "Active vibration control in palletised workholding system for milling". International Journal of Machine Tools and Manufacture. 46 **(12-13)**, 1626 - 1636.

Ratnasingham, J. (2008). "The implications of machining defects in wood planing operations (Part 1)". Woodworking International Journal., 10-11.

Razaeeian, A., Yousefi-Koma, A., Shasti, B. and Doosthoseini, A. (2008). "ANFIS modelling and feedforward control of shape memory alloy actuators". International Journal of Mathematical Models and Methods in Applied Sciences. 2 **(2)**, 228 - 235.

Renshaw, A. A. (1998). "Critical speed for floopy disks". Journal of Applied Mechanics. 65, 116 - 120.

Rojas, J., Liang, C. and Geng, Z. J. (1996). "Experimental investigation of active machine tool vibration control", Smart Structures and Materials 1996: Industrial and Commercial Applications of Smart Structures Technologies, San Diego, CA, USA, Feb. 27, 1996, vol. 2721, pp. 373-384, ISSN 0-8194-2096-4.

Rowley, C. W. and Batten, B. A. (2008). "Dynamic and closed-loop control". American Institute of Aeronautics and Astronautics. vol. 231, pp 40.

Sandak, J., Tanaka , C. and Ohtani, T. (2003). "Evaluation of surface smoothness by laser displacement sensor I: Effect of wood species". Journal of Wood Science. 49 **(4)**, 305-311.

Sandak, J. and Tanaka, C. (2005). "Evaluation of surface smoothness using a light-sectioning shadow scanner". Journal of Wood Science. 51 **(3)**, 270-273.

Seborg, D.E., Edgar, T. F. and Mellichamp, D. A. (2004). Process dynamics and control, 2nd Edition edn, John Wiley & Sons, New York.

Sims, N. D. and Zhang, Y. (2003). "Active damping for chatter reduction in high speed machining", Proceedings of AMAS Workshop on Smart Materials and Structures, Jadwisin, Poland, Sept. 2-5, 2003, pp. 195-212, .

Sitkei, G. and Magoss, E. (2003). "Optimum surface roughness of solid woods affected by internal structure and woodworking operations", Proceedings of the 16th International Wood Machining Seminar, Matsue, Japan, August 24-27, pp. 366 -371, .

Smith, M.L. (2001). Surface inspection techniques using the integration of innovative machine vision and graphical modelling techniques, Professional Engineering Publishing Limited, London and Bury St Edmunds, UK.

Smith, M. L. and Smith, L. N. (2005). "Dynamic photometric stereo - a new technique for moving surface analysis". Image and Vision Computing. 23, 841 - 852.

Srinivasan, A.V. and McFarland, D. M. (2001). Smart Structures: Analysis and Design, Cambridge University Press, Cambridge.

Suja Mani Malar, R. and Thyagarajan, T. (2009). "Artificial neural networks based modelling and control of continuous stirred tank reactor". American Journal of Engineering and Applied Sciences. 2 **(1)**, 229 - 235.

Tarng, Y. S., Kao, J. Y. and Lee, E. C. (2000). "Chatter suppression in turning operations with a tuned vibration absorber". Journal of Materials Processing Technology. 105, 55-60.

Teti, R., Jemielniak, K., O'Donnell, G. and Dornfeld, D. (2010). "Advanced monitoring of machining operations". CIRP Annals - Manufacturing Technology. 59, 717 -739.

Tewani, S. G., Rouch, K. E. and Walcott, B. L. (1995). "A study of cutting process stability of a boring bar with active dynamic absorber". International Journal of Machine Tools and Manufacture. 35 **(1)**, 91-108.

Tewari, A. (2002). Modern control design with matlab and simulink, John Wiley and Sons Ltd, West Sussex, England.

Tseng, C., Shen, J., Ku, C. and Shen, I. (2002). "Effects of elevated temperatures on rocking vibration of rotating disk and spindle systems". Journal of Tribology. 124 **(4)**, 794 - 800.

Tumer, I. Y., Srinivasan, R. S. and Wood, K. L. (1995). "Investigation of characteristic measures for the analysis and synthesis of precision-machined surfaces". Journal of Manufacturing Systems. 14 **(5)**, 378 - 392.

Tumer, I. Y., Wood, K. L. and Busch-Vishniac, I. J. (1997). "Improving manufacturing precision using the Karhunen-Loeve transform", Proceedings of DETC '97. 1997 ASME Design Engineering Technical Conference, Sacramento, California, Sept. 14 - 17, 1997, pp. 1 - 12, .

Tumer, I., Wood, K. and Busch-Vishniac, I. (1997b). "Monitoring fault condition during manufacturing using the Karhunen-Loeve transform", In 1997 ASME Mechanical Vibration and Noise Conference, System Health Monitoring Symposium, Sacramento, California, .

Wang, J. and Hsieh, M. F. (2009). "Vehicle yaw inertia and mass-independent adaptive steering control". Proceedings of the Institution of Mechanical Engineers, Part D: Journal of Automobile Engineering. 223 **(9)**, 1101-1108.

Wang, J. and Su, C. (2003). "Two degree-of-freedom modelling and robust chatter control in metal cutting by piezoelectricity", Proceedings of the 2003 American Control Conference, Denver, Colorado, June 4-6, 2003, vol. 4, pp. 3044 - 3048, ISSN 0-7803-7896-2.

Wang, M. and Fei, R. (1999). "Chatter suppression based on nonlinear vibration characteristic of electrorheological fluids". International Journal of Machine Tools and Manufacture. 39, 1925-1934.

Wang, X. G. and Sun, J. C. (2001). "Active sensing and control of vibration of circular saws - a comparison of optimal and variable structure control", Proceedings of the American Conference, Airlington, VA, June 25-27, 2001, pp. 4294 - 4299, ISSN 0-7803-6495-3.

Yang, D. (2006). Measurement of cutter marks on planed wood surfaces with machine vision methods. Ph.D Thesis, Loughborough University, Loughborough, United Kingdom.

Yang, D., Jackson, M. R. and Parkin, R. M. (2006). "Inspection of wood surface waviness defects using the light sectioning method". Proceedings of the Institution of

Mechanical Engineers, Part I: Journal of Systems Control and Engineering. 220 **(7)**, 617 - 626.

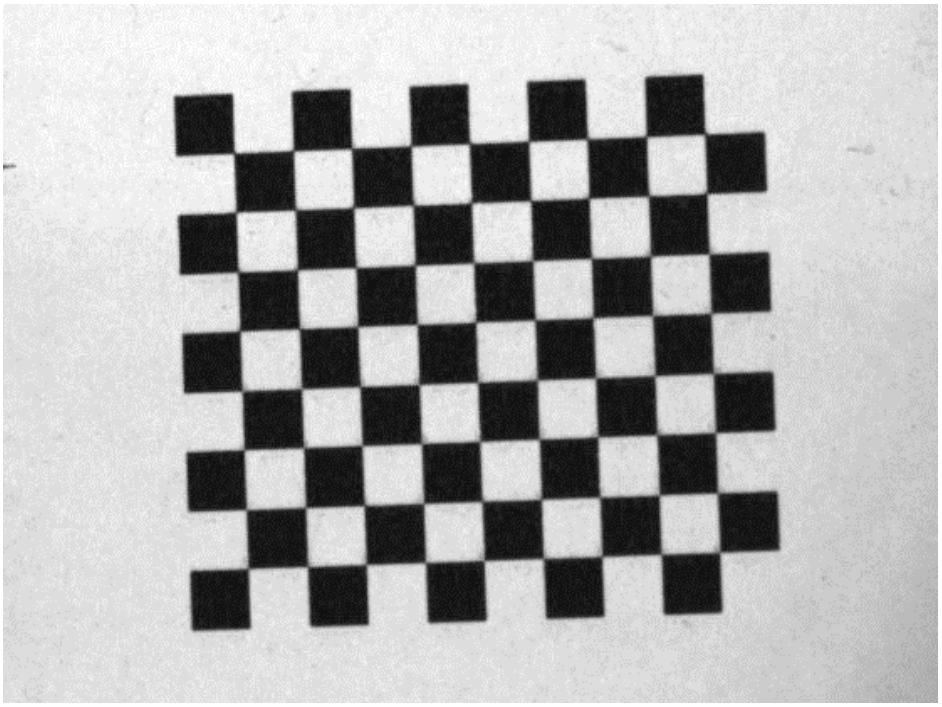
Young, P. C. and Willems, J. C. (1972). "An approach to the linear multivariable servomechanism problem". International Journal of Control. 15 **(5)**, 961 - 979.

Zhang, Y. and Sims, N. D. (2005). "Milling workpiece chatter avoidance using piezoelectric active damping: A feasibility study". Smart Materials and Structures. 14, 65-70.

Zhang, Z. (1999). "Flexible camera calibration by viewing a plane from unknown orientations", The Proceedings of the Seventh IEEE International Conference on Computer Vision, Kerkyra, Greece, Sept 20-27, 1999, vol. 1, pp. 666 - 673, ISSN 0-7695-0164-8.

Appendix A Camera Calibration

The method used for the camera calibration is to target the camera on a 9-by-10 checkerboard pattern of alternating black and with squares. The cell size is 2.65mm by 2.65mm. Such a small cell size has been used because the field of view (FOV) of the camera is just 52mm by 40mm. The required intrinsic parameters are then computed from multiple images (30 images) of the calibration pattern, acquired under different orientations. A minimum of two views of a 3-by-3 checkerboard pattern are required to solve the calibration problem. However, considerations for noise and numerical stability necessitate the collection of more images. A sample of the acquired images is shown below



Sample checkerboard pattern for camera calibration

MATLAB camera calibration toolbox developed by the Computational Vision Group in California Institute of Technology is used for the calibration. The toolbox is based on the calibration procedure developed in Heikkila and Silvan (1997). A C++ implementation of the toolbox is also available in OpenCV computer vision library.

The results of the calibration are shown below. In addition to the computation of the intrinsic parameters, estimates of the uncertainties on each of the computed parameters are also calculated by the calibration toolbox. The uncertainties vectors are three times the standard deviation of the estimation errors.

Focal Length: = [4602.48067 4606.12577] ± [5.44124 5.42088]

Principal Point: = [329.00 246.00] ± [0.0 0.0]

Skew Coef: = [0.00000] ± [0.00000] => angle of pixel axes = 90.00 ± 0.0 degrees

Distortion Coef: = [-0.11749 0.00 0.00 -0.00 0.00] ± [0.004 0.0 0.0 0.0 0.0]

Pixel Error: = [0.28424 0.25485]

Appendix B Test Rig State-Space Model

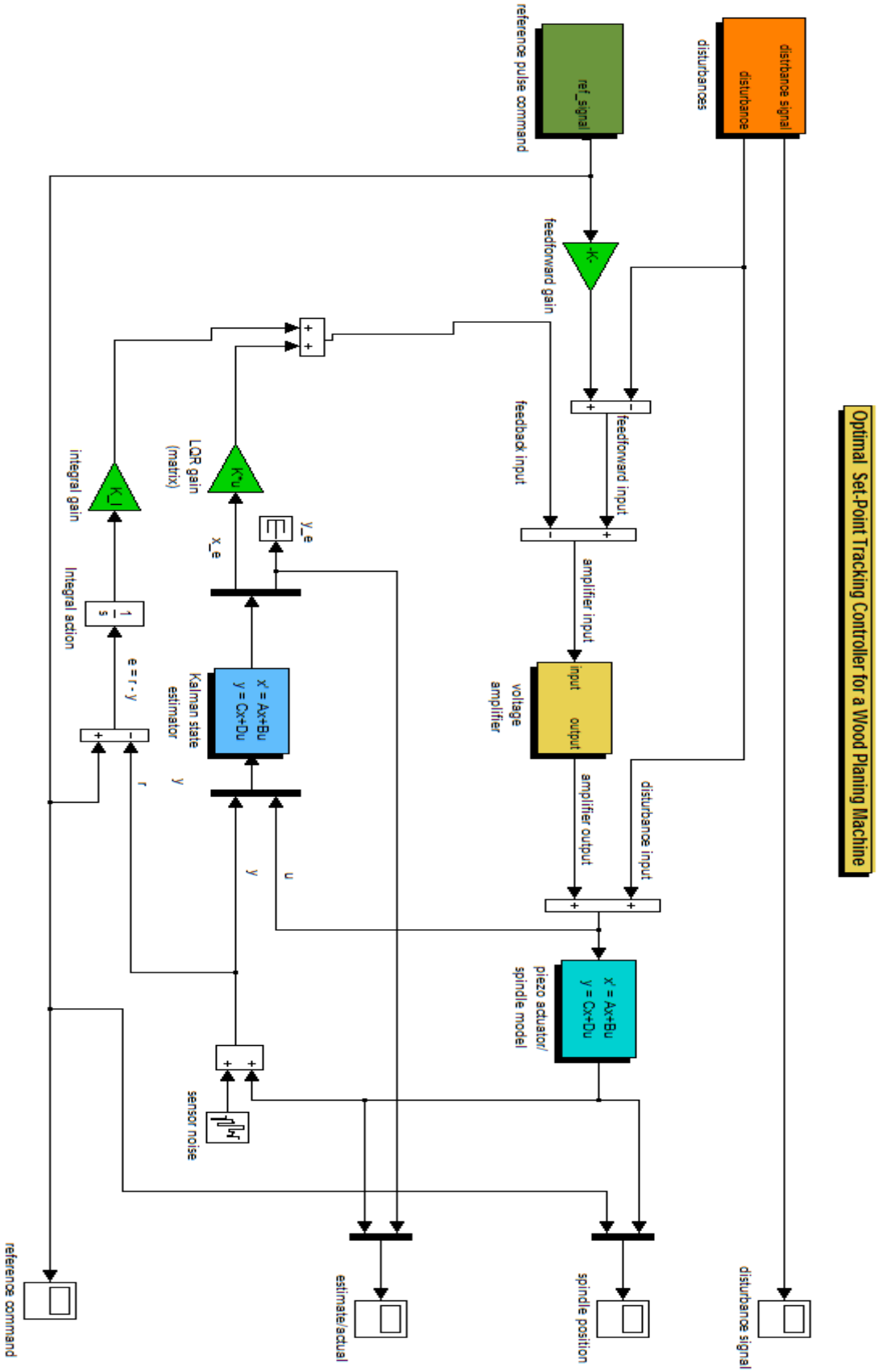
$$A = \begin{bmatrix} 0.11226 & -0.86957 & 0.086895 & -0.00182 \\ 0.11021 & -0.46907 & -0.23771 & 0.02389 \\ 0.83799 & 0.13691 & -0.31585 & -0.41242 \\ 0.16978 & -0.00895 & 0.84689 & -0.39016 \end{bmatrix}$$

$$B = \begin{bmatrix} 0.00064293 \\ -0.0012282 \\ 6.2384e-5 \\ -0.0004514 \end{bmatrix}$$

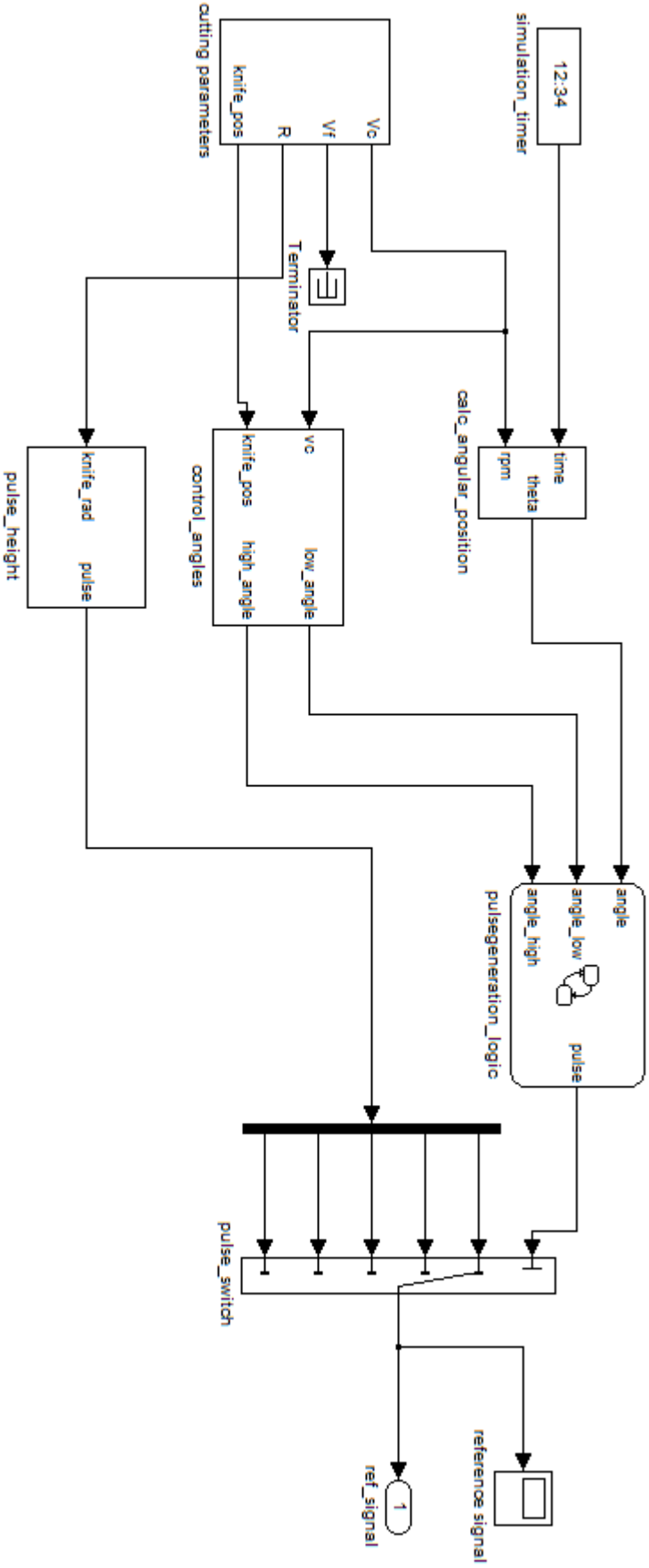
$$C = [61.513 \quad 33.193 \quad 2.8596 \quad -0.19078]$$

$$F = [-0.0045174 \quad -0.0092942 \quad 0.013664 \quad -0.012471]^T$$

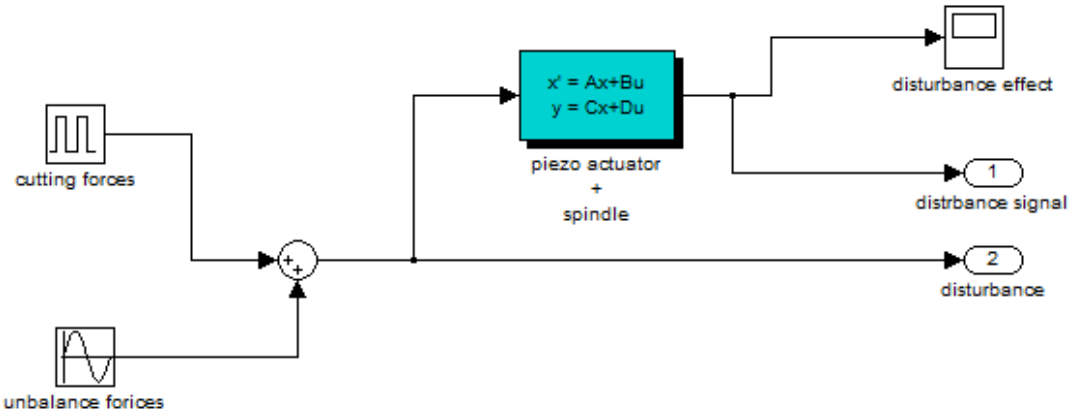
Appendix C Simulink Models for the Tracking Controller



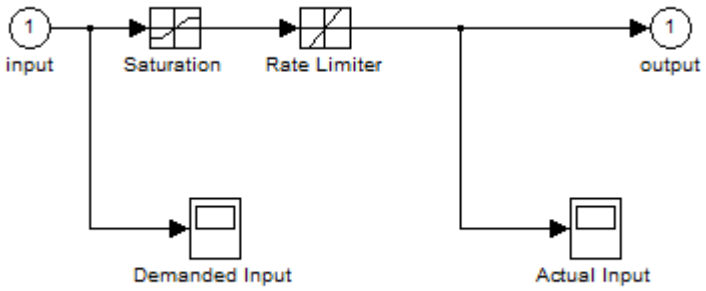
Reference Command Generator



Disturbance Model



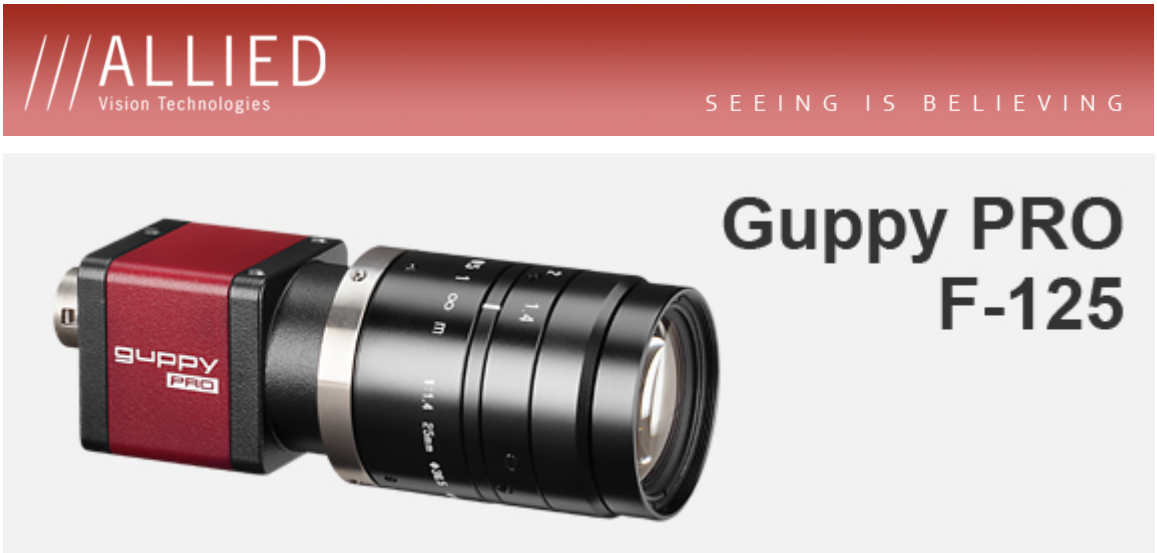
Voltage Amplifier Model



Appendix D Mitutoyo 543-391B Dial Indicator

	Measuring Range Max	12mm
	Accuracy	0.003mm
	Resolution	0.001mm
	Measuring Force Max	1.5N

Appendix E Machine Vision Test Rig Components



Description - FireWire camera - ICX445 CCD

The Guppy PRO F-125B/C is a FireWire camera (1394b) with the sensitive ICX445 CCD sensor and an ultra-compact housing. At full resolution, it runs 30 fps.

- Sony ICX445 EXview HAD CCD sensor
- Trigger
  - Programmable, trigger level control, single trigger, bulk trigger, programmable trigger delay
- Options
  - Various IR cut/pass filters
  - White medical housing

Smart Features

- AOI (separate AOI for auto features)
- Programmable LUT, gamma
- Debayering, color correction
- Gain
  - Auto/manual
  - Manual gain control: 0 - 24.4 dB
- Exposure
  - Auto/manual
  - Exposure time: 35 µs - 67 s
- Binning (2 x 2 b/w)
- Sub-Sampling (2 x 2 b/w)

Specifications

Guppy PRO	F-125
Interface	IEEE 1394b - 800 Mb/s, 1 port
Resolution	1292 x 964
Sensor	Sony ICX445
Sensor type	CCD Progressive
Sensor size	Type 1/3
Cell size	3.75 µm
Lens mount	C
Max frame rate at full resolution	30 fps
A/D	14 bit
	Output
Bit depth	8-14 bit
Mono modes	8/12/16
Color modes YUV	411/422
Color modes RGB	RGB8
Raw modes	8/12/16
	General purpose inputs/outputs (GPIOs)
Opto-coupled I/Os	1/3
	Operating conditions/Dimensions
Power requirements (DC)	8 V - 36 V
Power consumption (12 V)	3 W
Mass	80 g
Body Dimensions (L x W x H in mm)	44.8 x 29 x 29 mm incl. connectors
Regulations	CE, FCC Class B, RoHS

Typical applications:

- Machine vision
- Robotics
- Logistics
- Security and Surveillance
- Healthcare
- Ophthalmology
- Pharmaceutical industry
- Food inspection
- Motion analysis
- ITS/Traffic monitoring

Loughborough University

PURCHASE ORDER REQUEST FORM

Please order the following Goods/Services from

Company:	**Stemmer Imaging Ltd**	**Telephone Number:**	**01252 780022**
Contact:	**Mr Oliver Richford**	**Fax Number:**	**01252 780001**
Address:	**The Old Barn, Grange Court,**	**www.**	**stemmer-imaging.co.uk**
	Tongham, Surrey	**email:** **admin@**	**stemmer-imaging.co.uk**
Postcode:	**GU10 1DW**		

ITEMS REQUIRED

Description	Part No.	Qty	Unit Cost (£)	Total Cost
Monochrome area scan camera (AVT Guppy Pro F-125B)	Guppy Pro F-125B	1	674.00	674.00
Tripod adaptor for AVT Guppy Pro (AVT Adapter Guppy Pro)	Adapter Guppy Pro	1	26.25	26.25
High resolution lens	TAM M118FM16	1	155	155
				£855.25

Project Code	Product Code	Amount	Budget Holders Signature		
				Discount	5%
				Delivery	0%
				Sub-Total	£812.49
				VAT	£162.51
				Total	£975.00

Date:	08/07/2011	**Name of Requisitioner:**	P Ogun
		Telephone number:	01509 22 6579
		E-mail address:	p.s.ogun@lboro.ac.uk
		Signature:	

AUTHORISED BY DDP

Ordered By:_____ Date:_____Order Number: _____

Completed Inventory: Yes No Inventory Code:

High-Power LED Collimator Sources, 48-mm Clear Aperture (LCS-0470-05-48)



An LED collimator consists of a collimating lens and an LED emitter. The LED emitter is placed at the focal plane of the collimating lens. The collimating lens thus images the LED emitter into infinity. Mightex LED collimators employ a high-NA aspherical collimating lens for precision collimation and high light throughput.

LED collimators can be used as the light source in an illumination system. For example LED collimators can replace the standard lamp assembly in a microscope to provide stable, intense, and fast-modulated illumination. Typically the rest of the illumination optics will image the LED emitter onto the pupil of the imaging optics whereas the lens aperture on the collimator where intensity is uniform will be projected onto the object. In other illumination applications similar arrangement should be made to produce uniform and efficient illumination.

The LED emitters are mounted directly onto the metal base of the collimator which also features an integrated heat sink. This configuration minimizes thermal resistance between the LED emitter and the heat sink resulting in better heat dissipation. The collimating lens can be adjusted if needed for precise collimation. A locking ring fixes the lens position after adjustment.

Specifications

- Wavelength 470nm (Blue Color)
- Clear Aperture Diameter 48mm

Universal Two- and Four-Channel LED Controllers with External Triggers (SLC-SA02-US)



Mightex has developed a series of computer-controllable, multi-channel, universal LED drivers, which can be used to drive any type of LED in any of the three (3) modes: 'NORMAL' (or 'constant current'), 'STROBE', and/or external 'TRIGGER' mode. Each unit comes with PC-based software with a user-friendly GUI, which enables users to drive LEDs without the need to write any code. In addition, a powerful SDK and a rich RS232 command set are provided, in order for users to write their own software in order to integrate Mightex's LED drivers into their own systems. Furthermore, the drivers have a built-in security feature, allowing users to limit LED driving current and voltage.

ELECTRICAL SPECIFICATION:

Parameters	**SLC-AAxx-xx**	**SLC-AVxx-xx**	**SLC-SAxx-xx**	**SLC-SVxx-xx**	**Unit**
Power Supply Input Voltage, V_{dc}	9 ~ 24				V
Power Supply Input Current	< 4000				mA
Per Channel Driving Voltage (max) [1]	<23.5				V
Per Channel Driving Current	0 ~ 1000 ("NORMAL" MODE)				mA
	0 ~ 3500 ("STROBE" or "TRIGGER" MODE)				mA
Output Current Resolution	12				bit
Output Current Linearity	+/-4 (or +/-0.5%)				mA
Output Current Repeatability	+/-1 (or +/-0.2%)				mA
Trigger Input High Level	4.5 ~ 10.0				V
Trigger Input Low Level	0.8 (Max.)				V
Forward Voltage Monitoring Accuracy	N.A.	+/-10	N.A.	+/-10	mV

Notes: 1. Maximum Output Voltage is 0.5V less than the Power Supply Input Voltage. For instance, with a Power Supply Input Voltage of Vdc=24V, the Maximum Output Voltage Vmax would be Vdc-).5V=23.5V

2. Each output channel can be individually configured to work in one of the following three (3) modes, controlled through a PC-based software with GUI. In all three modes, overdrive current limit can be set:

Normal: Constant current output at any value from 0mA to 1000mA with 12-bit resolution. **Trigger:** External trigger signal could be used to turn on each individual channel, generating driving current with any user-defined waveform. Alternatively, each output channel can work under the "FOLLOWER" mode, in which the current output follows the waveform of the trigger input; and **Strobe:** Internal Strobe Generator generates frequencies as high as 25KHz. The strobe signal (i.e. current levels, duty cycle and strobe frequency) can be set through software. For AA and AV series, the strobe signal can be a user-defined arbitrary waveform with 128 data points.

3. Arbitrary Waveform. Using the included application software or SDK or RS232 command set, user may define any arbitrary waveform using 128 data points.

TIMING SPECIFICATION:

Parameters	**SLC-AAxx-xx**	**SLC-AVxx-xx**	**SLC-SAxx-xx**	**SLC-SVxx-xx**	**Unit**
Timing Resolution	20				µs
No of Data Points for Waveform Definition	128		2		
Trigger Pulse Width	100 (Minimum)				µs
Max Trigger Delay	25				µs

Loughborough University

PURCHASE ORDER REQUEST FORM

Please order the following Goods/Services from: (If tenders are required, compile tender list and attach)

Company:	**AMS Technologies Ltd**	**Telephone Number:**	**01455 556360**
Contact:	**Riccardo Tomassoni**	**Fax Number:**	**01455 552974**
Address:	**Unit 11, St Johns Business Park,**	**www.**	**amstechnologies.com**
	Lutterworth, Leicestershire	**email: uk_info @**	**amstechnologies.com**
Postcode:	**LE17 4HB**		

ITEMS REQUIRED

Description	Part No.	Qty	Unit Cost (£)	Total Cost
High-power LED Collimator Source, 470nm, 5W, 48mm aperture	LCS-0470-05-48	2	339	678
Universal Two-Channel LED Controllers with External Triggers	SLC-SA02-US	1	490	490

Project Code	Product Code	Amount	Budget Holders Signature		
				Discount	0%
				Delivery	£25.00
				Sub-Total	£1,168.00
				VAT	£233.60
				Total	£1,426.60

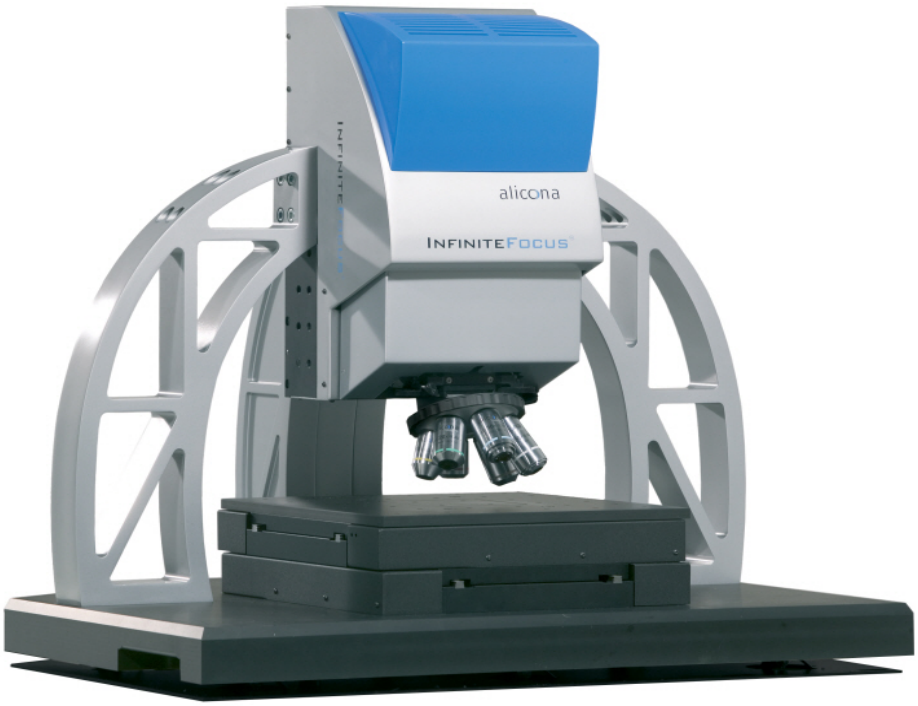
Date:	19/07/2011	**Name of Requisitioner:**	P Ogun
		Telephone number:	01509 22 6579
		E-mail address:	p.s.ogun@lboro.ac.uk
		Signature:	

AUTHORISED BY DDP

Ordered By:_____ Date:_____Order Number: _____

Completed Inventory: Yes No Inventory Code:

Appendix F Alicona InfiniteFocus Instrument



The Alicona InfiniteFocus is a high resolution optical system (non-contact) for 3D surface form and roughness measurement. The operating principle of InfiniteFocus is based on the variation of focus technique (Focus-Variation). The Focus-Variation technique uses small depth of focus of an optical system, combined with continuous vertical scanning, to generate 3D topographic model of the surface. The wood samples were measured using the following parameters:

Objective Lens Magnification	5x
Working distance	23.5mm
Field of View	2858µm x 2175µm
Vertical Resolution	410nm

The Alicona InfiniteFocus has a motorised X-Y table and seamless image stitching algorithm, which allowed the desired sample length to be measured. It is also equipped with a module for the calculation of area-based 2D surface profile measurement.

Appendix G Publications

Conference Papers

Ogun, P. S., Jackson, M. R. and Parkin, R. M. (2010). Determination of the surface reflectance properties of timber using photometric stereo technique. 2nd Computer Science and Electronic Engineering Conference (CEEC 2010), Sept 8-9, 2010, Colchester, UK, pp 1 – 5 ISBN 978-1-4244-9029-5.

Ogun, P. S., Jackson, M. R. and Parkin R. M. (2010). A mechatronic approach towards cutting tools inaccuracies compensation in rotary wood machining. The 14th International Conference on Mechatronics Technology (ICMT 2010), Nov 24-26, 2010, Osaka, Japan, pp 289 – 294.

Ogun, P. S., Jackson, M. R. and Parkin, R. M. (2011). Characterisation of defects on planed timber surfaces using the empirical mode decomposition method. The 15th International Conference on Mechatronics Technology (ICMT 2011), Nov 30 – Dec 2, 2011, Melbourne, Australia, ISBN 978-0-7326-4018-7.

Journals

Ogun, P. S., Jackson, M. R. and Parkin, R. M. (2012). In-process surface profile assessment of rotary machined timber using a dynamic photometric stereo technique. Proceedings of IMechE, Part I: Journal of Systems Control and Engineering. 226 (6), 823-830.

Ogun, P. S., Jackson, M. R. and Parkin, R. M. A mechatronic approach towards surface quality improvements in rotary wood machining.
Submitted to the Proceedings of IMechE, Part B: Journal of Engineering Manufacture.